1-1-2011

Design, Synthesis And Characterization Of Lipidated Pna-Peptide Conjugates As Potentialtherapeutic And Diagnostic Reagents

Yinyin Song
Washington University in St. Louis

Recommended Citation

Song, Yinyin, "Design, Synthesis And Characterization Of Lipidated Pna-Peptide Conjugates As Potentialtherapeutic And Diagnostic Reagents" (2011). *All Theses and Dissertations (ETDs)*. 643.
https://openscholarship.wustl.edu/etd/643

Washington University in St. Louis

Department of Chemistry

Dissertation Examination Committee

Dr. John-Stephen A. Taylor, Chair

Dr. Mikhail Berezin

Dr. Vladimir Birman

Dr. Suzanne E. Lapi

Dr. Joshua Maurer

Dr. Kevin D. Moeller

DESIGN, SYNTHESIS AND CHARACTERIZATION OF LIPIDATED PNA-PEPTIDE CONJUGATES AS POTENTIALTHERAPEUTIC AND DIAGNOSTIC REAGENTS

By Yinyin Song

A dissertation presented to the

Graduate School of Arts and Sciences

of Washington University in

partial fulfillment of the

requirements for the degree

of Doctor of Philosophy

August, 2011

St. Louis, Missouri

ABSTRACT OF THE DISSERTATION

Design, Synthesis and Characterization of Lipidated PNA-peptide Conjugates as Potential Therapeutic and Diagnostic Reagents

by

Yinyin Song

Doctor of Philosophy in Chemistry

Washington University in St. Louis, 2011

Professor John-Stephen A. Taylor, Chairperson

Peptide Nucleic Acids (PNAs), are an ideal choice for antisense and antigene tools and probes because of their stability and high binding affinity, but have limited application as therapeutic and diagnostic agents because of poor membrane permeability. To increase membrane permeability, we conjugated hydrophobic lipids or phospholipid molecules and hydrophilic cell penetrating peptides to the N and C terminus of PNAs, and studied their physical and biological properties.

After solid-phase automated synthesis, PNA-CPPs (TAT/Arg_9) were coupled with lipids or phospholipids before cleavage from the support and then purified by HPLC. The conjugates were characterized by UV-vis and MALDI, and by their ability to form vesicles in water and to partition between water and octanol. The size of the vesicles formed was determined by DLS. One of the Lipid-PNA-TAT conjugates was further tested in vivo as a potential PET imaging reagent after radiolabeling with bromine-76.

Acknowledgments

I would like to express my thanks to those who have supported me in the completion of this dissertation. First of all, I would like to thank my research advisor Dr. John-Stephen Taylor for his nice guidance, continuous support and patience during the past years. And I listed below those beautiful and precious golden moments in this progress.

1, I will never forget the moment Dr. Taylor repeated continuously and loudly several times "Be positive! Be positive! Be positive!", when the biggest shock jumped into my life as a big brain tumor in 2007. Thanks God for bringing those supportive and encouraging messages in this first darkest period of my life. At that moment I was really in urgent need of this word, because three operations followed in the next six months.

2, Being a patient, even if you don’t prefer to be but you still need to go to hospital much more frequently than others, makes me feel very sorry to admit honestly that so much time energy and passion inside had been eaten up that made me struggle at the edge of growing up maturely and professional as a real PhD. And Dr. Taylor was so considerate to try his best to put me always as a research assistant for the whole year, being greatly patient and supportive to allow me to gain back health, especially after those three operations from 2007 to 2008. At those times, I needed to rest and learn to walk like a newborn baby almost every time, not to mention the pain and tears.

3, For almost the whole year of 2009, I really couldn't understand and accept why my experimental results were so odd that I became vulnerable in body, mind and mood. Thank you so much that even in his worst temper, he had always been calm and nice and never shouted at me. This sounds to me that this is like Chinese people that are humble outside and arrogant inside, probably because our culture teaches us to smile politely always even when you are actually crying loudly inside. While here, American people teaches their children to be honest and frank inside first, then try to be the best yourself during your lifetime. And I began to feel that this makes American people look arrogant outside and humble inside. Actually I don't want to and don't prefer to compare to decide the better one. For me I probably think it is important to be really honest to ourselves and then to be humble and open to God's grace always, which could be a golden route to receive the real calmness, wisdom and happiness from the heaven. Not only for this but also for experimental support, I would like to say thank you, Dear Dr. Taylor.

Second, I would like to thank the members of my committee for their helpful suggestions in preparing this dissertation. I am especially grateful to Dr. Kevin Moeller and Dr. Vladimir Birman for their encouragement and valuable advice over the years.

Third, I am grateful to the former and current members for their friendship and support. And I wish to especially acknowledge Dr. Gang Shen, Dr. Yongjian Liu and Yuefei Shen for their kind help and precious advice during my research.

Finally and most important, I would like to thank my parents in China and some very dear and touching friends in California for their unconditional love with pure courage and support always standing at my back, which is exactly like a forever warm smile in my lifetime living memories. And many thanks to God for bring these people to me in these past years, when I slowly and gradually learned to be honest to myself from first the inside then to the outside, even during the moment when feeling hurt by my own shadow and feeling vulnerability inside.

Because of the pure unconditional love from those genuine human beings on this beautiful planet, I grew up little by little to learn how to be positive during the battle of growing up as a PhD. Since their love become the light at the seashore in the darkest night, which provided the only correct direction to the truth, this make me win back my breath as a real human being.

Table of Contents

Chapter 1

Introduction

Chapter 2

Lipid / Phospholipid-PNA-Peptide Conjugates to Down-Regulate Human Telomerase Activity

Chapter 3

Design and Synthesis of Lipid-PNA-Peptide Conjugates as Better Radiolabeled Reagent for PET Imaging

Chapter 4

Design and Synthesis of Lipid-PNA-Peptide Conjugates as mRNA accessible Reagents for inhibiting iNOS Activity in Acute Lung Injury

Chapter 5

List of Figures

Chapter 1

Chapter 2

Chapter 3

Chapter 4

List of Tables

Abbreviations

AIDS	acquired immunodeficiency syndrome
ASGP-R	asialoglycoprotein receptor
ATPs	adenosine triphosphate molecules
Boc	t-Butyloxycarbonyl group
BBB	blood-brain-barrier
BPO	bromoperoxidase
CatLip domain	cationic peptide lipid domain
CHCA	α-cyano-4-hydroxycinnamic acid
CMC	Critical Micelle Concentration
Cal. MW	calculated molecular mass results
CNS	central nervous system
CPP	Cell-penetrating peptide

CQ	chloroquine
DCC	N,N'-Dicyclohexylcarbodiimide
DCM	Dichloromethane
DIPEA	Diisopropylethylamine
DLS	Dynamic Light Scattering
DMEM	Eagle's minimal essential medium
DMF	Dimethylformamide
DNA	double-stranded Deoxyribonucleic acid
DMAP	4-Dimethylaminopyridine
DOTA	1,4,7,10-tetraazacyclododecane-N,N',N,N'-tetraacetic acid
EDTA	Ethylenediaminetetraacetic acid
EDC	1-(3-Dimethylaminopropyl)-3-ethylcarbodiimide hydrochloride
EGFP	enhanced green fluorescent protein gene
ELISA	Enzyme-linked immunosorbent assay
ESI	Electrospray ionization
FBS	Fetal bovine serum

Fmoc	Fluorenylmethyloxycarbonyl
GR	glucocoticoid receptor
HATU	2-(7-Aza-1H-benzotriazole-1-yl)-1,1,3,3-tetramethyluronium hexafluorophosphate
HIV-1	Human immunodeficiency virus type 1
HPLC	High performance liquid chromatography
hTERT	Reverse transcriptase of human telomerase
hTR	human telomerase RNA
IGF-1R	insulin-like growth factor1
IRF-1	interferon regulatory factor-1
K_D	dissociation constants
Lipo	Lipofecamine 2000
LPS	lipopolysaccharide
MALDI-TOF	Matrix-assisted laser desorption ionization time of flight
MAP	“model amphipathic peptide”
MASL	mRNA antisense-accessible sites library
MβCD	methyl-β-cyclodextrin

MPEx	a software called Membrane Protein Explorer
Mtt	4-Methyltrityl group
NF-κB	nuclear factor-κB
NLS	nuclear locatlization sequence
NMR	Nuclear magnetic resonance
iNOS	Inducible Nitric Oxide Synthase
ODN	Oligodeoxynucleotide
RNS	reactive nitrogen species
RT-ROL	reverse transcription with the random oligonucleotide libraries
PAGE	Polyacrylamide Gel Electrophoresis
PBS	Phosphate Buffered Saline
PCR	Polymerase Chain Reaction
PEG-PE	polyethyleneglycol-phosphatidylethanolamine
PET	Positron emission tomography
PTD	protein transduction domain
PNA	Peptide nucleic acid

RNA	Ribonucleic acid
SAGE	serial analysis of gene expression
TAT	An 86-101 residue trans-acting regulatory protein (9-11 kDa) produced early in HIV-1 infection
TFA	Trifluoroacetic acid
TLC	Thin Layer Chromatography
UV-Vis	Ultraviolet-visible

Chapter 1

Introduction

1.1 Peptide nucleic acids (PNAs) as therapeutic and diagnostic agents

In a living cell, genetic information is transferred from dsDNA (double-stranded DNA) to mRNA by the process of transcription and then from mRNA to protein by the process of translation. Thus, antigene technology refers to methods for inhibiting transcription, while antisense technology refers to methods for inhibiting translation.

Peptide nucleic acid (PNA) was first invented and reported by Peter Nielsen and colleagues in 1991 as a third-generation antigene and antisense oligonucleotide analog for applications in diagnosis and therapy. [1, 2] Stucturally designed as a hybrid of peptide and DNA, PNA is constructed with a charge neutral peptide backbone and nucleic acid bases, which enable them to Watson-Crick base pair with complementary DNA (deoxyribonucleic acid), RNA (ribonucleic acid) or PNA oligomers (Figure 1.1).

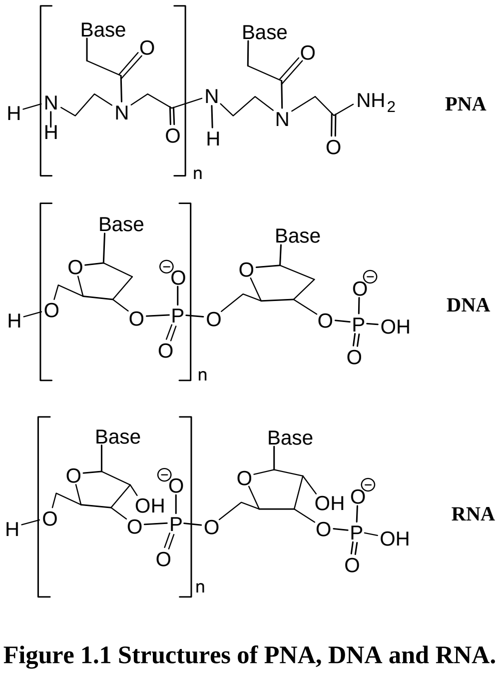

Figure 1.1 Structures of PNA, DNA and RNA.

Due to its neutral non-native peptide backbone, PNA has a number of attractive features for the development of probes and drugs. The neutral backbone of PNA eliminates electrostatic repulsion with a complementary DNA or RNA, thereby improving the binding affinity of PNA for DNA and RNA. Thus PNA-DNA or PNA-RNA duplexes are thermodynamically more stable than corresponding DNA-DNA and DNA-RNA complexes, [3-5] and retain sequence specificity, being able to form duplexes with complementary DNA or RNA by Watson-Crick base-pairng. (Figure 1.2) Because of its neutral charge and high binding affinity, PNA can also invade regions of secondary structure, and thus can bind complementary RNA or DNA sequences with great affinity and specificity, independency of ionic strength. Also due to its non-native peptide backbone PNA is not susceptible to degradation by nucleases and proteases and does not activate RNaseH degradation of a target mRNA.

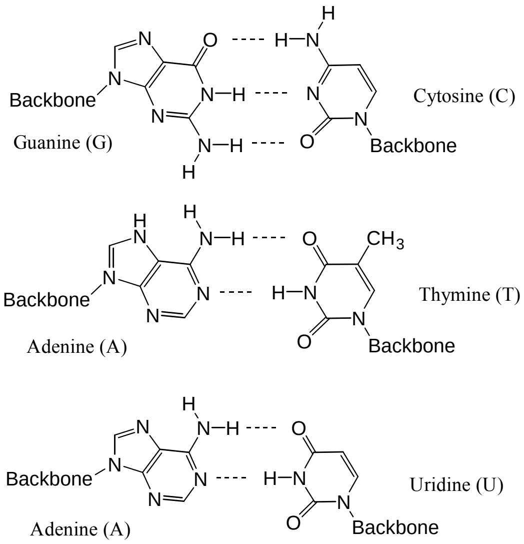

Figure 1.2 Watson-Crick Basepairs for PNA-DNA and PNA-RNA Duplexes

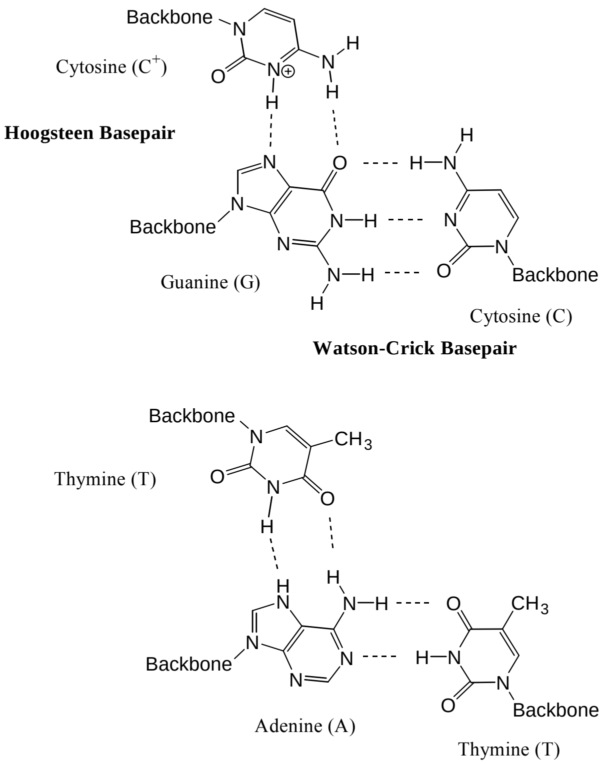

Figure 1.3 Watson-Crick and Hoogsteen Basepairs for PNA-DNA and PNA-RNA Triplexes.

PNA was originally expected to form a conventional triplex complexes with duplex DNA, PNA•$(DNA)_2$, with a homopyrimidine PNA strand binding to the major groove of the ds-DNA helix via Hoogsteen base pairing. However, actually it turned out that a triplex invasion complex of the form $(PNA)_2$•DNA was formed, in which one PNA strands binds to the homopurine DNA stretch by standard Watson-Crick base-pairing in an antiparallel orientation, while a second PNA strand binds the PNA-DNA duplex by Hoogsteen base-pairing probably in a parallel orientation (Figure 1.3). The triplex invasion complexes are very thermally stable with a T_m of more than 85°C, but the formation is slow and pH-dependent at physiological concentrations of salt, because cytosine needs to be protonated to be able to engage in Hoogsteen binding.

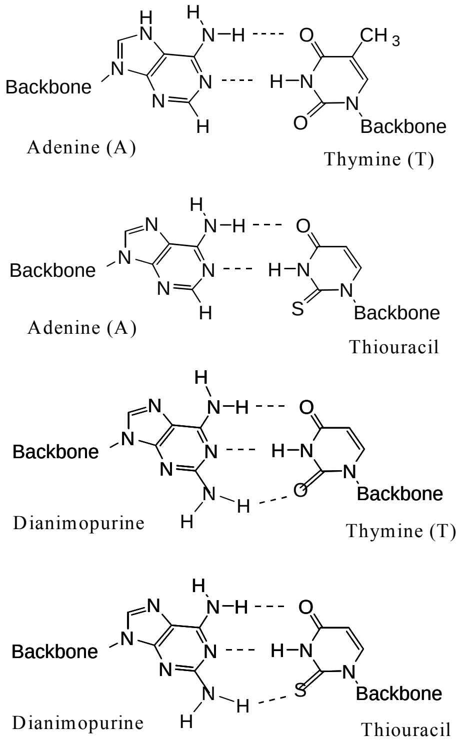

Figure 1.4 Four Types of Pseudocomplementary Basepairs Involved in Forming PNA Double Duplex Invasion Complexes

An alternative approach to targeting double stranded DNA involves designing PNAs that are complementary to each DNA strand, but that have little affinity for each other. Since the 2,6-diaminopurine / 2-thiouracil base pair is very unstable due to steric hindrance resulting from the replacement the oxygen with sulfur, two pseudo complementary PNA sequences cannot bind each other well, but can bind their DNA complement very well (Figure 1.4). Thus, after adenine and thymine are substituted with 2,6-diaminopurine and thiouracil respectively in all A/T base-pairs of PNA, double duplex invasion by pseudo complementary PNAs can take place.[6]

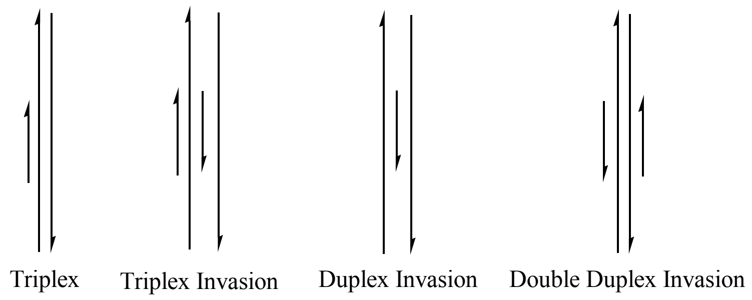

Figure 1.5 Different Structural Modes for Targeting Doubled Stranded DNA with PNA Oligomers.

To test the diagnostic and therapeutic potential of PNA, experiments were initially conducted in cell-free in vitro systems. As an antigene agent, PNA can bind the DNA template strand to form an invasive triplex complex, which results in complete arrest of mRNA elongation because of steric hindrance blocking the RNA polymerase. [7] PNA can also inhibit transcription by forming a triplex with a transcription factor binding site as shown for NF-kB transcription factor. [8] However, effective inhibition of transcription has not been shown to occur with double duplex invasion PNAs, which are formed by pseudo-complementary PNA binding to both the template and the non-template strand, probably because the RNA polymerase is able to disrupt the PNA-DNA duplexes and to continue transcription (Figure 1.5). [9]

As antisense reagents, PNA can arrest translation by forming duplexes and triplexes with mRNA. When PNA is targeted to positions near the start codon, translation initiation can be almost completely inhibited by a PNA binding duplex. [10-12] PNA can also bind at intron-exon junctions of pre-mRNA to form duplexes that inhibit RNA splicing reactions and thereby block maturation of the mRNA.[12]

1.2 Synthesis of PNA and PNA-conjugates

With the refinement of solid-phase PNA/peptide synthesis protocols and commercially available PNA monomers and amino acids, PNA and PNA-conjugates can be assembled on the solid support by Fmoc chemistry, as shown in Figure 1.6. [13]

Although the solid-phase methods are convenient and efficient, the small losses in each of the numerous coupling and deprotection steps place a practical upper limit to the maximum length of a PNA or PNA-conjugate. Thus, direct solid-phase synthesis is not practical for the assembly of longer PNA and PNA-conjugates. Furthermore, the accumulation of truncated oligomers may result in difficult purification and low overall yields.

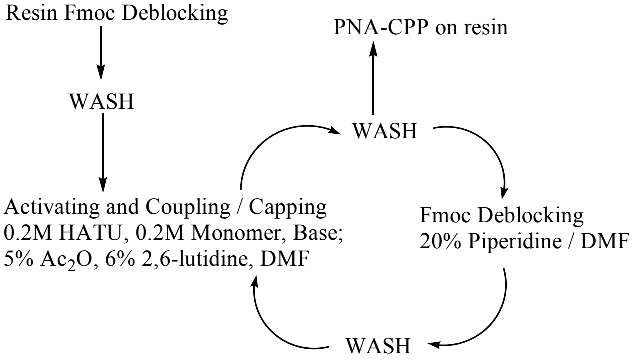

Figure 1.6 Fmoc Solid-phase Synthesis of PNA and PNA-peptide Conjugates

Fragment ligation is an alternative strategy for the assembly of PNA and PNA-conjugates. [14]

This strategy entails the synthesis and purification of PNA and the molecule to be conjoined. Then these two fragments are subsequently joined chemoselectively under the conditions that are compatible with the nucleobases and with the molecule to be conjoined. Different chemical ligation methods have been used, including disulfide bond formation, thio-maleimide linkage formation, and amide bonds formation (Figure 1.7).

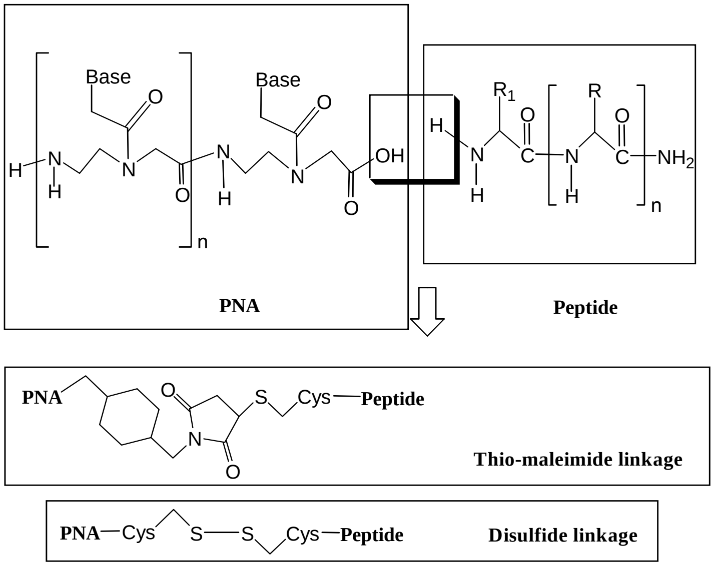

Figure 1.7 Structures of Linkages between PNA and Peptides: Disulfide, Thio-maleimide, Amide and Oxime Linkage.

1.3 Intracellular delivery of unmodified PNAs and modified PNAs

Because PNA is not membrane-permeable due to its size and neutral-charge backbone it does not spontaneously enter eukaryotic cells [22] and many methods have been developed to facilitate its entry.

1.3.1 Methods for intracellular delivery of unmodified PNAs

The first intracellular delivery method of unmodified PNA as antisense agent was by microinjection, and was used to inhibit the expression of SV40 large T antigen. In microinjection, a holding pipette was used to immobilize the cell by suction, and then the PNA solution was injected into the cell nucleus or cytoplasm via an injection pipette under pressure. Immuno-cytochemistry showed that PNAs were able to suppress T-Ag expression by for around 40% and 50%, [10] with at an intracellular concentration of about 1μM. Although microinjection proved to be an effective tool, it was only applicable for small-scale experiments as a laborious technique (Figure 1.8).

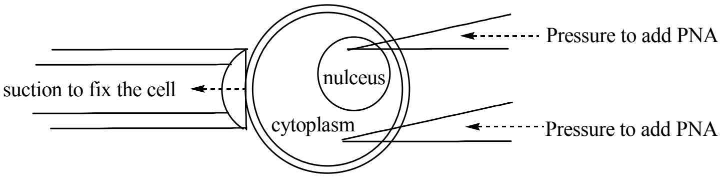

Figure 1.8 Microinjection to deliver PNA into cells

The second method of for intracellular delivery of unmodified PNA was by electroporation as illustrated by the 60% inhibition of telomerase activity by anti-telomerase PNAs in SV40 transformed fibroblasts . [15] The potential of PNA to specifically modulate the constitutive and alternative splicing of murine interleukin-5 receptor-a (IL-5Ra) pre-mRNA was also demonstrated using electroporation. A PNA was designed to inhibit splicing of exon 9 in the IL-5Ra pre-mRNA in a murine B lymphoma cell line which was expected to decrease IL-5Ra membrane isoform transcript expression and enhance expression of the soluble IL-5Ra isoform transcript. In vitro Experiments in cell culture showed a PNA sequence and dose specific repression of the membrane isoform mRNA which could be completely suppressed at 10μM PNA (Figure 1.9). [16]

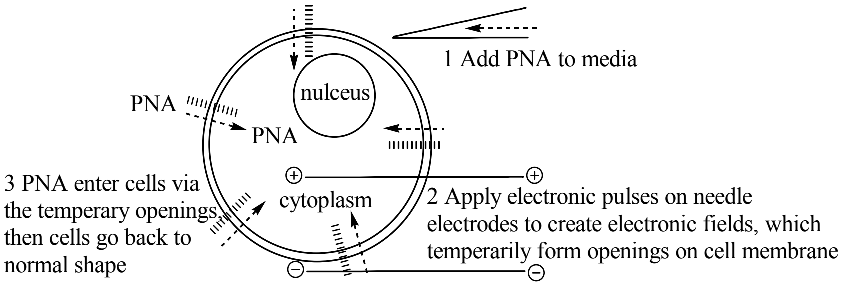

Figure 1.9 Electroporation to deliver PNA into cells

A third way of delivering unmodified PNA to cells was described by Corey's group [17], which took advantage of an established method for DNA transfection that makes use of cationic liposomes. In their approach, anti-telomerase PNA was hybridized to partially complementary DNA oligomers to render them negatively charged, and then using the cationic lipids to transfect the PNA/DNA complexes into cells. And they showed a subsequent study that the terminus of the 5' untranslated region of luciferase could be efficiently reached by lipid-mediated transfection of PNA/DNA complexes (Figure 1.10).

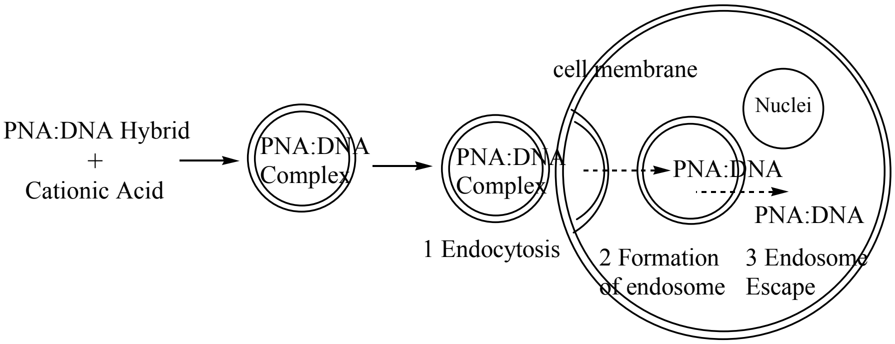

Figure 1.10 Cationic lipid-mediated transfection of PNA•DNA duplexes into cells

In some cases, unmodified PNAs can be directly taken up by cells, but this is not general and depends on the particular cell. For example, the Escherichia coli mutant strain AS19 containing a cell wall/membrane defect was able to uptake. PNA in micro molar concentrations as evidenced by specific inhibition of ribosomal RNA and translation of β-galactosidase and β-lactamase. [18, 19] Direct uptake of PNAs also occurs in some eukaryotic cells. In one case, PNA that was complementary to HIV_1 gag-pol in HIV-1 infected human lymphoma cell line H9, led to an effective disruption of ribosome frameshifting. [20]

1.3.2 Intracellular delivery of modified PNAs

In order to improve PNA transport into the cell, PNAs have also been modified to facilitate intracellular PNA penetration of cell membranes. Herein three main types of modifications are described and evaluated.

Lipophilic Conjugates

The first type of modification to be discussed is conjugation of PNA to lipophilic moieties, like adamantyl, triphenylphosphonium, cholesterol and cholic acid. The delivery efficiency of PNA modified with the adamantyl group was dependent on the cell type and the specific PNA sequence, as monitored by laser confocal microscopy analysis. Attempts to use adamantyl modified PNAs to suppress genes in a leukemic cell line NB4 were not very successful, however (Figure 1.11). [21, 22]

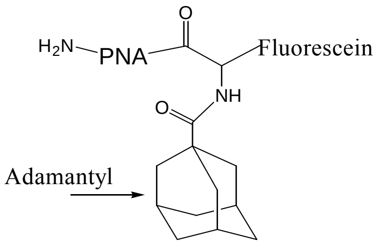

Figure 1.11 Adamantyl acetyl modified PNA conjugate

The intracellular uptake of PNA conjugates modified with triphenylphosphonium cation was tested in human osteosarcoma cells, human fibroblast cells and isolated mitochondria by methods such as confocal microscopy, immunogold-electron microscopy, and cell fractionation with immunoblotting. The results indicated that after enough mitochondrial uptake of the ph-PNAs took places with adding a concentration of 1μM of PNA conjugate during mitochondrial replication, the PNA conjugate cannot bind its target during replication of mitochondrial DNA in vivo (Figure 1.12). [23]

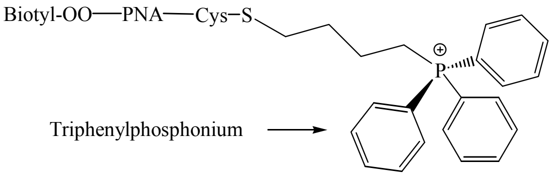

Figure 1.12 Triphenylphosphonium modified PNA conjugate

Cholesterol and its analogues are highly lipophilic molecules have been used to improve cellular delivery of oligonucleotides [24, 25], and DNAs [26, 27] as anticancer agents. The intracellular uptake properties of cholesterol-PNA conjugates, however, have not been proven to be as effective as cholesterol conjugated antisense oligonuleotide. [28, 29]

More recently, attempts have been made to make use of steroid receptors to enhance delivery of PNAs. DEX-bisPNA, consisting of a dexamethasone moiety linked to a PNA clamp (bisPNA) through a spacer, was synthesized and selected from several bifunctional steroid derivatives. [30] DEX-bisPNA was shown to bind to the glucocorticoid receptor (GR) which improved the intracellular delivery of the PNA and its translocation from the cytoplasm into the nucleus, resulting in an enhanced GR-dependent expression of the targeted reporter gene. However, this delivery system was limited for cells expressing steroid receptors (Figure 1.13).

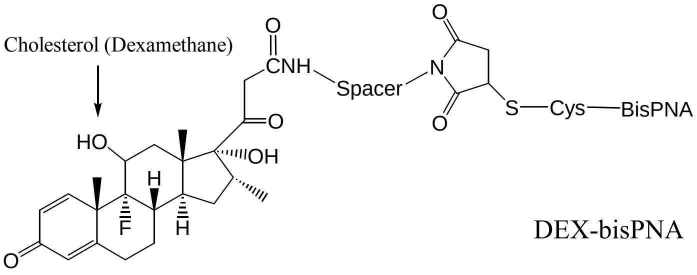

Figure 1.13 Dexamethasone modified PNA conjugate: DEX-bisPNA

Bile acids are also highly lipophilic and have been conjugated to PNA in an effort to improve intracellular delivery. One of bile acids, cholic acid, contains a 3-hydroxy group that could be used to conjugate it to the N-terminus of PNA. Unfortunately, the intracellular uptake of the PNA-cholic acid conjugate by the bile acid transporter has not been reported as yet. Only melting temperature experiments have been reported showing that cholic acid weakly improved binding to complementary DNA (ΔT_m = 3.5°C), in contrast to DNA-cholic acid conjugates that showed a substantial increase (ΔT_m = 8-11°C) in the thermal stability of DNA duplexes (Figure 1.14). [31]

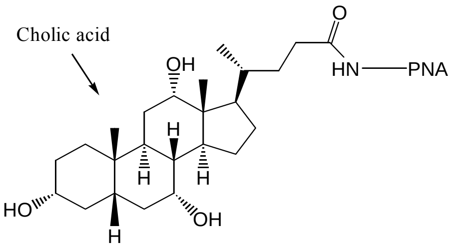

Figure 1.14 Cholic acid modified PNA conjugate

PNAs have also been conjugated to other types of lipophilic molecules, such as acridine, psoralen and anthraquinone, but for other purposes, and so their ability to enhance membrane permeability is not well documents. The DNA intercalator, 9-Aminoacridine, was conjugated to mono or bis-PNA to improve PNA strand invasion at different ion strength. [32, 33] Psoralen is a photoreactive DNA crosslinker that has been conjugated to PNA to enhance its binding to DNA, by forming bonds with pyrimidine bases in the DNA via [2+2]-cycloaddition reactions. [34] The PNA-anthraquinone conjugate was synthesized and used to deduce the structures of the complexes formed between the PNA and DNA by identifying the strongest cleavage sites of photo-cleavage reaction (Figure 1.15). [35]

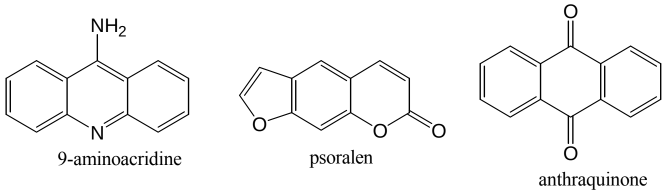

9-aminoacridine
psoralen
anthraquinone

Figure 1.15 Structures of 9-aminoacridine, psoralen and anthraquinone

Receptor Ligand Conjugates

The second type modification was conjugation of PNA to cell-specific receptor ligands with the purpose of improving intracellular delivery, like lactose, dihydrotestosterone, and insulin like growth factor I. [36, 37]

Wickstrom et al [36] conjugated PNA to a peptide, which specifically targeted the cell surface receptor for insulin-like growth factor1 (IGF-1R). Laser confocal microscopy demonstrated that only IGF-1R-expressing cells internalized the conjugated PNA, however, the PNA was exclusively found in vesicular compartments of the cytosol (Figure 1.16).

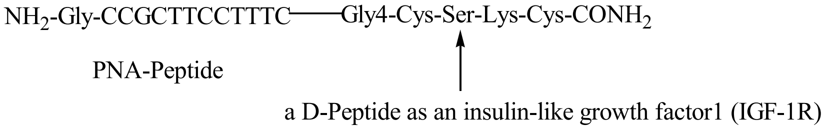

NH_2-Gly-CCGCTTCCTTTC——Gly4-Cys-Ser-Lys-Cys-$CONH_2$

Figure 1.16 PNA-Peptide conjugate containing a D-Peptide of insulin-like growth factor 1(IGF-1R)

Corey et al [38] conjugated lactose to anti-telomerase PNA, since lactose can be recognized by the hepatic asialoglycoprotein receptor (ASGP-R). Fluorescence experiments were conducted in two cell lines, HepG2 as liver carcinoma derived ASGP-R expressing cells and DU145 as prostate carcinoma ASGP-R negative cells. Although only the ASGP-R cells internalized the PNA-lactose conjugate, the uptake was weak and PNA conjugate was confined to vesicular compartments of the cytoplasm. (Figure 1.17)

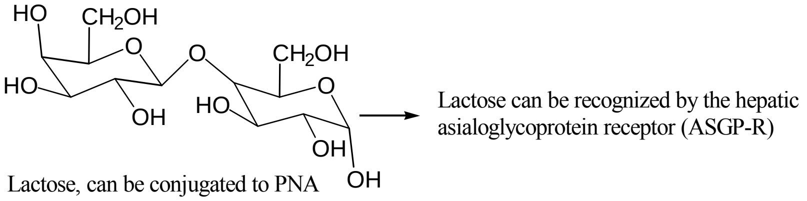

Figure 1.17 Structure of lactose

Boffa et al [37] used dihydrotestosterone (T)-PNA in two cell lines of LNACaP expressing the androgen receptor and the DU145 cell line that did not. Confocal scanning microscopy showed strong cytoplasmic and nuclear uptake of the T-PNA conjugate in LNACaP cells, while cytoplasmic uptake was limited in the DU145 cells. However, unmodified PNA demonstrated the opposite uptake result in two cell lines, making the cellular uptake of the T-PNA highly controversial (Figure 1.18).

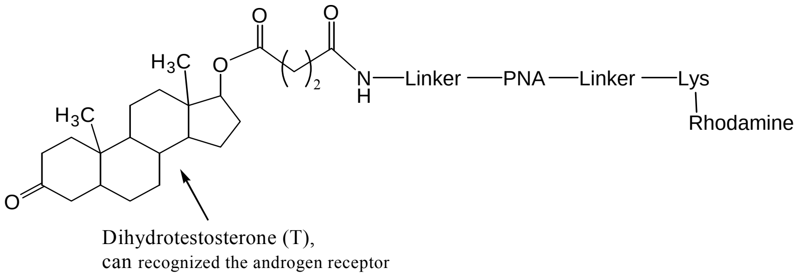

Figure 1.18 Dihydrotestosterone-PNA-Rhodamine conjugate

Cell penetrating peptide Conjugates

The third type modification was to conjugate PNAs to cell-penetrating peptides, which are known to penetrate biological membranes. The most well-studied CPPs included penetratin, transportan, nuclear localization sequence (NLS), polylysine, polyarginine, HIV-1 TAT(48-58), etc., shown as below (Table 1.1).

Table 1.1 Peptide sequences of penetratin, transportan, nuclear localization sequence (NLS), polylysine, polyarginine, HIV-1 TAT(48-58)

pAntp(43-58)/Penetratin :	RQIKIWFQNRRMKWKK
Transportan :	GWTLNSAGYLLGKINLKALAALAKKIL
Nuclear Location Sequence (NLS) :	PKKKKRKV
PolyLysine :	$(Lys)_n$
PolyArginine :	$(Arg)_n$
HIV-1 TAT (48-58)	YGRKKRRKRRR

PNA conjugates with penetratin have shown cell dependent differences in cellular uptake. In human prostate carcinoma, cutaneous melanoma, breast carcinoma, fibroblast and cervix carcinoma, the PNA-penetratin conjugates were found to be entrapped in vesicular compartments in the cytoplasm, and a very limited antisense effect was observed. The entrapment of PNAs in vesicle was shown by immunofluorescence studies, at a concentration of 10 μM of biotinylated penetratin-PNA conjugate. [39] In contrast, PNA-penetratin conjugates had a strong intracellular effect in primary magnocellular neuron cells. In these cells, a sequence-specific and dose-dependent down regulation of the prepro-oxytocin gene was demonstrated by RT-PCR (Reverse transcription-polymerase chain reaction). [40] And Pooga et al. demonstrated similar dose-dependent cell and sequence specific results for transportan-PNA conjugates. [41]

A 7-mer basic nuclear localization signal (NLS) peptide (PKKKKRKV) was also conjugated to improve the nuclear delivery of PNA in Burkitt's lymphomas (BL) cells, containing a hyperexpressed c-myc oncogene. Confocal microscopy showed that only the antisense PNA-NLS conjugates labeled with rhodamine entered intact isolated nuclei of BL cells, and the other two groups of PNA conjugates with a scrambled NLS peptide or without the NLS peptide were only delivered into the cytoplasm of

BL cells. The NLS antisense PNA conjugates also showed inhibition of c-myc expression by Western and Northern blotting. [42] BL cells were also exposed to Rhodamine-PNA-mycwt, Rhodamine-PNA-mycwt-NLS, or Rhodamine-PNA-mycwt-NLSscr, and analyzed by confocal microscopy. A 10 mM PNA-MYCwt-NLS concentration caused maximum inhibition of MYC expression of 75 % with only a 25 % decrease in cell viability, although a 30% decrease was already observed at 5 mM. The three panels were first used to show the phase contrast images of the optical section crossing the middle of the nuclei, and the three panels were then used to show the fluorescence images, and the three bottom panels were finally used to show the superimposed images of the phase contrast and fluorescence images.

Polylysine or lysine was also investigated for its ability to enhance intracellular delivery of PNA in HeLa cells (named after a patient died of cancers called Henrietta Lacks) by monitoring the production of enhanced green fluorescent protein gene (EGFP) which would only be expressed in the presence of the splice-correcting Lys-PNA conjugate. High levels of EGFP were observed in the presence of 1-10μM of PNA-$(\text{Lys})_n$ conjugates.[43]

1.4 Mechanism of intracellular delivery of PNA by cell-penetrating peptides

Cell-penetrating peptides (CPP), are short sequences of peptides that can facilitate entry of attached molecules into cells. To be classified as a CPP, a peptide needs to be shown to enter cells by at least three different assays. [44] CPPs can be divided into families or subgroups: protein derived (P), chimeric (C), and designed/synthetic (S). The largest family is the protein-derived CPPs. Penetratin or pAnt, as a homeodomain-derived peptide, is important among this first family. Homeoproteins are defined as a class of transcription factors that bind DNA through a common protein structure of 60 amino acids in length, called the homeodomain. The next family of CPPs is the chimeric peptides that are partly derived from naturally occurring peptides or proteins, and partly derived from synthetic peptides. The final family of synthetic CPPs is a type that have been designed and synthesized to facilitate the intracellular delivery, like the "model amphipathic peptide" (MAP) which forms amphipathic alpha helices, or polylysine and polyarginine that bear multiple positive charges.

There are three principal mechanisms [45] proposed to be involved in transporting molecules across the boundary cellular membranes, such as passive or gradient diffusion, facilitated diffusion, and active transport (Figure 1.19).

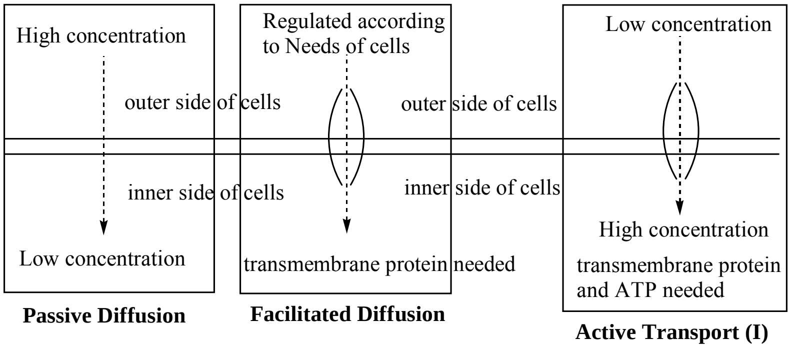

Figure 1.19 Three principal mechanisms of (1) passive diffusion, (2) facilitated diffusion and (3) active transport (I) for intracellular delivery of molecules through the cell membrane

Passive diffusion (Figure 1.19) is a spontaneous process in which the random motions of molecules or other particles move across the cell membrane from the outside region of high concentration into the inside region of lower concentration. The diffusion rate is dependent on the temperature, the molecular weight, and the differences between the outer and the inner concentrations of the molecule. This mechanism is usually used by small molecules without much selectivity.

Facilitated diffusion (Figure 1.19) is a transport process that is assisted by specific transmembrane integral proteins, and is not energy-dependent. In this case, the transmembrane proteins are ion-channels for ions or small molecules needed by the cell, and which are regulated by molecules binding to cell receptors.

Active transport is a transmembrane delivery system for molecules into cells or cell organelles from a region of low concentration to a region of high concentration, requiring of ATP (adenosine triphosphate) as cellular energy source. Two main types of active transport have been characterized, one involving direct movement of a molecule across the cell membrane with assistance from transport proteins, and another involving endocytosis in which the membrane engulfs molecules and then folds into a vacuole or vesicle that enters the cell (Figure 1.19 and 1.20).

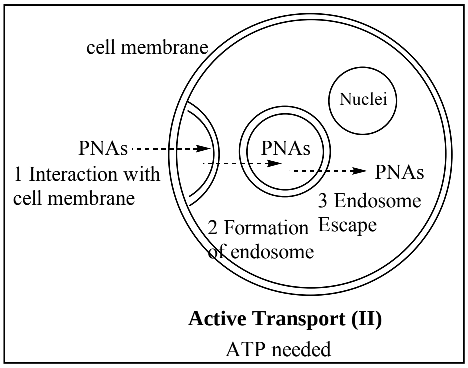

Figure 1.20 Mechanism of active transport (II) of molecules into cells

Since the transport mechanism of passive diffusion is limited by molecule size, this mechanism is not utilized by CPPs. Thus, CPPs enter cells either by facilitated diffusion or endocytosis. It was first proposed that CPPs, especially penetratin, poly-Arg and TAT [46-48], could pass through the plasma membrane via an energy-independent pathway of diffusion.

However, this mechanism became less popular when the entry mechanism for the TAT and the poly-arginine CPPs were re-evaluated by Lebleu B. et al [49], according to their evidences of fixation artifacts during the preparation of samples for microscopic observation, thus it was argued that CPPs and /or their cargoes can cross cell-membrane through endocytosis. In their fluorescence microscopy experiments, HeLa and CHO cells were either fixed with formaldehyde or left untreated. In the unfixed cells, small fluorescence spots were found in the cytoplasm providing as the first evidence that intracellular delivery of PNA-CPP conjugates was occurring by endocytosis.

Following this initial study, the mechanism of endocytosis of various CPPs with or without attached cargoes was extensively studied.

Three major endocytosis pathways [50] were identified as clathrin-mediated, caveolin-mediated and macropinocytosis, although the endocytosis process was actually more complex and involved a large network of protein-protein and protein-lipid interactions.

The clathrin-dependent endocytosis pathway [51] begins on the plasma membrane with a gradual invagination and formation of clathrin-coated vesicles, followed by its release into the cytoplasm. This pathway can be inhibited by potassium depletion or treatment with chlorpromazine as inhibitors. When HeLa cells were treated with chlorpromazine and Alexa-Fluor 488-tagged TAT peptide, a 50% inhibition of peptide uptake was observed. Similarly, HeLa cells treated with the Alexa-Fluor 488-tagged TAT peptide in potassium-free buffer resulted in a 40% inhibition of peptide uptake indicating that some of the uptake was due to the clathrin-dependent endocytosis pathway.

The caveolae-mediated endocytosis pathway [52] is involved in the intracellular signal transduction of raft-associated molecules. Caveolae are defined as small (50–70 nm) invaginations in the plasma membrane that constitute a subclass of detergent-resistant membrane domains with many cholesterol and sphingolipids. This caveolae-mediated endocytosis pathway [52] was shown to be involved with HIV-1 TAT fusion proteins proven with by Giacca et al. Transferrin is known to be internalized by binding to clathrin-coated invaginations on the plasma membrane which eventually detaches to form the clathrin-coated vesicles in cells, and can be disrupted by Triton X-100 extraction. In the presence of Triton X-100, no vesicles containing fluorescently labeled transferrin or TAT fusion proteins were observed, but could be observed in its absence, demonstrating the involvement of clathrin-dependent endocytosis of TAT peptide. When cells were treated with methyl-β-cyclodextrin (MβCD), a drug that extracts cholesterol from cell membranes and disrupts the lipid rafts for endocytosis TAT fusion proteins remained on the cell membrane without the apparent endocytosis. In contrast the internalization of transferrin was not affected by the drug.

Macropinocytosis is a receptor-independent form of endocytosis caused by plasma membrane ruffling. Macropinocytosis was demonstrated to occur for CPP conjugated large molecules with MW > 30,000 Da by Dowdy et al through confocal microscopy experiments.[53] In their experiments three macropinocytosis inhibitors were used to determine if peptides entered cells by lipid raft-mediated macropinocytosis, such as methyl-β-cyclodextrin (MβCD) which depletes cell surface associated cholesterol required to form lipid rafts, cytochalasin D as an inhibitor of F-actin, and EIPA as an inhibitor of the Na^+/H^+ exchange in the macropinosome formation. Treatment of cells with those three macropinosome inhibitors resulted in dose-dependent reduction of TAT peptide uptake. These observations demonstrated that lipid raft-mediated macropinocytosis was the endocytosis pathway by which TAT peptide to entered cells.

In order to improve the delivery efficiency of CPPs into the cytoplasm via endocytosis pathways, methods for enhancing endosomal escape were investigated. Endosome escape was reported to be facilitated by decreased endosomal pH, and inhibited by increased endosomal pH by Gellman et al. [54] No uptake of Flu-TAT or Flu-β-$(VRR)_4$ was seen in the presence of azide and deoxyglucose, but was observed upon prior treatment with 50 mM ammonium chloride for 30 min to lower the pH. These results demonstrated that endosome escape was facilitated by decreased endosomal pH by the addition of ammonium chloride.

In 2005 Nielsen and coworkers [55] reported that Ca^{2+} ion can effectively improve the intracellular delivery efficiency of CPP-antisensePNA conjugates. They found that a similar increase in intracellular uptake was obtained from using 6 mM of Ca^{2+} as from 120 μM of chloroquine (CQ). Chloroquine concentrations were typically used to raise vacuolar pH to facilitate endosomal release.

Another hypothesis [56-58] has been proposed to explain the efficiency by which cell penetrating peptides insert into membranes that was based on the thermodynamics for insertion of the peptides into the lipid bilayer from the surface bound state. The difficulty in predicting the thermodynamic properties from the sequence could explain the apparent lack of correlation between sequence and efficiency of entry, and partly agrees with the observations that the efficiency is cell-type or cargo-specific. The possibility that the thermodynamics of insertion could be used to predict the efficiency of membrane penetration raised interest in using theoretical calculations to help in the design of more effective CPPs.

Theoretical calculations to predict properties such as peptide binding and insertion into membranes using the Wimley-White hydrophobicity scales were developed by White and collaborators. The method of calculation using these scales was implemented in the Membrane Protein Explorer (MPEx) program, which is freely available through the Internet. [59]

They initially proposed that the probability of insertion of amphipathic α-helical peptide was related to the difference between the free energies of transfer between the POPC membrane interface and the hydrophobic interior of the bilayer [60]. These free energies can be estimated using the Wimley-White interfacial and octanol hydrophobicity scales, ΔG_{if} and ΔG_{oct}.

Then they tentatively proposed that a value of $\Delta G_{oct\text{-}if} = \Delta G_{oct} - \Delta G_{if} \leq 20$ kcal/mol would be the threshold for the successful insertion of peptide into cytoplasm membrane. If the value of $\Delta G_{oct\text{-}if}$ was below this value, the peptide would be able to insert transiently into the lipid bilayer probably through a small transient pore followed by some membrane reorganization. Some of the theoretically calculated values are provided below as benchmarks for CPP design, with the secondary structure of CPPs shown in parentheses. (Table 1.2)

Table 1.2 Theoretically calculated Gibbs free energy values for some CPP peptides

Penetratin:	$\Delta G_{oct\text{-}if} = +16.9$ kcal/mol	(60% helix)
TAT:	$\Delta G_{oct\text{-}if} = +19.4$ kcal/mol	(unstructured)
Tp10W:	$\Delta G_{oct\text{-}if} = +17.1$ kcal/mol	(60% helix)

Nonalysine: $\Delta G_{oct-if} = +20.8$ kcal/mol (unstructured)

Nonaarginine: $\Delta G_{oct-if} = +13.6$ kcal/mol (unstructured)

The magnitudes of the Gibbs free energies of binding and insertion, however, would be affected by the presence of negatively charged lipids in the membrane and specific tertiary structure like hydrogen bonds in the CPP peptides. At this point, the ΔG_{oct-if} can only be used as a qualitative measure to compare CPPs, but not as a quantitative one, as there is too much difference between the theoretical calculation of Gibbs free energy values and the experimental values determined from the dissociation constants (K_D).

The experimentally obtained the Gibbs free energy values were determined from dissociation constants K_D from the equation of $\Delta G = RT \ln K_D$. The Gibbs free energy values obtained then need to be modified by adding the cratic correction (thermodynamic correction from octanol to water) of - 2.4 kcal/mol and the electrostatic correction of - 4 kcal/mol depending on the CPP, leading to the equation $\Delta G = RT \ln K_D - 2.4$ kcal/mol $- 4$kcal/mol. The experimentally derived values can then be compared with the theoretical calculations using the Wimley-White interfacial scale [61].

While the theoretical calculations and the experimentally determined Gibbs free energy values are often not the same, they could be quite useful in designing new CPP with improved cell penetrating efficiency.

1.5 Choice of TAT as CPP to improve intracellular delivery

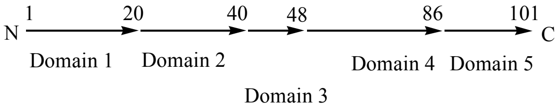

Figure 1.21 Physical domains of the 101-amino acid HIV-1 TAT protein

Given the large number of cell penetrating peptides that one could choose to enhance penetration of a diagnostic or therapeutic PNA, a decision had to be made as to which peptides to choose for the purpose. Among these, the TAT peptide appeared to be the best choice as discussed below.

Human immunodeficiency virus type 1 (HIV-1) is the etiological agent for the acquired immunodeficiency syndrome (AIDS). HIV-1 is a retrovirus that encodes a small nuclear transcriptional activator protein (TAT), which can be viewed as containing five physical domains [62,63] (Figure 1.21). Domain 1 (1-20 amino acids) consists of an acidic N-terminal region important for transactivation. Domain 2 (21-40 amino acids) contains a cysteine-rich DNA-binding region with a zinc-finger motif. Domain 4 (49-86 amino acids) has a basic region responsible for nuclear import (Figure 1.21). The TAT-derived peptide fragment receiving most attention as cell-penetrating peptide is in domain 4, which encompasses the whole basic region of the protein and its nuclear localization signal (NLS).

As a protein-derived cell-penetrating peptide, TAT is able to deliver attached cargoes into many cell types shown as below, which make it a promising “bio-carrier” for diagnostic and therapeutic applications. TAT uptake by most cells is time- and concentration- dependent, as indicated by reports of TAT-mediated cytoplasmic uptake of fusion protein [64-66], plasmid DNA [67-69], nanoparticles [70-74], liposomes [75-77], and micelles [78, 79]. This is the main reason why TAT was chosen as the CPP used for this thesis work.

In 1999 Steven F. Dowdy and coworkers found that the protein transduction domain (PTD) fused to 3-galactosidase protein can be delivered into all tissues in mice, including the brain. [64] Then in 2002 Guodong Cao and coworkers showed that injecting of a Bcl-xL fusion protein containing TAT protein transduction domain into mice decreased cerebral infarction (up to ~ 40%) in a dose-dependent manner. [65] In 2003 Steven F. Dowdy showed that fusing the TAT protein transduction domain (PTD) to the N-terminus of BCLXL and FNK facilitated the delivery of the proteins into cells and tissues in vivo resulting in protection of neuronal cells following ischemic stroke. [66]

Astriab-Fisher and coworkers used conjugates of antisense oligonucleotides (ODN) with the cell-penetrating TAT peptide to target an aberrant splice in a luciferase containing gene resulting in splicing correction and an increase in Luciferase activity in a dose-responsive manner in HeLa cells. The peptide-oligonucleotide conjugates progressively entered cells over a period of hours and were detected in cytoplasmic vesicles and in the nucleus. [67] Shu Yang and coworkers demonstrated that the HIV TAT(48-60) protein fragment can be used to construct cationic peptide-DNA complexes that can deliver exogenous DNA in vitro along with chloroquine to protect DNA from degradation and enhance cytoplasmic delivery of the peptide-DNA complexes. [68]

Yoshie Maitani and coworkers reported a tetra-arginine conjugated-PEG lipid-coated protamine (PD) as a promising gene delivery vector for gene delivery in tumor by intratumoral injection. And transfection efficiency in tumors and in vitro greatly depended on the charge ratios of $(Arg)_n$-B to DNA and the length of Arg residues. [69]

Ralph Weissleder et al conjugated different number of TAT peptides to superparamagnetic iron oxide nanoparticles in order to improve their intracellular uptake. They also demonstrated that increasing the numbers of TAT peptides per particle increases the cellular uptake of iron oxide nanoparticles in a nonlinear fashion. The increase in sensitivity of the MR imaging agents allowed in vivo tracking cells about 100-fold lower cell concentration than currently described. [70] In 2000, they designed and made a TAT peptide-derivatized superparamagnetic nanoparticle with a novel triple-label (magnetic, fluorescent, isotope) which could be efficiently delivered into hematopoietic and neural progenitor cells in vitro at around 10–30 pg of superparamagnetic iron per cell. It was found that single cells could be detected by magnetic resonance (MR) imaging in tissue samples in vivo, and that the cells could be recovered by magnetic separation columns. [71]

Later Karen L. Wooley, John S. Taylor and coworkers compared nanoparticle shape/size effect on cellular uptake concerning nanoparticles functionalized with TAT protein peptide, and detected that the small spherical nanoparticles had a higher intracellular incorporation rate into CHO (Chinese hamster ovary) cells than did those large cylindrical nanoparticles. [72] Other types of nanoparticles like biocompatible gold nanoparticles functioned with TAT PTD can transverse the cell membrane of human fibroblast cell lines in vitro. In this case, the size of the gold nanoparticles influenced the nuclear entry efficacy, with 5 nm particles being able to enter the nucleus while large 30nm particles were retained in the cytoplasm. [73] Vinod Labhasetwar and coworkers conjugated TAT peptide to nanoparticles in order to increase the transport of the encapsulated ritonavir (a protease inhibitor, PI) across the blood-brain-barrier (BBB) into the central nervous system (CNS). Their results showed that despite their larger size of ~300 nm (hydrodynamic diameter) which is much larger than the openings in the BBB (~8.1 nm), TAT-conjugated NPs were transported across to the parenchyma to maintain a therapeutic drug level for around four weeks. [74]

Vladimir P. Torchilin [75] and coworkers demonstrated that relatively large size drug carrying 200 nm liposomes can also be delivered into cells, if the TAT peptide is attached to the liposome surface through a spacer or a high MW polyethylene glycol. Otherwise steric hindrance blocks the direct contact between the TAT peptide and the cell surface, thereby abolishing intracellular delivery of the liposome into the cells. Later this same group [77] showed that not only pNP-PEG-PE (p-nitrophenylcarbonyl-PEG-phosphatidylethanolamine) but also pNP-PEG-DOPE (p-nitrophenylcarbonyl-PEG-dioleoyl phosphatidylethanolamine) can be delivered into cells by attaching TAT peptide to liposomes with covalent bonds respectively, then probably through a mechanism of spontaneous formation of certain membrane structures like vesicles or micelles.

Marjan M. Fretz [76] and coworkers found that coupling TAT peptide to the outer surface of liposomes resulted in enhanced endocytosis of the liposomes by ovarian carcinoma cells. Supporting evidence that the intracellular delivery mechanism involved endocytosis was provided by the inhibitory effect of heparin or dextran sulfate, and confocal microscopy studies showing that binding of the TAT-liposomes to the plasma membrane was followed by intracellular uptake in vesicular structures.

You Han Bae [78] and coworkers designed and assembled a TAT peptide conjugated micelle system which was completed and shielded with a pH-sensitive dib lock copolymer. The TAT micelles had particle sizes between 20 and 45 nm, and upon complexation showed particle sizes between 60 and 90 nm. Flow cytometry and confocal microscopy showed a higher uptake of TAT micelles into the cytoplasm and nucleus of the acidic tumors at pH 6.6 than that at pH 7.4, which indicated shielding at normal pH and deshielding at tumor pH. In 2009 Rupa R. Sawant and Vladimir P. Torchilin [79] attached TAT peptide to the ends of polyethyleneglycol-phosphatidylethanolamine (PEG-PE) micelles containing paclitaxel (PCT) with average sizes of 8-25 nm. Both in vitro and in vivo tests of TAT-modified micelles demonstrated an increased interaction with cancer cells compared to micelles without TAT, and an increase in cytotoxicity to different cancer cells in vitro.

In addition to the experimental results discussed above, thermodynamic factors were also considered in choosing TAT as the CPP for the thesis work. The theoretical value of Gibbs free energies were calculated according to the Wimley-White interfacial scales and hypothesis [59] described as before. Then the experimental value of Gibbs free energy was derived from the equation of $\Delta G=RT \ln K_D$. This experimental value can be compared with the theoretical value calculated from the Wimley-White interfacial scales, after adding the cratic correction of -2.4 kcal/mol, and the electrostatic correction of -4kcal/mol, depending on different CPPs. (Table 1.3)

Table 1.3 Theoretical and experimental values of Gibbs free energy for TAT peptide insertion into a membrane (I)

TAT : $\Delta G_{if} = +2.2$ kcal/mol (theoretical value)

$\Delta G_{exp} = RT\ln K_D – 2.4$ kcal /mol–4 kcal/mol= –7.4 kcal/mol (experimental value)

$\Delta\Delta G=9.6$ kcal/mol

As shown above, the experimental Gibbs free energy of binding is >9 kcal/mol ($\Delta\Delta G=9.6$ kcal/mol) more negative than the calculated value. This discrepancy between the theoretical and experimental values for TAT is too large to be explained solely by inaccuracies in the parameters. If a significant number of intramolecular hydrogen bonds were formed by the peptide, the binding free energy might be significantly lower. Using -0.4 kcal/mol for per residue to form intramolecular hydrogen bonds, the maximum total contribution from TAT peptide (11 amino acid residues) alone would be -4.4 kcal/mol. If the terminal free COO- group establishes a salt bridge with one of the Arg or Lys residues; this could further contribute about - 2 kcal/mol to the binding Gibbs energy. [60] Altogether, those hydrogen bonds would bring the value of ΔG_{if} to -4.2 kcal/ mol, which is closer to the -7.4 kcal/mol derived from experiment with $\Delta\Delta G$ = 3.2 kcal/mol. (Table 1.4)

Table 1.4 Theoretical calculation and Experimental values of Gibbs free energy for TAT peptides (II)

TAT : $\Delta G_{if} = +2.2\ \text{kcal/mol} – 4.4\text{kcal /mol} – 2\text{kcal/mol} = – 4.2\text{kcal/mol}$ (theoretical value)

$\Delta G_{exp} = RT\ln K_D – 2.4\text{kcal /mol} – 4\text{kcal/mol} = – 7.4\text{kcal/mol}$ (experimental value)

$\Delta\Delta G = 3.2$ kcal/mol

All the above information suggests that the large discrepancy in theoretical and experimental values for TAT peptide reveal a real difference between the assumed and the actual conformations of the TAT peptide on the membrane. Thus, it is highly possible that TAT peptide does not adopt a regular secondary structure. Probably additional hydrogen bonds were formed within the peptide involving the arginine side chains, which further lowered the free energy upon binding.

Although the Wimley-White theoretical estimates of TAT was not very close to the experimental determinations of the Gibbs energies of transfer calculation, like those shown before for the α-helical peptides of Tp10W and penetratin [60]. Fortunately the experimental value was lower than that from the theoretical calculation, which confirms that it should be an effective cell-penetrating peptide for intracellular delivery. Thus, this is a second reason for choosing TAT as the CPP used for thesis work.

Moreover, the continuing synthesis of PNA-peptide conjugates can be easily assembled by Fmoc chemistry on the solid support with TAT peptide, which was provided as the third reason.

1.6 Lipid modification of GRN163 to improve cell-membrane permeability [80]

While TAT peptide has been shown to deliver antisense agents into cells, the efficiency has still not been that great, and we were interested in seeing if we could further enhance the efficiency by attaching a lipophilic molecule. At the time that we were considering this problem, there were reports that attachment of lipids to an antisense telomerase agent greatly improved the bioavailability.

Most human cancer cells over-express telomerase, while this is not the case in somatic cells. Since inhibition of telomerase has been shown previously to lead to progressive telomere shortening, cell growth arrest or cell death due to the critically shortening of telomeres, telomerase became an attractive cancer therapeutic target over the past years. Among the several mechanisms, using antisense oligonucleotides directly targeting the hTR (human telomerase RNA) template to inhibit telomerase activity has shown the potential for application in cancer therapy. However, the major problem in the effective and general utilization of oligonucleotides as anti-telomerase cancer drugs is their low ability to transverse cell membrane.

In order to solve this problem, lipophilic carriers or liposomes as transfection reagents were used in vitro to facilitate the intracellular delivery ability of oligonucleotides, but this method cannot be applied easily in the clinic. Then, chemical modification of the oligonucleotides became another feasible way to improve the intracellular uptake. One successful modification was to replace the 3’-oxygen of oligonucleotides with 3’-nitrogen to make N3’-P5’ phosphoramidate and thio-phosphoramidates (GRN163 and GRN163L, Figure1.22) as effective telomerase inhibitors. Similarly better telomerase inhibition effect of these oligonucleotides was also demonstrated, when the transfection reagent were combined with them in the in vitro tests. Like the normal oligonucleotides, this needed to be improved before in vivo administration was feasible. Thereafter, a lipid modification of oligonucleotide thio-phosphoramidates of GRN163L was designed and tested for the telomerase inhibition by Britteney-Shea Herbert and coworkers, who found a greatly enhanced effect compared with the former generation of oligonucleotides of GRN163 without a lipid modification.

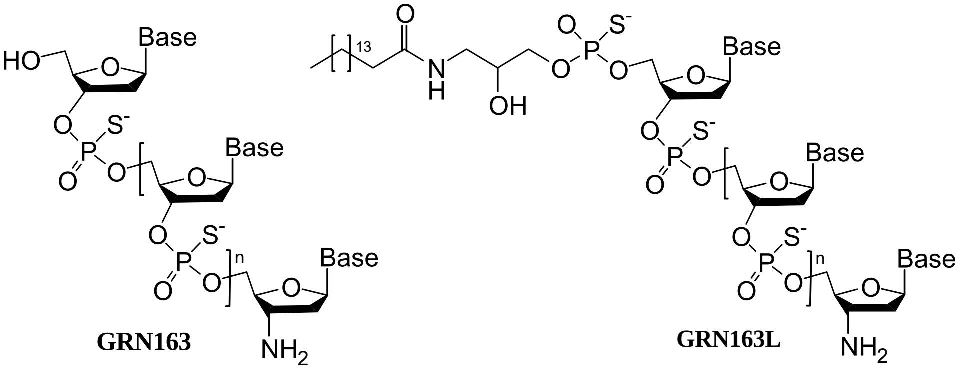

Figure 1.22 Structures of N3'-P5' phosphoramidate and thio-phosphoramidates (GRN163 and GRN163L) by replacing the 3'-oxygen of oligonucleotides with 3'-nitrogen

This was the first report to show that lipid modification enhanced the potency of the GRN163 telomerase inhibition, which was testified by in vitro in different cell lines. In the cell-free-based TRAP assay, GRN163 was still more potent than the lipid modified GRN163L, with an IC50 value of ~1.4 compared to ~7.8 nM for GRN163L. In immortal HME50-5E cells, the lipid-modified phosphoramidate GRN163L could inhibit telomerase activity much more effectively compared to GRN163, with an estimated IC50 value of ~150 nM compared to ~20 μM. Inhibition of telomerase activity by GRN163L was dose dependent, while the dose-dependent inhibition of GRN163 depended on the use of a transfection reagent. These facts suggested that conjugation of lipid to GRN163 improved significantly its cell-membrane permeability to better inhibit the telomerase activity inside the cell, without the use of transfection reagents. Similar telomerase inhibition results by GRN163 and GRN163L were also demonstrated in other cell lines, like tumorigenic HME50-T breast epithelial cell, MDA-MB-231 breast carcinoma cells, PC3 human prostate carcinoma cells, cervical tumor cells, glioblastoma tumor cells, hepatoma tumor cells, lung tumor cells, melanoma tumor cells, ovarian tumor cells, and prostate tumor cells. Thus the conjugation of a lipid to a PNA-TAT peptide conjugate was expected to further increase its bioavailability and was targeted for this Ph. D thesis study.

1.7 Determining accessible sites on native mRNAs for therapeutics by MASL

Another concern for the development of effective antisense PNA-based diagnostic and therapeutic agents is how best to select a specific sequence on an mRNA of interest to insure the highest binding affinity of the PNA. Because RNA molecules are folded, not all sites are equally accessible to an antisense agent. Therefore in order for antisense reagents to bind the target mRNAs stably and function smoothly as therapeutic or diagnostic reagents, the accessible binding sites of the corresponding mRNA need to be known first. Several experimental methods for mapping accessible sites on mRNA have been developed in past years, and ODN sequences identified by these methods demonstrated high affinity and selectivity for the corresponding target mRNA in vitro. However, because many of these methods utilized RNA substrates produced by in vitro transcription of cDNA clones, these methods resulted in nonnative mRNAs which lack the endogenous capping sequence and the poly(A) tail. [81-86] The RNAs produced in this way were also often truncated and contained parts of sequences arising from the transcription vector, and therefore may not fold exactly in the same way as native mRNAs do, thus leaving doubt about the precision of the accessible sites mapped.

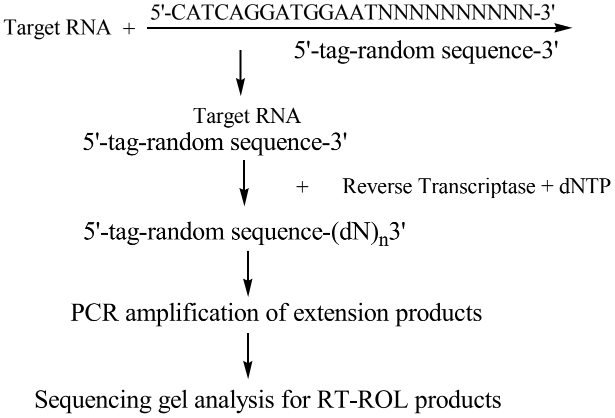

Figure 1.23 RT-ROL method (reverse transcription with the random oligonucleotide libraries) to map antisense-accessible sites on mRNA

To clear this doubt, a method that could map antisense-accessible sites on full-length native mRNA targets directly in the isolated total mRNAs from cell culture was required. In 2001 Allawi and coworkers [84] first developed the RT-ROL method (reverse transcription with the random oligonucleotide library), method for mapping accessible sites as shown above (Figure1.23). In their method, a sequence-randomized library of oligodeoxynucleotides (ODNs) linked to the 3'-end of a PCR-tag sequence was used to hybridize to the RNA. The ODNs were extended with reverse transcriptase and the extended products were amplified by using the PCR primers from the different sites along the target mRNAs. Then the PCR (Polymerase Chain Reaction) products could be aligned with specific sequences of the mRNA according to the PAGE (Polyacrylamide Gel Electrophoresis) results to deduce the antisense-accessible sites.

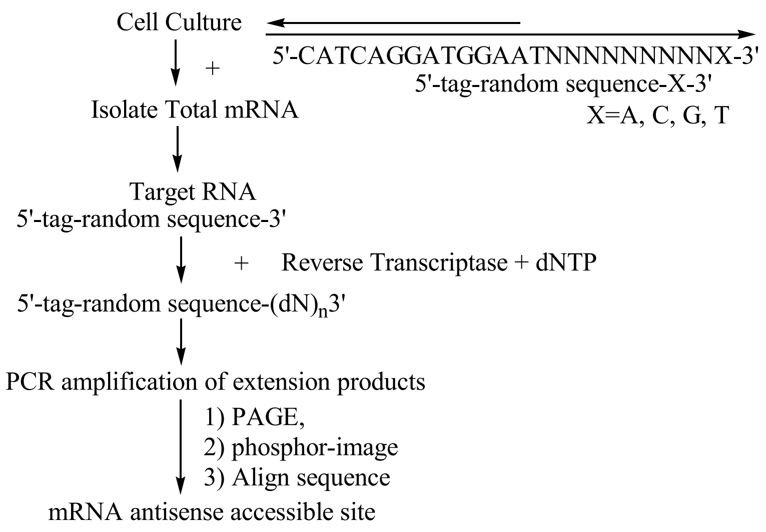

Figure 1.24 MASL method (mRNA antisense-accessible sites library) to improve the precision of RT-ROL method

One problem with the original method was the difficulty to assign the PCR product bands directly to a specific site on the mRNA, which resulted from the difficulty in determining the precise size of the PCR product. The other problem was that in vitro transcribed RNA was used as a substrate. To overcome these problems, a method named MASL (mRNA antisense-accessible sites library) was developed recently by Taylor group [87] with the purpose of improving the precision of the originally reported method by Allawi et al which also used native mRNA instead of in vitro transcribed mRNA (Figure1.24). [84]

In MASL four separate random primer libraries terminating in either A, C, G, or T are utilized to enable the observed PCR products to be aligned with a specific base in the sequence. This method was then employed on whole cell mRNA extract so that the mapping was carried out on native mRNA transcripts. The MASL accessible site library was then shown to allow high affinity sites to be identified that could be used for selecting highly effective antisense therapeutic agents and imaging probes from series of phosphorothioate oligodeoxynucleotides (ODNs), small interfering RNAs (siRNAs) and peptide nucleic acids (PNAs).

1.8 Specific aims of this thesis

The overall aim of this thesis was to develop diagnostic and therapeutic PNA agents for a variety of disease states that showed better cell penetrating and biodistribution properties than previously developed PNA agents. To this end we envisioned combining PNAs with cell penetrating peptides and lipids and then testing their properties in vitro and in vivo.

Based on previous studies, two well-studied cell penetrating peptides of TAT and Arg_9 were chosen to facilitate the intracellular delivery of a series of PNAs targeting different RNAs. Also considering the dramatic effects of attaching lipids to GRN163, we decided to also investigate adding lipid modifications to the N-terminus of the PNA.

We also hypothesized that the hydrophobic lipid chain might direct the self-assembly of the conjugates in aqueous environment to form different sized micelles depending on the length of the lipid. Hopefully, some combination of CPP and lipid would show optimal membrane permeation and biodistribution in vivo (Figure1.25).

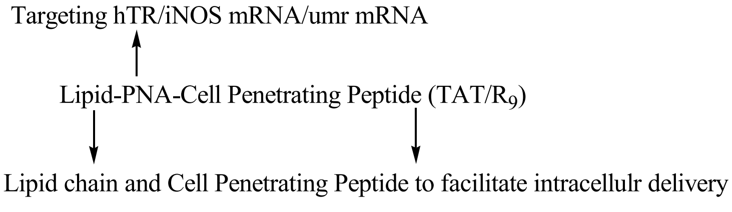

Figure 1.25 Design of Lipid-PNA-CPP Conjugates to facilitate intracellular delivery

To detect the location of the PNA in vivo, we also needed to add a fluorescent or radioimaging label to the PNA constructs. The TAT(48-58) peptide appears to be ideal for this purpose as it contains a tyrosine residual with a phenol side chain that can be conveniently radiolabeled with Br-76 for PET imaging studies (Positron Emission Tomography) in collaboration with Michael Welch's group in the Medical School.

The thesis work is divided into three studies involving lipidated PNA-cell penetrating peptide constructs (Figure1.26 and Figure1.27). The first (Chapter 2) involves the synthesis, characterization and study of the in vitro effectiveness of this class of PNAs as a potential therapeutic for telomerase inhibition, The second (Chapter 3) involves the synthesis, characterization and in vivo study of this class of PNAs as breast cancer imaging agents. The third (Chapter 4) involves the synthesis, characterization and in vitro study of this class of PNAs as lung injury therapeutic and imaging agents.

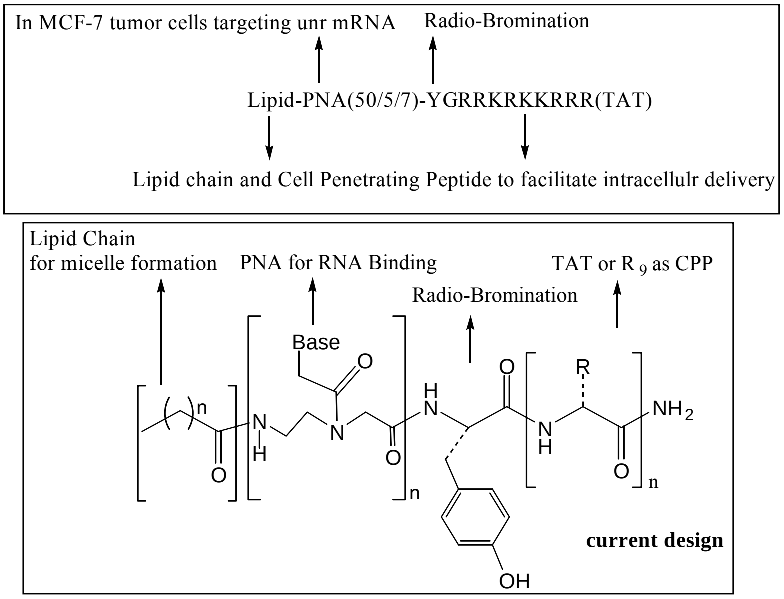

Figure 1.26 Design of Lipid-PNA-CPP Conjugates as diagnostic agents

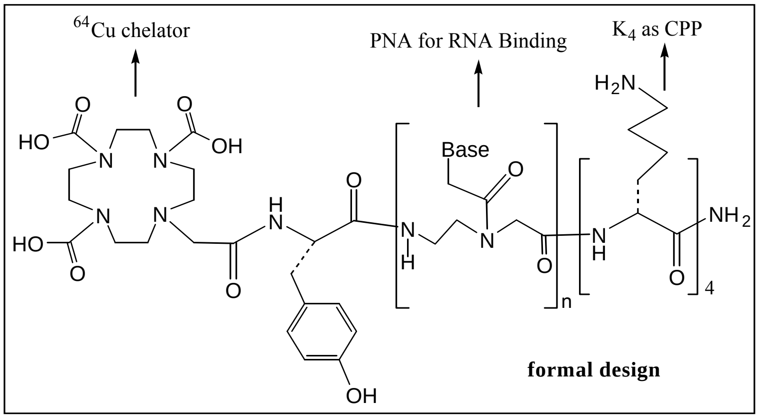

Figure 1.27 Formal design of PNA conjugates containing one radiolabelling end

References

1 Nielsen, P. E.; Egholm, M.; Berg, R. H.; Buchardt, O. Science 1991, 254, 1497-1500.

2 Nielsen, P. E. Bioconjug. Chem. 1991, 2, 1-12.

3 M. Egholm, P. E. Nielsen et al, Nature, 365, 1993, 566-568

4 K. K. Jensen, H. Orum, B. Norden, P. E. Nielsen, Biochemistry, 36, 1997, 5072-5077

5 U. Giesen, P. E. Nielsen et al, Nucleic Acids Research, 26, 1998, 5004-5006

6 J. Lohse, O. Dahl, P. E, Nielsen, Proc. Natl. Acad. Sci. USA, 96, 1999, 11804-11808

7 P.E. Nielsen, M. Egholm, O. Buchardt, Gene, 149, 1994, 139-145

8 T.A. Vickers, M. C. Grifith et al, Nucleic Acids Research, 23, 1995, 3003-3008

9 J. Lohse, O. Dahl, P.E. Nielsen, Proc. Natl. Acad. Sci. USA, 96, 1999, 11804-11808

10 J.C. Hanvey, N. J. Peffer et al, Science, 258, 1992, 1481-1485

11 H. Knudsen, P.E. Nielsen, Nucleic Acids Research, 24, 1996, 494-500

12 C. Gambacorti-Passerini, P.E. Nielsen et al, Blood, 88, 1996, 1411-1417

13 PNA Chemistry, for the Expedite™ 8900 Nucleic Acid Synthesis System, User's Guide, Copyright 2001, Applied Biosystems

14 Methods in Molecular Biology, VOLUME 208, Peptide Nucleic Acids Methods and Protocols, Edited by Peter E. Nielsen, chapter 1

15 M.A. Shammas, C.G. Simmons, D.R. Corey, R.J. Shamookler Reis, Oncogene 18, 1999, 6191-6200

16 J.G. Karras, M. Manoharan et al, Biochemistry, 40, 2001, 7853-7859

17 D.F. Doyle, D.R. Corey et al, Biochemistry, 40, 2001, 53-64

18 L. Good, P.E. Nielsen, Nat. Biotechnology, 16, 1998, 355-358

19 L. Good, P.E. Nielsen, Proc. Natl. Acad. Sci. USA, 95, 1998, 2073-2076

20 S. Sei, K. Nagashima, H. Mitsuya et al, J. Virol., 74, 2000, 4621-4633

21 T. Ljungstrom, H. Knudsen, P.E. Nielsen, Bioconjugate Chemistry, 10, 1999, 965-972

22 L. Mologni, E. Marchesi, P.E. Nielsen, C. Gambacori-Passerini, Cancer Research, 61, 2001, 5468-5473

23 A. Muratovska, MP. Murphy et al, Nucleic Acids Research, 29, 2001, 1852-1863

24 Dmitry A. Stetsenko, Michael J. Gait et al, Bioconjugate Chem., 12, 2001, 576-586

25 Martin K. Bijsterbosch et al, Nucleic Acids Research, 2000, 28(14), 2717-2725

26 Andrew J. Geall, Ian S. Blagbrough et al, Bioconjugate Chem., 2000, 11, 314-326

27 Darin Y. Furgeson, Sung Wan Kim et al, Bioconjugate Chem., 2003, 14, 840-847

28 Dmitry A. Stetsenko and Michael J. Gait, Bioconjugate Chem., 2001, 12, 576-586

29 Martin K. Bijsterbosch, et al, Nucleic Acids Research, 2000, Vol 28, No 14, 2717-2725

30 Alexandre G. Rebuffat, The FASEB Journal. 2002; 16:1426-1428

31 Colleen F. Bleczinski, Clemens Richert et al, J. Am. Chem. Soc., 1999, 121, 10889-10894

32 T. Bentin, P. E. Nielsen, J. Am. Chem. Soc., 2003, 125, 6378-9

33 G. Karup, P. E. Nielsen et al, Int. J Pept. Protein Res., 1988, 32, 331-343

34 N. T. Thuong, C. Helene, Angewandte Chemie-International Edition in English, 1993, 32, 666-690.

35 B. Armitage, G. B. Schuster, Nucl. Acids Res., 1997, 25, 4674-4678.

36 Soumitra Basu, Eric Wickstrom, Bioconjug. Chem., 8, 1997, 481–488.

37 Lidia C. Boffa, Patricia L. Morris et al, Cancer Research, 2000, 60, 2258

38 X. Zhang, C.G. Simmons, D.R. Corey, Bioorg. Med. Chem. Lett., 2001, 11, 269-1272.

39 R. Villa, et al, FEBS Lett., 473, 2000, 241-248;

40 G. Aldrian-Herrada, et al, Nucleic Acids Res., 26, 1998, 4910-4916.

41 M. Pooga, U. Soomets, M. Hallbrink et al, Nat. Biotechnol. 16, 1998, 857-861.

42 G. Cutrona, L.C. Boffa et al, Nat. Biotechnol., 2000, 18, 300-303.

43 P. Sazani, et al, Nucleic Acids Res., 29, 2001, 3965-3974.

44 Cell-Penetrating Peptides: Methods and Protocols (Methods in Molecular Biology) by Ülo Langel (Editor) (Hardcover, Springer Procotols)

45 Charlotte Amerley Pratt; Donald Voet; Judith G. Voet, (2002). Fundamentals of biochemistry upgrade. New York: Wiley. pp. 264-266.

46 Wender, P. A., Rothbard, J. B. et al, *Proc Natl Acad Sci*, **2000**, USA, 97, 13003-8.

47 Rothbard, J. B., Khavari, P. A. et al, *Nat Med*, **2000**, 6, 1253-7.

48 Futaki, S., *Int J Pharm.*, **2002**, 245, 1-7.

49 Richard, J. P., Lebleu, B. et al, J Biol Chem, 2003, 278, 585-90.

50 Marko Kaksonen, Christopher P. Toret, David G. Drubin, Nature Reviews: Molecular Cell Biology, 7, 404-414

51 Richard, J.P., Lebleu, B. et al, 2005, J. Biol. Chem., 280, 15300-15306

52 Fittipaldi, A., Giacca, M., 2003, J. Biol. Chem., 278, 34141-34149

53 Kaplan, I. M., Wadia, J. S., and Dowdy, S. F., J Control Release, 2005, 102, 247-253.

54 Potocky, T.B., Menon, A.K., Gellman, S.H., 2003, J. Biol. Chem., 278, 50188-50194

55 S. Takehiko, P. Stanislava, P.E. Nielsen et al, Chemistry & Biology, 2005,12, 923-929

56 Morris, M. C., Depollier, J., Mery, J., Heitz,F., Divita, G., *Nat Biotech*, 2001, 19, 1173-1176.

57 Almeida, P. F., and Pokorny, A., *Biochemistry*, 2009, 48, 8083-93.

58 Zorko, M., and Langel, U., *Adv Drug Deliv Rev*, 2005, 57,529-545.

59 Jaysinghe, S., Hristova, K., Wimley, W., Snider, C., and White, S. H., 2009, Membrane Protein Explorer (MPEx). *http://www.blanco.biomol.uci.edu/mpex.*

60 Almeida, P. F., and Pokorny, A., *Biochemistry*, 2009, 48, 8083-8093.

61 White, S. H., and Wimley, W. C., *Annu. Rev. Biophys. Biomol. Struct.*, 1999, 28, 319-365.

62 K. T. Jeang, X. Hua, E. A. Rich, Journal of Biological Chemistry, 1999, 274, 28837-28840

63 Steven Ruben, Craig A. Rosen, Journal of Virology, 63(1), 1989, 1-8

64 Steven R. Schwarze, Steven F. Dowdy et al, Science, 1999, 285, 1569-1572

65 Guodong Cao, Jun Chen et al, Journal of Neuroscience, 2002, 22(13), 5423-5431

66 Catherine Denicourt, Steven F. Dowdy, TRENDS in Pharmacological Sciences, 2003, 24(5), 216-218

67 Anna Astriab-Fisher, Dimitri Sergueev, R. L. Juliano et al, Pharmaceutical Research, 2002, 19(6), 744-754

68 Shu Yang, Rodney F. Minchin et al, Journal of Controlled Release, 2009, 135, 159-165

69 Takashi Fujita, Yoshie Maitani et al, Journal of Controlled Release, 2008, 129, 124-127

70 Ming Zhao, Ralph Weissleder et al, Bioconjugate Chem., 2002, 13, 840-844

71 Maïté Lewin, Ralph Weissleder et al, Nature Biotechnology, 2000, 18, 410-414

72 Ke Zhang, John S. Taylor, Karen L. Wooley, Bioconjugate Chem., 2008, 19, 1880-1887

73 Berry, C.C., Curtis, A.S.G. et al, IEEE Transactions on NanoBioscience, 2007, 6(4), 262-269

74 Kavitha S. Rao, Vinod Labhasetwar et al, Biomaterials, 2008, 29, 4429-4438

75 Vladimir P. Torchilin, Ram Rammohan et al, PNAS, 2001, 98(15), 8786–8791

76 M. M. Fretz, G. A. Koning et al, Biochimica et Biophysica Acta, 2004, 1665, 48- 56

77 T. S. Levchenko, V. P. Torchilin et al, Methods in Enzymology, 372, 19, 339-349

78 Vijay A. Sethuraman, You Han Bae, Journal of Controlled Release, 2007, 118, 216-224

79 Rupa R. Sawant, Vladimir P. Torchilin, International Journal of Pharmaceutics, 2009, 374, 114-118

80 Brittney S. Herbert, Sergei M. Gryaznov et al, Oncogene, 2005, 24, 5262-5268

81 Ho SP, Trainor GL. et al, 1996, Nucleic Acids Res, 24, 1901-1907

82 Ho SP, Sakai RR. et al, 1998, Nat Biotechnol, 16, 59-63

83 Sun Y, Wang S. et al, 2006, Mol Vis, 12, 1364-1371

84 Allawi HT, Dong F, Ip HS, Neri BP, Lyamichev VI., 2001, RNA, 7, 314-327

85 Zhang HY, Wahlestedt C. et al, 2003, Nucleic Acids Res 31, e72

86 Fang H., Yue X., Li X., Taylor J.S., 2005, Nucleic Acids Res, 33: 6700-6711

87 Huafeng Fang, Yuefei Shen, John S. Taylor, RNA, 2010, 16, 1429-1435

Chapter 2

Lipid / Phospholipid-PNA-Peptide Conjugates to Down-Regulate Human Telomerase Activity

Abstract

Telomerase is a ribonucleoprotein that has been found to maintain the cellular immortality of cancer cells. Therefore, much attention has focused on developing inhibitors of telomerase activity. Antisense oligonucleotides targeting the RNA component or human telomerase have shown excellent anti-telomerase activity in vitro. Herein we have investigated whether or not lipid / phospholipid-PNA-R_9 / TAT conjugates targeting the hTR can better down-regulated human telomerase activity than non-lipidated PNAs.

2.1 hTR as a promising target for inhibition of telomerase activity

Human telomerase is ribonucleoprotein complex that compensates for the loss of telomeric sequences, due to the DNA end replication problem, [1] by adding tandem repeats of d(TTAGGG) to telomeres at the ends of chromosomes (Figure 2.1). The essential role of telomerase is to ensure chromosome integrity. [2] It is composed of a catalytic protein subunit, the telomerase reverse transcriptase component (hTERT), one or more additional proteins, and a 451-base integral RNA component of hTR (human Telomerase RNA). The RNA component, hTR, which serves as a template for the synthesis of the telomeric repeats, [3] is critical for the telomerase activity in vitro and in vivo.

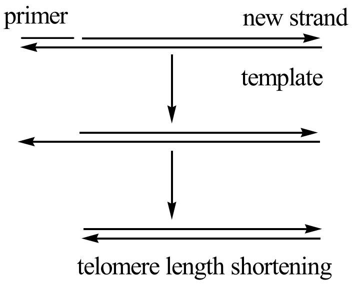

Figure 2.1 Telomere shortening in normal cells

Telomerase activity has been detected in over 85% of tumors, [4] but not in somatic cells. Telomerase activity is activated and expressed in cancer cells but not in most normal somatic cells (Figure 2.2). Biochemical and genetic studies have established a relationship between telomere maintenance and extended life span of human cells, which is mediated through the expression of the catalytic sub-unit of telomerase (hTERT). Because of this, telomerase has attracted much attention as a target for anti-cancer therapy. Telomeres are maintained mainly through telomerase, and telomere shortening may make tumor cells more sensitive to chemotherapy agents.

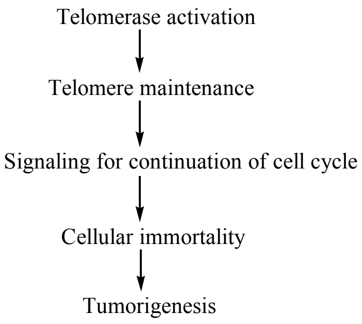

Figure 2.2 A relationship between Telomerase activation and Tumorigenesis

Understanding the structure and function of telomerase has led to a number of strategies for the development of inhibitors. [5] These include antisense oligonucleotides targeting hTR [6-10] (RNA component) or hTERT [11] (reverse transcriptase) mRNA, traditional small molecule reverse transcriptase inhibitors and agents able to promote and/or stabilize G-quartet formation in telomere DNA. [12, 13]

Among these strategies, targeting hTR with antisense oligonucleotides offers several advantages for inhibitor development. [14] First, hTR Watson-Crick basepairs with telomere DNA in order to template DNA synthesis, which makes hTR an ideal target for antisense oligonucleotides. Second, the design of antisense oligonucleotide-based inhibitors is straightforward, because the 11-base hTR sequence in the template region [15] has already been sequenced. (Figure 2.3) Third, the synthesis of antisense oligomers and other conjugates is also straightforward. Last, oligonucleotides or other conjugates containing mismatched bases can be used for control experiments to demonstrate the mechanism of action.

3'- G A A G A G U $\boxed{\text{C A A U C C C A A U}}$ C U G U U U **U - 5'**

60 template 40

Figure 2.3 Human telomerase RNA (hTR) template region

2.2 Design and synthesis of lipid/phospholipid-PNA-CPP conjugates

The application of PNAs as genetic diagnostic and therapeutic regents is hampered by their low solubility in physiological buffers, tendency to form aggregates, and insufficient cellular uptake and poor biodistribution due to rapid excretion in vivo. Fortunately, PNA can be easily modified, and one can easily attach peptides and other molecules to either end to improve its biophysical and biochemical properties.

A number of arginine-rich cell-penetrating peptides (CPPs) appear to confer a high level of cellular uptake to what they are attached, [16, 17] probably because of the guanidinium headgroups on the arginine residues. It has been proposed that the ability to form bidentate hydrogen bonds, characteristic of guanidinium groups, may enable it to bind to proteoglycans associated with the plasma membrane, [18,19] and this binding may be the first step in transduction. This seems to agree with the kinetic analyses, which indicate that oligomers of arginine composed of six of more amino acids cross biological membranes very efficiently. Detailed kinetic assays of nonamers of arginine illustrate that R_9 is significantly more effective at crossing biological membranes than the nonapeptides of TAT(49-57). [20]

Structural considering, TAT(48-58, YGRRKRKKRRR) was also an arginine-rich peptide containing eleven amino acid residuals as shown below (Table 2.1), and the lysine residue is structurally like the arginine residual with a side-chain containing a positive charge at the end. These structures of the lysine and the arginine residuals enable TAT peptide to form hydrogen bonds within the peptide and then adopt an irregular secondary structure. This would explain the large discrepancy between the theoretical value and the experimental value of the Gibbs free energy for membrane insertion, which indicates a difference between the assumed and the actual conformations of the TAT peptide on the membrane. [21-23]

Table 2.1 Theoretical calculation and Experimental values of Gibbs free energy for TAT peptides

TAT : ΔG_{if} = +2.2 kcal/mol–4.4kcal/mol–2kcal/mol = –4.2kcal/mol (theoretical value)

ΔG_{exp} = RTlnK$_D$–2.4kcal/mol–4kcal/mol = –7.4kcal/mol (experimental value)

$\Delta\Delta G$ = 3.2 kcal/mol

Later in 2008, Uffe Koppelhus et al [25] demonstrated that the nuclear antisense activity of PNA oligomers can be dramatically enhanced by conjugation of PNA to a CatLip domain (cationic peptide lipid domain), consisting of polyarginines or TAT peptide and fatty acid. And this enhancement of the nuclear antisense activity was facilitated up to 2 orders of magnitude by the improved intracellular delivery of CatLip domain, which was higher than that obtained by using the peptide alone (Figure 2.4).

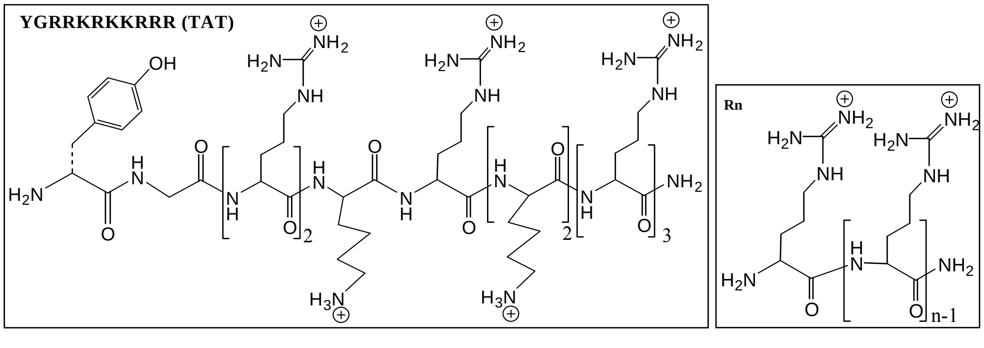

Figure 2.4 Structures of TAT(48-58) and R$_n$ peptides

David Corey's group [26] used overlapping PNAs to determine that recognition of cytidines 50-52 within the template region was critical for efficient inhibition. The 13-mer PNA sequence TAGGGTTAGACAA showed the best anti-telomerase activity of all 17 PNAs directed to template sites within the hTR, followed by five other PNA sequences. PNA conjugates directed to other sites within the hTR were poor inhibitors of telomerase holoenzyme.

Xuan Yue et al [27] investigated a 13-mer (CAGTTAGGGTTAG) and an 8-mer (TAGGGTTA) PNA sequence from those six best inhibitors discovered by David Corey. She found that the longer 13-mer PNA sequence which was conjugated to Arg_9 had a better intracellular delivery effect and a better telomerase inhibition bioactivity.

A further improvement in antisense agents targeting the telomerase hTR was found by Brittney-Shea Herbert [28] and coworkers. They found that lipid-modification of a N3'-P5' thiophosphoramidate oligonucleotide inhibitor GRN163 greatly improved the in vivo effectiveness of the inhibitor as GRN163L.

Based on these prior results, we reasoned that an improved anti telomerase PNA could be designed by adding either a lipid or phospholipid to one end of the optimal 13-mer PNA sequence (TAGGGTTAGACAA) and either the TAT peptide or Arg_9 to the other end as shown below (Figure 2.5). To this end, a library of antisense PNA conjugates of PNA-TAT, Lipid-PNA-TAT, Lipid-PNA-R_9 and Phospholipid-PNA-R_9 were designed and synthesized by solid phase chemistry as shown below, and then studied for their ability to inhibit human telomerase (Figure 2.6).

Targeting hTR for Telomerase Inhibition

↑

Lipid(Phospholipid)-PNA(Telm)-Cell Penetrating Peptide(R_9/TAT)

↓ ↓

Lipid(Phospholipid) chain and Cell Penetrating Peptide to facilitate delivery into cells

Figure 2.5 Design of Lipid(Phospholipid)-PNA(Telm)-CPP(R_9/TAT) conjugates

Pal-P-Telm-R₉

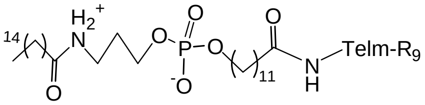

P-Telm-R₉

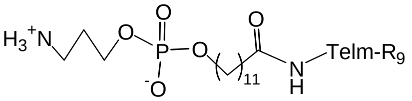

Lipid-Telm-R₉

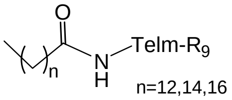

Telm-R₉ Telm-R_9

Lipid-Telm-TAT

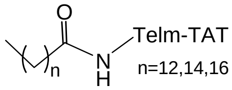

Telm-TAT Telm-TAT

Figure 2.6 Structures of Pal-P-Telm-R_9, P-Telm-R_9, Lipid-Telm-R_9, Telm-R_9, Lipid-Telm-TAT and Telm-TAT conjugates

2.3 Experimental Procedures

Materials and Methods

All reactions were performed under an argon or nitrogen atmosphere unless otherwise specified. All commercially available materials were used without further purification unless otherwise noted. Anhydrous solvents for reactions, such as DMF, DCM, and acetonitrile were either used as obtained from Sigma-Aldrich or distilled from an appropriate drying agent. All chemicals and reagents used were of the highest purity available. Acetonitrile, trifluoroacetic acid, m-cresol and reagents for automated PNA synthesis were purchased from Aldrich. Fmoc-D-Arg(Pbf)-OH was purchased from Novabiochem for solid-phase synthesis of R_9 on an Expedite TM 8900 synthesizer. The 11-mer Fmoc-protected TAT on resin, Fmoc-YGRRQRKKRRR-PAL-PEG-PS was purchased from GL Biochem. Fmoc-PAL-PEG-PS resin for automated PNA synthesis was purchased from Applied Biosystems. PNA-R_9 conjugates were assembled on an Applied Expedite TM 8900 synthesizer (Applied Biosystems). ^{1}H NMR and ^{31}P NMR spectra were recorded on VarianUnityPlus-300. Trimethyl phosphate was used as the external reference for ^{31}P NMR. And all PNA conjugates were purified by reversed-phase high-performance liquid chromatography (HPLC) on a Beckman System Gold instrument equipped with a UV-vis array detector, using a Microsorb-MV 300-5 C-18 column (250×4.6mm column, 300A pore size, Varian Inc.). HPLC fractions were collected and concentrated under vacuum in a SpeedVac Evaporator (Savant Inc.). UV-vis absorption of all PNA conjugates was determined with a Bausch and Lomb Spectronic1001 spectrophotometer and a Varian Cary 100 bio UV-vis spectrophotometer. Concentration of all PNA conjugates was determined by the Beer-Lambert law using standard extinction coefficients at UV wavelength of maximum absorbance of 260nm to calculate both amounts and Partition Ratios. All PNA conjugates were characterized by MALDI-TOF on a PerSpective Voyager RP MALDI-TOF mass spectrometer in linear mode using insulin as the internal reference, and α-cyano-4-hydroxycinnamic acid (CHCA) as the matrix. Fluorescence spectra were measured on a Varian Cary Eclipse fluorescence spectrophotometer to determine CMC (Critical Micelle Concentration). Telomerase PCR ELISA kit was purchased from Roche Applied Sciences.

Syntheses of the Phosphodiester Intermediate (Compound 2) [25]

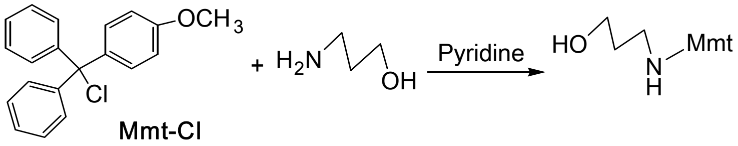

Figure 2.7 Preparation of 3-((4-Methoxyphenyl)diphenylmethylamino)propan-1-ol

4-Methoxytriphenylmethyl chloride (Mmt-Cl) (2 g, 6.5 mmol) was dissolved in anhydrous pyridine (20 mL), and 1-amino-propanol (6.87 g, 91.5 mmol) was added and stirred at room temperature for 3 days. The pyridine was evaporated and EtOAc was added. The organic phase was extracted with saturated aqueous NaCl solution (3 × 100 mL), dried with Na_2SO_4, filtered, and concentrated. The residue was evaporated and purified by column chromatography to afford the product 3-((4-methoxyphenyl)diphenylmethylamino) propan-1-ol in 66 % yield. ^{1}H NMR ($CDCl_3$, 300 MHz). δ 7.2-7.4 (m, 10H), 7.13 (d, 2H), 6.75 (d, 2H), 7.26 (m, 2H), 3.8 (t, 2H), 3.7 (s, 3H), 2.3 (t, 3H), 1.63 (m, 2H).

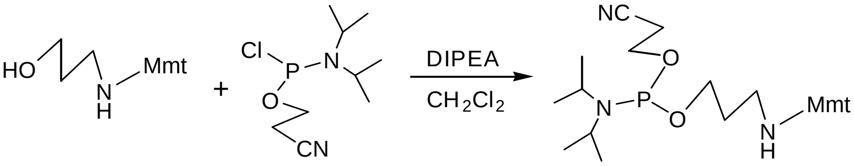

Compound 1

Figure 2.8 Preparation of **Compound 1**[26]

3-((4-Methoxyphenyl)diphenylmethylamino)propan-1-ol (0.74 g, 2.33 mmol) was dissolved in freshly distilled CH_2Cl_2 (23 mL). N,N-Diisopropylethylamine (1.63 mL, 9.34 mmol) was added, followed by 2-cyanoethyl N,N-diisopropylchlorophosphoramidite (1.04 mL, 4.67 mmol). The mixture was stirred at room temperature for 8 h before addition of saturated aqueous NH_4Cl solution (100 mL). The aqueous layer was extracted with EtOAc (3 × 100 mL). The combined organic extracts were dried with Na_2SO_4, filtered, and concentrated. The residue was purified by column chromatography with (SiO_2, EtOAc:Hexane=v/v=1:1, 3% Et_3N) to afford product, Compound **1** in 42 % yield. ^{1}H NMR (CD_2Cl_2, 300 MHz), δ 7.15-7.4 (m, 10H), 7.1 (d, 2H), 6.7 (d, 2H), 3.7 (s, 3H), 3.6 (m, 2H), 3.45 (m, 2H), 2.42 (t, 3H), 2.15 (t, 2H), 1.72 (m, 2H), 1.2 (m, 2H), 1-1.1 (s, 4H). ^{31}P NMR (CD_2Cl_2, 121.4 MHz) δ =+145 ppm

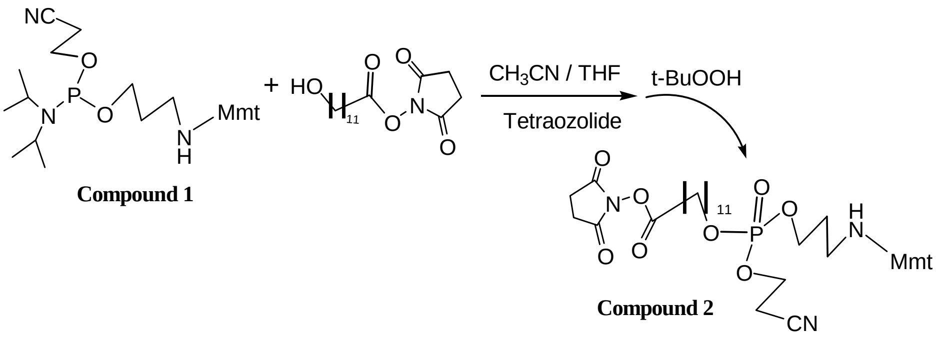

Figure 2.9 Preparation of **Compound 2**[26]

Compound **1** (1.303 g, 2.38 mmol) from the previous step was dissolved in freshly distilled CH_2Cl_2 (9 mL) and CH_3CN (9 mL). 2,5-Dioxopyrrolidin-1-yl-12-hydroxydodecanoate (0.75 g, 2.38 mmol) was added, followed by diisopropylammonium tetrazolide (0.41 g, 2.38 mmol). The mixture was stirred at room temperature for 12 h before addition of tert-butyl hydroperoxide (5 M, 1.83 mL). The reaction was quenched after 2 h with saturated aqueous $NaHCO_3$ solution (100 mL). The aqueous layer was extracted with EtOAc (3 × 100 mL). The combined organic extracts were dried with Na_2SO_4, filtered, and concentrated. The oil was purified by chromatography (SiO_2, 50% EtOAc in hexanes) to afford Compound **2** (0.75 g, 42%) as pale yellow oil: ^{1}H NMR (CD_2Cl_2, 300 MHz) δ 7.54 (m, 4H), 7.42 (m, 2H), 7.36 (m, 4H), 7.26 (m, 2H), 6.87 (m, 2H), 4.26 (m, 2H), 4.14 (m, 2H), 4.06 (m, 2H), 3.85 (s, 3H), 2.83 (s, 4H), 2.73 (t, J= 6.2 Hz, 2H, CH_2CN), 2.65 (t, J= 7.5 Hz, 2H, CH_2CONHS), 2.28 (m, 2H), 1.93 (m, 2H), 1.78 (m, 4H), 1.35 (m, 14H); ^{13}C NMR (CD_2Cl_2, 75 MHz) δ 169.6, 169.1, 158.3, 146.7, 130.0, 128.7, 128.0, 126.5, 117.0, 113.3, 70.6, 68.5, 66.6, 66.5, 62.0, 55.4, 40.0, 31.6, 31.1, 30.5, 29.7, 29.6, 29.3, 29.0, 25.9, 25.6, 24.9, 19.9; ^{31}P NMR (CD_2Cl_2, 121.4 MHz) δ= - 0.1ppm.

Solid-phase Synthesis of Telm-R$_9$ and Telm-TAT conjugates

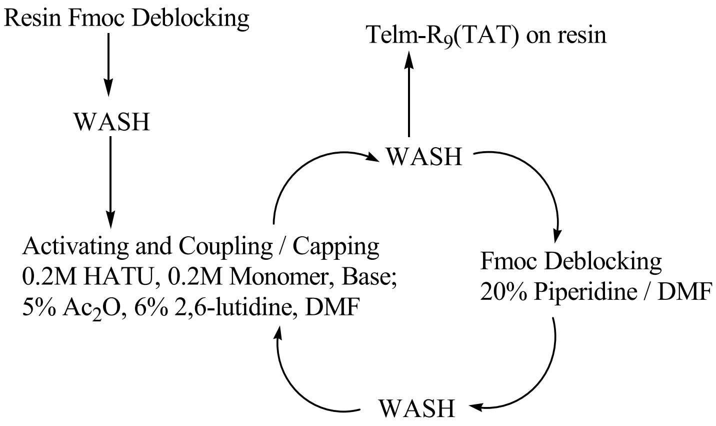

Figure 2.10 Solid-phase Synthetic procedures of Lipid/Phospholipid-Telm-CPP(R$_9$/TAT) conjugates

Telm-R$_9$ and Telm-TAT conjugates [27] were all prepared by automated standard Fmoc chemistry on 2μmol scale following the general synthesis procedure shown in Figure 2.10. Then the resin with Telm-R$_9$/TAT conjugate was washed with anhydrous DMF (3×1 mL) and DCM (3×1 mL) respectively, dried with nitrogen for cleavage and purification.

Synthesis of Lipid-Telm-R$_9$ and Lipid-Telm-TAT conjugates

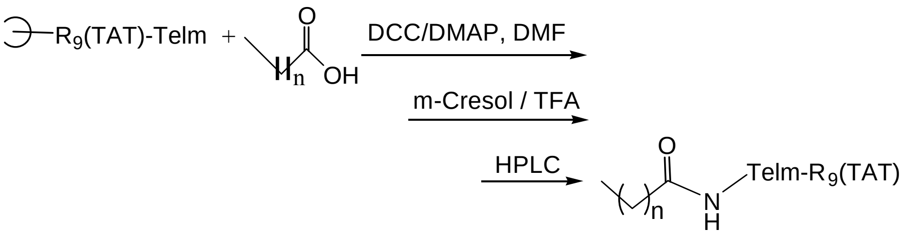

Lipid-Telm-R$_9$(TAT)

n=12,14,16

Figure 2.11 Solid-phase Synthesis of Lipid-Telm-R$_9$/TAT conjugates

After the Telm-R_9/TAT conjugates [28] were synthesized on the resin, the resin was washed and dried by the automated standard Fmoc chemistry synthesis procedure. After this, the resin with the conjugates was added into an anhydrous DMF solution (100 μL) containing the fatty acid (20 μmol), DCC (20 μmol) and DMAP (20 μmol) and shaken overnight at room temperature. The resin with the lipid-Telm-R_9/TAT conjugate was then washed with anhydrous DMF (3×1 mL) and DCM (3×1 mL) respectively, and dried with nitrogen prior to cleavage and purification.

Synthesis of Pal-P-Telm-R_9, P(CN)-Telm-R_9 and P-Telm-R_9 conjugates [26]

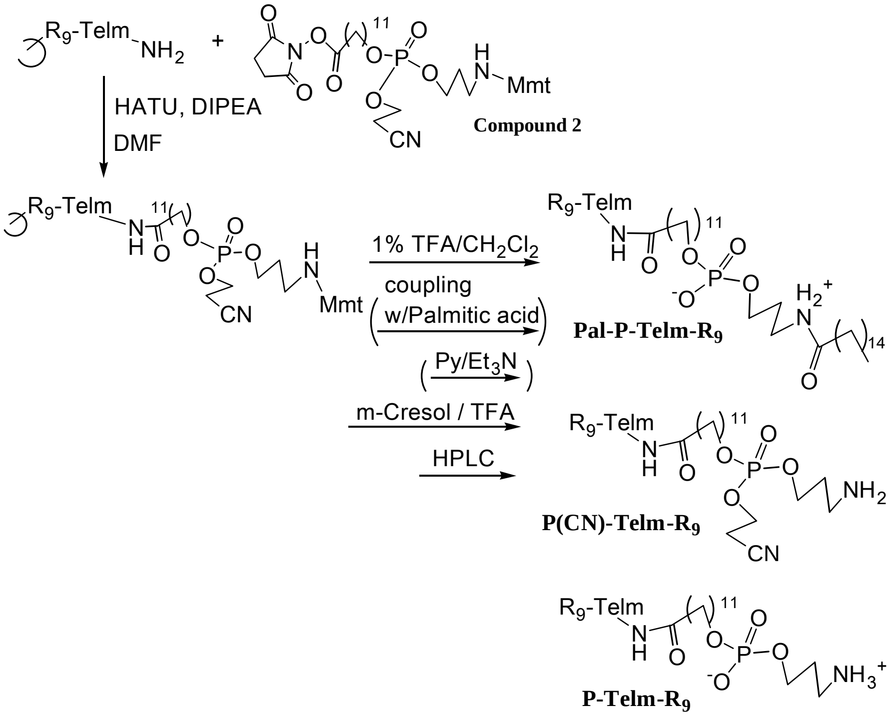

Figure 2.12 Solid-phase synthesis of Pal-P-Telm-R_9, P(CN)-Telm-R_9 and P-Telm-R_9 conjugates

After Telm-R_9 conjugates were synthesized, the resin was washed and dried by the programmed steps, and then added to an anhydrous DMF solution containing the phosphodiester intermediate Compound **2** (20 μmol), HATU (20 μmol), DIPEA (20 μmol) and 100 μL DMF and shaken overnight at room temperature. The resin was then washed with anhydrous DMF and DCM three times respectively, and dried with nitrogen. Then 1% TFA in DCM solution (6×1 mL) was added to remove the Mmt group on the N-terminus before washing with 2% DIPEA and DCM three times each to remove the residual acid. The resin was then dried and added to an anhydrous DMF solution (100 μL) of palmitic acid (20 μmol), DCC (20 μmol), DMAP (20 μmol) and shaken overnight. The resin was then washed with anhydrous DMF/ DCM three times respectively, and dried with nitrogen. The resin was then added into an anhydrous DMF solution (100 μL) containing pyridine (20 μmol) and triethyl amine (20 μmol) and shaken overnight. The resin was washed with anhydrous DMF and DCM three times respectively before cleavage and purification to afford Pal-P-TelmR$_9$ and P-TelmR$_9$ conjugates. [26] Under the similar condition to repeat this synthesis route without the deblocking step of pyridine/triethyl amine, P(CN)-TelmR$_9$ and P-Telm-R$_9$ conjugates [26] were obtained.

Cleavage, Purification and Characterization of the Telm-CPP conjugates

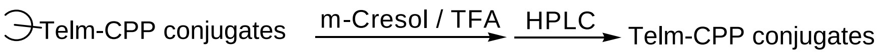

Figure 2.13 Cleavage and Purification of Telm-CPP conjugates

After the synthesis of the conjugates on the resin was completed, the resin was incubated in 400 μL TFA/m-cresol (4:1) for 3 h [27] to remove the protecting groups. Then the Telm-CPP conjugates were precipitated by the addition of 10 volumes of ice-cold diethyl ether. The crude product was collected by centrifugation and purified by reverse phase HPLC with a 65-min 1 mL/min linear gradient from 5 to 70% of buffer B (0.1% TFA in CH$_3$CN) in buffer A (0.1% TFA in dd water). The fractions containing the desired Telm-CPP conjugates were evaporated, dissolved in dd water, and characterized with MALDI-TOF with 1% CHCA in 1:1 ratio of acetonitrile to 0.1% TFA in dd water.

Determination of Critical Micelle Concentration (CMC) [29]

Stock solutions of Pal-P-Telm-R_9 and Lipid-Telm-R_9 conjugates were diluted in water to different concentrations. Two buffers, with or without NaCl were made in 2% methanol/water containing 10 μM pyrene, 150 mM NaCl, 5 mM Tris•HCl, pH=7 and 10 μM pyrene, 5 mM Tris•HCl, pH=7. Two series of samples were made with or without NaCl for each PNA conjugate, by mixing 25 μL buffer and 25 μL stock solutions of different concentrations. Fluorescence emission spectra were obtained by exciting the pyrene at 300 nm. The ratio of intensity of the first (373 nm) and third (383 nm) emission peaks was plotted against PNA concentration to determine the CMC from the breakpoint in a bilinear fit to the data.

Telomerase Activity Assay

This assay was carried out in Dr. Tej Pandita's laboratory at the Washington University School of Medicine.

First, 293 cells were plated at a density of 2×10^5 per well in a 24-well plate and allowed to adhere overnight. Then the medium was removed and the cells were transfected with 1.25 μM, 2.5 μM or 5 μM PNA-CPP conjugates, respectively. After a 72 h incubation, the medium was again discarded, and the cells were washed with cold PBS three times, followed by the addition of 100 μL trypsin solution (0.05% Trypsin/EDTA) in each well. The trypsin was then inactivated by the addition of 400 μL regular growth medium. Cells were collected by centrifugation at 3000 rpm for 5 min and their telomerase activity was analyzed by Telomerase PCR ELISA kit.

2.4 Results and Discussion

Antisense PNA conjugates and controls for targeting hTR template region, like Telm-R_9(TAT), Lipid-Telm-R_9(TAT), P-Telm-R_9, P(CN)-Telm-R_9 and Phosphorlipid-Telm-R_9 conjugates were synthesized, purified by HPLC and characterized with MALDI and studied as inhibitors of human telomerase activity. As shown below, MALDI (matrix-assisted laser desorption ionization) was used to test and affirm the presence of the correct PNA conjugates through comparison with the calculated and experimentally determined molecular masses.

Table 2.2 MALDI for Telm-R_9, Ted-Telm-R_9, Pal-Telm-R_9, Ste-Telm-R_9, Pal-P-Telm-R_9, P-Telm-R_9, P(CN)-Telm-R_9, Ted-Telm-TAT, Pal-Telm-TAT, Ste-Telm-TAT and Telm-TAT conjugates

Sample	Cal. MW	MALDI	Figure No (Appendix)
Telm-R_9	5011	5015	Figure A2.3
Ted-Telm-R_9 (n=12)	5222	5225	Figure A2.9
Pal-Telm-R_9 (n=14)	5250	5251	Figure A2.6
Ste-Telm-R_9 (n=16)	5278	5279	Figure A2.12
Pal-P-Telm-R_9	5585	5586	Figure A2.15
P-Telm-R_9	5347	5347	Figure A2.18
P(CN)-Telm-R_9	5400	5401	Figure A2.21
Ted-Telm-TAT (n=12)	5360	5356	Figure A2.35
Pal-Telm-TAT (n=14)	5388	5389	Figure A2.38
Ste-Telm-TAT (n=16)	5416	5419	Figure A2.41

Telm-TAT	5149	5149	Figure A2.32

Because the lipidated and phospholipid modified PNA conjugates have hydrophobic tails and charged head groups, they are amphiphilic, and it seemed likely that they would form micelles in aqueous phase, which might be relevant to their mechanism of uptake by cells through endocytosis or membrane fusion. [30] By using a pyrene-based fluorescence assay, the critical micelle concentrations (CMC) of four PNA conjugates were determined in two buffers with NaCl or without NaCl. Because the positively charged cell penetrating peptide chains would be expected to repel each other in a micelle, it was expected that CMC of PNA conjugates would be lower in the presence of salt. This was indeed demonstrated by the CMC of 4 μM for the phosholipid-Telm-R_9 in the presence of NaCl and 6 μM in the absence of NaCl, and both are lower than the corresponding CMC values of lapidated PNA conjugates in aqueous phase. This trend was also observed by Gang Shen's CMC results [30] with phospholipid PNA conjugate (decreasing from 1.7 to 1.0 μM) and lipid PNA conjugates (decreasing from 9.2 to 4.5 μM), which were synthesized and tested by a splice-correction Luciferase assay later. However, the CMC's in NaCl solution were not lower than those in solutions without NaCl, probably because the differences between the lengths of lipid chains were too small to be shown statistically stable.

Table 2.3 CMC for Ted-Telm-R_9, Pal-Telm-R_9, Ste-Telm-R_9, Pal-P-Telm-R_9 conjugates

Sample	CMC (w/NaCl µM)	Figure No (Appendix)	CMC (w/o NaCl µM)	Figure No (Appendix)
Ted-Telm-R_9 (n=12)	11	Figure A2.23	12	Figure A2.22

Pal-Telm-R_9 (n=14)	14	Figure A2.25	11	Figure A2.24
Ste-Telm-R_9 (n=16)	6	Figure A2.27	5.5	Figure A2.26
Pal-P-Telm-R_9	4	Figure A2.29	6	Figure A2.28

The PNA conjugates were then tested for their ability to inhibit the telomerase activity in vitro. Six different Lipid-Telm-R_9 and Phospholipid-Telm-R_9 conjugates and three controls including no treatment, Telm-R_9 and GRN163L were tested in vitro at a concentration of 1 μM for 72 h. Except for P(CN)-Telm-R_9 and Ted-Telm-R_9 conjugates which showed slight telomerase inhibition, the other conjugates showed no significant activity, compared with GRN163L. Previously, however, Xuan Yue from our group [27] and coworkers had found significant inhibition by 13-mer PNA(CAGTTAGGGTTAG)-Arg_9 conjugates.

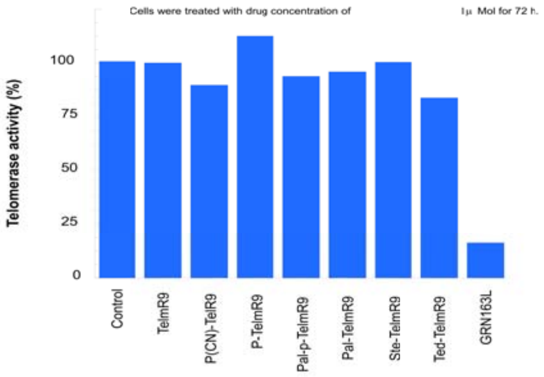

Figure 2.14 Telomerase Activity Assay in vitro

Because no initial promising results were observed and funding for this project was terminated, these bioassays were not repeated and no further bioassays were carried out. It is possible, however, that further testing under different conditions would have shown some activity, perhaps at higher concentrations approaching the CMD. Therefore, more bioactivity tests would need to be conducted before any solid conclusion can be drawn.

References

1 Black, E. Nature, 1991, 350, 569-573

2 Greider, C. W. Annu. Rev. Biochem., 1996, 65, 337-365

3 Nugent, C. I.; Lundblad, V. Genes & Dev., 1998, 12, 1073-1085

4 Shay, J.W.; Bacchetti, S., Eur. J. Cancer 1997, 33, 787-791

5 Zaffaroni, N.; Villa, R.; Pennati, M.; Folini, M. Mini Reviews in Medicinal Chemistry 2003, 3, 51-60

6 Noton, J . C.; Piatyszek, M. A.; Wright, W.E.; Shay, J. W.; Corey, D. R. Nat. Biotechnol. 1996, 14, 615-618

7 Hamilton, S. El; Pitts, A. E.; Katipally, R. R.; Jia, X.; Rutter, J. P.; Davies, B. A.; Shay, J. W.; Wright, W. E.; Corey, D. R. Biochemistry 1997, 36, 11873-11880

8 Pitts, A. E.; Corey, D. R. Proc. Natl. Acad. Sci. U. S. A. 1998, 95, 11549-11554

9 Herbert, B. S.; Pitts, A. E.; Baker, S. I. Hamilton, S. E.; Wright, W. E.; Shay, J. W.; Corey, D. r. Proc. Natl. Acad. Sci. U. S. A. 1999, 96, 14276-14281

10 Elayadi, A. N.; Braasch, D. A.; Corey, D. R. Biochemistry 2002, 41, 9973-9981

11 Folini, M.; Berg, K.; Millo, E.; Villa, R.; Prasmickaite, L.; Daidone, M. G.; Benatti, U; Zaffaroni, N. Cancer Res. 2003, 63, 3490-3494

12 Folni, M.; Pennati, M.; Zaffaroni, N. Curr. Med. Chen. Anti-Cancer Agents, 2002, 2, 605-612

13 Rezler, E. M.; Bearss, D. J.; Hurley, L. H., Annu. Rev. Pharmacol. Toxicol. 2003, 43, 359-379

14 Corey, D. R. Oncogene 2002, 21, 631-637

15 Theimer, Carla A., Feigon, Juli, *Current Opinion in Structural Biology*, 2006, 16**,** 307-318

16 Ben-Tal, N., Honig, B., Peitzsch, R. M., Denisov, G., McLaughlin, S., 1996, Biophys. J. 71, 561-575

17 Murray, D., Arbuzova, A., Hangyás-Mihál振ne, G., Gambhir, A., Ben-Tal, N., Honig, B., and McLaughlin, S., 1999, Biophys. J. 77, 3176-3188

18 Wimley, W. C., Hristova, K., Ladokhin, A. S., Silvestro, L., Axelsen, P. H., and White, S. H., 1998, J. Mol. Biol. 277, 1091-1110

19 Mosior, M, and McLaughlin, S., 1992, Biochemistry, 31, 1767-1773

20 Wender, P. A.; Mitchell, D. J.; Pattabiraman, K.; Pelkey, E. T.; Steinman, L.; et al. Proc. Natl. Acad. Sci. U. S. A., 2000, 97, 13003-13008

21 Jaysinghe, S., Hristova, K., Wimley, W., Snider, C., White, S. H., 2009, Membrane Protein Explorer (MPEx). *http://www.blanco.biomol.uci.edu/mpex.*

22 Almeida, P. F., Pokorny, A., *Biochemistry*, 2009, 48, 8083-8093

23 White, S. H., Wimley, W. C., *Annu. Rev. Biophys. Biomol. Struct*., 1999, 28, 319-365

24 Jean Philippe Richard, Leonid V. Chernomordik, The Journal of Biological Chemistry, 280, 15300-15306

25 Uffe Koppelhus, Takehiko Shiraishi, Peter E. Nielsen et al, 2008, 19, 1526-1534

26 Hamilton, S. E., Corey, David. R., Biochemistry, 1997, 36, 11873-11880

27 Manjula Ararwal, Xuan Yue, John-Stephen A. Taylor, Tej K. Pandita et al, Cancer Research, 2008, 68, 9, 3370-3378

28 Brittney-Shea H.; Genelle C. G.; Amelia H.; Krisztina P.; et al; Oncogene, 2005, 24, 5262-5268

29 Goddard, E. D., Turro, N. J., Kuo, P. L., 1985, Langmuir, 1, 352-5.

---

30 Gang Shen et al, Bioconjugate Chem., 2009, 20, 9, 1729-1736

Chapter 3

Design and Synthesis of Lipid-PNA-Peptide Conjugates as Better Antisense PET Imaging Agents

Abstract

Positron emission tomography (PET), as noninvasive imaging technique, is a sensitive and specific imaging modality used to investigate diseases at the cellular and molecular levels. Of the various PET agents that have been developed to image gene expression in small animal models, oligonucleotides appear attractive for the development of new tracers with high specificity, considering that an ODN with more than 16 bases can target a unique sequence in the whole human genome. Herein a library of Lipid-PNA-TAT conjugates targeting the unr mRNA that is overexpressed in MCF-7 breast cancer cells were designed and synthesized. The PNAs contained a tyrosine as part of the N terminal of TAT(48-60) peptide sequence which could be radiolabeled with Br-76. The lipidated PNA conjugates were studied for their potential to image MCF-7 tumors in vivo by biodistribution assays.

3.1 Bromine-76 Labeled Radiotracers with promising application in Positron emission tomography

Radiohalogenated organic compounds are commonly used in research and the clinic as radiopharmaceutical probes for molecular imaging via positron emission tomography (PET) or internal radiotherapy at the cellular level. [1] Compared with radiofluorination, radiobromination has attracted more attention for use in imaging slower physical processes, due to the relatively long half-time of 16.2 hours for Br-76, compared to 110min for F-18. Bromine-labeled compounds have some advantages over iodine-labeled compounds, because they are more stable due to a stronger C-Br bond, and because free iodide tends to accumulate in the thyroid. [2]

Br-76 decays simultaneously by positron emission (57%) and by electron capture (43%), [3] making such agents capable of both PET imaging and radiation therapy. The Br-76 nuclide can be conveniently produced via the ^{76}Se(p,n)^{76}Br reaction on most medical cyclotrons. [4]

With a half-life of 16.2 h, a Br-76-labelled tracer lives long enough to allow target-tissue-selective distribution, but sufficiently short so that the bulk of the dose can be delivered to the tissue prior to metabolism and elimination of the radiopharmaceutical. Organic compounds can be readily labeled with high specific activity (SA), which is a general requirement for the design and the development of Br-76-labelled tracers with high target-specificity activity. [5, 6]

Biological molecules often contain aromatic rings onto which Br-76 can be conveniently introduced by using very high specific activity [Br-76] bromide ion in the presence of an oxidant. Considering that oligodeoxynucleotides (ODN) with more than 16 bases can target unique sequences in the whole human genome [7], there is the opportunity that ODNs labeled with [Br-76] radionuclides could become promising as new radiotracers with high specificity for PET imaging and therapeutic applications.

3.2 Design and Synthesis of Lipid-PNA-CPP conjugates

Unfortunately, naturally occurring ODNs cannot be directly used as nuclear imaging probes because they are rapid degraded in vivo by endo- and exonucleases. In addition, ODNs cause degradation of target mRNA by RNAse H. In order to increase the in vivo stability of ODNs without significantly influencing their biophysical and targeting properties, chemical modifications of the sugar-phosphate backbone are required, which increases the difficulty and complexity in the preparation steps of the radiotracers, compared with relatively easily-obtained PNAs through solid-phase synthesis procedure.

To function usefully as a biological radioprobe, antisense PNAs must target a uniquely overexpressed mRNA in the tumor cells. Previously the Taylor group discovered from a search of NCBI SAGE (serial analysis of gene expression) database that the unr mRNA is approximately 7 times more highly expressed in the MCF-7 breast cancer cell line than it is in any normal tissue cell line, and that it is present in about 5,000 copies per cell, making it an ideal initial target for imaging studies. By using a RT-ROL method for mapping antisense binding sites on native mRNA, three antisense PNAs were identified with high binding affinity for the unr mRNA.

The Taylor group then showed that these PNAs with four lysines at the C terminus and a DOTA moiety at the N terminus were able to image MCF-7 tumors in mice by PET (Figure1.39 and Figure1.40). Though these PNAs showed sequence selective uptake by the tumor, they were rapidly excreted and showed little tumor uptake. Herein we designed and synthesized a library of lipidated antisense PNA(50/5/7)-TAT conjugates that were expected to be better retained and show higher tumor uptake. The PNA conjugates were synthesized by Fmoc chemistry on solid support, characterized, and evaluated as potential imaging probes for MCF-7 tumors in vivo (Figure 3.1 and Figure 3.2).

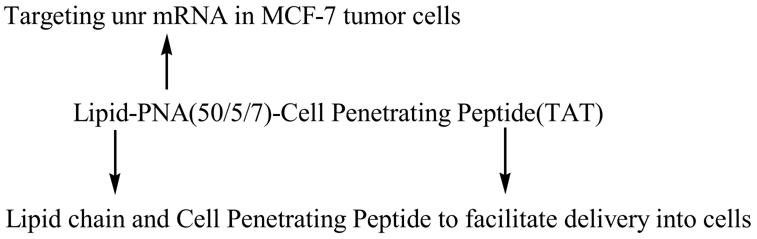

Figure 3.1 Design of Lipid-PNA(50/5/7)-TAT conjugates

Lipid-PNA50-TAT

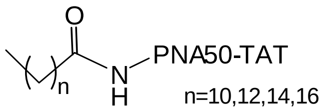

Lipid-PNA5-TAT

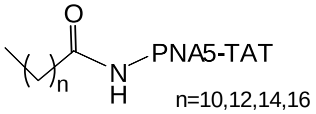

Lipid-PNA7-TAT

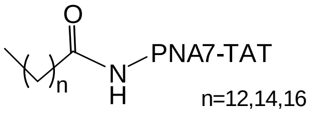

PNA(50/5/7)-TAT PNA(50/5/7)-TAT

Figure 3.2 Structures of Lipid-PNA(50/5/7)-TAT and PNA(50/5/7)-TAT conjugates

3.3 Experimental Procedures

Materials and Methods

All reactions were performed under an argon or nitrogen atmosphere unless otherwise specified. All commercially available materials were used without further purification unless otherwise noted. Anhydrous solvents for reactions, such as DMF, DCM, and acetonitrile were either used as obtained from Sigma-Aldrich or distilled from an appropriate drying agent. All chemicals and reagents used were of the highest purity available. Acetonitrile, trifluoroacetic acid, m-cresol and reagents for automated PNA synthesis were purchased from Aldrich. The 11-mer Fmoc-protected TAT on resin for solid-phase synthesis (Fmoc-YGRRQRKKRRR-PAL-PEG-PS) was purchased from GL Biochem. Fmoc-PAL-PEG-PS resin for automated PNA synthesis was purchased from Applied Biosystems. PNA(50/5/7)-TAT conjugates were assembled on an ExpediteTM 8900 Nucleic Acid Synthesis System purchased by Applied Biosystems. And all PNA conjugates were purified by reversed-phase high-performance liquid chromatography (HPLC) on a Beckman System Gold instrument equipped with a UV-vis array detector, using a Microsorb-MV300-5 C-18 column (250 × 4.6mm column, 300 Ǻ pore size, Varian Inc.). HPLC fractions were collected and concentrated under vacuum in a SpeedVac evaporator (Savant). UV-vis absorption of all PNA conjugates was determined with a Bausch and Lomb Spectronic1001 spectrophotometer or a Varian Cary 100 bio UV-vis spectrophotometer. The concentration of PNA conjugates were determined by the Beer-Lambert law using standard extinction coefficients for the PNA bases at 260nm. All PNA conjugates were characterized by MALDI-TOF on a PerSpective Voyager RP MALDI-TOF mass spectrometer in linear mode using insulin as the internal reference. A-cyano-4-hydroxycinnamic acid (CHCA) was used as the matrix. Fluorescence spectra were measured on a Varian Cary Eclipse fluorescence spectrophotometer to determine CMC (critical micelle concentration). DLS data were obtained in dd water on Zetasizer Nano ZS using disposable Low Volume Cells purchased from Malvern Instruments Inc. Br-76 was produced at the Washington University cyclotron facility by the ^{76}Se(p,n)^{76}Br nuclear reaction on a ^{76}Se-enriched Cu_2Se target. ^{76}Br was recovered via a dry distillation method. The radionuclide was in the form of [^{76}Br]NH_4Br in 0.6 M NH_4OH. The solution was filtered through a C-18 Sep-Pak light cartridge (Waters Corp.) and blown down to dryness under very mild N2 flow at 130 °C. High-performance liquid chromatography (HPLC, Dionex, Sunnyvale, CA, USA) was performed with an ultraviolet detector operating at 231 nm and a radioactive detector. Agilent Zorbax SB-C18 250 × 4.6 mm 5 μm analytical column and Agilent Zorbax SC-C18 250 × 9.4 mm 5 μm semi-preparative column were used for analysis and preparative purification, respectively. Acetonitrile and water were used as the HPLC mobile phase. RadioTLC was performed using a Bioscan System 2000 imaging scanner (Bioscan, Washington, DC, USA). All animal experiments were conducted in compliance with the Guidelines for the Care and Use of Research Animals published by the Animal Studies Committee of Washington University in St. Louis, School of Medicine.

Synthesis of PNA(50/5/7)-TAT conjugates

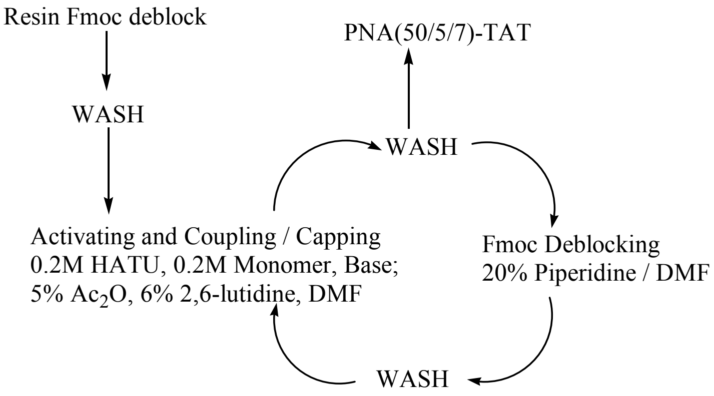

Figure 3.3 Solid-phase synthetic procedure for the synthesis of PNA(50/5/7)-TAT conjugates

PNA(50/5/7)-TAT conjugates[8] were prepared by automated standard Fmoc chemistry procedures on a 2 μmol scale after TAT was synthesized on resin by a company. The resin with PNA(50/5/7)-TAT conjugates was washed with anhydrous DMF (3 × 1 mL) and DCM (3 × 1 mL) respectively, dried with nitrogen for cleavage and purification.

Synthesis of Lipid-PNA(50/5/7)-TAT conjugates

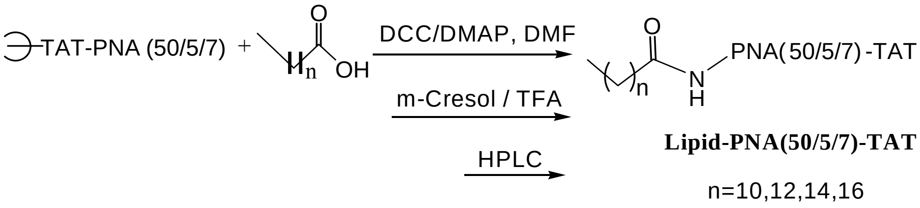

Figure 3.4 Solid-phase Synthesis of Lipid-PNA(50/5/7)-TAT conjugates

After the PNA(50/5/7)-TAT conjugates[9] were prepared on the resin, the resin was washed and dried by automated standard steps and then added into an anhydrous DMF solution (100 μL) containing the fatty acid (20 μmol), DCC (20 μmol) and DMAP (20 μmol) and shaken overnight at room temperature. The resin with Lipid-PNA-R_9(TAT) conjugates was washed with anhydrous DMF (3 × 1 mL) and DCM (3 × 1 mL) respectively, dried with nitrogen for cleavage and purification.

Cleavage, Purification and Characterization of PNA(50/5/7) conjugates

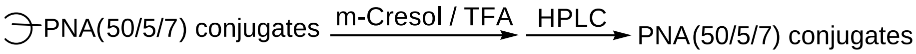

Figure 3.5 Cleavage and purification of PNA(50/5/7) conjugates

After the automated synthesis and post-synthetic modification in vials, the resin was incubated in 400 μL TFA/m-cresol (4:1) [20] for 3 h. The released PNA(50/5/7)-TAT conjugates were then precipitated by the addition of 10 volumes of ice-cold diethyl ether. The crude product was collected by centrifugation and purified by reverse phase HPLC with a 65 -min 1 mL/min linear gradient of 5 to 70% buffer B (0.1% TFA in CH_3CN) in buffer A (0.1%TFA in dd water). The fractions containing the desired PNA conjugates were evaporated, dissolved in dd water, and characterized by MALDI-TOF with a matrix prepared from 1% CHCA in 1:1 ratio of acetonitrile vs 0.1% TFA in dd water.

Determination of Critical Micelle Concentration (CMC) [10]

Stock solutions of Lipid-PNA(50/5/7)-TAT conjugates were diluted in water to different concentrations. Two buffers, with or without NaCl in 2% methanol/water as (10 μM pyrene, 150 mM NaCl, 5 mM Tris, pH=7) and (10 μM pyrene, 5mM Tris, pH=7). Two series of CMC samples were made with or without NaCl for each PNA conjugate, by mixing 25 μL buffer and 25 μL of stock solutions of different concentrations. Fluorescence emission spectra were obtained by exciting the pyrene at 300 nm. The ratio of intensity of the first (373 nm) and third (383 nm) emission peaks was plotted against PNA concentration to determine the CMC from the breakpoint in a bilinear fit to the data.

Dynamic Light Scattering (DLS) Analysis [11]

Stock solutions of Lipid-PNA(50/5/7)-TAT conjugates were diluted in water to different concentrations. Dynamic light scattering data was used to calculate the average micelle size at different concentrations on a Malvern Nano ZS. The average micelle size was plotted against PNA concentration to determine the minimum average micelle size range.

Determination of Partition Ratios [12]

Equal volumes (10mL) of octanol and water were mixed completely and allowed to separate into two clear layers. Lipid-PNA(50/5/7)-TAT conjugates were then dissolved in equal volumes (0.15mL) of the two clear layers for each sample. The solution was vortexed to allow complete mixing before measuring the concentration of the solute in each solvent by UV-vis spectroscopy at 260 nm. The partition ratio was calculated as the ratio of the absorption in water vs the absorption in 1-octanol.

[Br-76] Radiolabeled PNA conjugates (Carried out by Yongjian Liu in Dr. Michael Welch's laboratory at School of Medicine)

The radiolabeling of Br-76 for Pal-PNA50-TAT, Pal-PNA50S-TAT, PNA50-TAT and PNA50S-TAT conjugates was done with bromoperoxidase (BPO) and hydrogen peroxide at room temperature for 1 h in an aqueous phase. Then each radiolabeling reaction solution was purified by TLC and HPLC to obtain the Br-76 radiolabeled PNA conjugates with the yield of more than 90%. During the HPLC purification step, both the UV-vis detector for PNA-peptide and the radioactivity detector for Br-76 were simultaneously monitored to ensure that the fractions collected by HPLC were the desired Br-76 radiolabeled PNA conjugates. The concentrations of the purified Br-76 radiolabeling PNA conjugates were given in Table 3.1. As for the TLC and HPLC data, see the **Attached Data Sheet** at the end of Chapter 3 for detail as evidence.

Biodistribution Assay (Carried out by Yongjian Liu in Dr. Michael Welch's laboratory at School of Medicine)

Four HPLC-purified PNA conjugates at a specific activity of 10 μCi/100 μL were injected via the tail vein into female nu/nu mice (a group of 15) with MCF-7(IL) tumors and estrogen pellets. The biodistribution of the radioactivity in % ID/gram for eight different organs and tumors were collected and averaged for 5 mice for three time points of 1 h, 4 h and 24 h after injection.

3.4 Results and Discussion

Eleven antisense Lipid-PNA-TAT conjugates and three controls were synthesized and characterized by MALDI, CMC, DLS and partition ratio. As shown below, MALDI (matrix-assisted laser desorption ionization) was used to test and confirm the presence of the correct PNA conjugates in a specific HPLC fraction.

Table 3.1 Sequences of PNA-TAT used as PNA50-TAT, PNA50S-TAT, PNA5-TAT and PNA7-TAT

Sample	Sequence
PNA50-TAT	TGGTGTGCTTTGTGGATG-YGRKKRRQRRR
PNA50S-TAT	CATCCACAAAGCACACCA-YGRKKRRQRRR
PNA5-TAT	CATTATGTCCATTGTTGT-YGRKKRRQRRR
PNA7-TAT	TTTCCCAGTCCGTCGGTC-YGRKKRRQRRR

Table 3.2 MALDI for Lipid-PNA(50/5/7)-TAT and PNA(50/5/7)-TAT conjugates

Sample	Cal MW	MALDI	Figure No (Appendix)

Ste-PNA50-TAT	6810	6828.5	Figure A3.18
Pal-PNA50-TAT	6782	6784	Figure A3.9
Ted-PNA50-TAT	6754	6764.58	Figure A3.15
Lau-PNA50-TAT	6726	6741.32	Figure A3.12
PNA50-TAT	6544	6548.6	Figure A3.3
PNA50S-TAT	6327	6329.7	Figure A3.6
Ste-PNA5-TAT	6673	6688.64	Figure A3.33
Pal-PNA5-TAT	6407	6658.38	Figure A3.30
Ted-PNA5-TAT	6617	6629.43	Figure A3.27
Lau-PNA5-TAT	6589	6599.28	Figure A3.24
PNA5-TAT	6407	6407	Figure A3.21
Ste-PNA7-TAT	6620	6628.59	Figure A3.45
Pal-PNA7-TAT	6592	6603.12	Figure A3.42
Ted-PNA7-TAT	6564	6573.29	Figure A3.39
PNA7-TAT	6354	6350.4	Figure A3.36

By using a pyrene-based fluorescence assay, the critical micelle concentrations (CMC) of the eleven Lipid-PNA-TAT conjugates were determined in two aqueous buffers of with NaCl or without NaCl. The CMC values of almost all Lipid-PNA-TAT conjugates in the aqueous buffer with NaCl were lower than those CMC values of corresponding Lipid-PNA-TAT conjugates in the aqueous buffer without NaCl, except for Lau-PNA50-TAT. This trend was also found by Gang Shen [14] for Lipid-PNA-R_9 conjugates, utilizing a Luciferase splice-correction PNA sequence. The similarity was probably because the TAT group containing six arginine residues along with two lysine residues thereby having a similar positive charge repelling each other in a micelle or a vesicle formed.

Considering the different lengths of the lipid chains used in those lipid-PNA-TAT conjugates, no apparent relation or trend was found between the length of the lipid chains and the CMC values, probably because the differences between the lengths of lipid chains were too small to be shown any detectable differences in CMC, or because the pyrene based CMC method used was not sensitive or accurate enough to detect subtle differences.

Table 3.3 CMC for Lipid-PNA(50/5/7)-TAT conjugates

Sample	CMC (w/NaCl µM)	Figure No (Appendix)	CMC (w/o NaCl µM)	Figure No (Appendix)
Ste-PNA50-TAT	9.4	Figure A3.64	15.5	Figure A3.63
Pal-PNA50-TAT	9	Figure A3.62	14	Figure A3.61
Ted-PNA50-TAT	10	Figure A3.60	14	Figure A3.59
Lau-PNA50-TAT	12.4	Figure A3.58	11.7	Figure A3.57
Ste-PNA5-TAT	15.5	Figure A3.72	18.8	Figure A3.71
Pal-PNA5-TAT	7.8	Figure A3.70	23.4	Figure A3.69
Ted-PNA5-TAT	10	Figure A3.68	18.8	Figure A3.67
Lau-PNA5-TAT	14.1	Figure A3.66	15.6	Figure A3.65
Ste-PNA7-TAT	13	Figure A3.78	20.8	Figure A3.77
Pal-PNA7-TAT	20.7	Figure A3.76	26.1	Figure A3.75

Ted-PNA7-TAT	7.5	Figure A3.74	12.5	Figure A3.73

Because these Lipid-PNA-TAT conjugates contained hydrophobic tails and hydrophilic PNA-TAT parts, it was likely that those amphiphilic conjugates would form micelles in aqueous phase, which might explain their better uptake into cells through endocytosis or membrane fusion [30]. However, from the DLS results, the vesicle sizes formed from Lipid-PNA-TAT conjugates in the aqueous phase was found to be in the range of 90-260nm. This size range falls into the category of large size vesicles with spherical shape, which may be optimal for macropinocytosis, instead of micelle-induced intracellular delivery. And the relatively large vesicles size formed from those Lipid-PNA-TAT conjugates in the aqueous phase was probably due to the lack of the strong electrostatic repulsion at the ends of the PNAs, while PNA and lipid chain were neutral.

Table 3.4 DLS for Lipid-PNA(50/5/7)-TAT conjugates

Sample	DLS (nm)	Figure No (Appendix)
Ste-PNA50-TAT	290.2	Figure A3.49
Pal-PNA50-TAT	222.2	Figure A3.48
Ted-PNA50-TAT	303.9	Figure A3.47
Lau-PNA50-TAT	247.4	Figure A3.46
Ste-PNA5-TAT	210.8	Figure A3.53
Pal-PNA5-TAT	185.6	Figure A3.52
Ted-PNA5-TAT	94.7	Figure A3.51

Lau-PNA5-TAT	108.4	Figure A3.50
Ste-PNA7-TAT	184.9	Figure A3.56
Pal-PNA7-TAT	204	Figure A3.55
Ted-PNA7-TAT	260.1	Figure A3.54

The water/octanol partition ratios results of the Lipid-PNA-TAT conjugates showed that most of the Lipid-PNA-TAT conjugates greatly preferred the aqueous phase instead of the organic octanol phase. These results are in accord with the formation of micelles in which the positively charged peptide ends are exposed to water, while the hydrophobic lipid tails are buried within the core of the micelle.

Table 3.5 Partition Ratio for Lipid-PNA(50/5/7)-TAT conjugates

Sample	Partition Ratio (dd water/octanol)
Ste-PNA50-TAT	232
Pal-PNA50-TAT	258.5
Ted-PNA50-TAT	241.2
Lau-PNA50-TAT	612.6
Ste-PNA5-TAT	245.2
Pal-PNA5-TAT	347.2
Ted-PNA5-TAT	244.98
Lau-PNA5-TAT	464.4
Ste-PNA7-TAT	158.9
Pal-PNA7-TAT	258.4
Ted-PNA7-TAT	175.8

Since the purpose of designing and synthesizing the lipid-PNA-TAT conjugates was to test their application as potential radioactive imaging agents for PET, Pal-PNA50-TAT and Pal-PNA50S-TAT conjugates were radiolabeled by Br-76 with bromoperoxidase (BPO) and hydrogen peroxide and purified by TLC and HPLC. The bromine-76 radiolabeling yield was calculated to be more than 90% from analysis of the UV-vis and radioactivity HPLC detection data, which indicated that the reaction for radiolabelling with Br-76 was very successful (Table 3.1).

Table 3.6 [Br-76] Radiolabeling yield of PNA conjugates

Sample	mCi/μmol
Pal-PNA50-TAT	140
Pal-PNA50S-TAT	160
PNA50-TAT	53.5
PNA50S-TAT	52.8

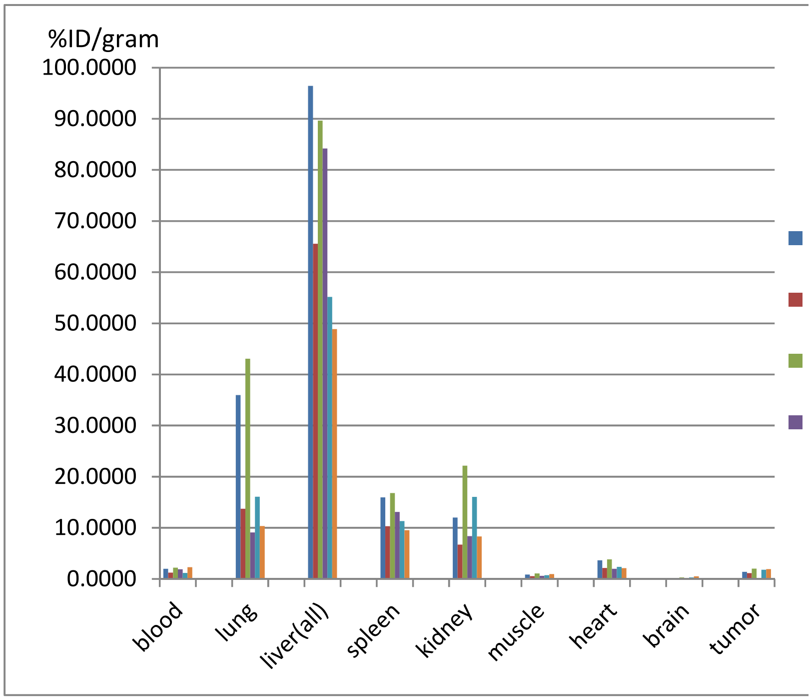

Figure 3.6 Biodistribution (% ID/gram) of Pal-PNA50-TAT and Pal-PNA50S-TAT conjugates

Table 3.7 Biodistribution of Pal-PNA50-TAT and Pal-PNA50S-TAT conjugates in %ID/gram

%ID/gram	**1 h Pal-PNA50-TAT**	**1 h Pal-PNA50S-TAT**	**4 h Pal-PNA50-TAT**
blood	2.0+/-0.4	1.2+/-0.3	2.21+/-0.27
lung	36.0+/-8.7	13.7+/-1.0	43.1+/-11.9
liver(all)	96+/-16	66.6+/-7	89.7+/-11.7
spleen	16.0+/-4.2	10.3+/-0.5	16.8+/-4.7
kidney	12.00+/-0.62	6.7+/-0.7	22.1+/-5.2
muscle	0.84+/-0.13	0.56+/-0.08	1.09+/-0.27
heart	3.7+/-0.90	2.15+/-0.33	3.81+/-0.55

brain	0.185+/-0.050	0.12+/-0.02	0.291+/-0.056
tumor	1.39+/-0.28	1.14+/-0.28	2.03+/-0.33

%ID/gram	**24h Pal-PNA50-TAT**	**24h Pal-PNA50S-TAT**	**4 h Pal-PNA50S-TAT**
blood	1.16+/-0.03	2.29+/-0.36	1.91+/-0.14
lung	16.1+/-3.0	10.3+/-1.3	9.1+/-1.4
liver(all)	55+/-11	49+/-18	84+/-5
spleen	11.3+/-1.9	9.5+/-4.0	13.1+/-0.9
kidney	16.0+/-1.0	8.3+/-2.8	8.4+/-1.2
muscle	0.71+/-0.07	0.97+/-0.15	0.62+/-0.07
heart	2.35+/-0.59	2.10+/-0.31	2.00+/-0.34
brain	0.27+/-0.04	0.51+/-0.03	0.200+/-0.014
tumor	1.78+/-0.43	1.9+/-0.3	1.43+/-0.13

The Pal-PNA50-TAT and Pal-PNA50S-TAT conjugates were injected into female nu/nu mice to test their biodistribution in vivo. Considering the biodistribution data of % ID/gram in the organs and tumors collected, the sense sequence of Pal-PNA50S-TAT conjugate showed apparently higher % ID/gram values than those of the antisense sequence of Pal-PNA50-TAT conjugate.

And when the biodistribution values of % ID/gram were considered, the highest % ID/gram value was found in liver, followed by those moderate % ID/gram values in lung, spleen and kidney, and even lower % ID/gram values in other four organs, while in tumor only 1-2 % ID/gram was obtained. However, as far as the biodistribution data in tumor were concerned, more experiments need to be conducted before any solid conclusions can be drawn since the % ID/gram values were too low to be used.

Compared with the previous biodistribution results of Cu64-DOTA-Y-PNA50-K_4 conjugates by Xiankai Sun [13] and coworkers, this bromine-radiolabeling Pal-PNA50-TAT conjugates (Pal-PNA50-(Br-76)TAT) showed that lipidation results in better and longer blood retention of up to 1.8 % ID/gram at 24 hours. There was also much less loss through the kidneys.

The biodistribution data clearly illustrated that the tumor-specificity of Pal-PNA50-TAT conjugate still needs to be improved if one hopes to be able to better image the tumor. The lack of sequence-specificity of tumor uptake was probably due to the self-blocking effect in vivo which induced lower tumor-specific targeting of Pal-PNA50-TAT, which was also shown similarly in Xiankai Sun's result. [13] Because applied as a radiolabelled agent being delivered to the targeting tumor, not all the Pal-PNA50-TAT molecules bear the radioactive Br-76 at that moment, then those radio-inactive agents tend to also target the tumor as self-blocking agents without radio-imaging activity. To improve the intracellular uptake of the PNA conjugates into tumors, may require screening a variety of lipid and cell penetrating peptide combinations, including phospholipids [14] and perhaps perfluorinated lipids [15], in an effort to reduce the size of the micelles to allow higher intracellular uptake through endocytosis.

References

1 For reviews, see: Handbook of Radiopharmaceuticals (2003) (Welch, M. J., and Redvanly, C. S., Eds.) John Wiley & Sons Ltd., New York.

2 Rowland, D. J., McCarthy, T. J., and Welch, M. J. (2003) (Welch, M. J., and Redvanly, C. S., Eds.) Handbook of Radiopharmaceuticals pp441-65, Chapter 14, John Wiley & Sons Ltd., New York.

3 Radiopharmaceuticals for Positron Emission Tomography (1993) (Sto¨cklin, G., and Pike, V. W., Eds.) p 3, Springer, New York.

4 Tolmachev, V., Lo¨vqvist, A., Einarsson, L., Schultz, J., and Lundqvist, H. (1998) *Appl. Radiat. Isot.* 49, 1537–1540.

5 Dong Zhou, Terry L. Sharp, Nicole M. Fettig, Hsiaoju Lee, Jason S. Lewis, John A. Katzenellenbogen, Michael J. Welch, Nuclear Medicine and Biology, 35, 2008, 655 – 663

6 Dong Zhou, Haibing Zhou, Carl C. Jenks, Jason S. Lewis, John A. Katzenellenbogen, and Michael J. Welch, Bioconjugate Chem. 2009, 20, 808–816

7 Woolf, T. M., Melton, D. A., and Jennings, C. G., 1992, Proc. Natl.Acad. Sci. U.S.A., 89, 7305-7309.

8 Thomson, S. A., Josey, J. A., Cadilla, R., Gaul, M. D., Hassman, C. F., et al, 1995, *Tetrahedron*, 51, 6179–94.

9 Oquare, B. Y., Taylor, J. S., Bioconjugate Chem., 2008, 19, 2196–2204.

10 Goddard, E. D., Turro, N. J., Kuo, P. L., 1985, *Langmuir*, 1, 352-5.

11 Zetasizer Nano application note MRK809-01.

12 http://en.wikipedia.org/wiki/Partition_coefficient

13 Xiankai Sun, Huafeng Fang, Xiaoxu Li, Raffaella Rossin, Michael J. Welch, John-Stephen

---

Taylor, Bioconjugate Chem., 2005, 16, 294-305

14 Gang Shen, et al, Bioconjugate Chem., 2009, 20, 9, 1729-1736

15 Nicholas C. Yoder, et al, J Am Chem Soc., 2007, 129, 29, 9037-9043

Chapter 4

Design and Synthesis of Lipid-PNA-Peptide Conjugates as mRNA accessible Reagents for inhibiting iNOS Activity in Acute Lung Injury

Abstract

Nitric oxide synthase (NOS) has been shown to be overexpressed in acute lung injury and a number of human tumors compared to normal tissues and therefore potentially represents a potential target in future anticancer therapies. Due to lack of exact gene transcription mechanism of iNOS in tumor cells, effort was put into development of method (mRNA antisense-accessible sites library [MASL]) to generate rapidly a library of antisense-accessible sites on native mRNAs. Then a library of antisense lipid-PNA-TAT conjugates was obtained through solid-phase synthesis, in order for studying the effectiveness of inhibiting the activity of iNOS induction via Griess assay in vitro.

4.1 Nitric Oxide Synthase (NOS) and mechanisms of iNOS induction in human cells

Nitric oxide synthase (NOS) is a dimeric enzyme that consists of two identical monomers: a reductase domain with sharing a high degree of sequence homology with P450 reductase, [1] and a heme containing oxygenase domain responsible for the production of nitric oxide. [2, 3] The reductive domain supplies reducing equivalents to the oxygenase domain, where nitric oxide is produced by a two-step oxidation of L-arginine to L-citrulline in the presence of oxygen.[3]

Three distinct isoforms of the enzyme nitric oxide synthase (NOS) have been found encoded by three different genes: endothelial, neuronal and inducible NOS genes. [4] The three isoforms differ in both structure and function [5] but share about 50% sequence homology [6] with distinct catalytic activity for each isoform. The endothelial and neuronal types (eNOS and nNOS) are constitutive and calcium/calmodulin dependent, and are regulated primarily by calcium influx and generate low levels of nitric oxide for short periods of time. The inducible NOS type (iNOS) is not dependent upon calcium/calmodulin for enzymatic action, and is induced by cytokines in almost every cell type. Inducible NOS can locally generate high concentrations of NO for prolonged periods of time.

In human cells iNOS is induced in response to cell injury and maximal induction of the iNOS gene occurs in the presence of two signals: IFNc and other stimulus such as an endotoxin. The stimulus binds to a κB element in the iNOS promoter [7] to activate the transcription factor NF-κB (nuclear factor-κB), and IFNc binds to elements in the NOS promoter to activate the transcription factor IRF-1 (interferon regulatory factor-1). [8, 9] Then synergism between NF-κB and IRF-1 is believed to be achieved through the interaction between these two transcription factors while binding to the iNOS promoter, which leads to modifications in the physical structure of the iNOS 5' flanking region. [7] This is a general description of iNOS pathway in most human cells where NO-mediated cytotoxicity is essential in fighting infection, even if the exact mechanisms in specific cell types need further examinations.

As far as iNOS induced lung infection and inflammation is concerned, although NO· is produced by several isoforms enzyme of NO synthase, the increased production of NO· is primarily due to induction of type 2 NOS enzyme (iNOS2) in various cell types. [10] According to experiments in normal wild type cells and in type 2 nitric oxide synthase-deficient (iNOS2-/-) mice, almost all the biomarkers concerning lung injury and NO production were less pronounced in iNOS2-deficent (iNOS2-/-) mice than in wild-type mice.

The exact mechanism by which iNOS2 is induced in acute lung inflammation and injury is incompletely understood. It was suggested that iNOS2 participates in the acute inflammatory response to (LPS) lipopolysaccharide by multiple mechanisms: involvement in proinflammatory cytokine signaling and alteration of the expression of various genes that affect inflammatory-immune responses to LPS. [11]

The mechanism of iNOS2 in airway inflammation and injury has been proposed to be initiated by the formation of reactive nitrogen species (RNS) that induce oxidative injury to host cells and promote inflammation. RNS appeared to specifically regulate cytokine signaling in various mononuclear cells, appeared to be involved in allergic airway inflammation by selectively downregulating IFNɣ-activity, [12] and appeared to participate in proinflammatory cytokine signaling by activating the transcription factor nuclear factor (NF-κB) in hemorrhagic shock. [13] These observations would implicate NO· in early stages of the inflammatory response was preceding the formation of RNS, and was responsible for the activation and regulation of NF-κB (the transcription factor), a key event in the initiation of inflammation. [14] However, studies of this key event uncovered both stimulatory and inhibitory effects of NO·, which involved several signaling proteins. Thus it was most possible that the different types of effects of NO· on NF-κB signaling depend on cell type, the relative NO· concentration, and/or the stages of the inflammatory response. [15-19]

4.2 Design and Synthesis of Lipid-PNA-CPP conjugates as iNOS-mRNA as possible diagnostic and therapeutic reagents

As discussed above, the exact mechanism of this iNOS2 induction responsible for NO production in acute lung inflammation and injury still remains unclear on molecular level. However, iNOS2 deficiency corresponds to an attenuated inflammatory response and reduced injury in various models of airway inflammation, [20-26] as demonstrated in animal experiments using wild-type and iNOS knockout mice. Thus it would appear that agents capable of imaging iNOS induction and suppressing iNOS induction could be useful as diagnostic and therapeutic agents for lung injury.

One possible approach to developing diagnostic and therapeutic agents targeting iNOS would be to use antisense PNA conjugates that have high affinity for iNOS mRNA. Under this condition possibility to design iNOS inhibition reagents still leaves open, should the knowledge of antisense-accessible sites on native iNOS mRNAs be available. And as discussed in the introduction, a method called MASL (mRNA antisense-accessible sites library) was developed recently by Taylor group [27] based on the original reported method by Allawi and coworkers.[28] A number of antisense-accessible sites were identified by MASL on native iNOS mRNA extracted from cells, that were shown to have high binding affinity and able to inhibit iNOS expression.

Herein we describe the design, synthesis and characterization of a library of antisense Lipid-PNA(480/240)-TAT conjugates (Figure 4.2). These conjugates were evaluated for their potential as both antisense therapeutic agents and diagnostic imaging agents for iNOS.

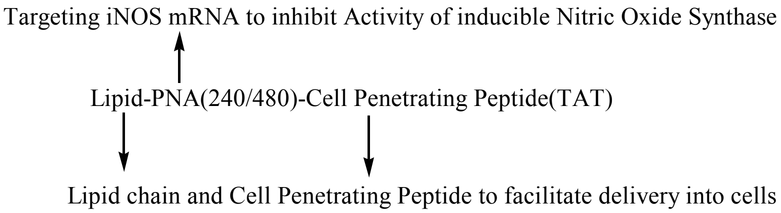

Figure 4.1 Design of Lipid-PNA(240/480)-TAT conjugates

Lipid-PNA(480/240)-TAT

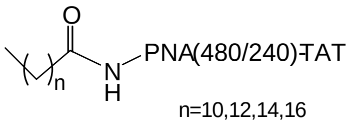

PNA(480/240)-TAT PNA(480/240)-TAT

Figure 4.2 Structures of Lipid-PNA(480/240)-TAT and PNA(480/240)-TAT conjugates

4.3 Experimental Procedures

Materials and Methods

All reactions were performed under an argon or nitrogen atmosphere unless otherwise specified. All commercially available materials were used without further purification unless otherwise noted.

Anhydrous solvents for reactions, such as DMF, DCM, and acetonitrile were either used as obtained from Sigma-Aldrich or distilled from an appropriate drying agent. All chemicals and reagents used were of the highest purity available. Acetonitrile, trifluoroacetic acid, m-cresol and reagents for automated PNA synthesis were purchased from Aldrich. The 11-mer Fmoc-protected TAT on resin for solid-phase synthesis (Fmoc-YGRRQRKKRRR-PAL-PEG-PS) was purchased from GL Biochem. Fmoc-PAL-PEG-PS resin for automated PNA synthesis was purchased from Applied Biosystems. PNA(50/5/7)-TAT conjugates were assembled on ExpediteTM 8900 Nucleic Acid Synthesis System purchased by Applied Biosystems. And all PNA conjugates were purified by reversed-phase high-performance liquid chromatography (HPLC) on a Beckman System Gold instrument equipped with a UV-vis array detector, using a Microsorb-MV300-5 C-18 column (250 × 4.6mm column, 300 Å pore size, Varian Inc.). HPLC fractions were collected and concentrated under vacuum in a SpeedVac evaporator (Savant). UV-vis absorption of all PNA conjugates was determined with a Bausch and Lomb Spectronic1001 spectrophotometer or a Varian Cary 100 bio UV-vis spectrophotometer. The concentration of PNA conjugates was determined by the Beer-Lambert law using standard extinction coefficients for the PNA bases at 260nm. All PNA conjugates were characterized by MALDI-TOF on a PerSpective Voyager RP MALDI-TOF mass spectrometer in linear mode using insulin as the internal reference. A-cyano-4-hydroxycinnamic acid (CHCA) was used as the matrix. Fluorescence spectra were measured on a Varian Cary Eclipse fluorescence spectrophotometer to determine CMC (critical micelle concentration). DLS data were obtained in dd water on Zetasizer Nano ZS using disposable Low Volume Cells purchased from Malvern Instruments Inc. Griess and Cell Viability assay kits were both purchased from Promega Inc.

Synthesis of PNA(480/240)-TAT conjugates

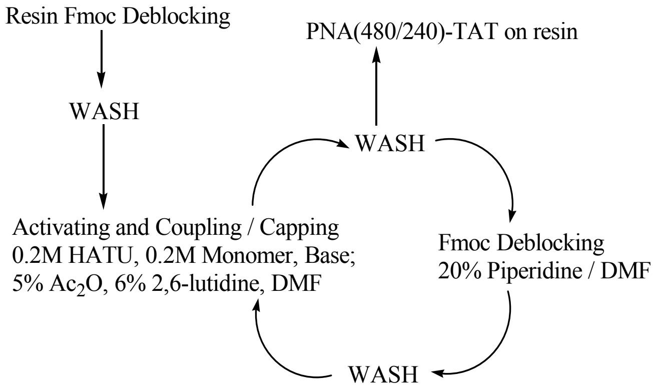

Figure 4.3 Solid-phase synthetic procedure [29] for the synthesis of PNA(480/240)-TAT conjugates

PNA(480/240)-TAT conjugates were all prepared by automated standard Fmoc chemistry procedures on a 2 µmol scale, in Fmoc-deprotected mode. The resin with PNA(480/240)-TAT conjugates was washed with anhydrous DMF (3 × 1 mL) and DCM (3 × 1 mL) respectively, dried with nitrogen for cleavage and purification.

Synthesis of the Lipid-PNA(480/240)-TAT conjugates

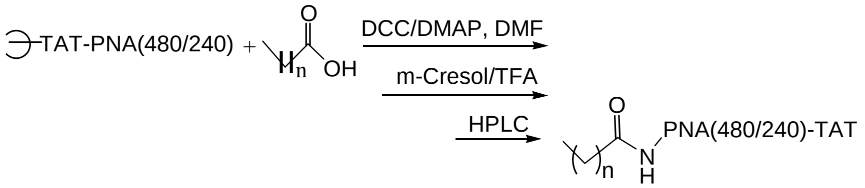

Lipid-PNA(480/240)-TAT

n=10,12,14,16

Figure 4.4 Solid-phase Synthesis of Lipid-PNA(480/240)-TAT conjugates

After the PNA(480/240)-TAT conjugates[30] were prepared on the resin, the resin was washed and dried by automated steps and then added into an anhydrous DMF solution (100 µL) containing the fatty acid (20 µmol), DCC (20 µmol) and DMAP (20 µmol) and shaken overnight at room temperature. The resin with Lipid-PNA(480/240)-TAT conjugates was washed with anhydrous DMF (3 × 1 mL) and DCM (3 × 1 mL) respectively, dried with nitrogen for cleavage and purification.

Cleavage, Purification and Characterization of PNA(480/240) conjugates

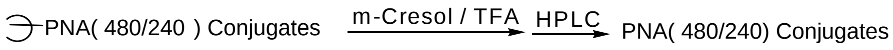

Figure 4.5 Cleavage and purification of PNA(480/240) conjugates

After the automated synthesis and post-synthetic modification in vials, the resin was incubated in 400 μL TFA/m-cresol (4:1) [29] for 3 h. The released PNA(480/240)-TAT conjugate was then precipitated by the addition of 10 volumes of ice-cold diethyl ether. The crude product was collected by centrifugation and purified by reverse phase HPLC with a 65 -min 1 mL/min linear gradient of 5 to 70% buffer B (0.1% TFA in CH_3CN) in buffer A (0.1%TFA in dd water). The fractions containing the desired PNA(480/240) conjugates were evaporated, dissolved in dd water, and characterized by MALDI-TOF with a matrix prepared from 1% CHCA in 1:1 ratio of acetonitrile vs 0.1% TFA in dd water.

Determination of Critical Micelle Concentration (CMC) [31]

Stock solutions of Lipid-PNA(480/240)-TAT conjugates were diluted in water to different concentrations. Two buffers, with or without NaCl in 2% methanol/water as (10 μM pyrene, 150 mM NaCl, 5 mM Tris, pH=7) and (10 μM pyrene, 5mM Tris, pH=7). Two series of CMC samples were made with or without NaCl for each PNA conjugate, by mixing 25 μL buffer and 25 μL of stock solutions of different concentrations. Fluorescence emission spectra were obtained by exciting the pyrene at 300 nm. The ratio of intensity of the first (373 nm) and third (383nm) emission peaks was plotted against PNA concentration to determine the CMC from the breakpoint in a bilinear fit to the data.

Dynamic Light Scattering (DLS) Analysis [32]

Stock solutions of Lipid-PNA(480/240)-TAT conjugates were diluted in water to different concentrations. Dynamic light scattering data was used to calculate the average micelle size at different concentrations on a Malvern Nano ZS. The average micelle size was plotted against PNA concentration to determine the minimum average micelle size range.

Determination of Partition Ratios [33]

Equal volumes of octanol and water were mixed completely and allowed to separate into two clear layers. Lipid-PNA(480/240)-TAT conjugates were dissolved in equal volume of the two clear layers. The solution was vortexed to allow complete mixing before measuring the concentration of the solute in each solvent by UV-vis spectroscopy at 260nm. The partition ratio was calculated as the ratio of the absorption in water vs the absorption in 1-octanol.

Griess Assay of iNOS inhibition by Lipid-PNA480-TAT, PNA480-TAT and PNA480-Lys_4 conjugates (Carried out in our laboratory by Yuefei Shen, and PNA480-Lys_4 was Yuefei's sample)

Mouse peritoneal macrophage RAW264.7 (ATCC TIB-71) cells were maintained in DMEM containing 10% FBS, streptomycin (100 mg/mL), and penicillin (100 units/mL) at 37 ° C in a humidified incubator with 5% CO_2. RAW264.7 cells were seeded in 24-well plates with 1×10^5 per well in 600 mL DMEM with 10% FBS and incubated for 24 h. The cells were then washed three times with PBS, after which 400 mL DMEM (no FBS) and 100 mL opti-MEM (Invitrogen) were added with various concentrations of Lipid-PNA480-TAT with CQ (Chloroquine) and Lipid-PNA480-TAT without CQ; PNA480-TAT with CQ or without CQ, PNA480-Lys$_4$ with CQ or without CQ; with or without different controls like siRNA481, Lipo (Lipofectamine 2000), CQ (Chloroquine), Lipo & CQ, and LPS (Lipopolysaccharides). 6 h later, LPS (Lipopolysaccharides from *Escherichia coli* 055:B5, Sigma, 1 mg/mL), IFN-g (mouse, recombinant, *E. coli*, Calbiochem, 100 ng/mL; LPS), and 60 mL FBS were added with DMEM to make a total of 600 mL and further incubated. After an additional 18 h, an aliquot of the supernatant (50 mL) was removed for assay of NO by the Griess assay (Promega) and quantified by the absorbance at 540 nm.

Cytotoxicity Assay of Lipid-PNA480-TAT, PNA480-TAT and PNA480-Lys$_4$ conjugates

The cytotoxicity of the PNAs was evaluated by the CellTiter-Glo Luminescent Cell Viability Assay (Promega Co.). Mouse peritoneal macrophage RAW264.7 (ATCC TIB-71) cells were seeded in a 96-well plate at a density of 1×10^4 cells/well and cultured for 24 h in 100 μL DMEM containing 10% FBS. Thereafter, the medium was replaced with 100 μL fresh medium containing various concentrations of Lipid-PNA480-TAT with CQ (Chloroquine) and Lipid-PNA480-TAT without CQ; PNA480-TAT with CQ or without CQ, PNA480-Lys$_4$ with CQ or without CQ; with or without different controls like siRNA481, Lipo (Lipofectamine 2000), CQ (Chloroquine), Lipo & CQ, and LPS (Lipopolysaccharides). After 24 h incubation at 37 °C, 100 μL of CellTiter-Glo reagent were added. The contents were mixed, and the plate was allowed to incubate at room temperature for 10 minutes to stabilize the luminescence signal. Luminescence intensities were recorded on a Luminoskan Ascent luminometer (Thermo Scientific) with an integration time of 1s per well. The relative cell viability was calculated as the ratio of the luminescence in the presence and absence of PNA conjugates.

4.4 Result and Discussion

Eight antisense Lipid-PNA(480/240)-TAT conjugates and three controls were synthesized and characterized by MALDI, and their CMC, DLS sizes, and partition ratios. As shown below, MALDI (matrix-assisted laser desorption ionization) was used to identify the HPLC fraction containing the PNA conjugates (Table 4.2).

Table 4.1 Sequences of PNA-TAT used in PNA480-TAT, PNA480(MM)-TAT, PNA240-TAT

Sample	Sequence
PNA480-TAT	TGAAATCCGATGTGGCCT-YGRKKRRQRRR
PNA480(MM)-TAT	TAGAATCCAGTGGTGCCT-YGRKKRRQRRR
PNA240-TAT	TGTCCTTTTCCTCTTTCA-YGRKKRRQRRR

Table 4.2 MALDI for Lipid-PNA(480/240)-TAT and PNA(480/240)-TAT conjugates

Sample	Cal MW	MALDI	Figure No (Appendix)
Ste-PNA480-TAT	6717	6727.55	Figure A4.15
Pal-PNA480-TAT	6689	6703.55	Figure A4.12

Ted-PNA480-TAT	6661	6674.86	Figure A4.9
Lau-PNA480-TAT	6633	6642.08	Figure A4.6
PNA480-TAT	6451	6446.6	Figure A4.3
PNA480(MM)-TAT	6451	6449.1	Figure A4.18
Ste-PNA240-TAT	6560	6567.63	Figure A4.33
Pal-PNA240-TAT	6532	6537.73	Figure A4.30
Ted-PNA240-TAT	6504	6515.89	Figure A4.27
Lau-PNA240-TAT	6476	6486	Figure A4.24
PNA240-TAT	6294	6292.8	Figure A4.21

The critical micelle concentrations (CMC) of eleven Lipid-PNA-TAT conjugates were determined by using a pyrene-based fluorescence assay in two aqueous buffers of with NaCl or without NaCl. And it was demonstrated that CMC values of almost all Lipid-PNA-TAT conjugates in the aqueous buffer with NaCl were lower than the values of the corresponding Lipid-PNA-TAT conjugates in the aqueous buffer without NaCl, except Ste-PNA480-TAT (Table 4.3). This trend was also found by Gang Shen [34] for lipid-PNA-R_9 conjugates, which were used in the Luciferase splice-correction assays. The similarity is probably because the positively charged TAT group contains several arginine and lysine residues that confer a similar positive charge as does the Arg_9 peptide.

Considering the different lengths of the lipid chains used in those lipid-PNA-TAT conjugates, no apparent relation or trend was found between the length of the lipid chains and the CMC values, probably because the differences between the lengths of lipid chains were too small to be show any detectable differences from CMC tests, or because the sensitivity of CMC tests was not enough by pyrene-based fluorescence assays.

Table 4.3 CMC for Lipid-PNA(480/240)-TAT and PNA(480/240)-TAT conjugates

Sample	CMC (w/NaCl μM)	Figure No (Appendix)	CMC (w/o NaCl μM)	Figure No (Appendix)
Ste-PNA480-TAT	12.5	Figure A4.49	9.4	Figure A4.48
Pal-PNA480-TAT	11.3	Figure A4.47	18.8	Figure A4.46
Ted-PNA480-TAT	9.4	Figure A4.45	18.8	Figure A4.44
Lau-PNA480-TAT	14	Figure A4.43	14.1	Figure A4.42
Ste-PNA240-TAT	13	Figure A4.57	15.6	Figure A4.56
Pal-PNA240-TAT	18.8	Figure A4.55	25	Figure A4.54
Ted-PNA240-TAT	9.4	Figure A4.53	15.6	Figure A4.52
Lau-PNA240-TAT	19.5	Figure A4.51	23.4	Figure A4.50

Because these Lipid-PNA-TAT conjugates contained hydrophobic tails and hydrophilic PNA-TAT parts, it was likely that those amphiphilic conjugates would form micelles in aqueous phase, which might explain their better uptake into cells through endocytosis or membrane fusion. [30] DLS suggested that the possible vesicle sizes formed from Lipid-PNA-TAT conjugates in the aqueous phase was in the range of 200-400 nm (Table 4.4). This size range falls into the category of large vesicles with spherical shape, which may be optimal for macropinocytosis, instead of micelle-induced intracellular delivery. The relatively large vesicles size formed from those Lipid-PNA-TAT conjugates in the aqueous phase was probably due to the lack of the strong enough electronic repulsion at the ends, while PNA and lipid chain was neutral.

Table 4.4 DLS for Lipid-PNA(480/240)-TAT and PNA(480/240)-TAT conjugates

Sample	DLS (nm)	Figure No (Appendix)
Ste-PNA480-TAT	283.5	Figure A4.37
Pal-PNA480-TAT	415.5	Figure A4.36
Ted-PNA480-TAT	234	Figure A4.35
Lau-PNA480-TAT	232	Figure A4.34
Ste-PNA240-TAT	213.4	Figure A4.41
Pal-PNA240-TAT	320.3	Figure A4.40
Ted-PNA240-TAT	245.1	Figure A4.39
Lau-PNA240-TAT	341.3	Figure A4.38

The partition ratios showed that most of the Lipid-PNA-TAT conjugates were dissolved in the aqueous phase instead of the organic octanol phase, which is consistent with micelle formation that only exposed the hydrophilic TAT peptide to the water and sequestered the highly hydrophobic lipid portion (Table 4.5).

Table 4.5 Partition Ratio for Lipid-PNA(480/240)-TAT and PNA(480/240)-TAT conjugates

Sample	Partition Ratio (dd water/octanol)

Ste-PNA480-TAT	170.8
Pal-PNA480-TAT	139.14
Ted-PNA480-TAT	147.6
Lau-PNA480-TAT	143.75
Ste-PNA240-TAT	210.76
Pal-PNA240-TAT	369.1
Ted-PNA240-TAT	373.8
Lau-PNA240-TAT	334.5

The lipidated PNA-TAT conjugates were then tested for their ability to inhibit iNOS induction by monitoring the production of nitric oxide. It was found that iNOS inhibition increased with the increasing length of lipid chain, however, the cytotoxicity also increased as well (Figure 4.6 and Figure 4.7). (Lipid-PNA, 2 μM)

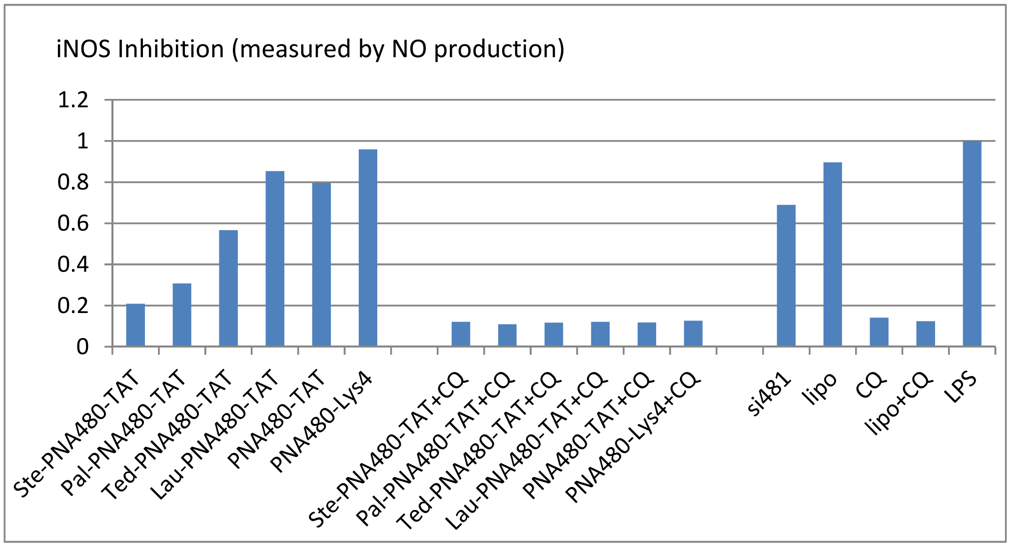

Figure 4.6 Griess Assay of iNOS Inhibition by Lipid-PNA480-TAT, PNA480-TAT and PNA480-Lys$_4$ conjugates

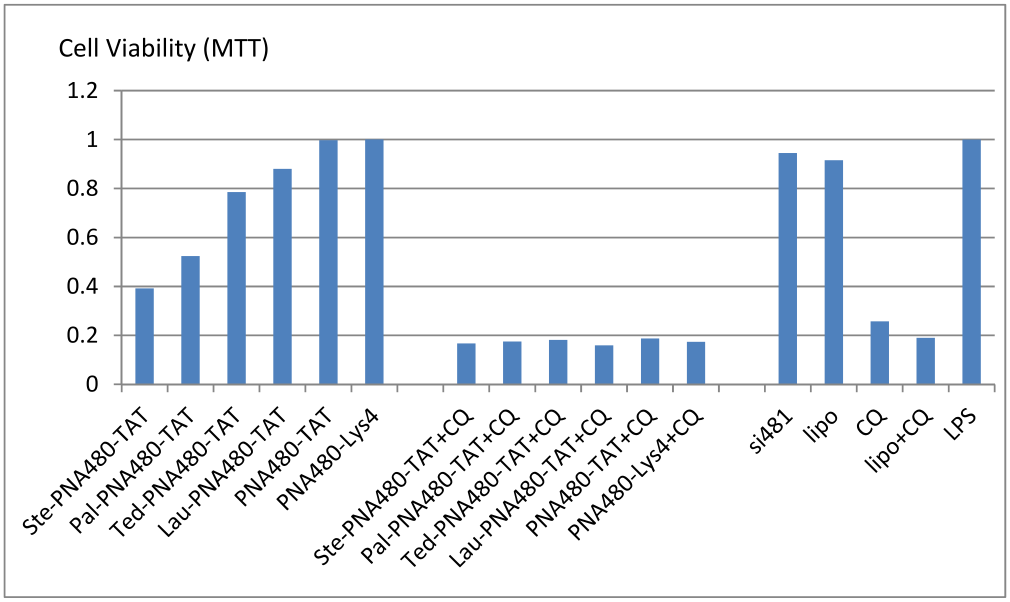

Figure 4.7 Cell Viability Assay of Lipid-PNA480-TAT, PNA480-TAT and PNA480-Lys$_4$ conjugates

The Griess and cytotoxicity assays were then carried out at different concentrations of Lipid-PNA480-TAT, PNA480-TAT and PNA480-Lys$_4$ conjugates to find out the optimal concentration for iNOS inhibition. At 0.5 μM PNA almost no iNOS relative inhibition was observed but then it increased along with increasing cytotoxicity. When the NO production was divided by cell viability to measure the NO relative production, the Ste-PNA480-TAT conjugate and Pal-PNA480-TAT conjugate both showed the low NO relative production at 2 μM (Figure 4.8). To be more specific, at 2 μM the NO relative Production value of Ste-PNA480-TAT conjugate was the lowest as 0.35, and at 2 μM the NO relative Production value of Pal-PNA480-TAT conjugate was the lowest as 0.3 (Figure 4.9). Considering the concentration used at 1 μM, Ste-PNA480-TAT conjugate showed the best relative iNOS inhibition among all the PNA conjugates, while at the concentration of 2

μM Pal-PNA480-TAT conjugate showed the best relative iNOS inhibition among all the PNA conjugates (Figure 4.9).

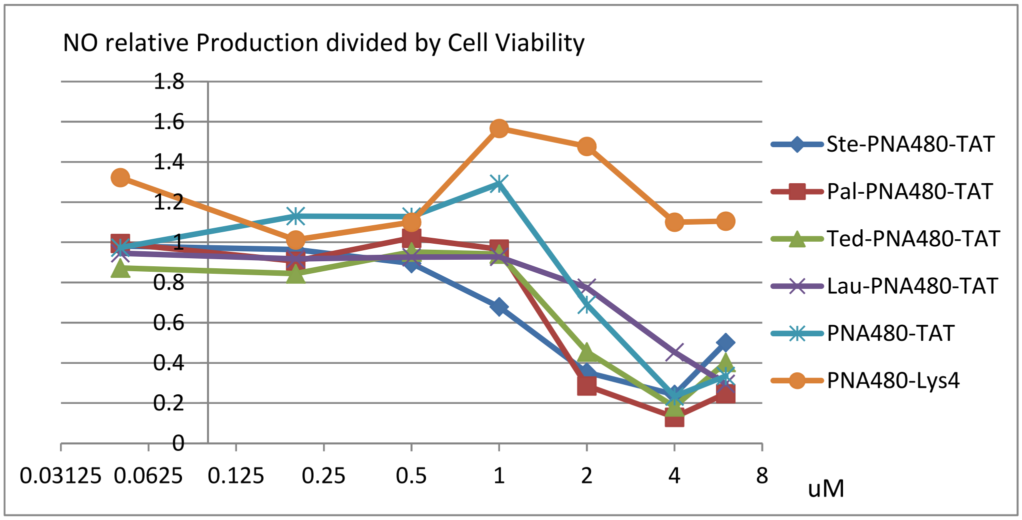

Figure 4.8 Griess Assay of NO relative Production divided by Cell Viability by Lipid-PNA480-TAT, PNA480-TAT and PNA480-Lys$_4$ conjugates

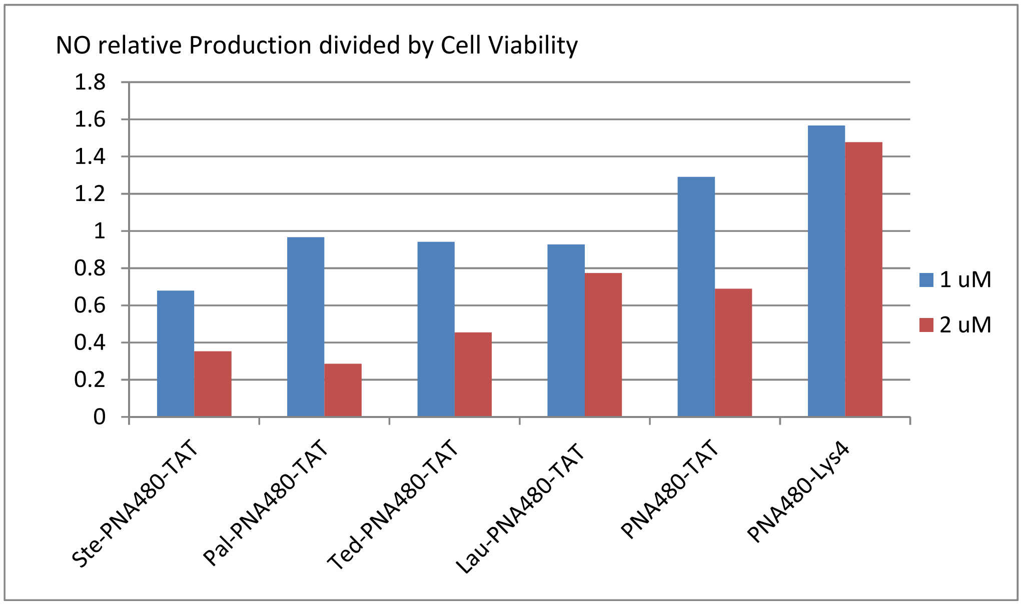

Figure 4.9 Griess Assay of NO relative production divided by cell viability by Lipid-PNA480-TAT, PNA480-TAT and PNA480-Lys$_4$ conjugates

Since 90% of cells died with 100 μM CQ to facilitate the intracellular delivery of Lipid-PNA480-TAT conjugate and the Lipofectamine 2000 was proven to be of much less cytotoxicity and little iNOS inhibition. Different concentrations of Lipofectamine 2000 were tested for their ability to improve iNOS inhibition of the PNA conjugates at 1 μM concentration. Although Ste-PNA480-TAT showed better iNOS inhibition at 20 μM of Lipofectamine 2000 than that at 10 μM as far as NO production was concerned, the very low cell viability value made the relative NO production divided by cell viability at 20 μM Lipofectamine 2000 not as good as that at 10 μM Lipofectamine 2000. And according to these results from Griess assay and the cell viability assay, the best iNOS inhibition was observed at10 μM Lipofectamine 2000 when 1 μM of Ste-PNA480-TAT and Pal-PNA480-TAT conjugates were used (Figure 4.10).

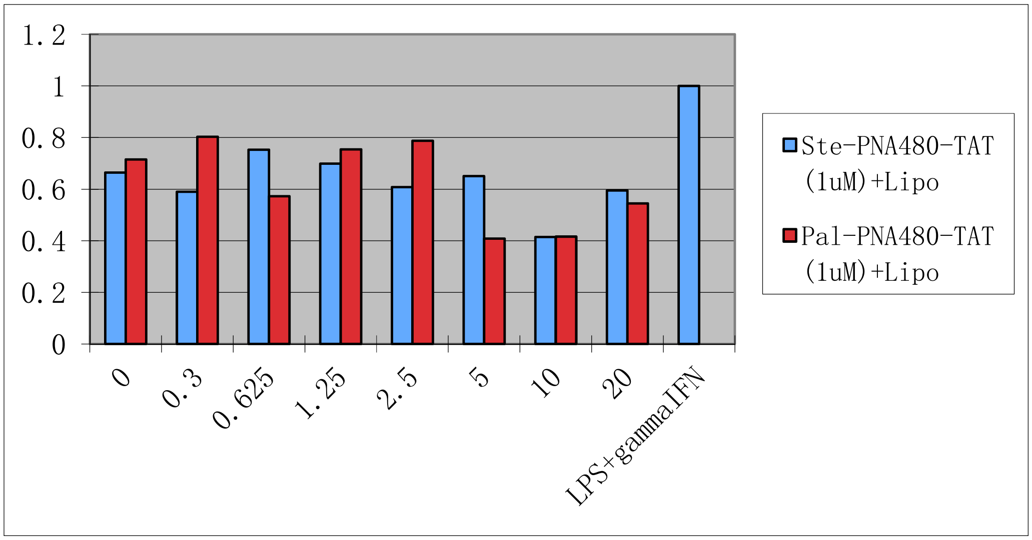

Figure 4.10 Griess Assay of NO relative Production divided by Cell Viability of Lipid-PNA480-TAT, PNA480-TAT and PNA480-Lys$_4$ conjugates with different concentrations of Lipofectamine

To obtain better iNOS inhibition, a deeper understanding of the complex mechanisms concerning inflammation in lung injury will be required along with improved antisense agents. One possible improvement may be to attach a phospholipid [34] or a perfluoroacid chain [35] to the PNA conjugates which may form micelles of smaller size that may be better taken up through endocytosis.

Reference

1 D.S. Bredt, P.M. Hwang, C.E. Glatt, C., Nature, 351, 1991, 714-718

2 B. Hemmens, B. Mayer, Methods Mol.Biol., 100, 1998, 1-32

3 O.W. Griffith, D.J. Stuehr, Annu. Rev. Physiol., 57, 1995, 707-736

4 C. Nathan, Q.W. Xie, J. Biol. Chem., 269, 1994, 13725-13728

5 D.J. Stuehr, Annu. Rev. Pharmacol. Toxicol., 37, 1997, 339-359

6 W.K. Alderton, C.E. Cooper, R.G. Knowles, Biochem. J., 357, 2001, 593-615

7 M. Saura, C. Zaragoza, C. Bao, A. McMillan, C.J. Lowenstein, J. Mol. Biol., 289, 1999, 459-471

8 E. Martin, C. Nathan, Q.W. Xie, J. Exp. Med., 180, 1994, 977-984

9 R. Kamijo, H. Harada, T. Matsuyama, M. Bosland, J. Gerecitano, D. Shapiro, J. Le, S.I. Koh, T. Kimura, S.J. Green, et al., Science, 263, 1994, 1612-1615

10 Van der Vliet A, Cross CE, Am J Med, 109, 398-421, 2000

11 Kerryn McCluskie, Maria G. Belvisi et al, JPET, 2004, 311(2), 625-633

12 Xiong Y, Karupiah G, Hogan SP, Foster PS, Ramsay AJ, J Immunol, 162: 445-452, 1999

13 Hierholzer C, Harbrecht B, Tweardy DJ et al, J Exp Med 187: 917-928, 1998

14 Barnes PJ, Karin M, N Engl J Med, 336, 1066-1071, 1997

15 Connelly L, Palacios-Callender M et al, J Immunol, 166, 3873-3881, 2001

16 Lander HM, Sehajpal P, Levine DM, Novogrodsky A, J Immunol, 150, 1509-1516, 1993

17 Raychaudhuri B, Dweik R, Connors MJ, Thomassen MJ et al, Am J Respir Cell Mol Biol, 21, 311-316, 1999

18 Walley KR, McDonald TE, Higashimoto Y, Hayashi S, Am J Respir Crit Care Med, 160, 698-704, 1999

19 Yan L, Wang S, Rafferty SP, Wesley RA, Danner RL, Blood , 90, 1160-1167, 1997

20 Akaike T and Maeda H. Nitric oxide and virus infection. Immunology, 101, 300-308, 2000

21 Fakhrzadeh L, Laskin JD, Laskin DL, Am J Respir Cell Mol Biol, 26, 413-419, 2002

22 Karupiah G, Chen JH, Mahalingam S, Nathan CF, MacMicking JD, J Exp Med, 188, 1541-1546, 1998

23 Kristof AS, Goldberg P, Laubach V, Hussain SN, Am J Respir Crit Care Med, 158, 1883-1889, 1998

24 Srivastava KD, Rom WN, Jagirdar J, Yie TA, Gordon T, Tchou-Wong KM, Am J Respir Crit Care Med, 165, 527-533, 2002

25 Ullrich R, Bloch KD, Ichinose F, Steudel W, Zapol WM, J Clin Invest, 104, 1421-1429, 1999

26 Xiong Y, Karupiah G, Hogan SP, Foster PS, Ramsay AJ, J Immunol, 1999, 162, 445-452

27 Huafeng Fang, Yuefei Shen, John S. Taylor, RNA, 2010, 16, 1429-1435

28 Allawi HT, Dong F, Ip HS, Neri BP, Lyamichev VI., 2001, RNA, 7, 314-327

29 Thomson, S. A., Josey, J. A., Cadilla, R., Gaul, M. D., Hassman, C. F., et al, 1995, Tetrahedron, 51, 6179-94

30 Oquare, B. Y., Taylor, J. S., Bioconjugate Chem., 2008, 19, 2196-2204

31 Goddard, E. D., Turro, N. J., Kuo, P. L., 1985, Langmuir, 1, 352-355

32 Zetasizer Nano application note MRK809-01

33 http://en.wikipedia.org/wiki/Partition_coefficient

34 Gang Shen, et al, Bioconjugate Chem., 2009, 20, 9, 1729-1736

35 Nicholas C. Yoder, et al, J Am Chem Soc., 2007, 129, 29, 9037-9043

Chapter 5 Conclusions and Future Directions

In this thesis, three series of Lipid-PNA-CPP (TAT/R_9) conjugates were designed, synthesized and characterized by MALDI, UV-vis, partition coefficients CMC and DLS. Selected PNAs were also evaluated for their ability to inhibit telomerase, iNOS production, and to image breast cancer. The goal was to see if an improved intracellular delivery of the neutral PNA conjugates could be obtained, via self-assembly of the amphiphilic PNA conjugates in aqueous environment to form vesicles. All the lipidated PNA-CPP conjugates showed and ability to form micelles in solution at about 10 µM concentration, and to greatly favor water over octanol. The vesicles formed, however, appeared to be much larger than expected, and could be considered rather large at 200-300 nM, which may explain their bioactivity and biodistribution properties.

In a very limited study of lipidated PNAs targeting human telomerase, only P(CN)-Telm-R_9 and Ted-Telm-R_9 conjugates showed detectable telomerase inhibition. This was unexpected given previous studies which showed that lipidation, and in particular phospholipidated, improved the ability of PNA-Arg_9 to correct a splicing error in HeLa cells. Clearly the studies would have to be repeated before any solid conclusions can be drawn about their effectiveness as telomerase inhibitors.

More detailed studies of iNOS inhibition by the lipidated PNA-CPP conjugates showed that the Ste-PNA480-TAT conjugate with the longest lipid chain showed the best iNOS inhibition at 1 µM, and Pal-PNA480-TAT conjugate with the second longest lipid chain showed the best inhibition at 2 μM. The extent of iNOS inhibition could be improved by addition of Lipofectamine 2000, which could be explained by assembly of the lipidated PNAs with the cationic liposomes formed by Lipofectamine.

The lipidated Pal-PNA50-(^{76}Br)TAT showed greatly improved biodistribution in mice compared to the ^{64}Cu64-DOTA-Y-PNA50-K$_4$, being retained in the blood to a much greater extent with a %ID/gram of 1.8 at 24 hours, and not being excreted very quickly. There was however significant liver uptake which might have been due to the large vesicle size of 200-300 nm. Also, no tumor specificity was observed, suggesting that either the tumor was oversaturated with the PNA imaging agent or that the PNA was not entering the tumor cells. It may be that lipidated PNAs that form smaller vesicles or micelles will show even greater blood retention and better tumor specificity.

While the current set of lipidated PNA-CPP conjugates is promising, far more work will be needed to further develop these conjugates as practical agents for imaging and therapy. Potential avenues for further development are fluorinated lipids, and methods of attachment of the lipid to the PNA that can be cleaved by endogenous enzymes or the lower pH found in endosomes to facilitate release of the PNA. Also fluorescent probes could be attached to facilitate tracking of the conjugates inside cells to ascertain their mechanism of entry by confocal microscopy.

Appendix_Chapter 2

HPLC, UV, MALDI

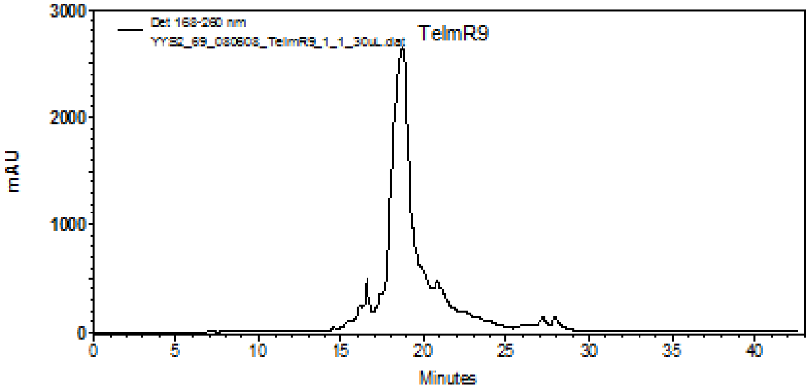

Figure A2.1 HPLC of Crude TelmR9 (major peak, collecting 18min-19.5min)

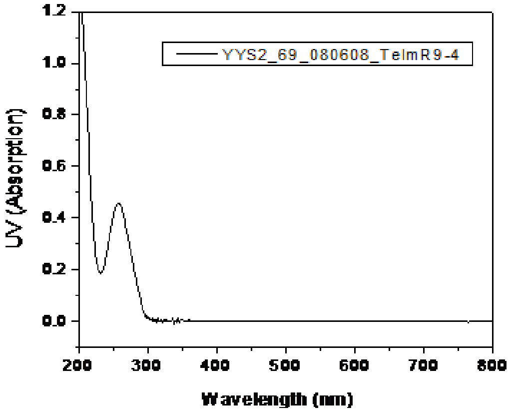

Figure A2.2 UV of TelmR9

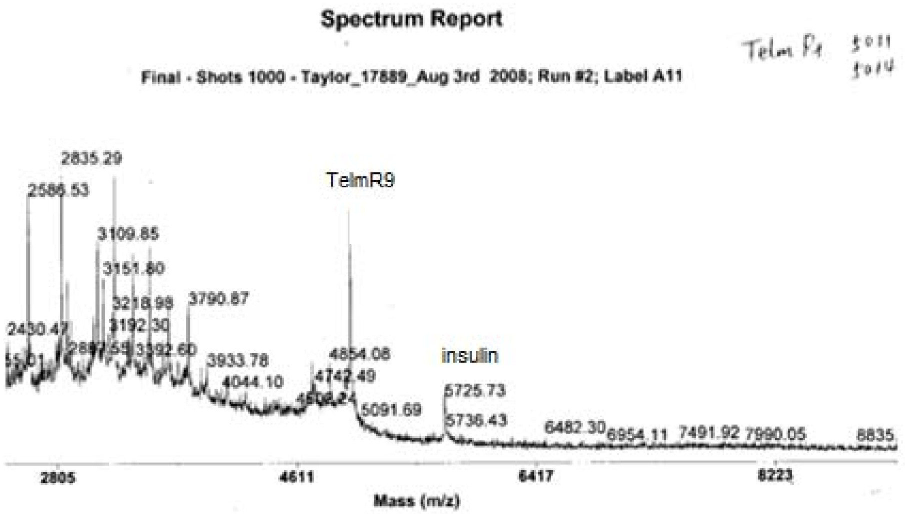

Figure A2.3 MALDI of TelmR9

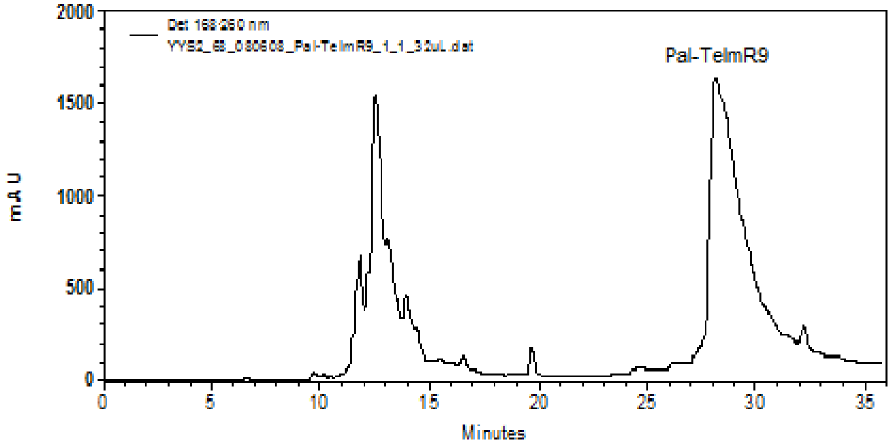

Figure A2.4 HPLC of Crude Pal-TelmR9 (second major peak, collecting 28min-30min)

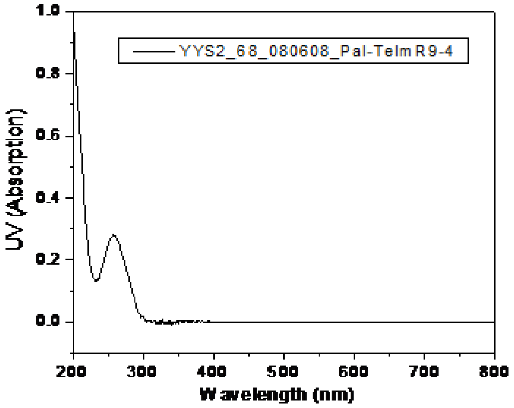

Figure A2.5 UV of Pal-TelmR9

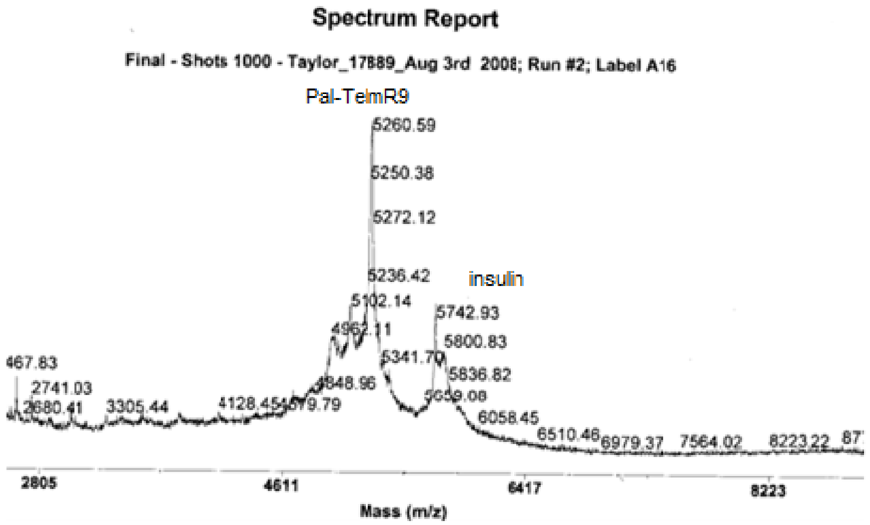

Figure A2.6 MALDI of Pal-TelmR9

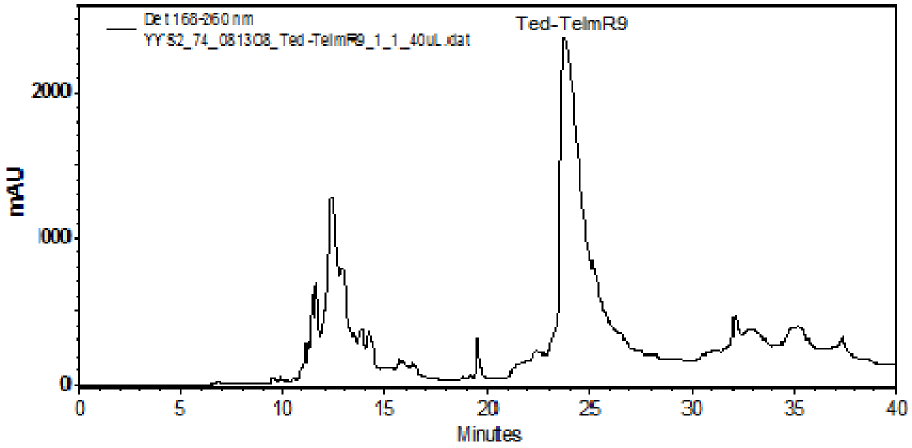

Figure A2.7 HPLC of Crude Ted-TelmR9

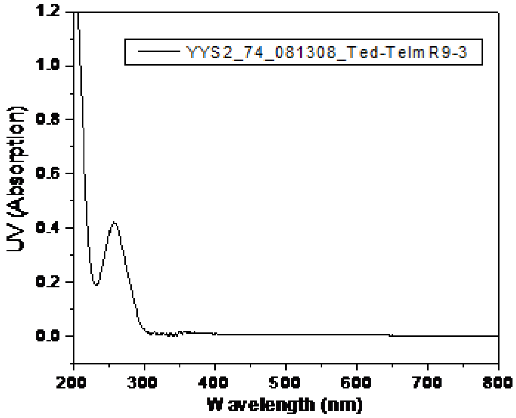

Figure A2.8 UV of Ted-TelmR9

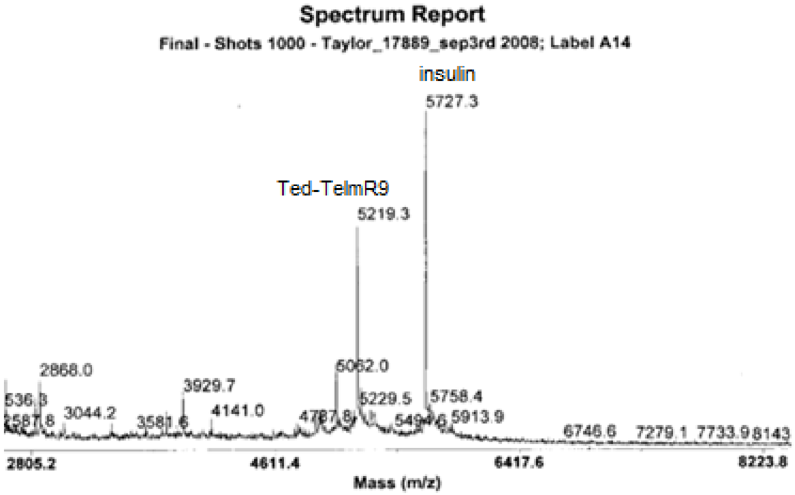

Figure A2.9 MALDI of Ted-TelmR9

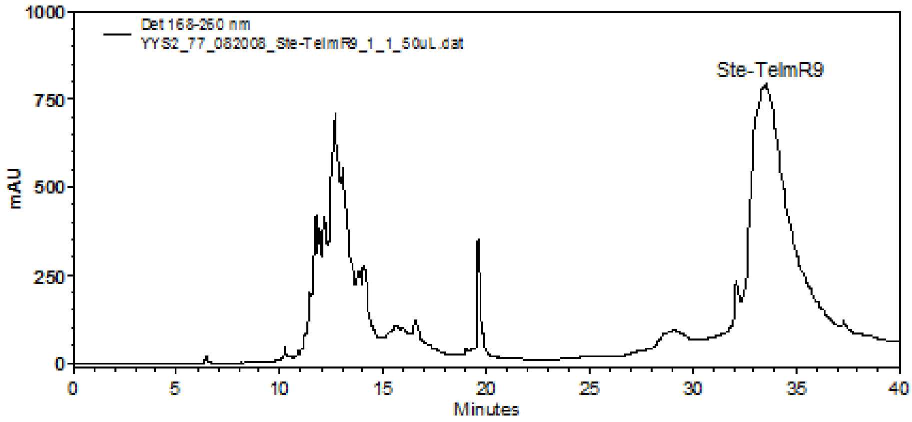

Figure A2.10 HPLC of Crude Ste-TelmR9

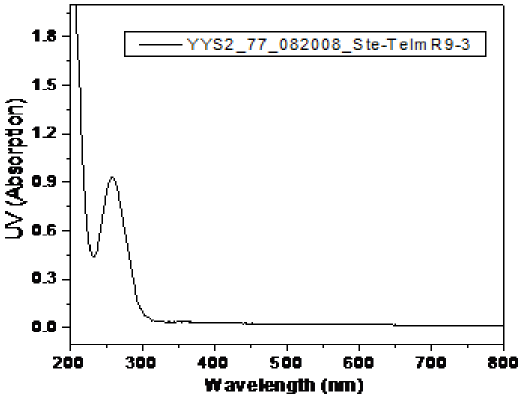

Figure A2.11 UV of Ste-TelmR9

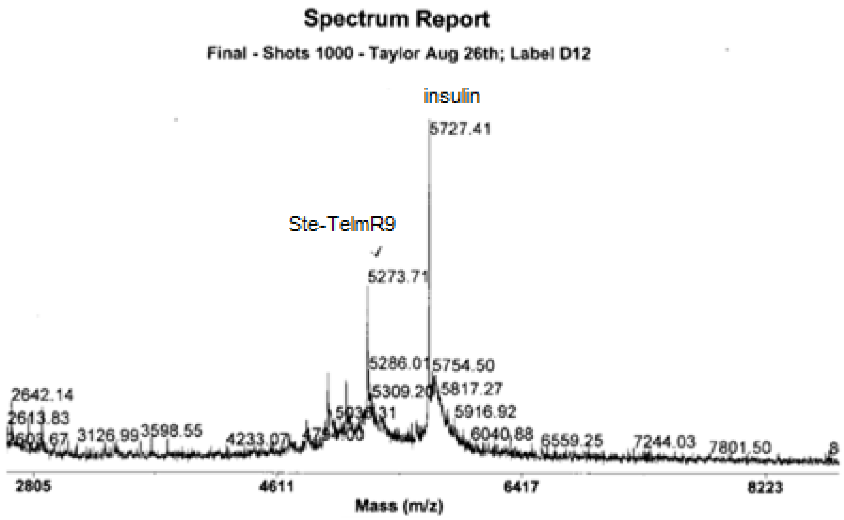

Figure A2.12 MALDI of Ste-TelmR9

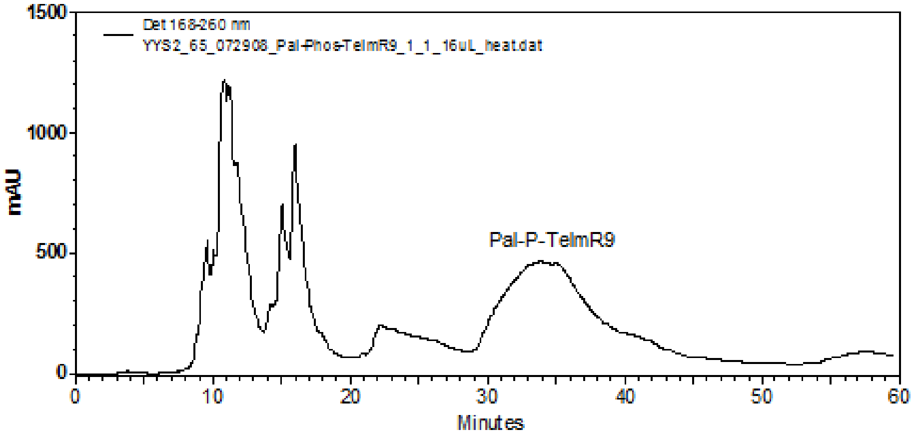

Figure A2.13 HPLC of Crude Pal-P-TelmR9

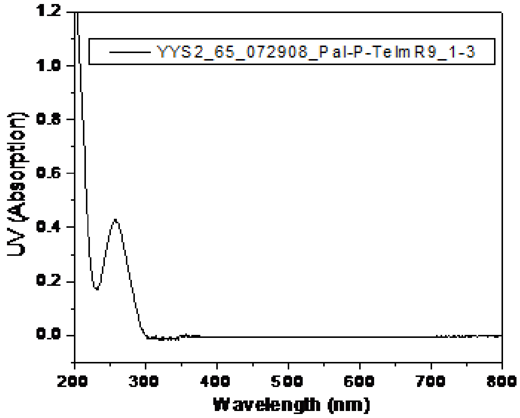

Figure A2.14 UV of Pal-P-TelmR9

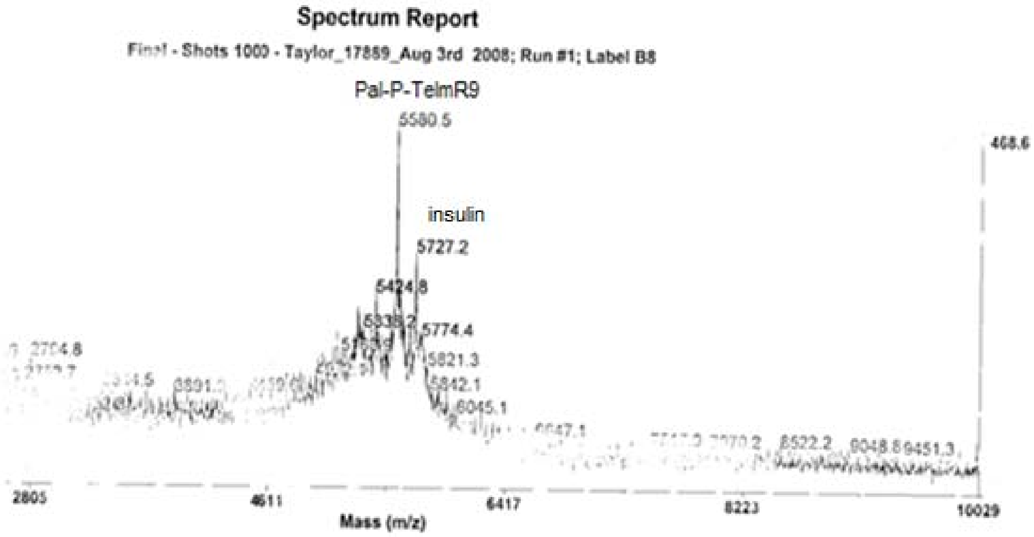

Figure A2.15 MALDI of Pal-P-TelmR9

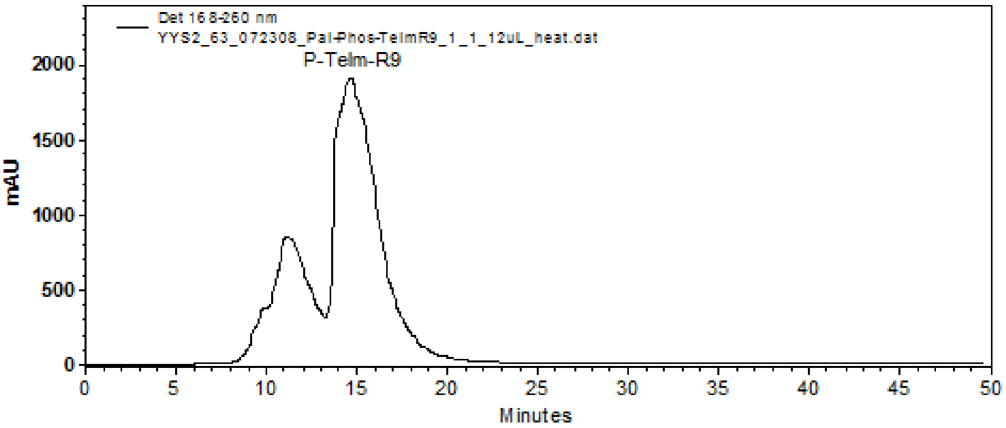

Figure A2.16 HPLC of Crude P-TelmR9

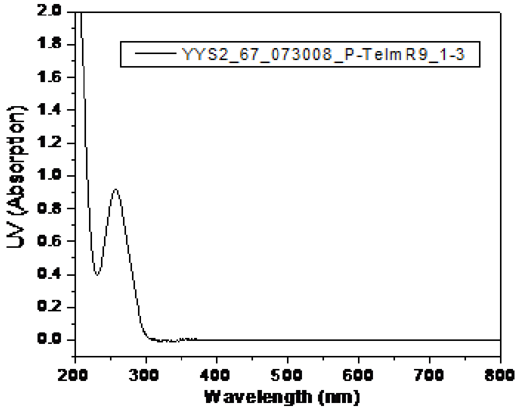

Figure A2.17 UV of P-TelmR9

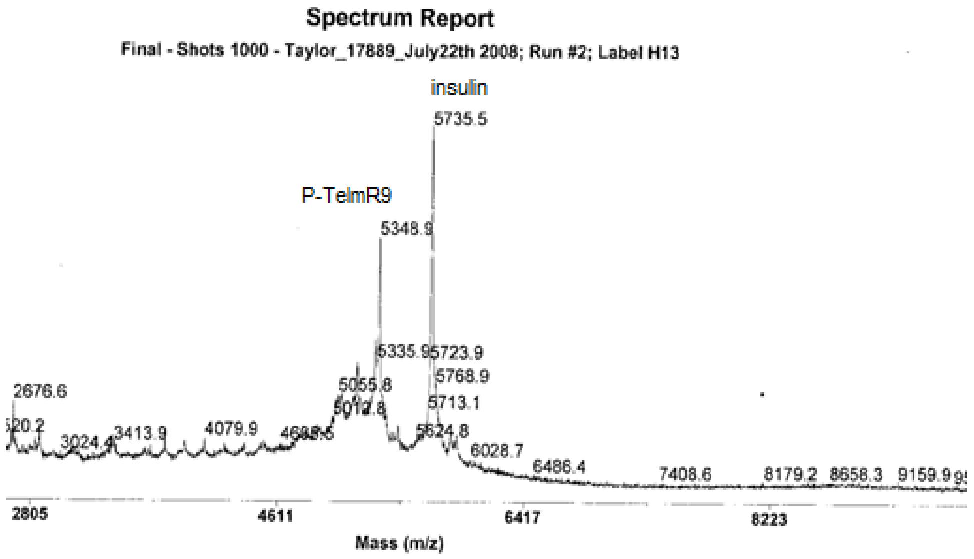

Figure A2.18 MALDI of P-TelmR9

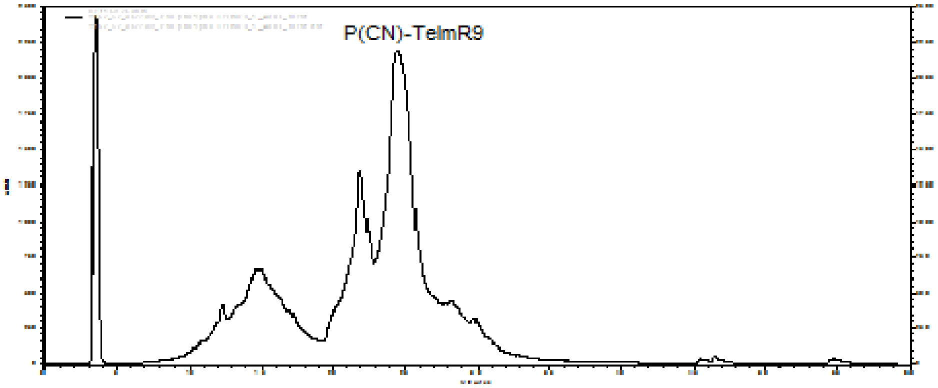

Figure A2.19 HPLC of Crude P(CN)-TelmR9

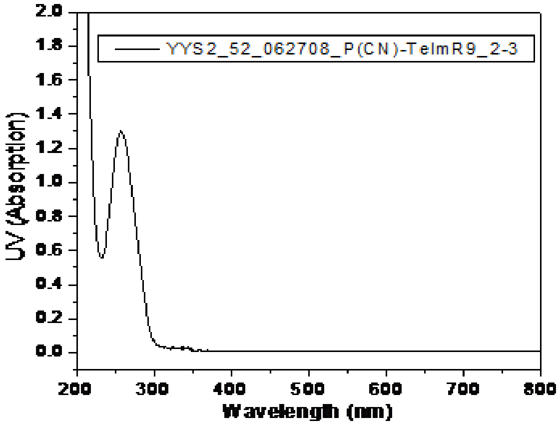

Figure A2.20 UV of P(CN)-TelmR9

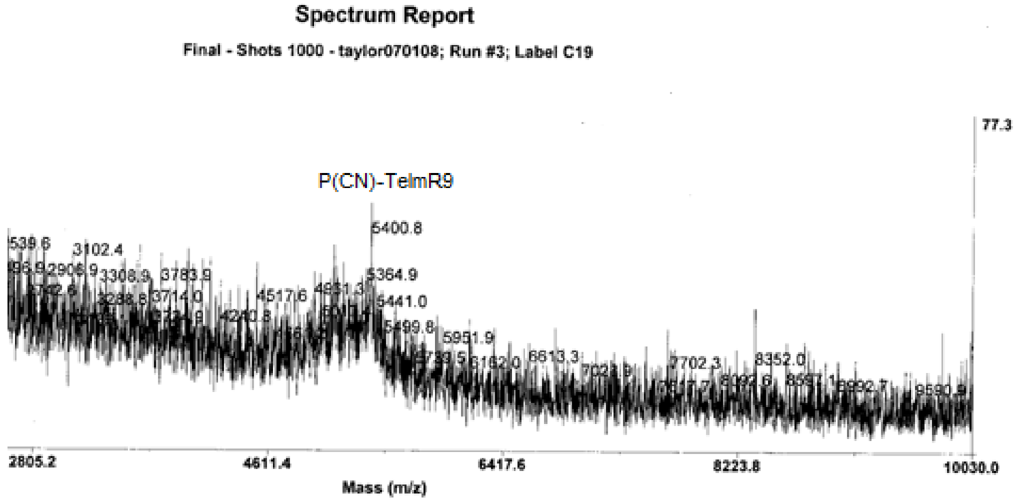

Figure A2.21 MALDI of P(CN)-TelmR9

DLS, CMC

C(μM)	I373/I383
0.007	1.489592

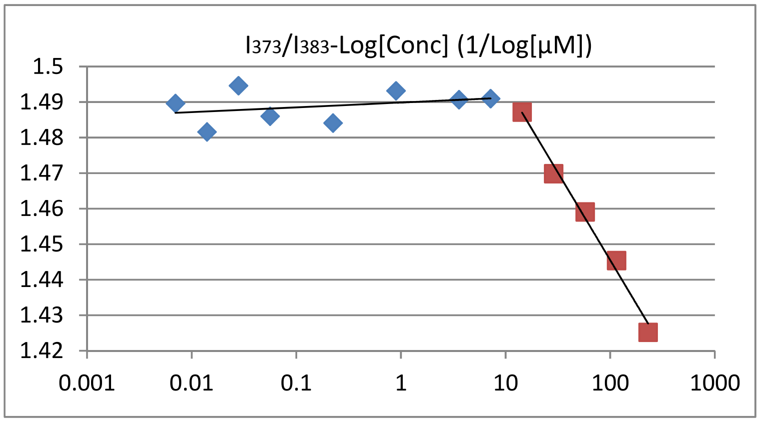

Figure A2.22 Ted-Telm-R$_9$_CMC_without NaCl

0.014	1.481585
0.028	1.494602
0.0561	1.486009
0.2245	1.484102
0.898	1.493159
3.593	1.490662
7.187	1.490957
14.375	1.487184
28.75	1.469855
57.5	1.459077
115	1.445387
230	1.425188

C(µM)	I373/I383
0.014	1.564565
0.028	1.565888
0.0561	1.564237
0.1122	1.557741
0.449	1.558463
1.796	1.562648
3.593	1.557264
7.187	1.567101
14.375	1.544717

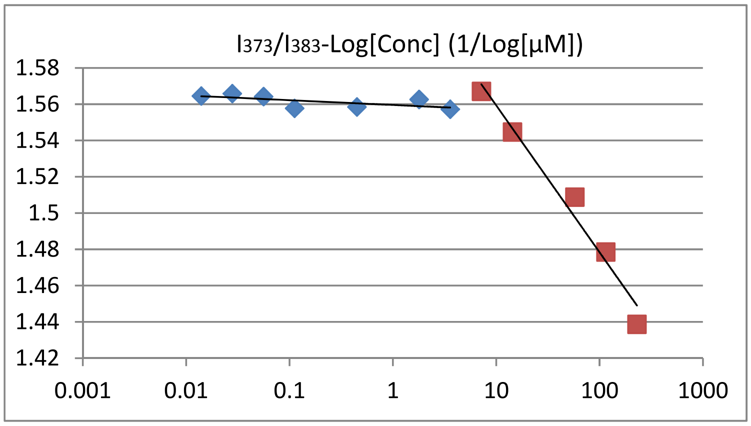

57.5	1.508859
115	1.478573
230	1.438731

Figure A2.23 Ted-Telm-R$_9$_CMC_with NaCl

C(µM)	I373/I383
0.007	1.49728
0.014	1.497403
0.028	1.49194
0.0561	1.491416
0.1122	1.503641

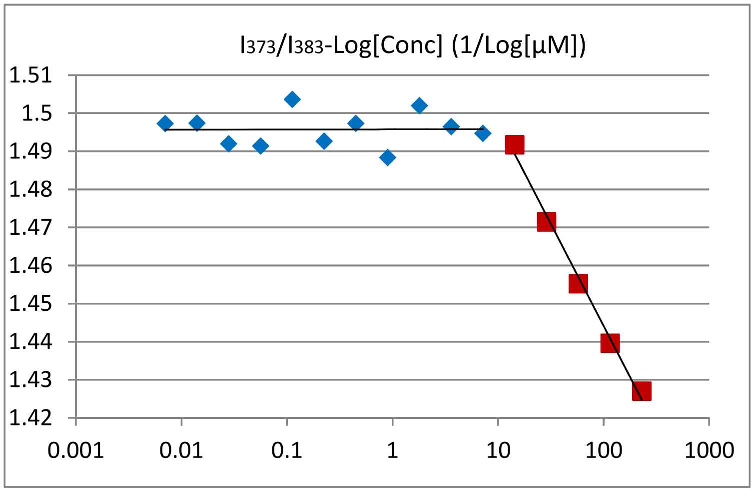

Figure A2.24 Pal-Telm-R_9_CMC_without NaCl

0.2245	1.492667
0.449	1.497314
0.898	1.488354
1.796	1.501953
3.593	1.496456
7.187	1.494717
14.375	1.49172
28.75	1.471479
57.5	1.455226
115	1.439605
230	1.427022

C(μM)	I373/I383
0.007	1.538614
0.028	1.535606
0.0561	1.547129
0.1122	1.506758
0.2245	1.534514
0.449	1.490662
1.796	1.485111
3.593	1.534557

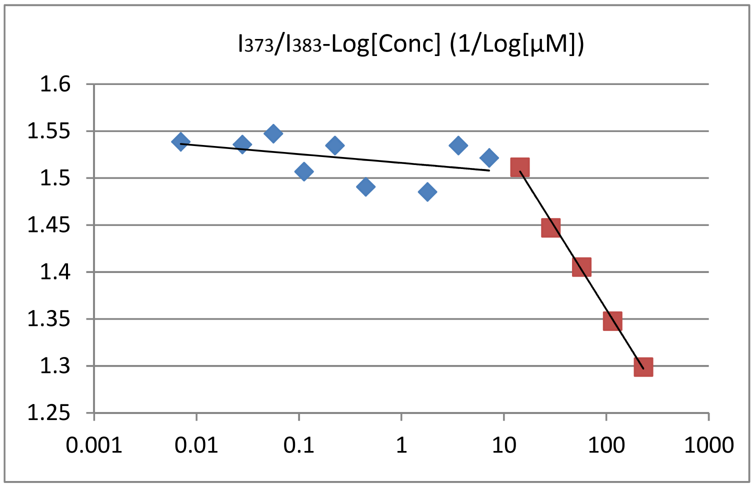

7.187	1.521369
14.375	1.511606
28.75	1.447094
57.5	1.405209
115	1.34771
230	1.298826

Figure A2.25 Pal-Telm-R_9_CMC_with NaCl

C(μM)	I373/I383
0.0046	1.474278
0.00915	1.462107
0.0366	1.464239
0.07325	1.467733
0.1465	1.46105

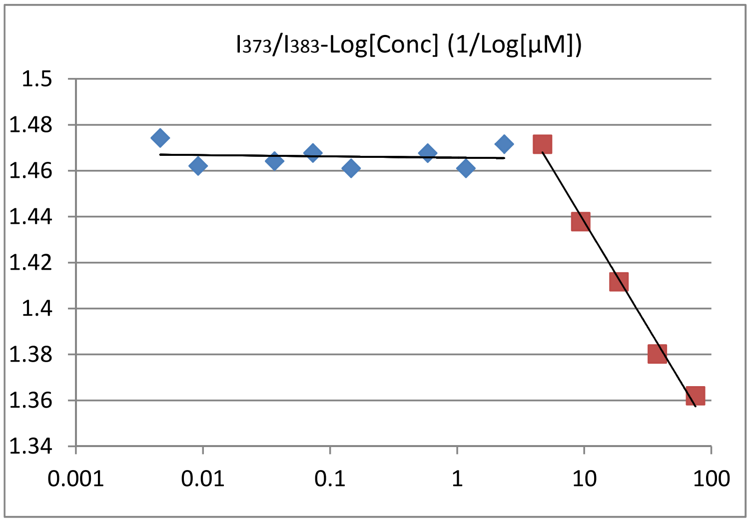

Figure A2.26 Ste-Telm-R_9_CMC_without NaCl

0.586	1.467712
1.172	1.461071
2.344	1.471603
4.6875	1.471599
9.375	1.43791
18.75	1.411696
37.5	1.380256
75	1.36202

C(μM)	I373/I383
0.0046	1.502483
0.00915	1.504624
0.0183	1.503585
0.07325	1.502258
0.1465	1.508147
0.293	1.501909
0.586	1.50954
1.172	1.508971
2.344	1.505241

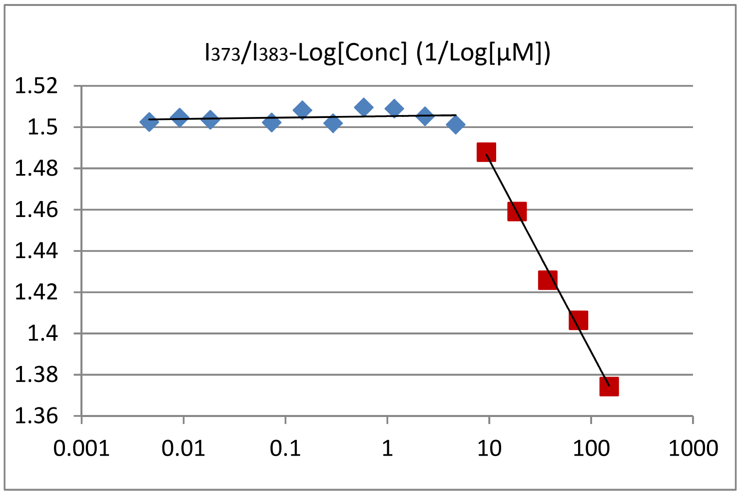

4.6875	1.501257
9.375	1.487843
18.75	1.459117
37.5	1.425819
75	1.40639
150	1.374231

Figure A2.27 Ste-Telm-R_9_CMC_with NaCl

C(μM)	I373/I383
0.007	1.466884
0.014	1.470579
0.029	1.46447
0.115	1.467743
0.23	1.467847

0.46	1.460247
0.94	1.475048
1.875	1.466211
3.75	1.47215
7.5	1.458236
15	1.405613
30	1.342321
60	1.301647

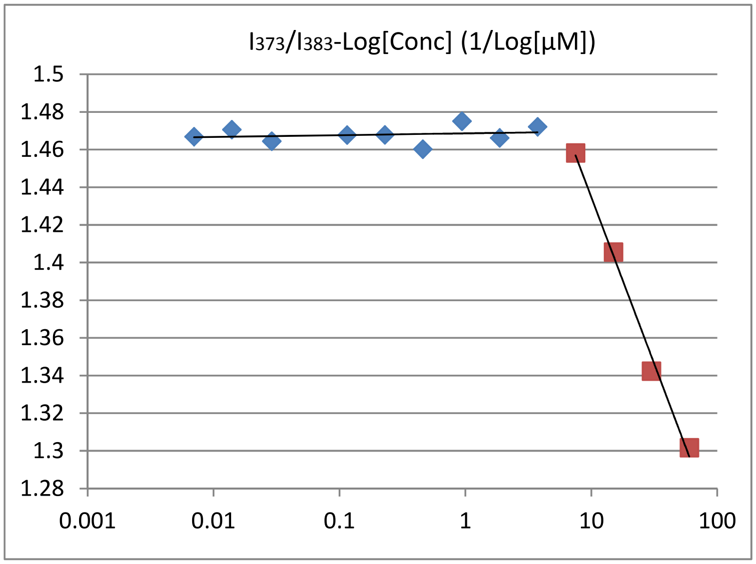

Figure A2.28 Pal-P-Telm-R$_9$_CMC_without NaCl

C(µM)	I373/I383
0.007	1.467015
0.014	1.466367
0.029	1.469527
0.0575	1.462331
0.115	1.467442
0.46	1.461654
0.94	1.462199

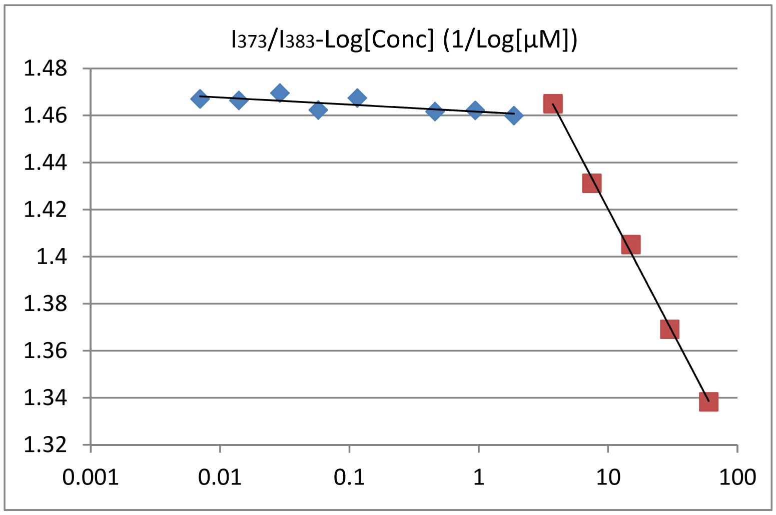

1.875	1.459948
3.75	1.465002
7.5	1.431186
15	1.405136
30	1.36912
60	1.338266

Figure A2.29 Pal-P-Telm-R$_9$_CMC_with NaCl

HPLC, UV, MALDI

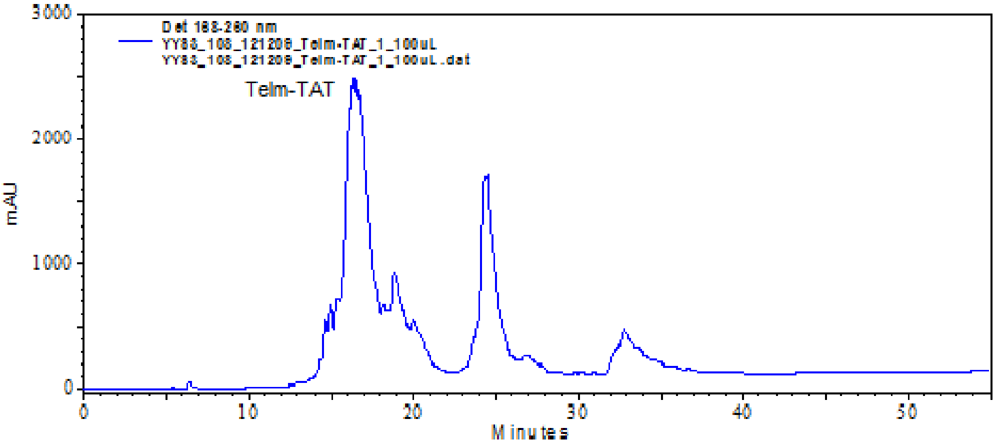

Figure A2.30 HPLC of Crude Telm-TAT

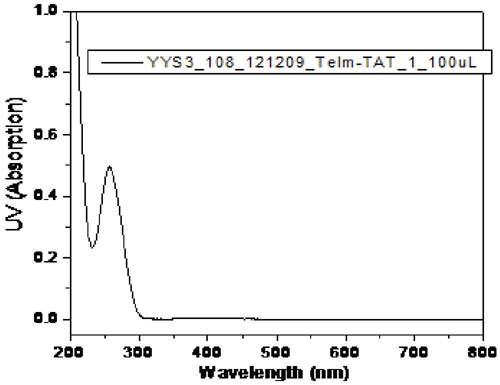

Figure A2.31 UV of Telm-TAT

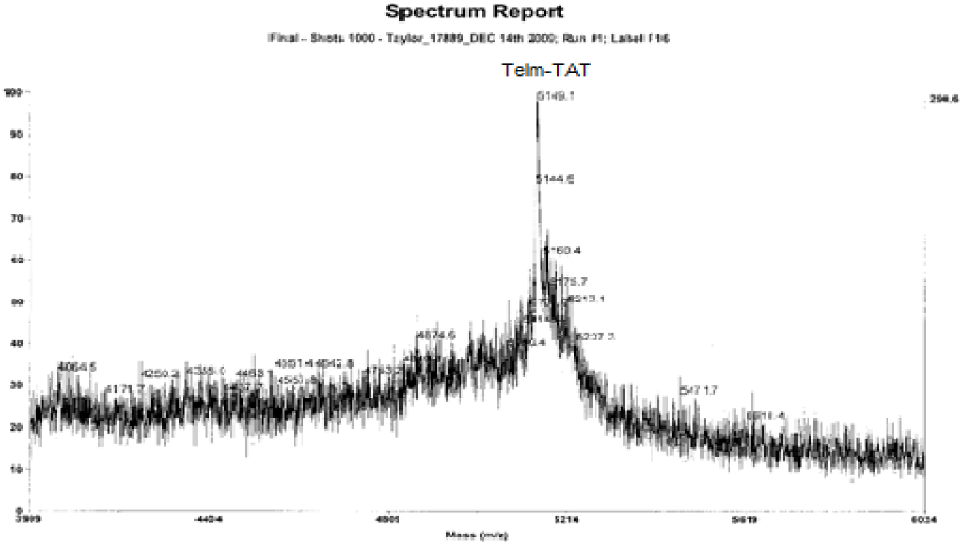

Figure A2.32 MALDI of Telm-TAT

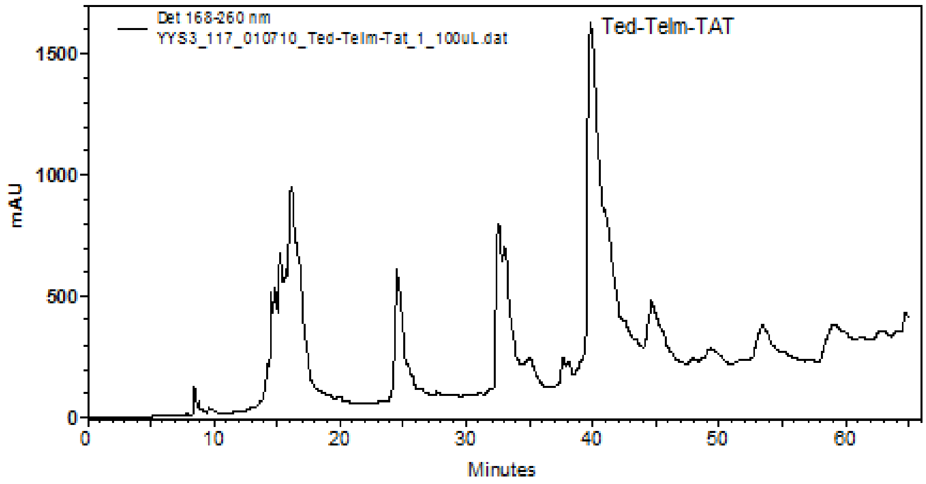

Figure A2.33 HPLC of Crude Ted-Telm-TAT

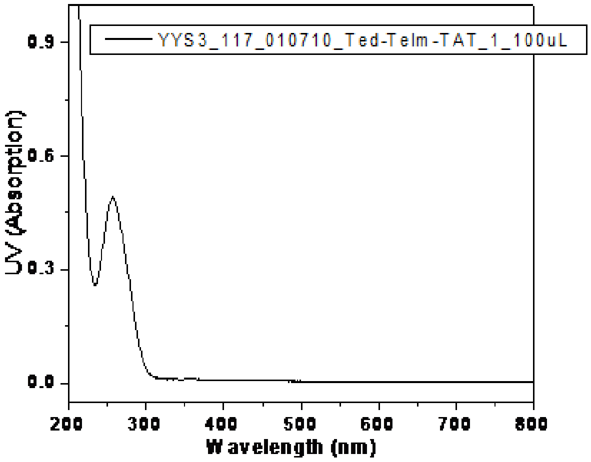

Figure A2.34 UV of Ted-Telm-TAT

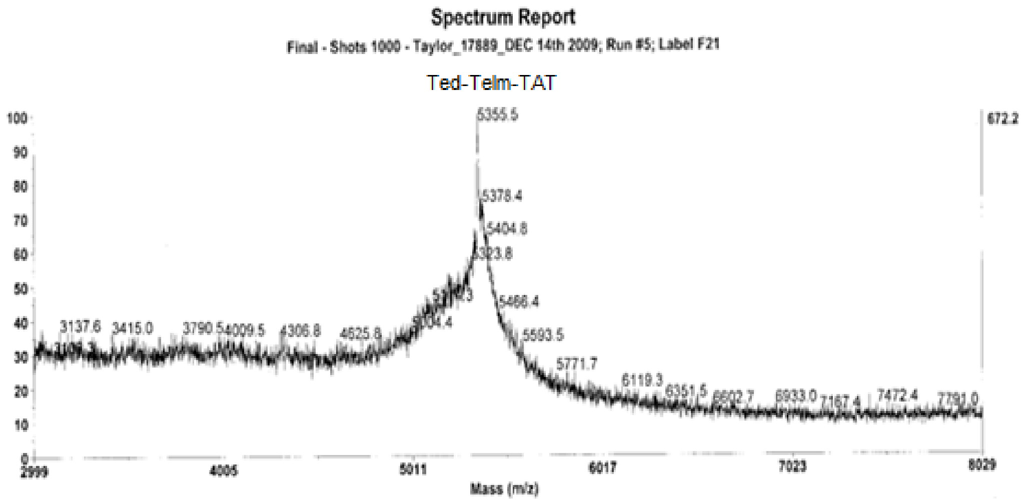

Figure A2.35 MALDI of Ted-Telm-TAT

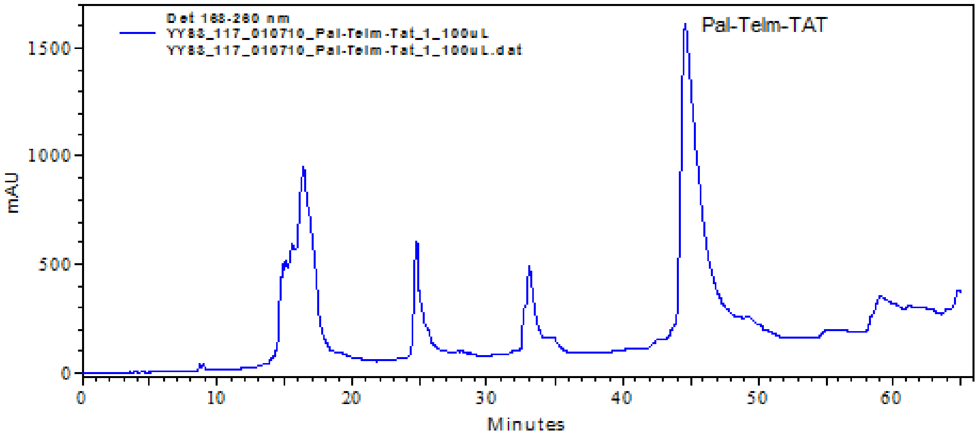

Figure A2.36 HPLC of Crude Pal-Telm-TAT

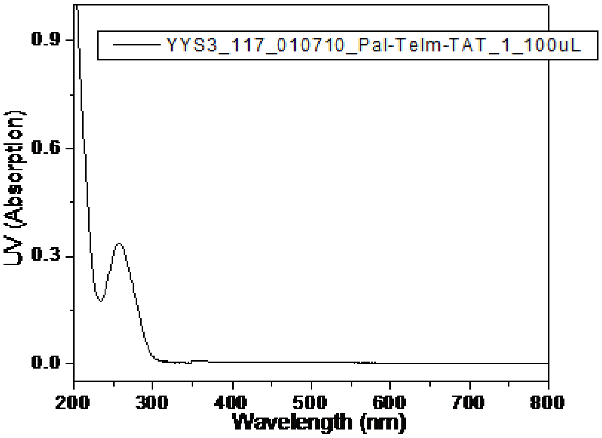

Figure A2.37 UV of Pal-Telm-TAT

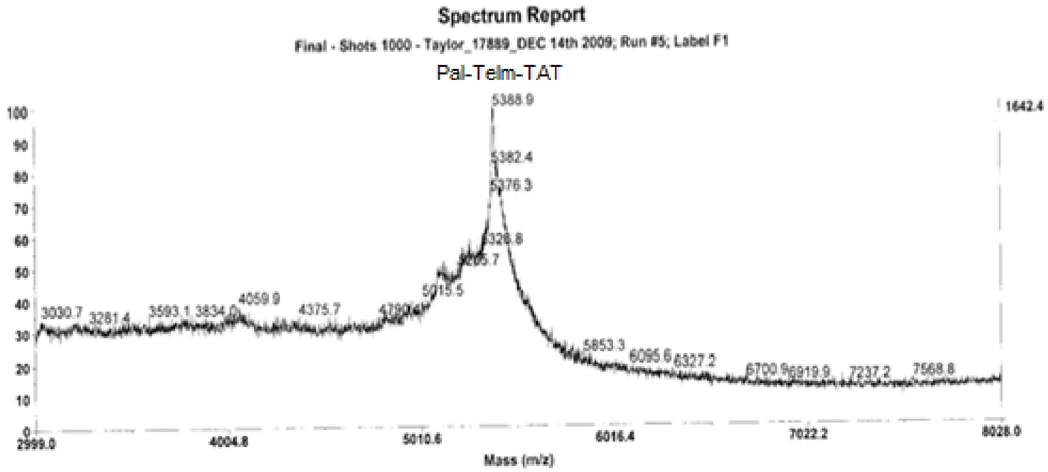

Figure A2.38 MALDI of Pal-Telm-TAT

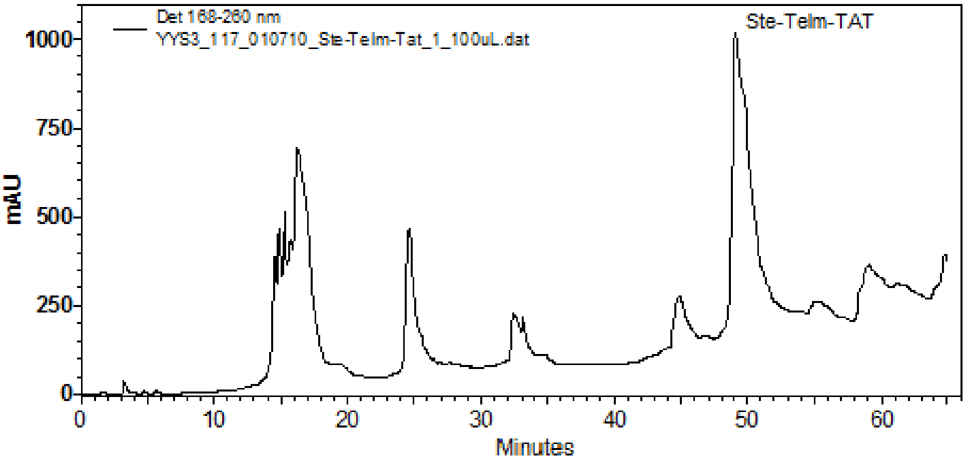

Figure A2.39 HPLC of Crude Ste-Telm-TAT

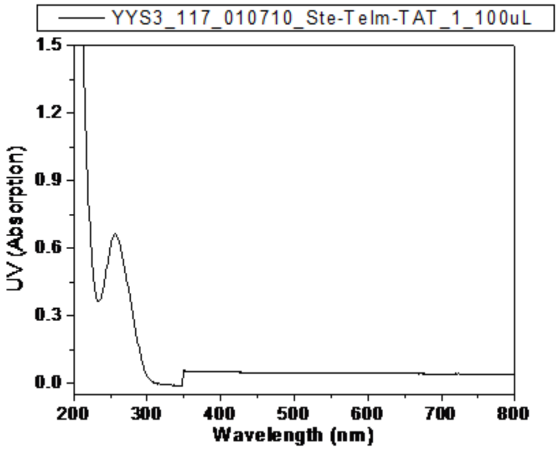

Figure A2.40 UV of Ste-Telm-TAT

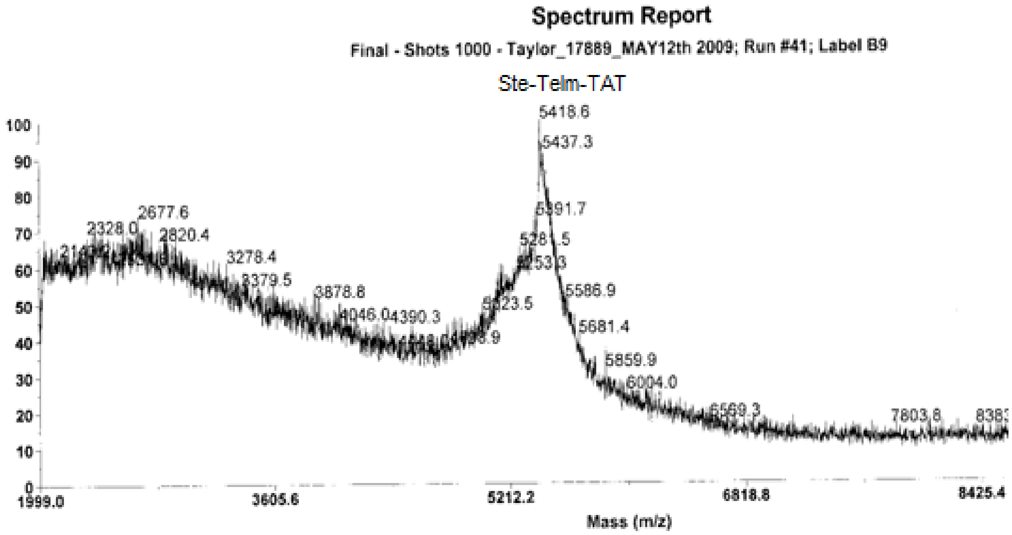

Figure A2.41 MALDI of Ste-Telm-TAT

Appendix_Chapter 3

HPLC, UV, MALDI

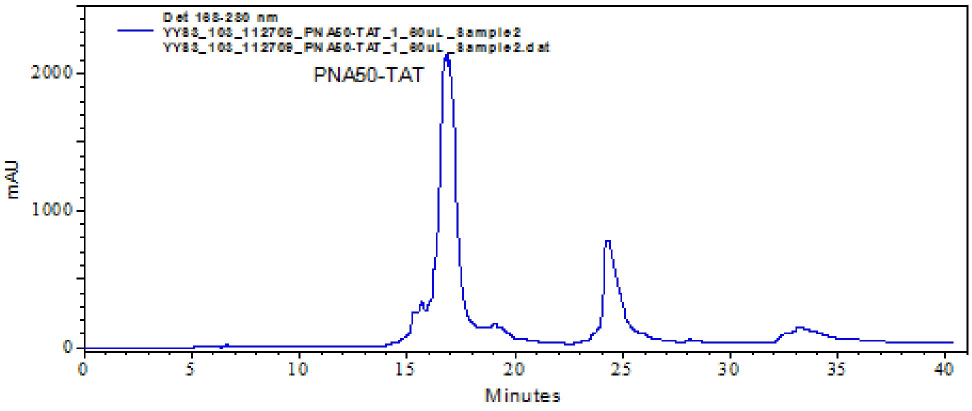

Figure A3.1 HPLC of Crude PNA50-TAT (major peak, collecting 16.3min-17.5min)

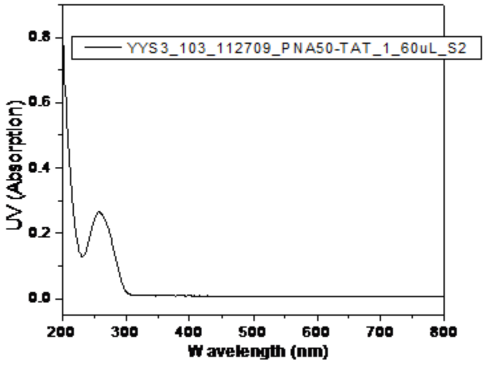

Figure A3.2 UV of PNA50-TAT

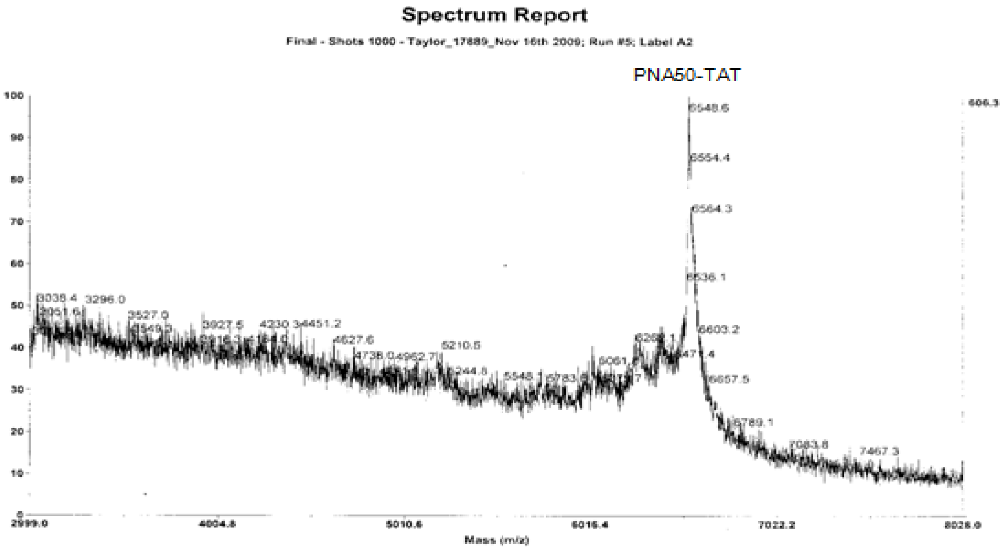

Figure A3.3 MALDI of PNA50-TAT

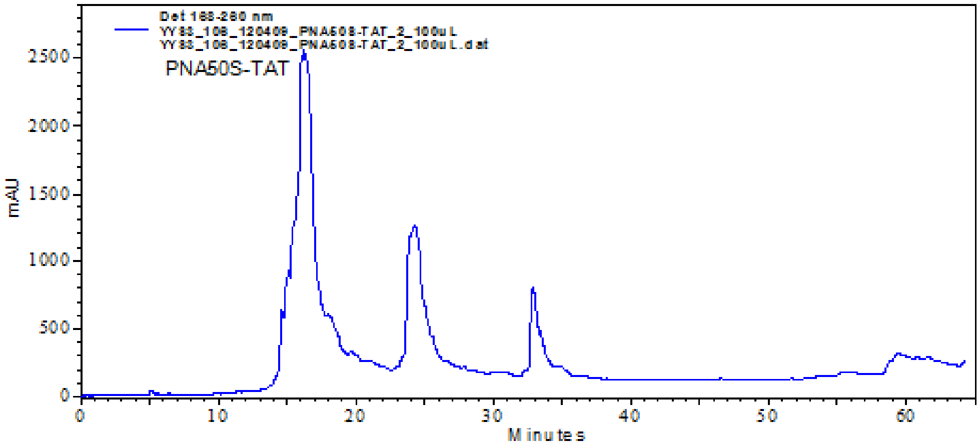

Figure A3.4 HPLC of Crude PNA50S-TAT

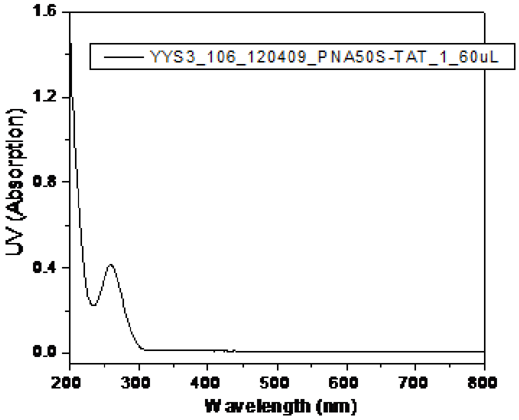

Figure A3.5 UV of PNA50S-TAT

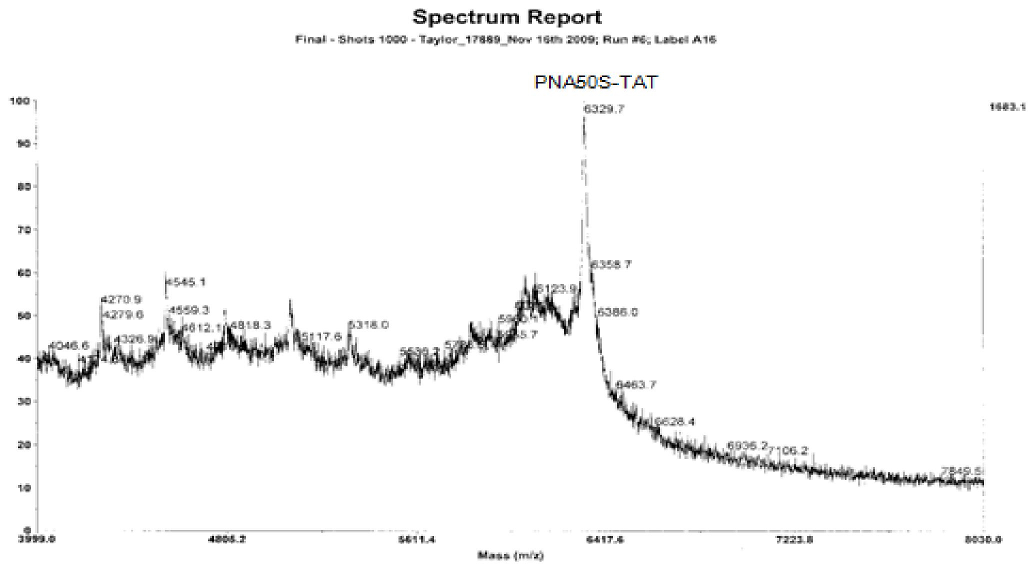

Figure A3.6 MALDI of PNA50S-TAT

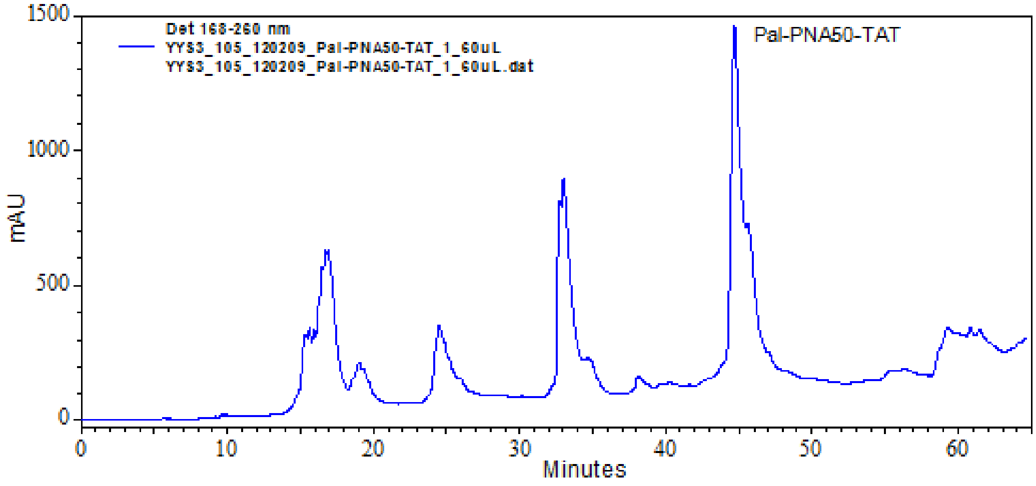

Figure A3.7 HPLC of Crude Pal-PNA50-TAT

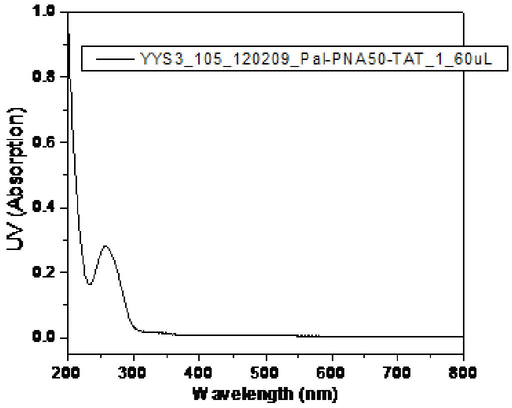

Figure A3.8 UV of Pal-PNA50-TAT

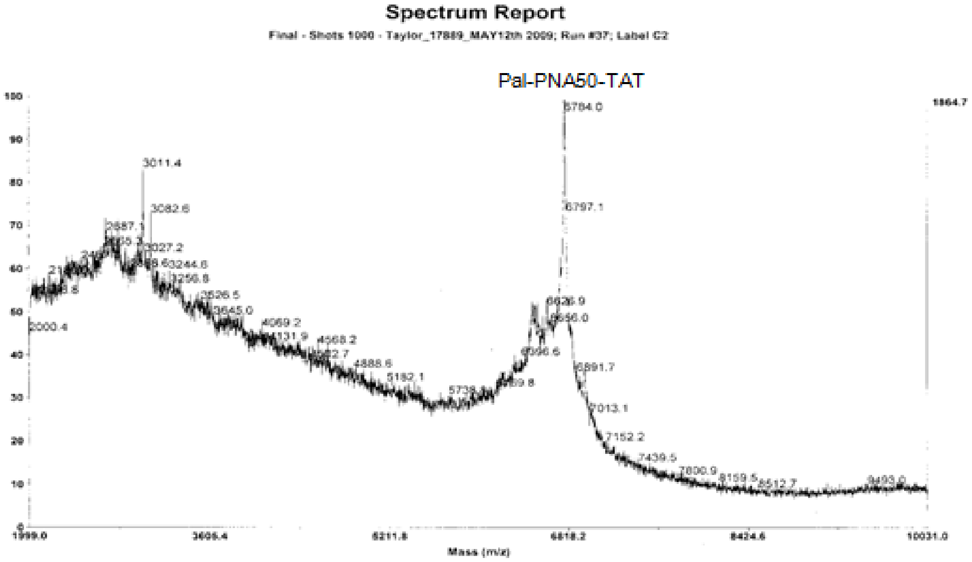

Figure A3.9 MALDI of Pal-PNA50-TAT

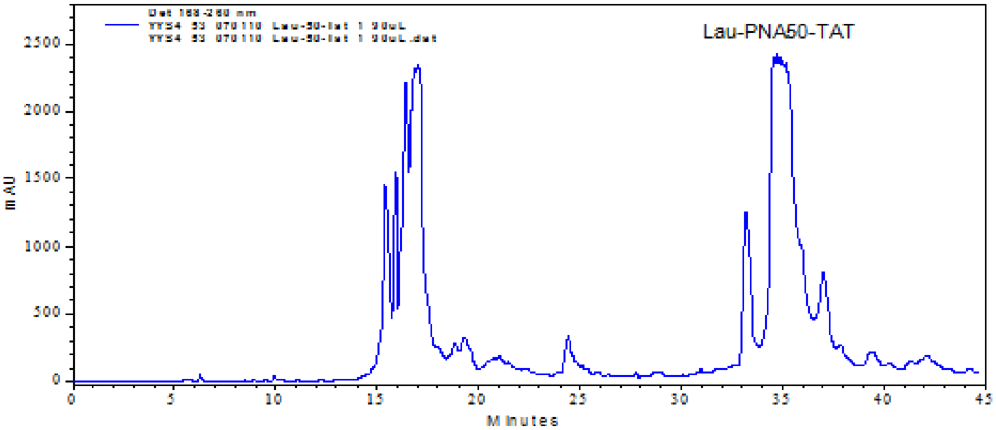

Figure A3.10 HPLC of Crude Lau-PNA50-TAT

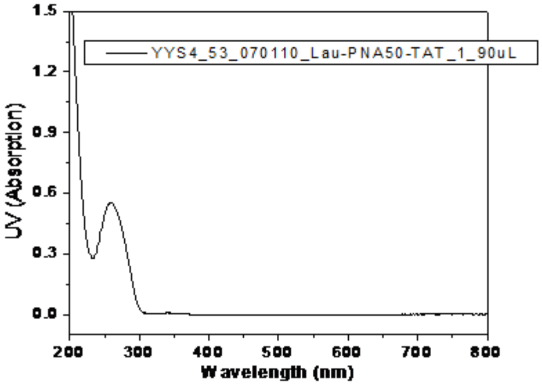

Figure A3.11 UV of Lau-PNA50-TAT

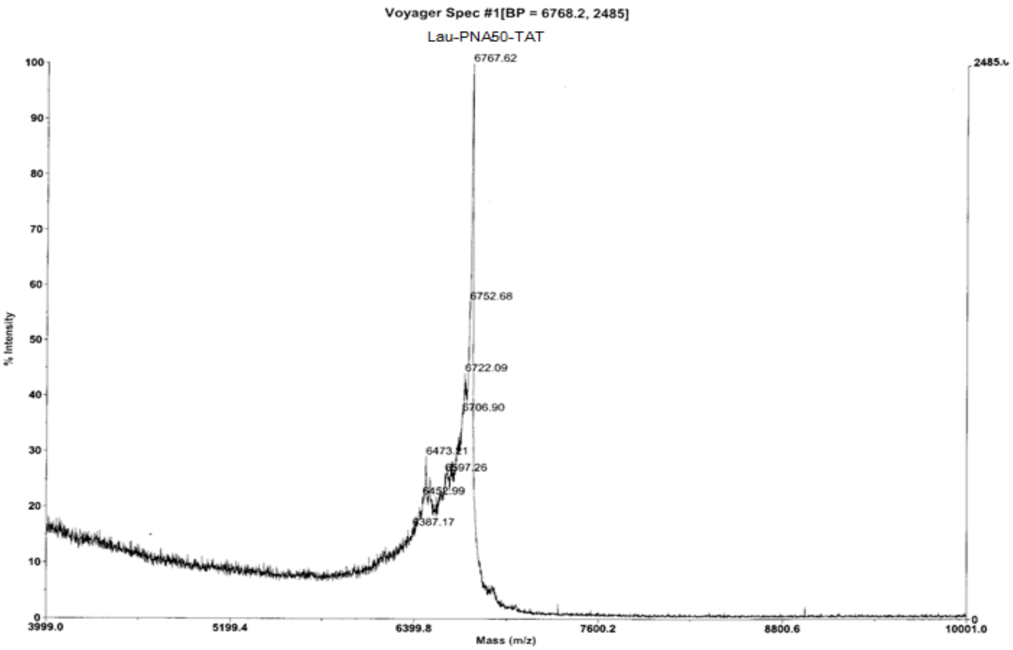

Figure A3.12 MALDI of Lau-PNA50-TAT

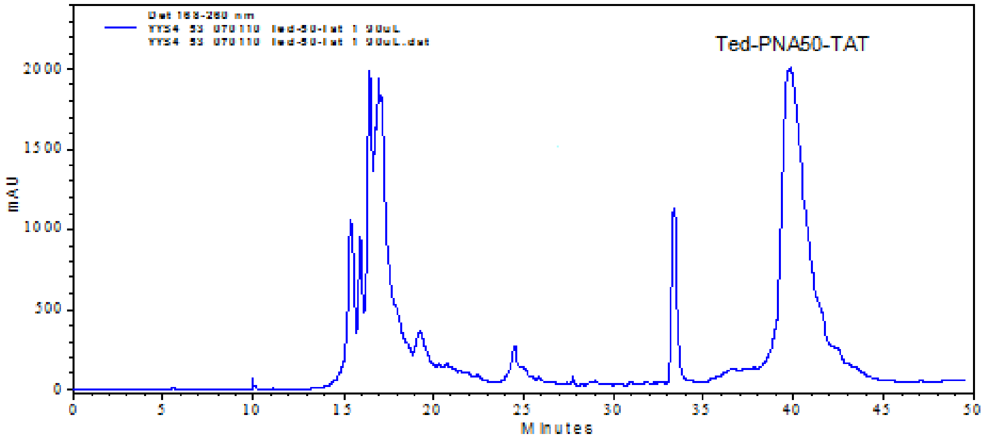

Figure A3.13 HPLC of Crude Ted-PNA50-TAT

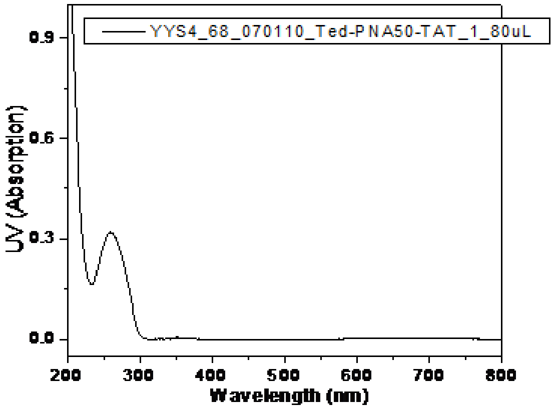

Figure A3.14 UV of Ted-PNA50-TAT

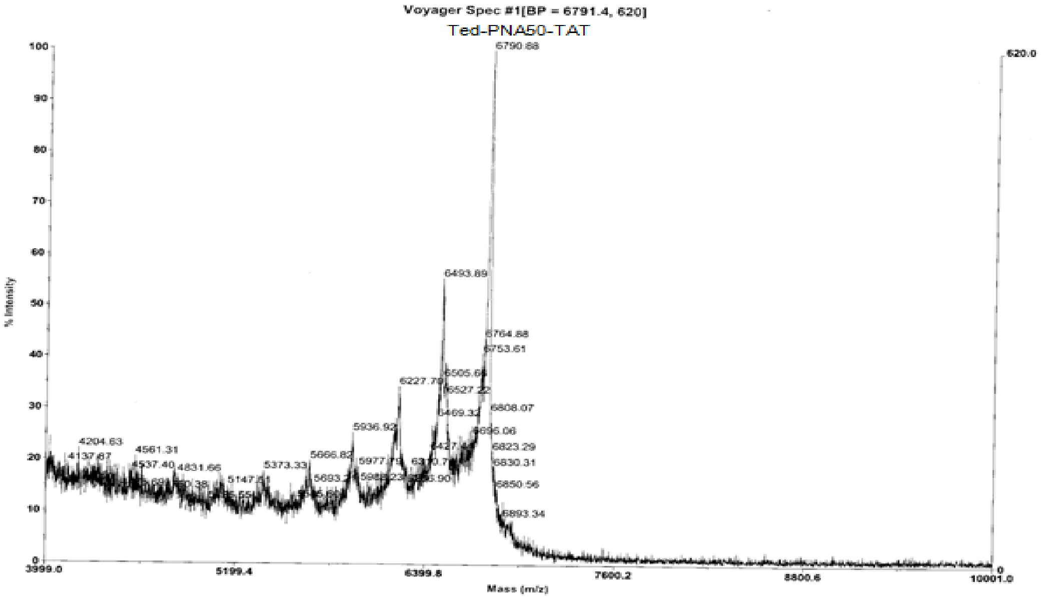

Figure A3.15 MALDI of Ted-PNA50-TAT

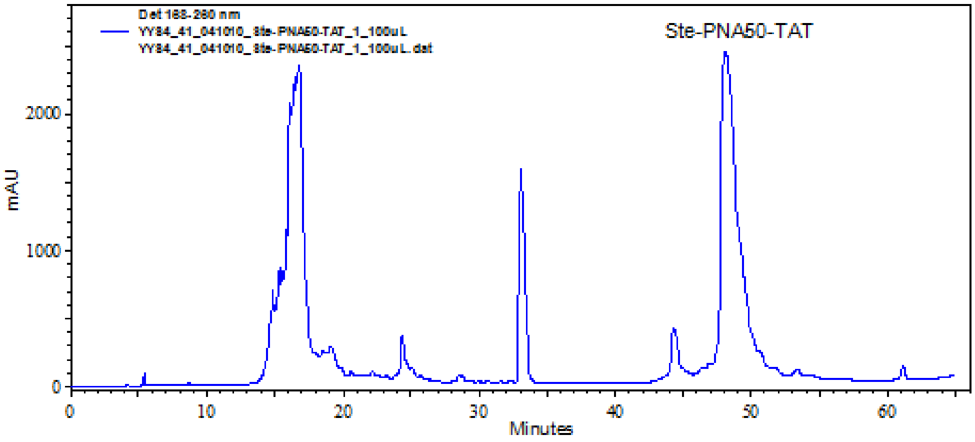

Figure A3.16 HPLC of Crude Ste-PNA50-TAT

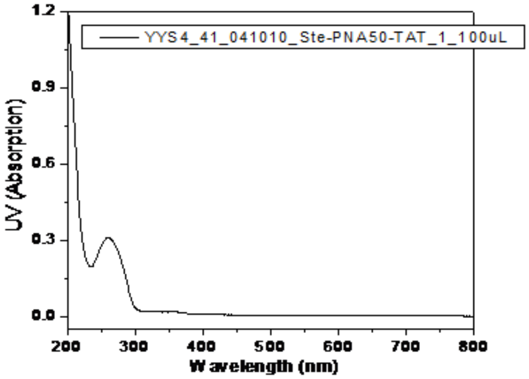

Figure A3.17 UV of Ste-PNA50-TAT

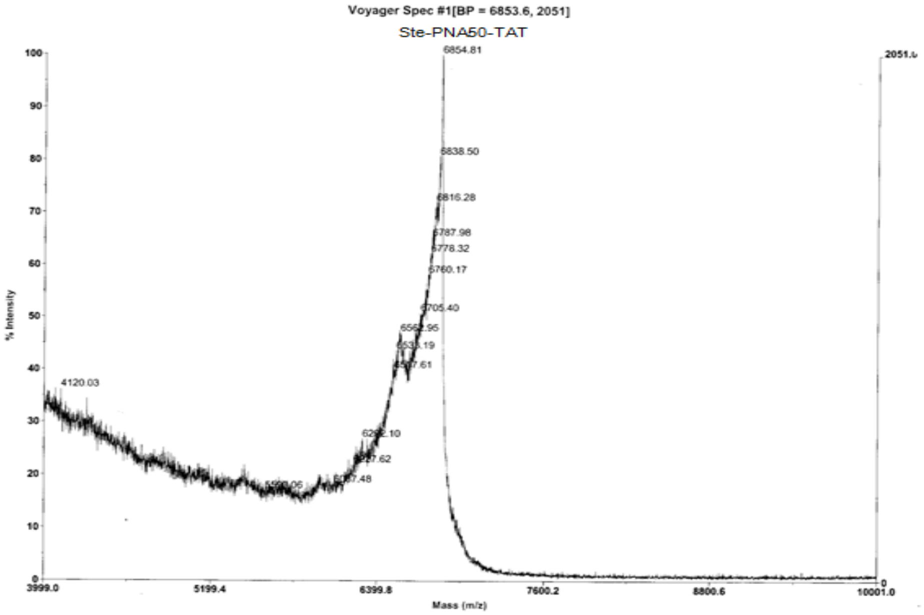

Figure A3.18 MALDI of Ste-PNA50-TAT

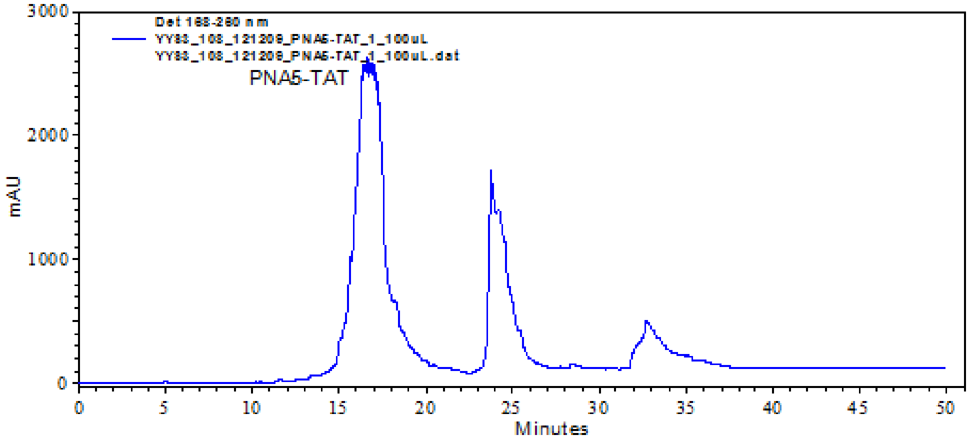

Figure A3.19 HPLC of Crude PNA5-TAT

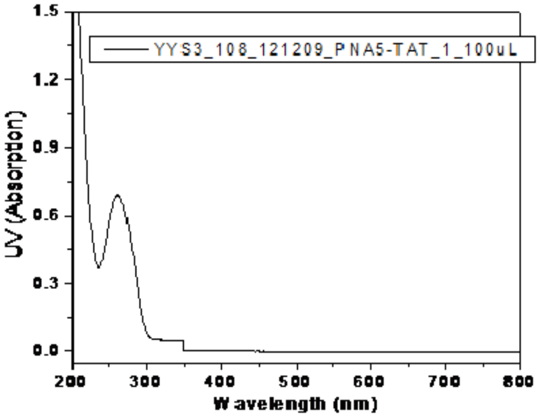

Figure A3.20 UV of PNA5-TAT

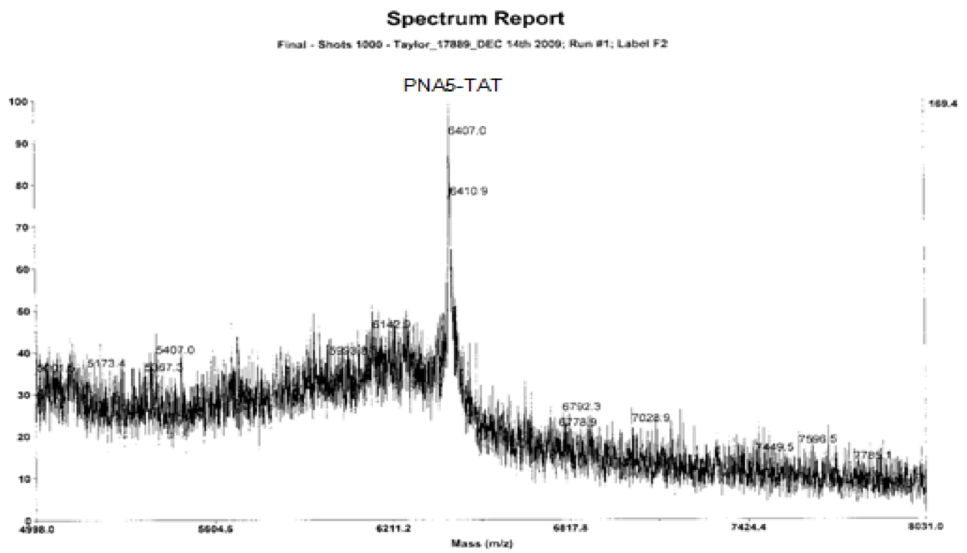

Figure A3.21 MALDI of PNA5-TAT

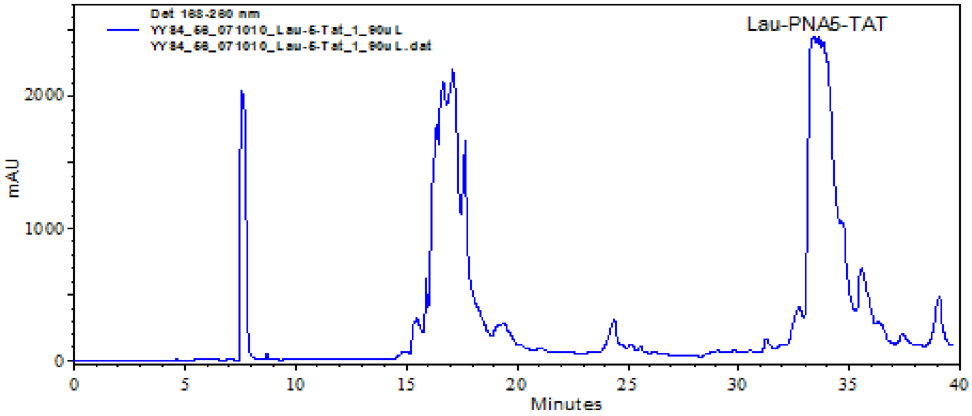

Figure A3.22 HPLC of Crude Lau-PNA5-TAT

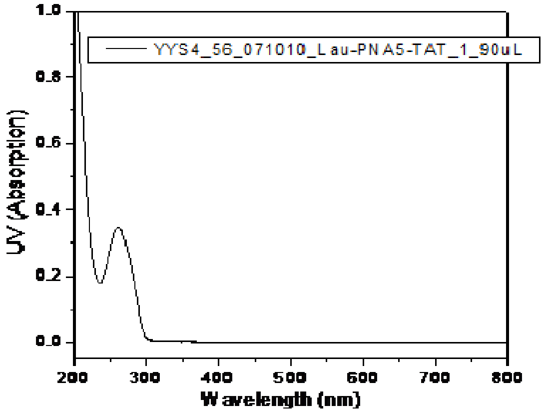

Figure A3.23 UV of Lau-PNA5-TAT

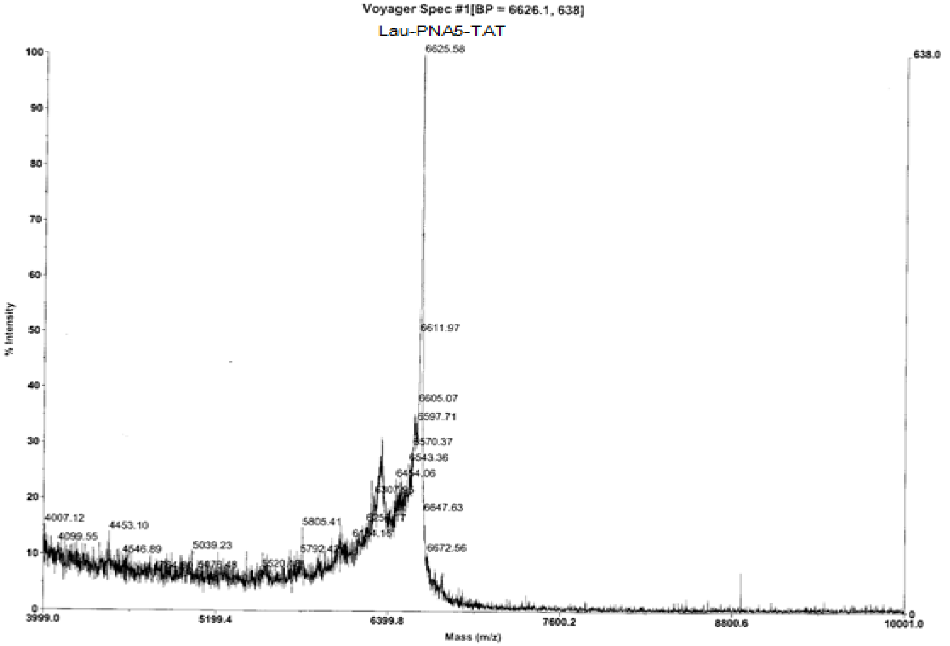

Figure A3.24 MALDI of Lau-PNA5-TAT

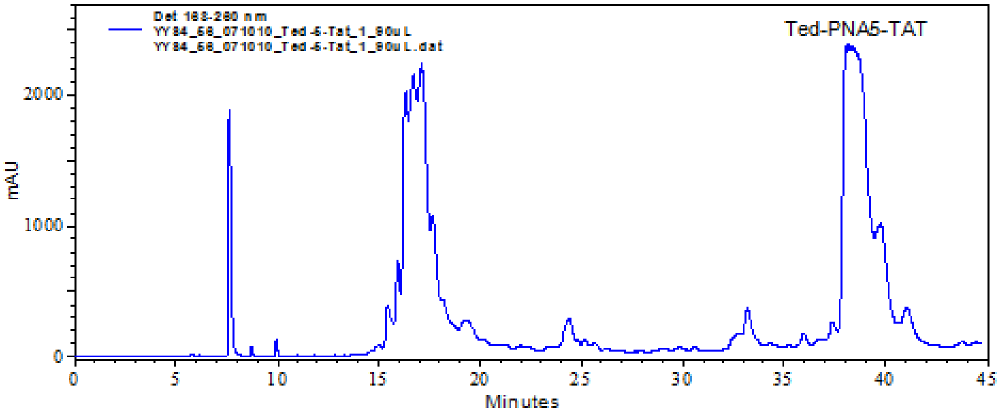

Figure A3.25 HPLC of Crude Ted-PNA5-TAT

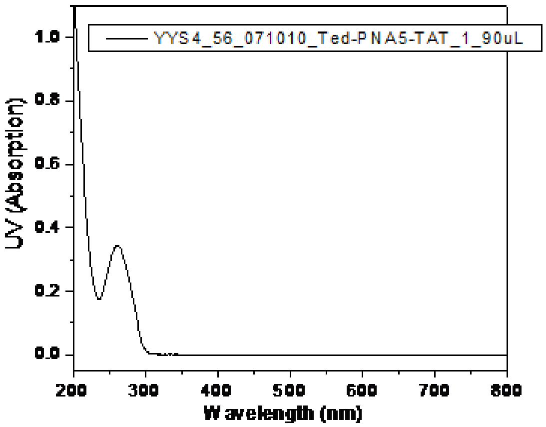

Figure A3.26 UV of Ted-PNA5-TAT

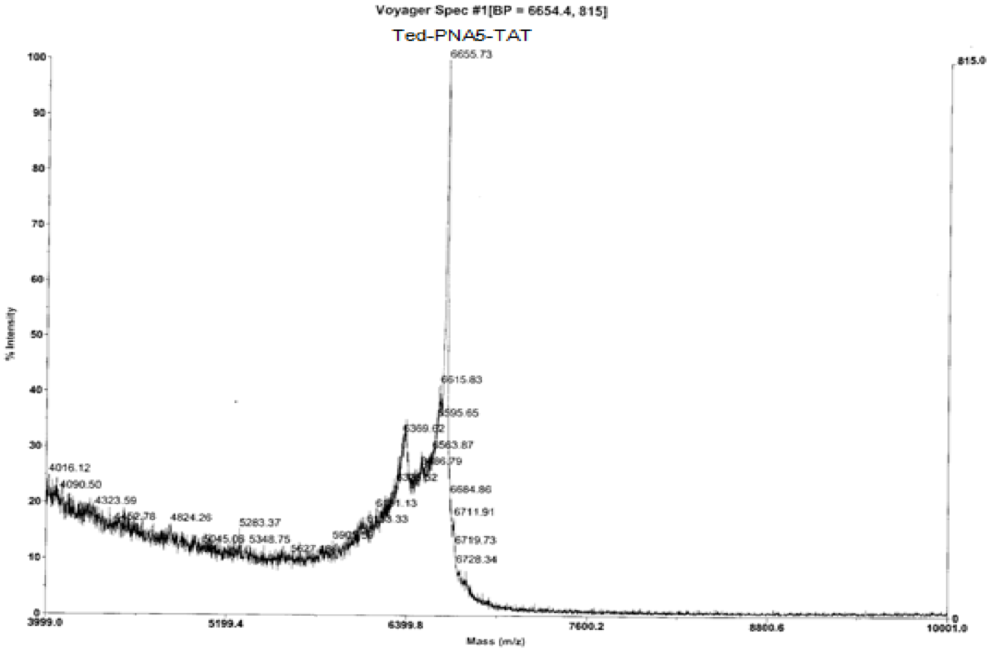

Figure A3.27 MALDI of Ted-PNA5-TAT

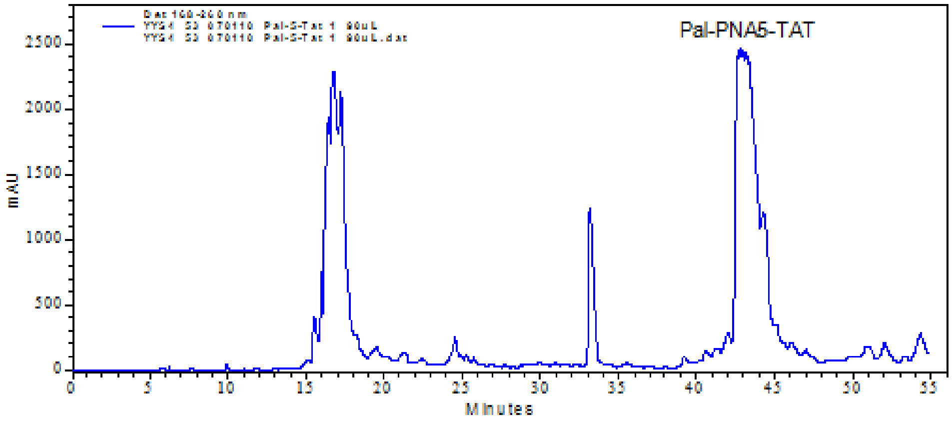

Figure A3.28 HPLC of Crude Pal-PNA5-TAT

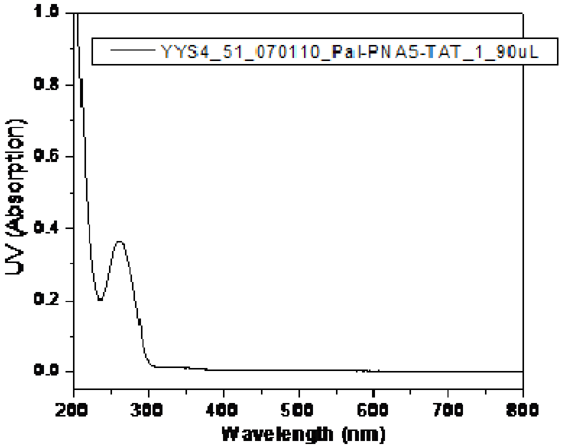

Figure A3.29 UV of Pal-PNA5-TAT

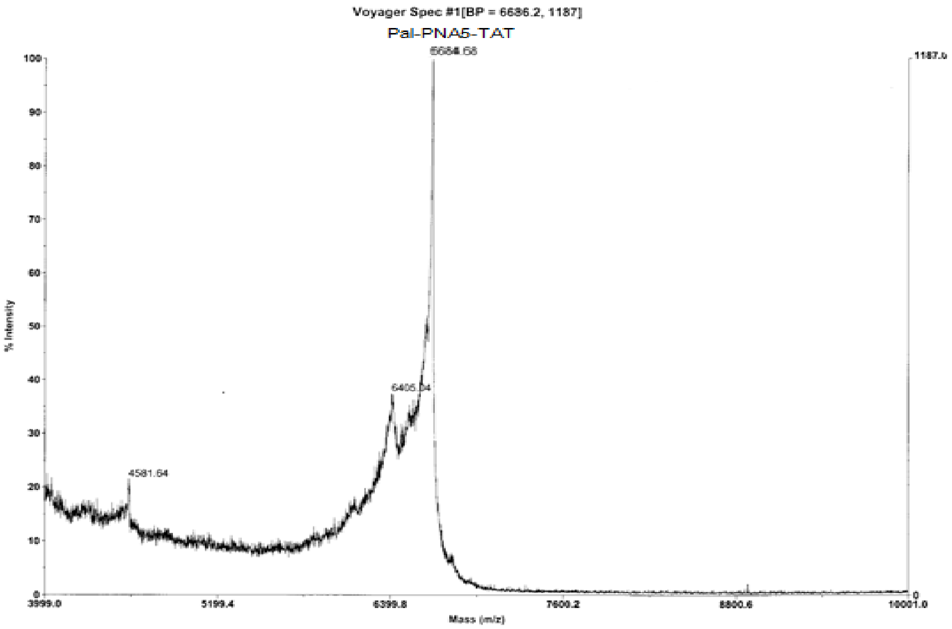

Figure A3.30 MALDI of Pal-PNA5-TAT

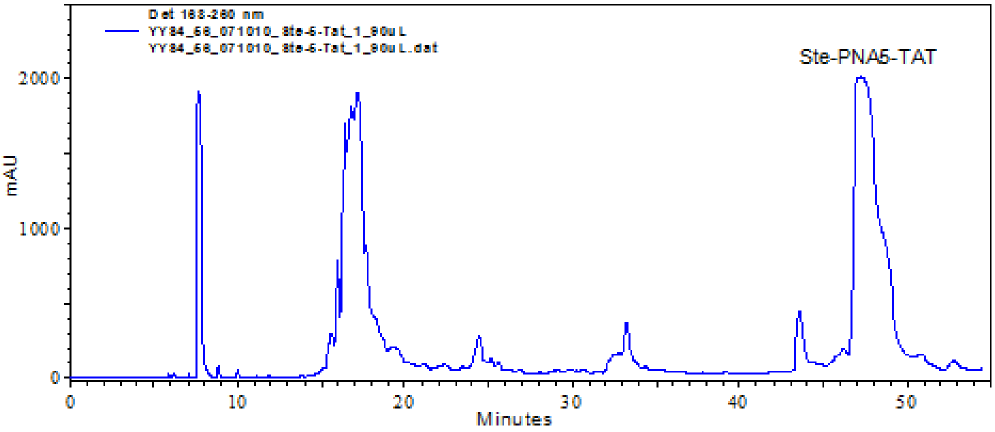

Figure A3.31 HPLC of Crude Ste-PNA5-TAT

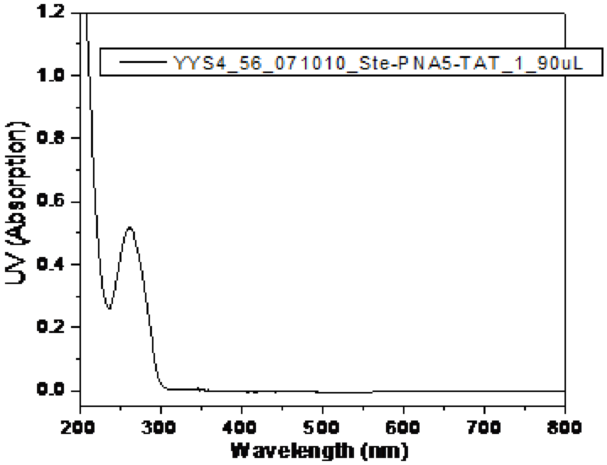

Figure A3.32 UV of Ste-PNA5-TAT

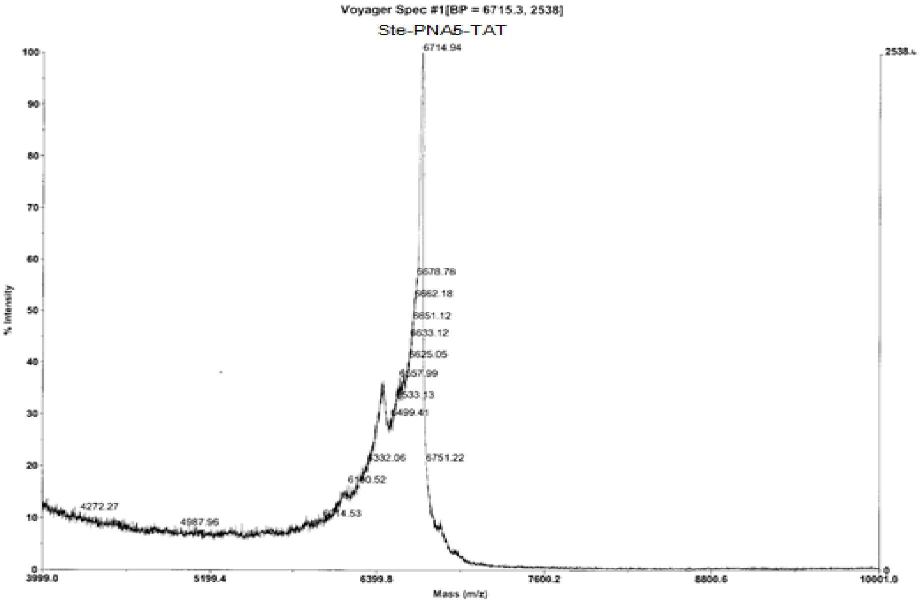

Figure A3.33 MALDI of Ste-PNA5-TAT

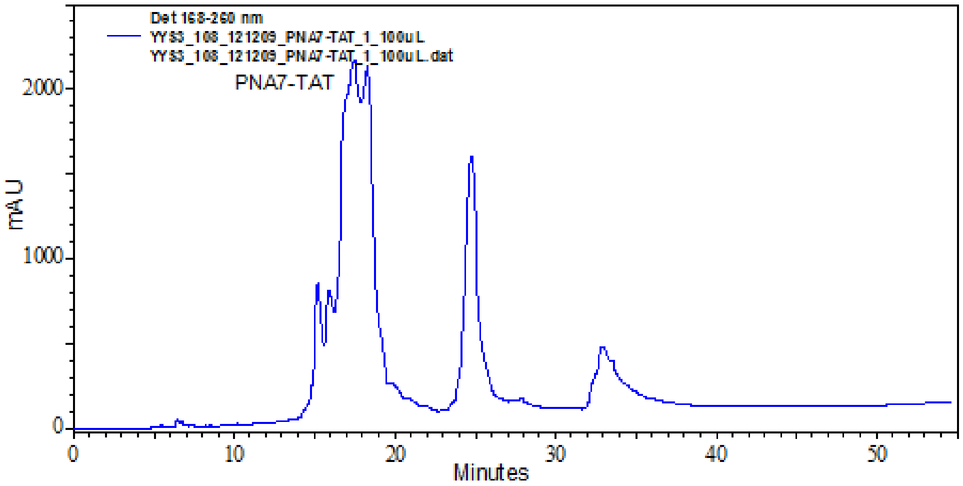

Figure A3.34 HPLC of Crude PNA7-TAT

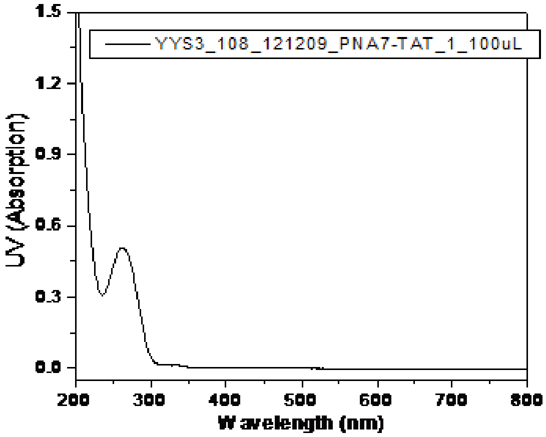

Figure A3.35 UV of PNA7-TAT

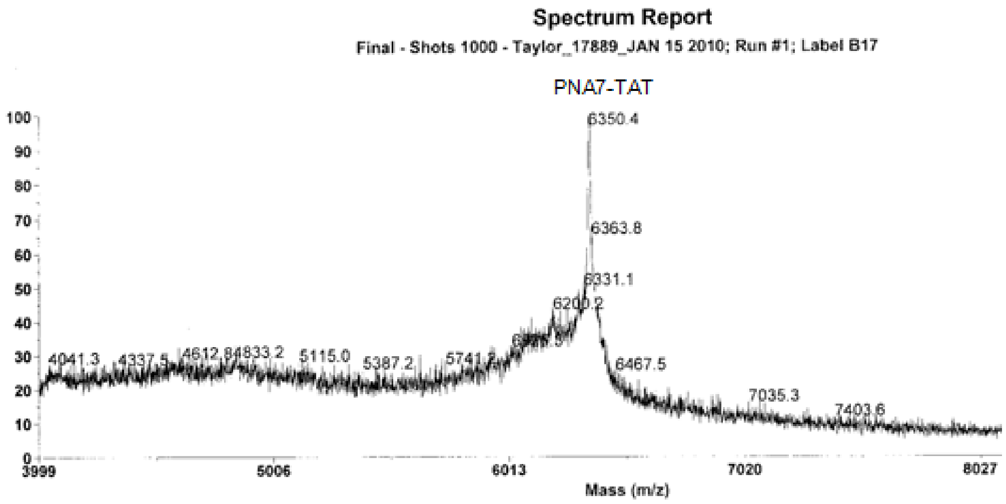

Figure A3.36 MALDI of PNA7-TAT

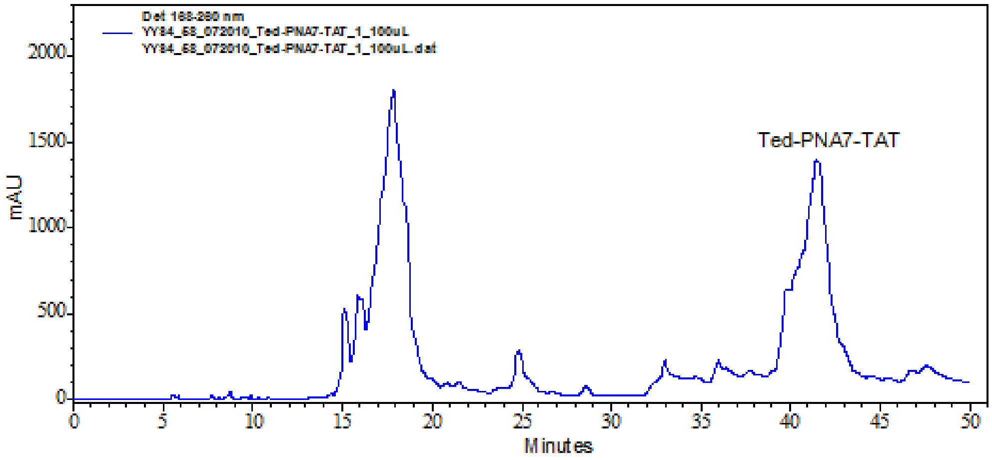

Figure A3.37 HPLC of Crude Ted-PNA7-TAT

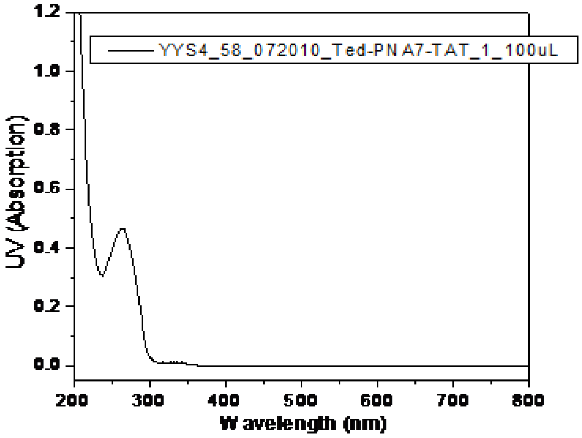

Figure A3.38 UV of Ted-PNA7-TAT

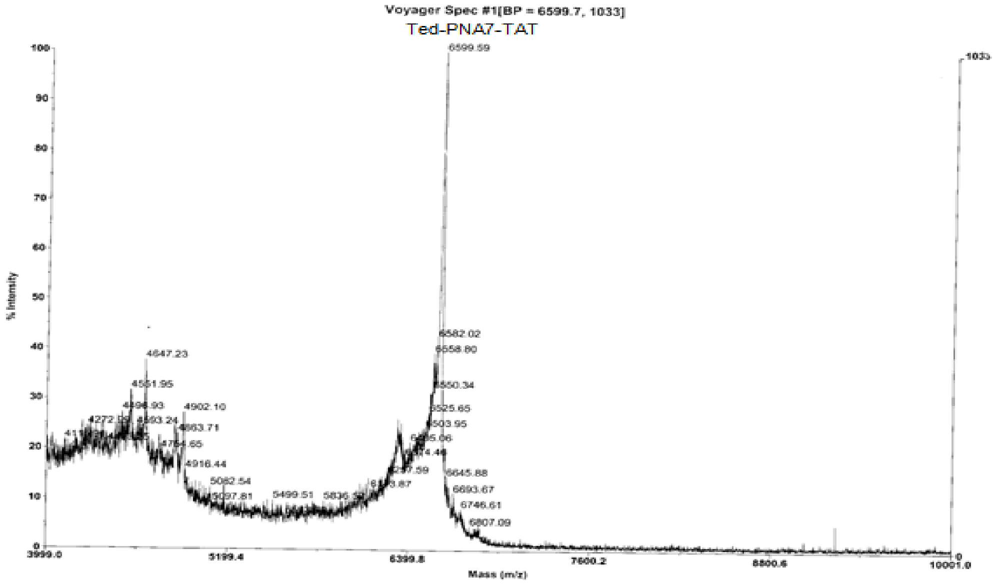

Figure A3.39 MALDI of Ted-PNA7-TAT

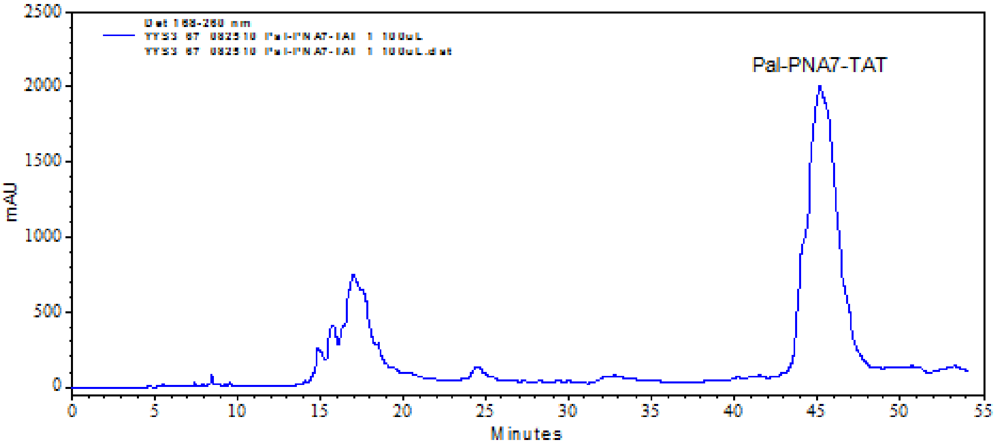

Figure A3.40 HPLC of Crude Pal-PNA7-TAT

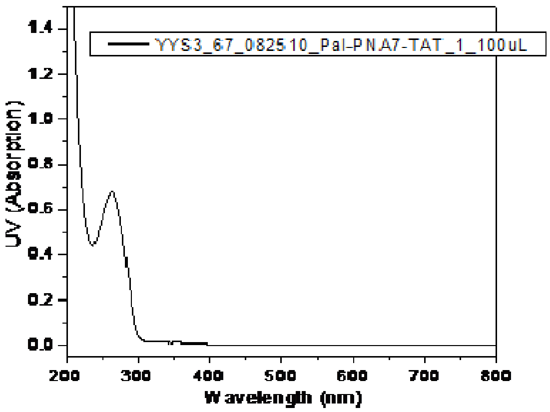

Figure A3.41 UV of Pal-PNA7-TAT

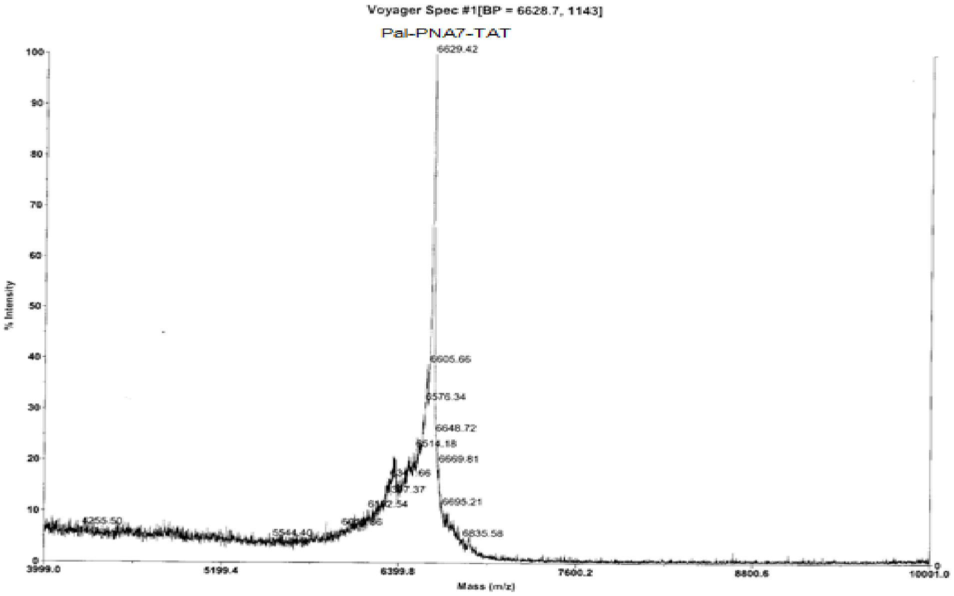

Figure A3.42 MALDI of Pal-PNA7-TAT

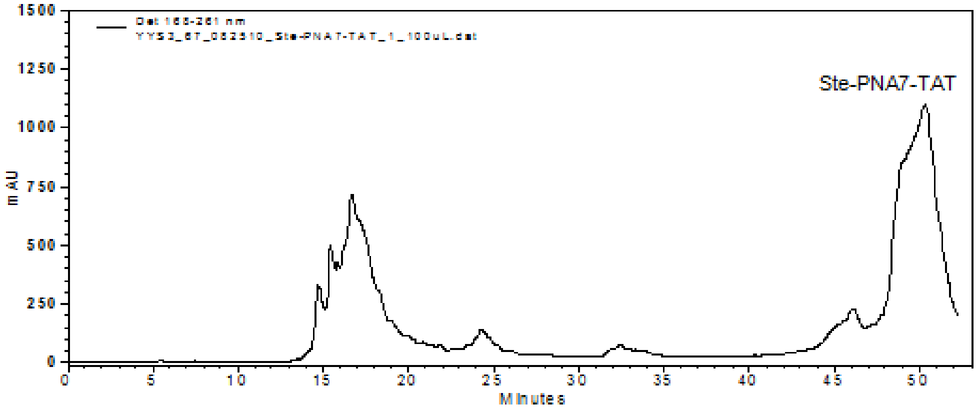

Figure A3.43 HPLC of Crude Ste-PNA7-TAT

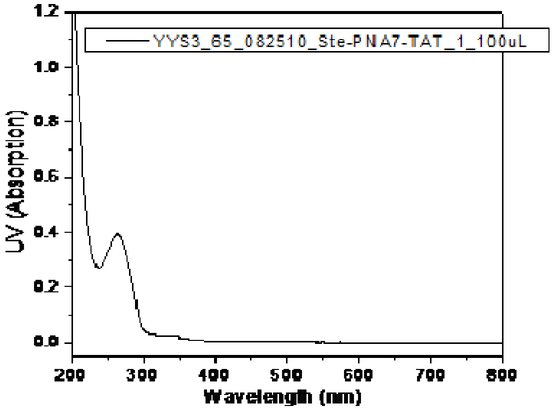

Figure A3.44 UV of Ste-PNA7-TAT

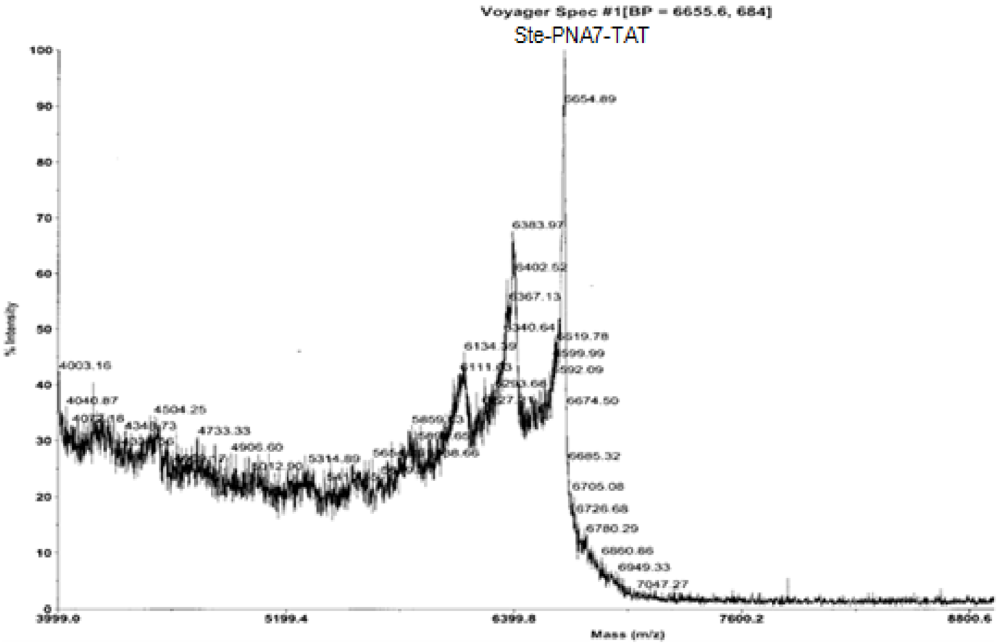

Figure A3.45 MALDI of Ste-PNA7-TAT

DLS, CMC

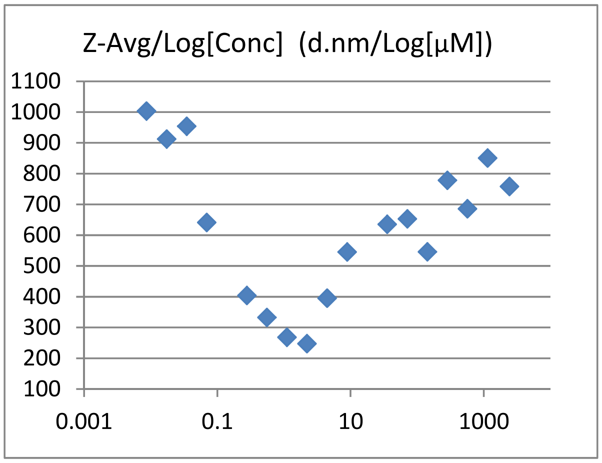

Figure A3.46 Lau-PNA50-TAT_DLS

Conc (µM)	Z-Ave (d.nm)	PdI
2417.382	758	0.685
1136.16954	850.5	0.628
568.08477	685.7	0.587
284.042385	778	0.614
142.021193	545.8	0.619
71.0105963	653	0.667
35.5052981	635.2	0.682
8.87632453	545.2	0.776
4.43816227	395.1	0.588
2.21908113	**247.4**	**0.481**
1.10954057	268.1	0.539
0.55477028	332.6	0.486
0.27738514	403.8	0.635
0.06934629	641	0.89
0.03467314	953.7	1
0.01733657	912.3	0.811
0.00866829	1003	0.947

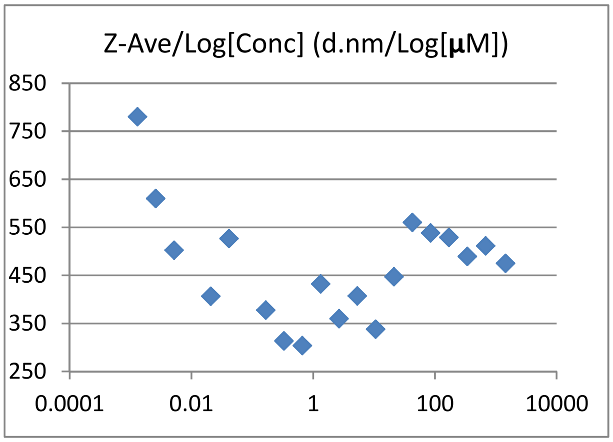

Figure A3.47 Ted-PNA50-TAT_DLS

Conc (µM)	Z-Ave (d.nm)	PdI
1445.538	475.2	0.724
679.40286	511.4	0.71
339.70143	489.6	0.578
169.850715	529	0.559
84.9253575	538.4	0.655
42.46267875	560.2	0.707
21.23133938	447.3	0.501
10.61566969	337.9	0.538
5.307834844	407.2	0.689
2.653917422	359.7	0.537
1.326958711	432.1	0.72
0.663479355	**303.9**	**0.586**
0.331739678	313.6	0.614
0.165869839	377.6	0.781
0.04146746	526.8	0.531
0.02073373	406.6	0.418
0.005183432	502.3	0.619
0.002591716	610	0.707
0.001295858	780.5	0.7

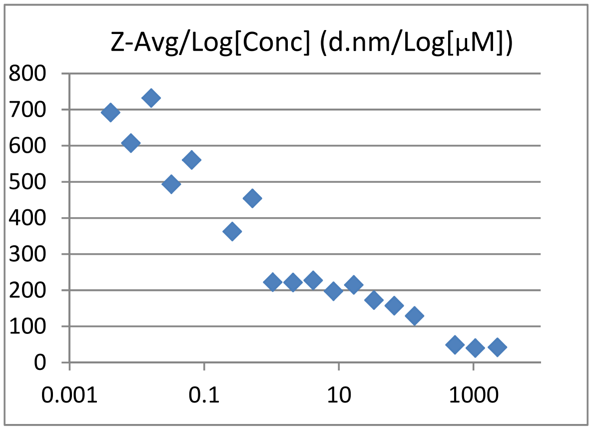

Figure A3.48 Pal-PNA50-TAT_DLS

Conc (µM)	Z-Ave (d.nm)	PdI
2269.25	42.26	1
1066.5475	39.93	1
533.27375	48.99	1
133.318438	128.8	0.473
66.6592188	157.5	0.423
33.3296094	172.9	0.39
16.6648047	215	0.393
8.33240234	197.4	0.371
4.16620117	227.2	0.437
2.08310059	221.5	0.369
1.04155029	**222.2**	**0.349**
0.52077515	454.1	0.491
0.26038757	362.5	0.365
0.06509689	560.8	0.507
0.03254845	493.3	0.452
0.01627422	732	0.873
0.00813711	607.4	0.549
0.00406856	691.9	0.542

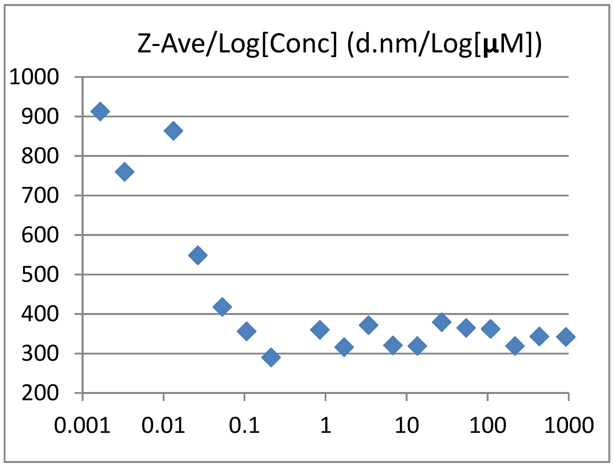

Figure A3.49 Ste-PNA50-TAT_DLS

Conc (μM)	Z-Ave (d.nm)	PdI
924.557	341.8	0.529
434.54179	343.2	0.46
217.270895	319.2	0.489
108.635448	362.3	0.405
54.3177238	364.7	0.49
27.1588619	379.3	0.477
13.5794309	319.2	0.557
6.78971547	320.5	0.523
3.39485773	371.6	0.501
1.69742887	316.2	0.602
0.84871443	359.7	0.594
0.21217861	**290.2**	**0.46**
0.1060893	356.2	0.512
0.05304465	417.8	0.612
0.02652233	548.5	0.684
0.01326116	863.4	0.785
0.00331529	759.8	0.827
0.00165765	912.6	0.739

Conc (μM)	Z-Ave (d.nm)	PdI
1517.346	94.53	0.531
713.15262	89.29	0.58
379.3365	94.16	0.389
178.288155	91.4	0.434
94.834125	82.8	0.31
44.57203875	89.22	0.368
23.70853125	82.13	0.313
11.14300969	86.97	0.323
5.927132813	87.51	0.297
2.785752422	92.49	0.264
1.481783203	100.1	0.279
0.696438105	103.3	0.316
0.370445801	103.2	0.29
0.174109526	105.9	0.308
0.09261145	119	0.397
0.043527382	**108.4**	**0.303**
0.023152863	152.8	0.395
0.010881845	162.7	0.377
0.005788216	143	0.461
0.002720461	170.9	0.42

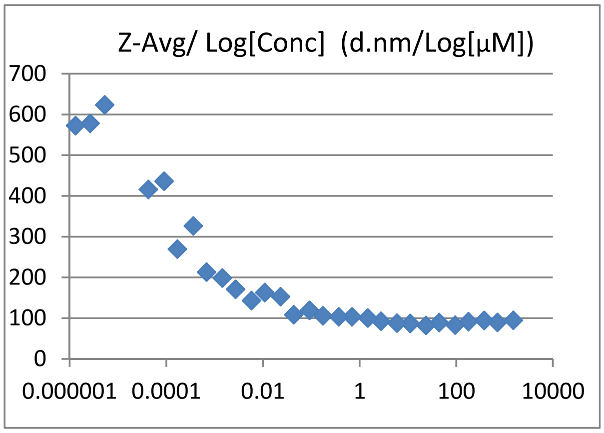

Figure A3.50 Lau-PNA5-TAT_DLS

0.001447054	198.6	0.426
0.000680115	212.7	0.465
0.000361763	326.3	0.545
0.000170029	269.4	0.51
9.04409E-05	435.9	0.74
4.25072E-05	415.9	0.693
5.3134E-06	623.4	0.802
2.6567E-06	577.8	0.601
1.32835E-06	572.3	0.687

Conc (μM)	Z-Ave (r. nm)	PdI
1514.769	91.21	0.579
711.94143	91.63	0.66
355.970715	96.73	0.772
177.9853575	90.13	0.428
88.99267875	81.02	0.458
44.49633938	77.23	0.372
22.24816969	79.31	0.275
11.12408484	84.26	0.239
5.562042422	94.8	0.354
2.781021211	96.58	0.383
1.390510605	93.28	0.287
0.695255303	106.1	0.325

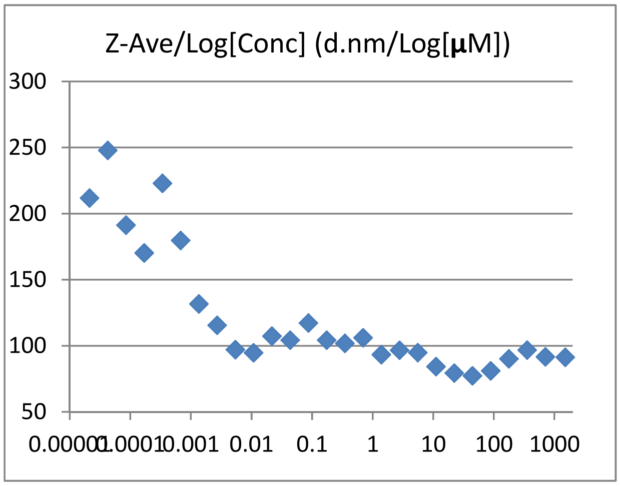

Figure A3.51 Ted-PNA5-TAT_DLS

0.347627651	101.9	0.293
0.173813826	104.2	0.284
0.086906913	117.2	0.395
0.043453456	104.2	0.298
0.021726728	107.3	0.354
0.010863364	**94.7**	**0.339**
0.005431682	97.02	0.406
0.002715841	115.5	0.345
0.001357921	131.7	0.428
0.00067896	179.7	0.541
0.00033948	222.9	0.535
0.00016974	170.2	0.467
8.487E-05	191.3	0.669
4.2435E-05	247.8	0.553
2.12175E-05	211.8	0.616

Conc (μM)	Z-Ave (r.nm)	PdI
1244.3	368.4	0.577
584.821	323.1	0.54
292.4105	336	0.542
146.20525	199.6	0.51
73.102625	155	0.55
36.5513125	158.8	0.51
18.2756563	179	0.617
9.13782813	184.2	0.53
4.56891406	185.3	0.632
2.28445703	182.7	0.572
1.14222852	**185.6**	**0.55**

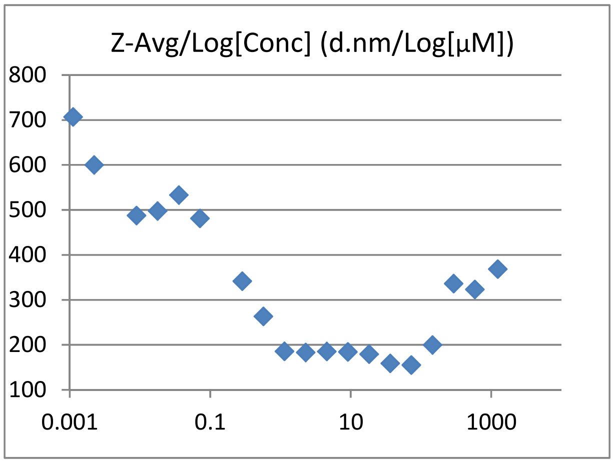

Figure A3.52 Pal-PNA5-TAT_DLS

0.57111426	263.1	0.481
0.28555713	341.4	0.586
0.07138928	481.1	0.653
0.03569464	532.9	0.64
0.01784732	497.5	0.692
0.00892366	487.6	0.73
0.00223092	600	0.846
0.00111546	706.9	0.855

Conc (μM)	Z-Ave (d.nm)	PdI
1349.9	142.3	0.775
634.453	126.3	0.882
317.2265	186.2	0.597
158.61325	174.9	0.589
79.306625	195.5	0.463
39.6533125	176.7	0.39
19.82665625	194.8	0.337
9.913328125	171.5	0.317
4.956664063	179.6	0.302
2.478332031	188.2	0.359
1.239166016	191.7	0.355

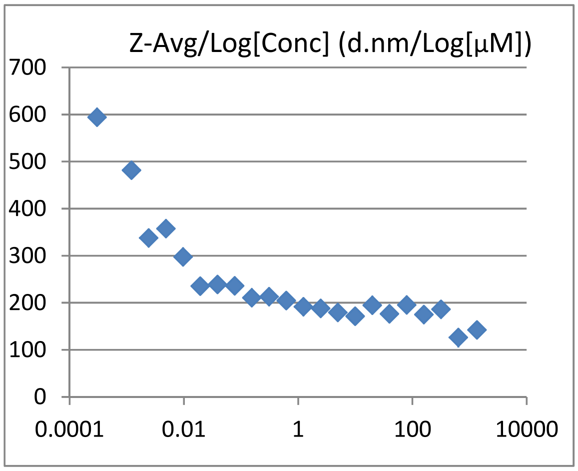

Figure A3.53 Ste-PNA5-TAT_DLS

0.619583008	204.9	0.36
0.309791504	213	0.331
0.154895752	**210.8**	**0.318**
0.077447876	236.2	0.392
0.038723938	239	0.405
0.019361969	235.4	0.399
0.009680984	297.5	0.43
0.004840492	357.8	0.433
0.002420246	337.7	0.457
0.001210123	481.8	0.514
0.000302531	594.4	0.65

Conc (μM)	Z-Ave (d.nm)	PdI
962.52	211.5	0.533
452.3844	142.7	0.932
113.0961	175.5	0.627
56.54805	224.1	0.689
28.274025	241.2	0.467
14.1370125	238.7	0.415
7.06850625	240.1	0.478
3.53425313	252.2	0.387
1.76712656	280.5	0.392
0.88356328	**260.1**	**0.396**
0.44178164	277.9	0.359
0.22089082	330.6	0.453

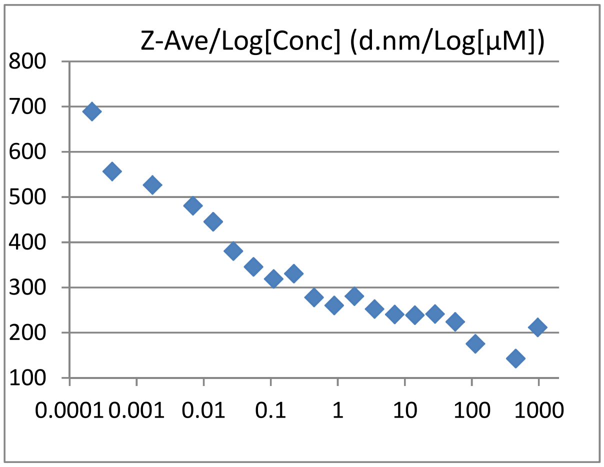

Figure A3.54 Ted-PNA7-TAT_DLS

0.11044541	318.9	0.473
0.05522271	345.4	0.475
0.02761135	380.5	0.397
0.01380568	445.2	0.511
0.00690284	480.6	0.654
0.00172571	526.4	0.527
0.00043143	556.3	0.543
0.00021571	689	0.611

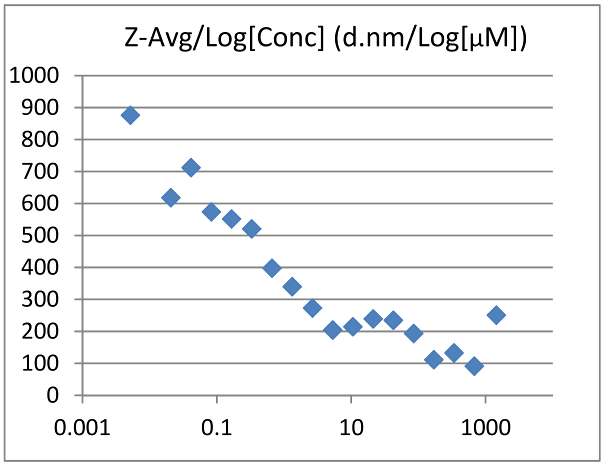

Figure A3.55 Pal-PNA7-TAT_DLS

Conc (µM)	Z-Ave (d.nm)	PdI
1443.9	250.7	0.436
678.633	91.11	0.774
339.3165	132.6	0.77
169.65825	111.3	0.925
84.829125	193	0.689
42.4145625	234.6	0.381
21.2072813	238.9	0.502
10.6036406	214.3	0.433
5.30182031	**204**	**0.151**
2.65091016	272.6	0.399
1.32545508	339.4	0.492
0.66272754	397.5	0.446
0.33136377	520.5	0.556
0.16568188	551.2	0.535
0.08284094	573.4	0.489
0.04142047	711.8	0.555
0.02071024	617.8	0.567
0.00517756	875.7	0.685

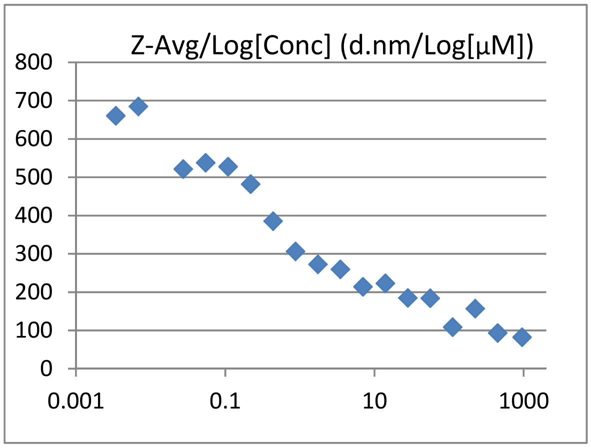

Figure A3.56 Ste-PNA7-TAT_DLS

Conc (µM)	Z-Ave (d.nm)	PdI
952.8	82.16	0.926
447.816	92.95	0.834
223.908	156.8	0.426
111.954	108.5	0.927
55.977	183.9	0.488
27.9885	**184.9**	**0.449**
13.99425	222.7	0.395
6.997125	**213.6**	**0.342**
3.4985625	259.5	0.401
1.74928125	272.3	0.543
0.87464063	306.2	0.433
0.43732031	385.3	0.664
0.21866016	481.8	0.504
0.10933008	527.6	0.514
0.05466504	537.8	0.545
0.02733252	521.1	0.503
0.00683313	684.7	0.585
0.00341656	660.4	0.639

Conc(µM)	I373/I383
0.073242	1.404998
0.073242	1.403494
0.146484	1.39044
0.292969	1.386537

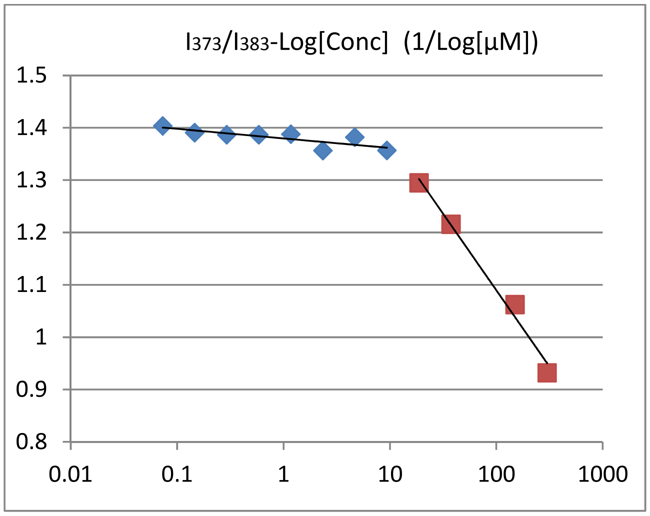

Figure A3.57 Lau-PNA50-TAT_CMC_without NaCl

0.585936	1.386483
1.171875	1.38756
2.34375	1.356266
4.6875	1.381842
9.375	1.356513
18.75	1.294857
37.5	1.215593
150	1.062168
300	0.931826

Conc (µM)	I373/I383
0.073242	1.413549
0.146484	1.410754
0.292969	1.416197
0.585936	1.405095
1.171875	1.399434
2.34375	1.41277
4.6875	1.398416
9.375	1.404099
18.75	1.337945

37.5	1.177535
75	1.051559
150	0.952677
300	0.857981

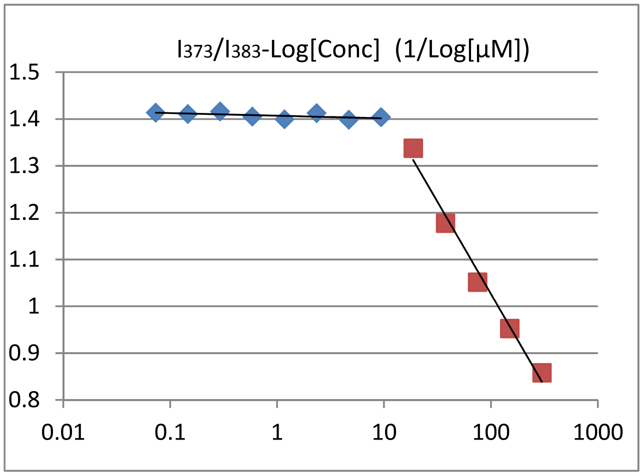

Figure A3.58 Lau-PNA50-TAT_CMC_with NaCl

Conc(µM)	I373/I383
0.109863	1.340022
0.219727	1.344872
0.439453	1.340209
0.878906	1.35444
1.757813	1.349269
3.515625	1.325332
7.03125	1.356878
14.0625	1.316379

28.125	1.238023
56.25	1.010434
112.5	0.791126
225	0.672177

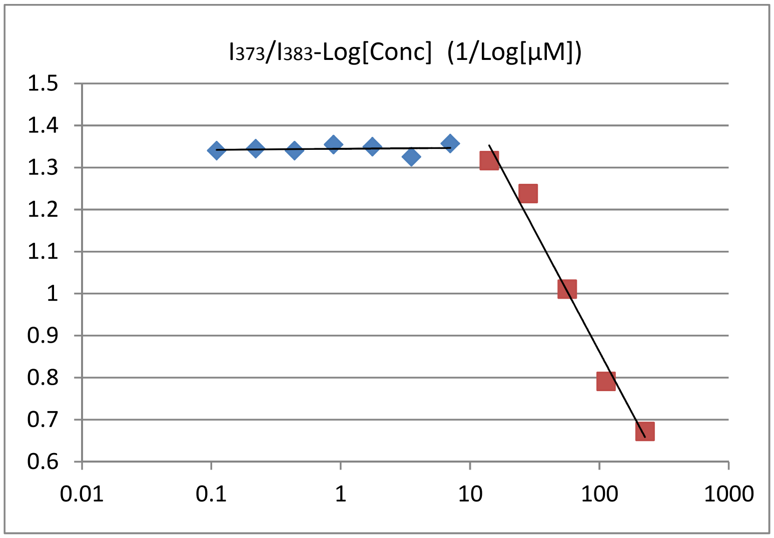

Figure A3.59 Ted-PNA50-TAT_CMC_without NaCl

Conc(µM)	I373/I383
0.054932	1.396002
0.109863	1.429219
0.219727	1.403175
0.439453	1.412767
0.878906	1.43128

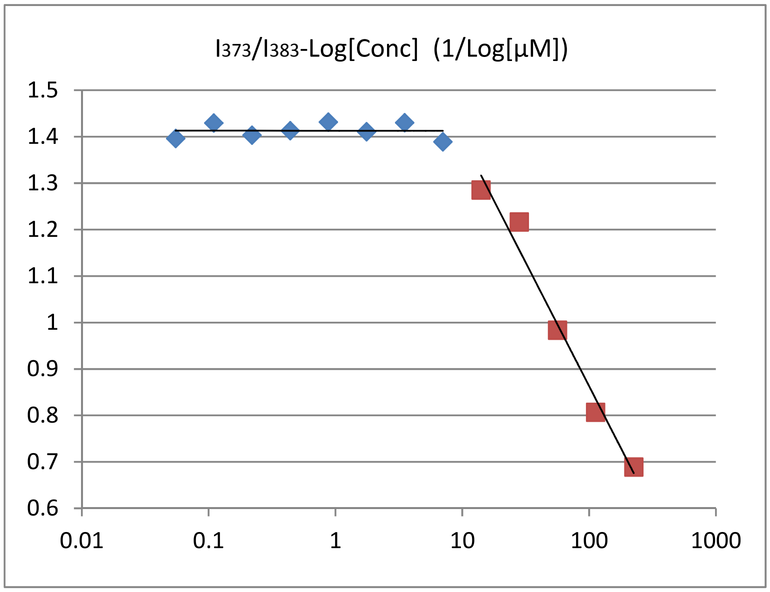

1.757813	1.41046
3.515625	1.429787
7.03125	1.388973
14.0625	1.285161
28.125	1.216224
56.25	0.983569
112.5	0.806825
225	0.689082

Figure A3.60 Ted-PNA50-TAT_CMC_with NaCl

Conc(μM)	I373/I383
0.073242	1.556521
0.146484	1.52818
0.292969	1.538579
0.585938	1.559674
1.171188	1.541349
2.34375	1.530526
4.6875	1.557907
9.375	1.542227

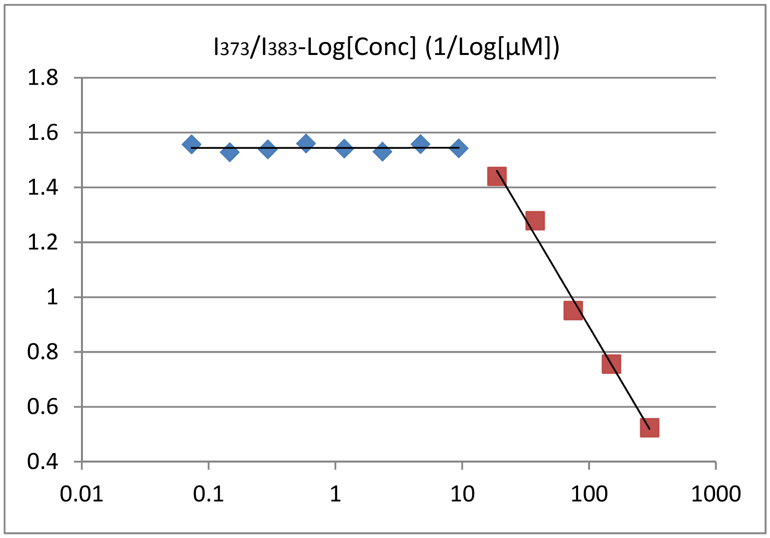

18.75	1.440106
37.5	1.278774
75	0.951462
150	0.755962
300	0.524218

Figure A3.61 Pal-PNA50-TAT_CMC_without NaCl

Conc(µM)	I373/I383
0.073242	1.491407
0.146484	1.501707
0.292969	1.529079
0.585938	1.528324
1.171188	1.485904
2.34375	1.503573

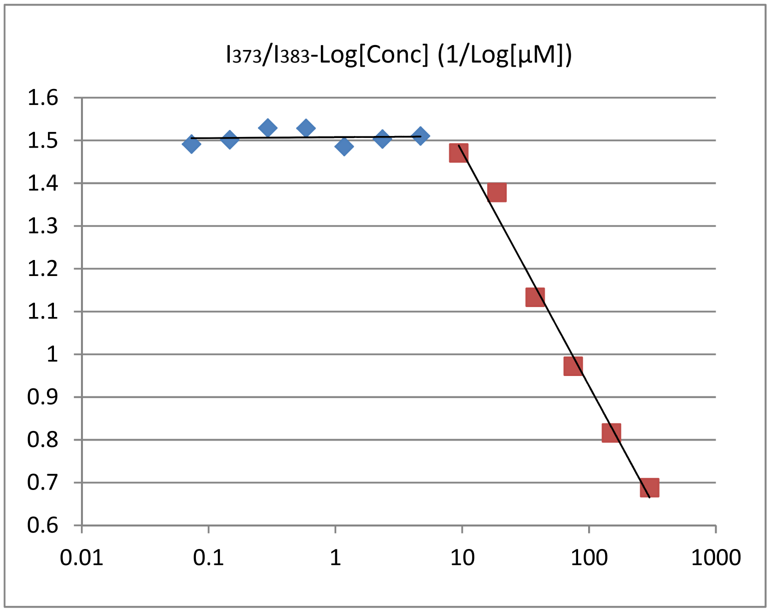

4.6875	1.510682
9.375	1.471018
18.75	1.378507
37.5	1.133297
75	0.972155
150	0.816353
300	0.687906

Figure A3.62 Pal-PNA50-TAT_CMC_with NaCl

Conc(μM)	I373/I383
0.036621	1.546954
0.073242	1.538435
0.146484	1.552924
0.292969	1.529204
0.585938	1.544755
1.171875	1.548352
2.34375	1.529075
4.6875	1.52951

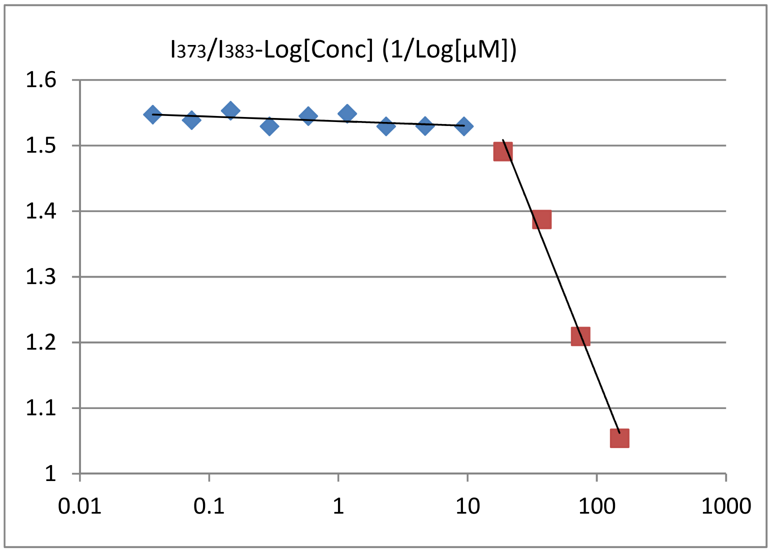

9.375	1.529084
18.75	1.490792
37.5	1.387451
75	1.209281
150	1.053989

Figure A3.63 Ste-PNA50-TAT_CMC_without NaCl

Conc(µM)	I373/I383
0.036621	1.580941
0.073242	1.57357
0.146484	1.580962
0.292969	1.535655
0.585938	1.52839
1.171875	1.5258
2.34375	1.521326

4.6875	1.541627
9.375	1.506571
18.75	1.365271
37.5	1.038377
75	0.819959
150	0.633239

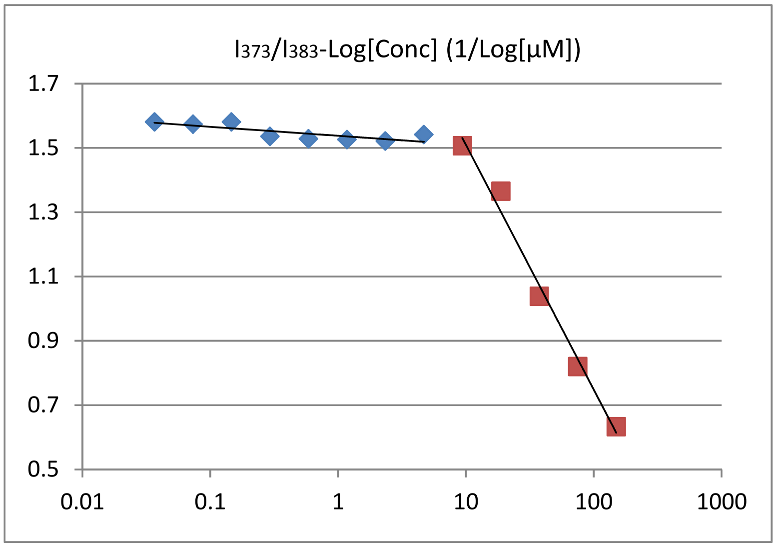

Figure A3.64 Ste-PNA50-TAT_CMC_with NaCl

Conc(µM)	I373/I383
0.073242	1.51946
0.146484	1.476673
0.292969	1.478724
0.585938	1.476153
1.171875	1.483842
2.34375	1.457541
4.6875	1.438296

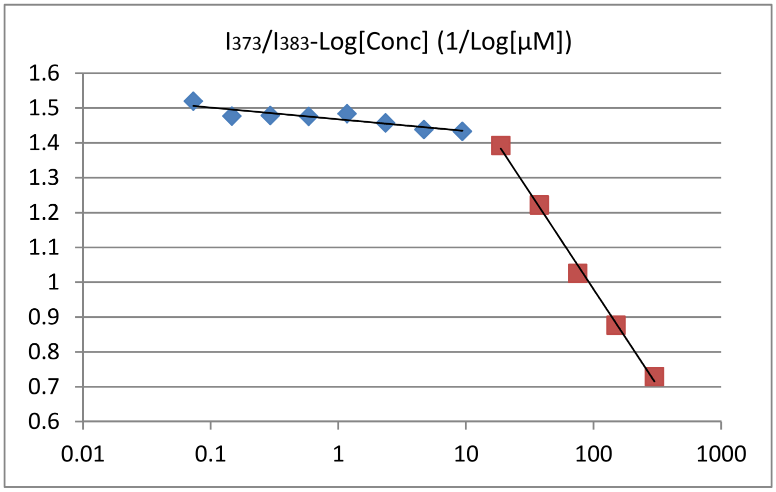

9.375	1.433204
18.75	1.392636
37.5	1.221884
75	1.025795
150	0.877138
300	0.72958

Figure A3.65 Lau-PNA5-TAT_CMC_without NaCl

Conc(µM)	I373/I383
0.073242	1.472441
0.146484	1.468961
0.292969	1.50234
0.585938	1.467566
1.171875	1.441925
2.34375	1.482727

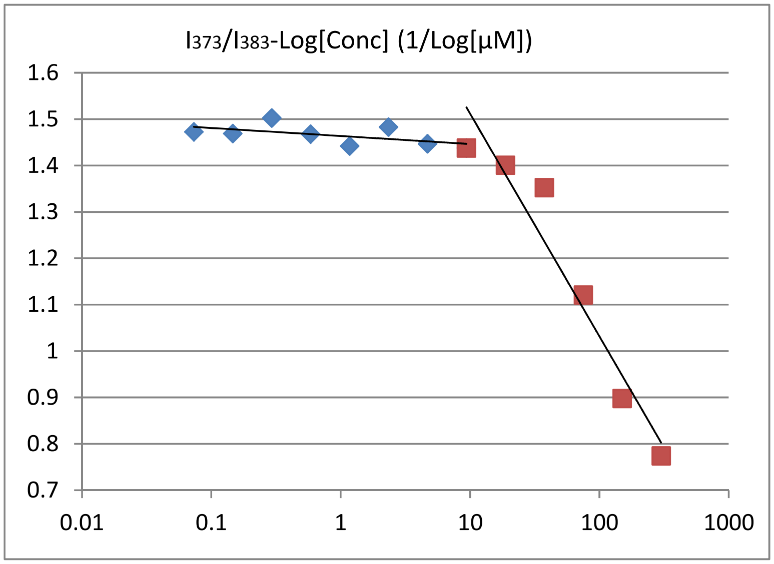

4.6875	1.446814
9.375	1.437899
18.75	1.400976
37.5	1.352408
75	1.120911
150	0.897925
300	0.773937

Figure A3.66 Lau-PNA5-TAT_CMC_with NaCl

Conc(μM)	I373/I383
0.036621	1.372476
0.073242	1.358689
0.146484	1.361572
0.292969	1.372267
0.585938	1.342976
2.34375	1.335562
4.6875	1.316505

9.375	1.321656
18.75	1.28829
37.5	1.180975
75	0.996703
150	0.853303

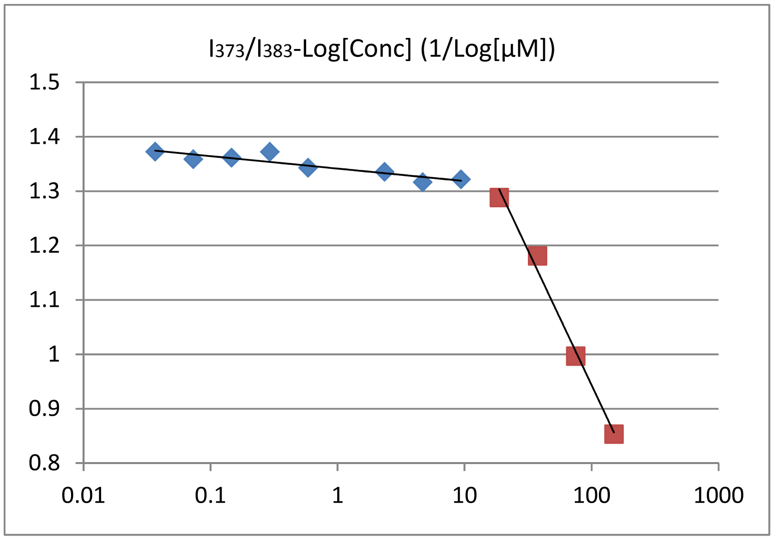

Figure A3.67 Ted-PNA5-TAT_CMC_without NaCl

Conc(μM)	I373/I383
0.073242	1.501411
0.146484	1.524147
0.292969	1.477427
0.585938	1.50338
1.171875	1.485371
2.34375	1.476161
4.6875	1.490786

9.375	1.449708
18.75	1.360025
37.5	1.180808
75	0.922754
150	0.749952

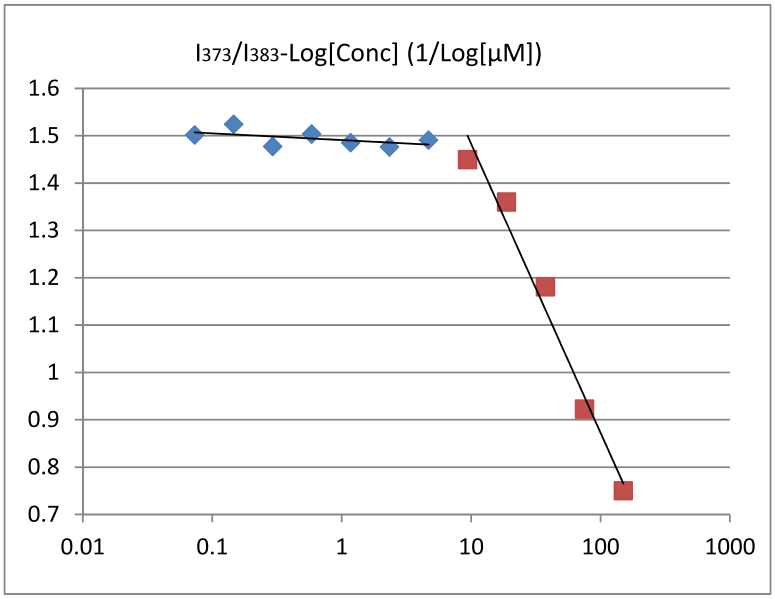

Figure A3.68 Ted-PNA5-TAT_CMC_with NaCl

Conc(μM)	I373/I383
0.061035	1.382814
0.12207	1.42456
0.244141	1.407194
0.488281	1.335691
0.976563	1.337416
1.953125	1.31787
3.90625	1.337039
7.8125	1.346432

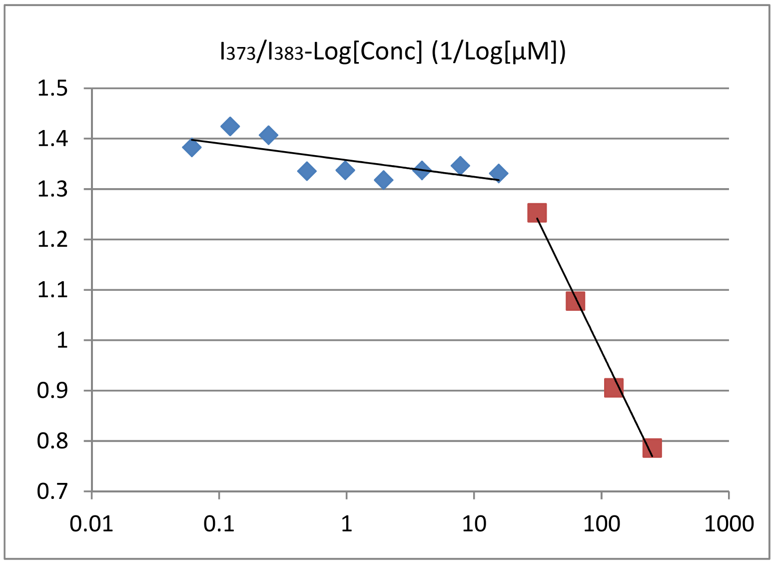

15.625	1.331061
31.25	1.253025
62.5	1.078024
125	0.9058
250	0.786331

Figure A3.69 Pal-PNA5-TAT_CMC_without NaCl

Conc(µM)	I373/I383
0.061035	1.42754
0.12207	1.448865
0.244141	1.446877
0.488281	1.417716
0.976563	1.452516
1.953125	1.431694
3.90625	1.406524

7.8125	1.416878
15.625	1.30522
31.25	1.119771
62.5	1.001058
125	0.84131
250	0.747721

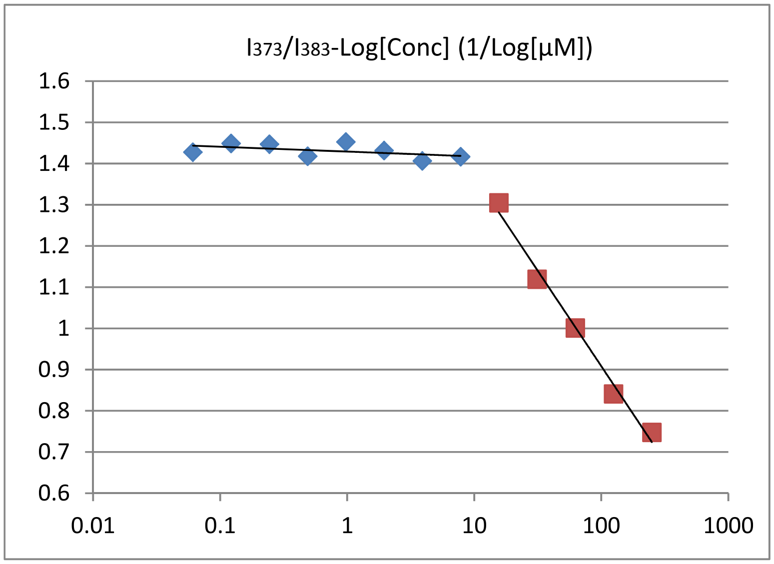

Figure A3.70 Pal-PNA5-TAT_CMC_with NaCl

Conc(μM)	I373/I383
0.073242	1.414205
0.146484	1.397047
0.292969	1.39251
0.585938	1.382898
1.171875	1.381357
2.34375	1.363379
4.6875	1.369738
9.375	1.358316

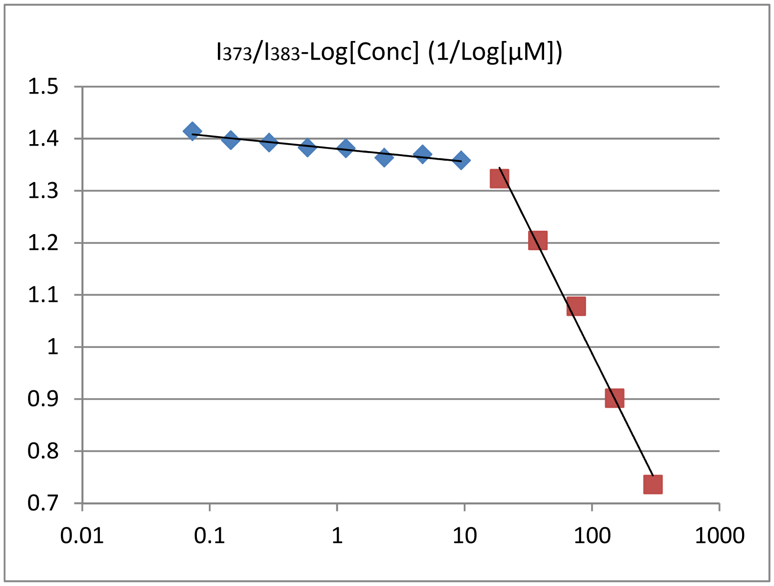

18.75	1.323311
37.5	1.204597
75	1.07821
150	0.901711
300	0.735917

Figure A3.71 Ste-PNA5-TAT_CMC_without NaCl

Conc(µM)	I373/I383
0.073242	1.473574
0.146484	1.437582
0.292969	1.457236
0.585938	1.481257
1.171875	1.471057
2.34375	1.4422
4.6875	1.452284

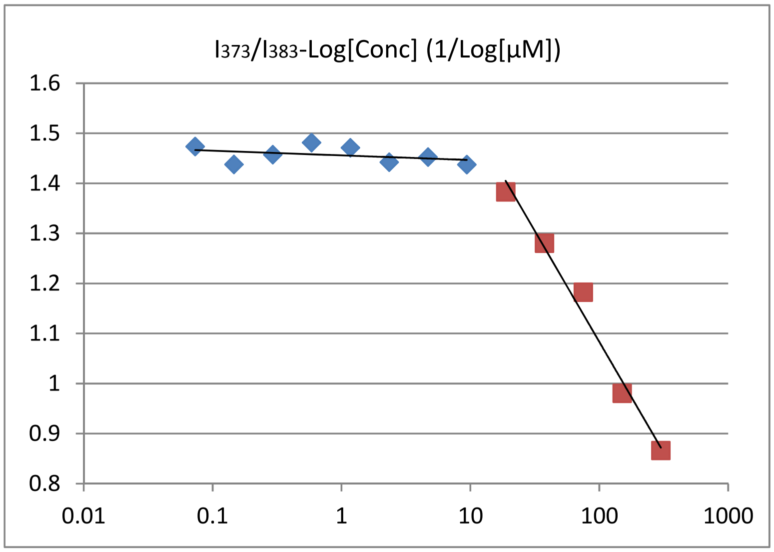

9.375	1.43741
18.75	1.382907
37.5	1.280299
75	1.182513
150	0.980553
300	0.866199

Figure A3.72 Ste-PNA5-TAT_CMC_with NaCl

Conc(μM)	I373/I383
0.048828	1.407267
0.097656	1.415206
0.195313	1.394877
0.390625	1.39321
0.78125	1.385847
1.5625	1.389588
3.125	1.385841

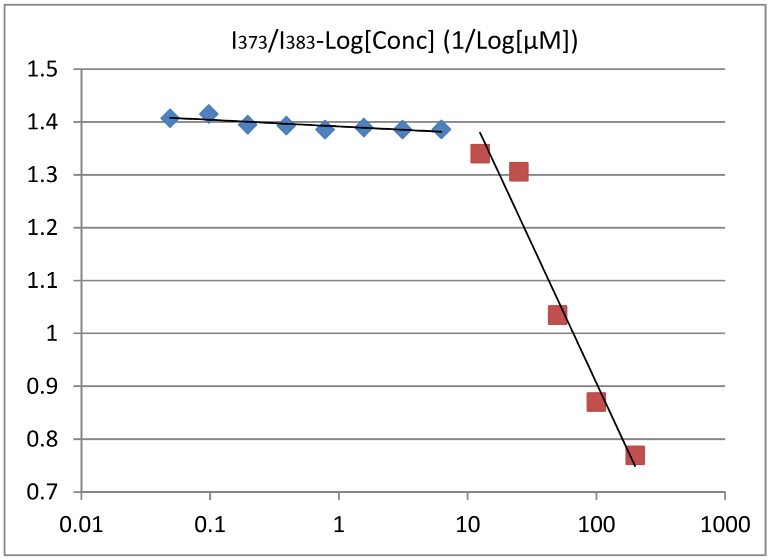

6.25	1.38606
12.5	1.340232
25	1.306131
50	1.034889
100	0.870455
200	0.769697

Figure A3.73 Ted-PNA7-TAT_CMC_without NaCl

Conc(µM)	I373/I383
0.048828	1.469491
0.097656	1.409112
0.195313	1.479408
0.390625	1.456333
0.78125	1.457504
1.5625	1.451384
3.125	1.44017

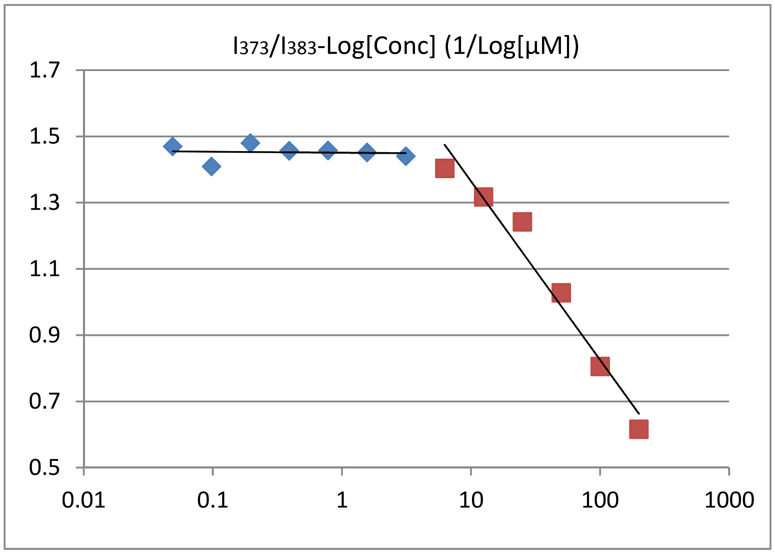

6.25	1.403456
12.5	1.317163
25	1.242415
50	1.028183
100	0.805606
200	0.615911

Figure A3.74 Ted-PNA7-TAT_CMC_with NaCl

Conc(μM)	I373/I383
0.12207	1.373276
0.244141	1.360979
0.488281	1.348214
0.976563	1.323253
1.953125	1.325216
3.90625	1.324751
7.8125	1.319098

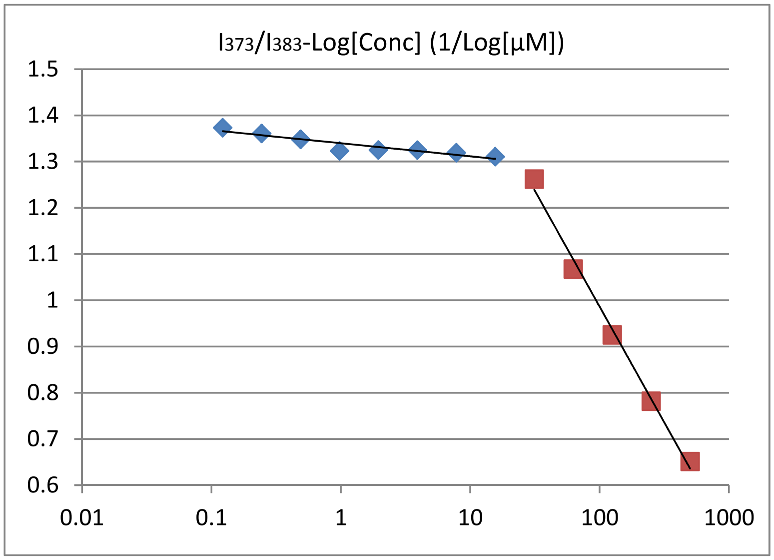

15.625	1.310729
31.25	1.262326
62.5	1.067739
125	0.925072
250	0.781648
500	0.651409

Figure A3.75 Pal-PNA7-TAT_CMC_without NaCl

Conc(μM)	I373/I383
0.12207	1.385098
0.244141	1.415289
0.488281	1.411881
0.976563	1.382267
1.953125	1.401636
3.90625	1.384779
7.8125	1.378799

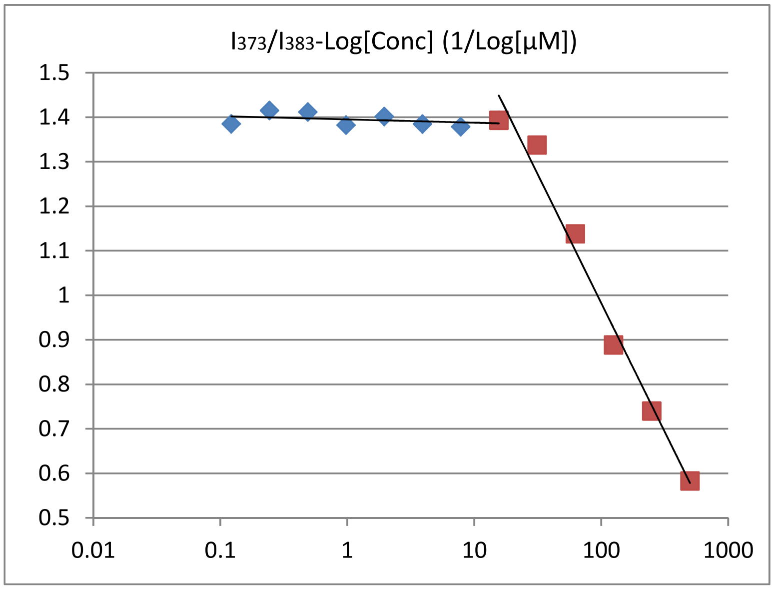

15.625	1.393228
31.25	1.337793
62.5	1.138196
125	0.888779
250	0.740145
500	0.582866

Figure A3.76 Pal-PNA7-TAT_CMC_with NaCl

Conc(μM)	I373/I383
0.048828	1.444417
0.097656	1.444014
0.195313	1.438119
0.390625	1.43887
0.78125	1.425487
1.5625	1.419644
3.125	1.406051
6.25	1.406568

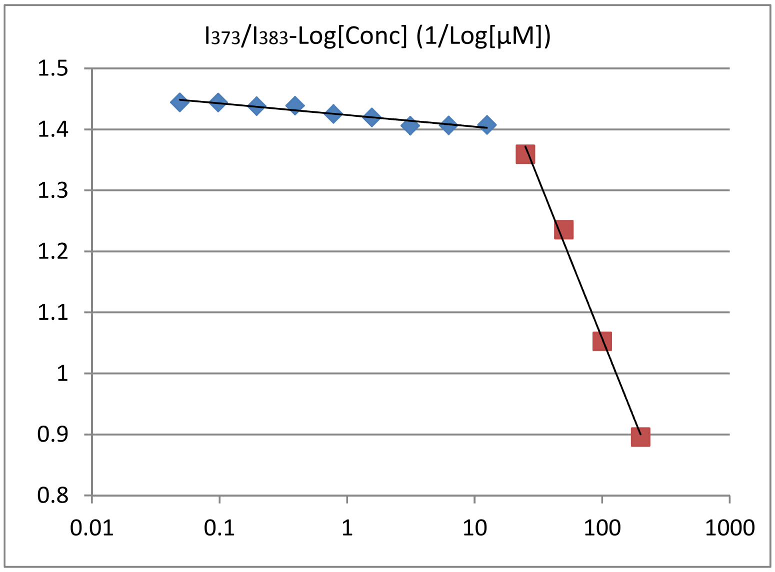

12.5	1.407357
25	1.35944
50	1.235891
100	1.052852
200	0.895853

Figure A3.77 Ste-PNA7-TAT_CMC_without NaCl

Conc(μM)	I373/I383
0.048828	1.480655
0.097656	1.451629
0.195313	1.462045
0.390625	1.468321
0.78125	1.439608
1.5625	1.472842

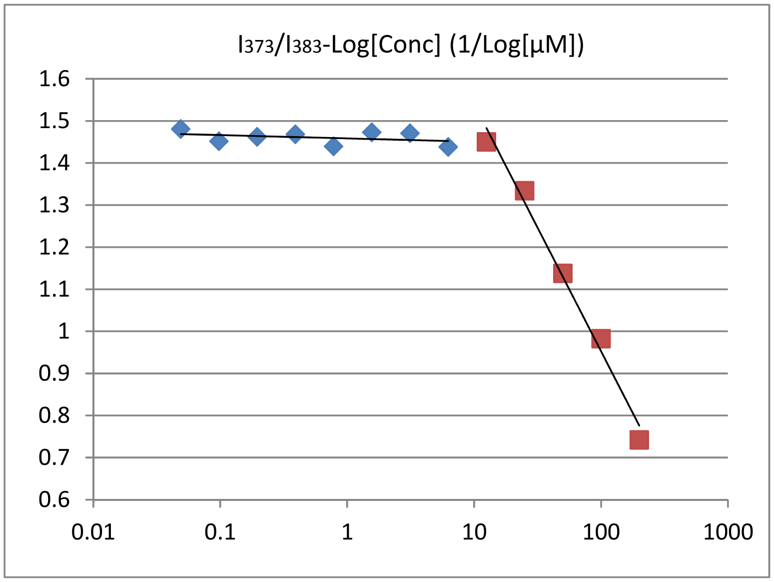

3.125	1.470755
6.25	1.438181
12.5	1.450423
25	1.334262
50	1.137911
100	0.982921
200	0.742168

Figure A3.78 Ste-PNA7-TAT_CMC_with NaCl

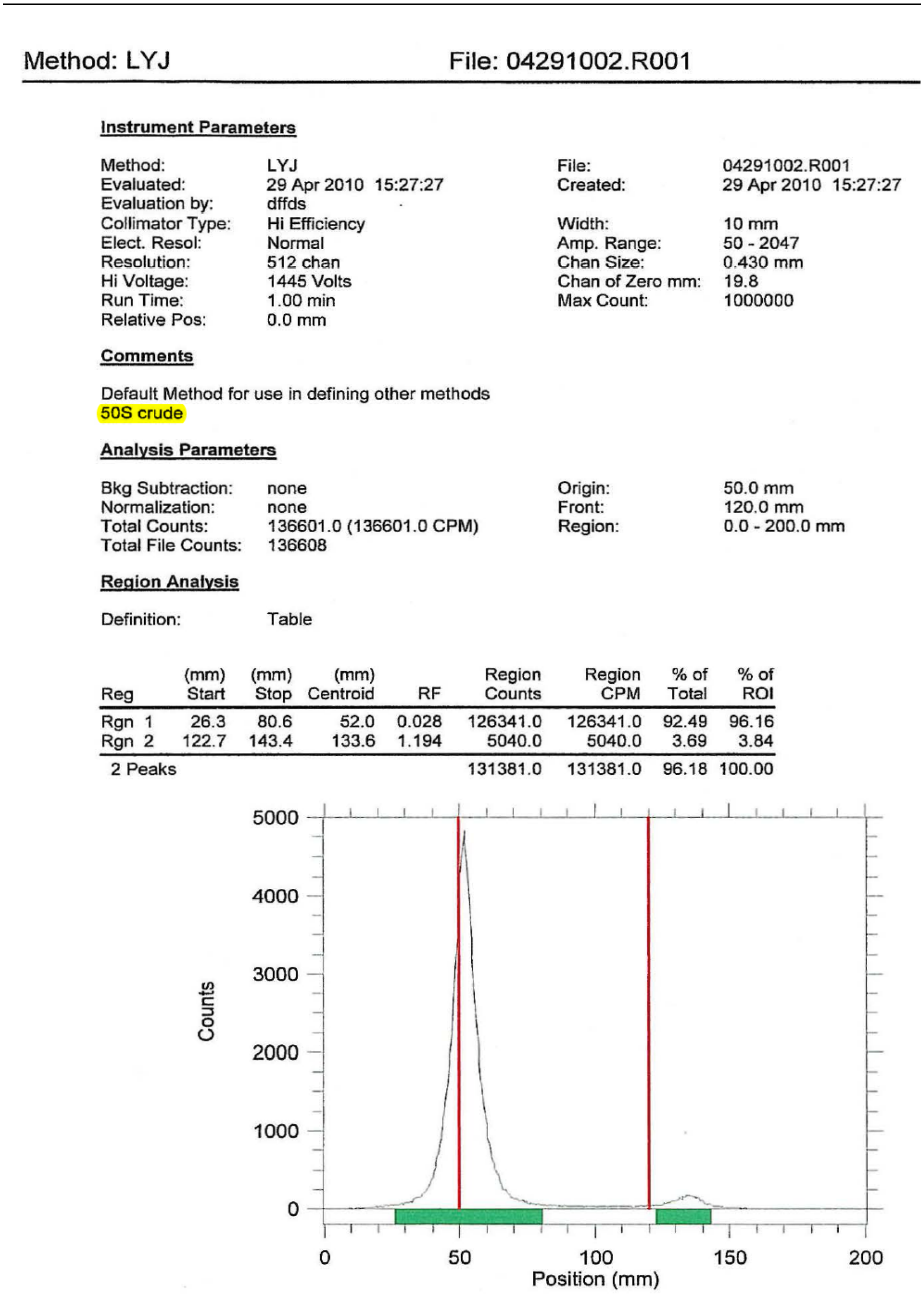

Method: LYJ File: 04291002.R001

Instrument Parameters

Method:	LYJ	File:	04291002.R001
Evaluated:	29 Apr 2010 15:27:27	Created:	29 Apr 2010 15:27:27
Evaluation by:	dffds		
Collimator Type:	Hi Efficiency	Width:	10 mm
Elect. Resol:	Normal	Amp. Range:	50 - 2047
Resolution:	512 chan	Chan Size:	0.430 mm
Hi Voltage:	1445 Volts	Chan of Zero mm:	19.8
Run Time:	1.00 min	Max Count:	1000000
Relative Pos:	0.0 mm		

Comments

Default Method for use in defining other methods
50S crude

Analysis Parameters

Bkg Subtraction:	none	Origin:	50.0 mm
Normalization:	none	Front:	120.0 mm
Total Counts:	136601.0 (136601.0 CPM)	Region:	0.0 - 200.0 mm
Total File Counts:	136608		

Region Analysis

Definition: Table

Reg	(mm) Start	(mm) Stop	(mm) Centroid	RF	Region Counts	Region CPM	% of Total	% of ROI
Rgn 1	26.3	80.6	52.0	0.028	126341.0	126341.0	92.49	96.16
Rgn 2	122.7	143.4	133.6	1.194	5040.0	5040.0	3.69	3.84
2 Peaks					131381.0	131381.0	96.18	100.00

Figure A3.79 TLC of Br-76 Radiolabling of Pal-PNA50S-TAT conjugate

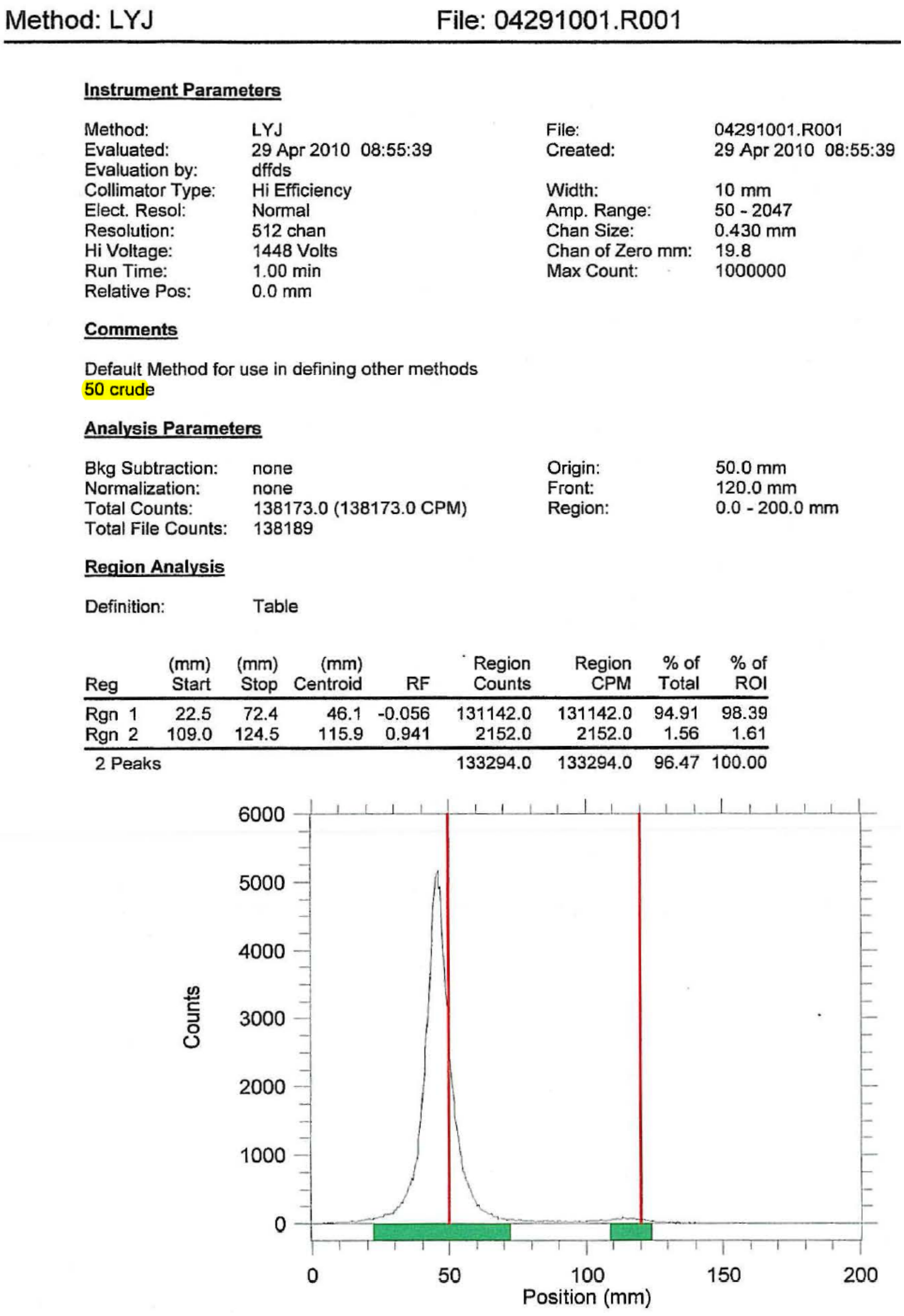

Method: LYJ File: 04291001.R001

Instrument Parameters

Method: LYJ
Evaluated: 29 Apr 2010 08:55:39
Evaluation by: dffds
Collimator Type: Hi Efficiency
Elect. Resol: Normal
Resolution: 512 chan
Hi Voltage: 1448 Volts
Run Time: 1.00 min
Relative Pos: 0.0 mm

File: 04291001.R001
Created: 29 Apr 2010 08:55:39
Width: 10 mm
Amp. Range: 50 - 2047
Chan Size: 0.430 mm
Chan of Zero mm: 19.8
Max Count: 1000000

Comments

Default Method for use in defining other methods
50 crude

Analysis Parameters

Bkg Subtraction: none
Normalization: none
Total Counts: 138173.0 (138173.0 CPM)
Total File Counts: 138189

Origin: 50.0 mm
Front: 120.0 mm
Region: 0.0 - 200.0 mm

Region Analysis

Definition: Table

Reg	(mm) Start	(mm) Stop	(mm) Centroid	RF	Region Counts	Region CPM	% of Total	% of ROI
Rgn 1	22.5	72.4	46.1	-0.056	131142.0	131142.0	94.91	98.39
Rgn 2	109.0	124.5	115.9	0.941	2152.0	2152.0	1.56	1.61
2 Peaks					133294.0	133294.0	96.47	100.00

Figure A3.80 TLC of Br-76 Radiolabling of Pal-PNA50-TAT conjugate

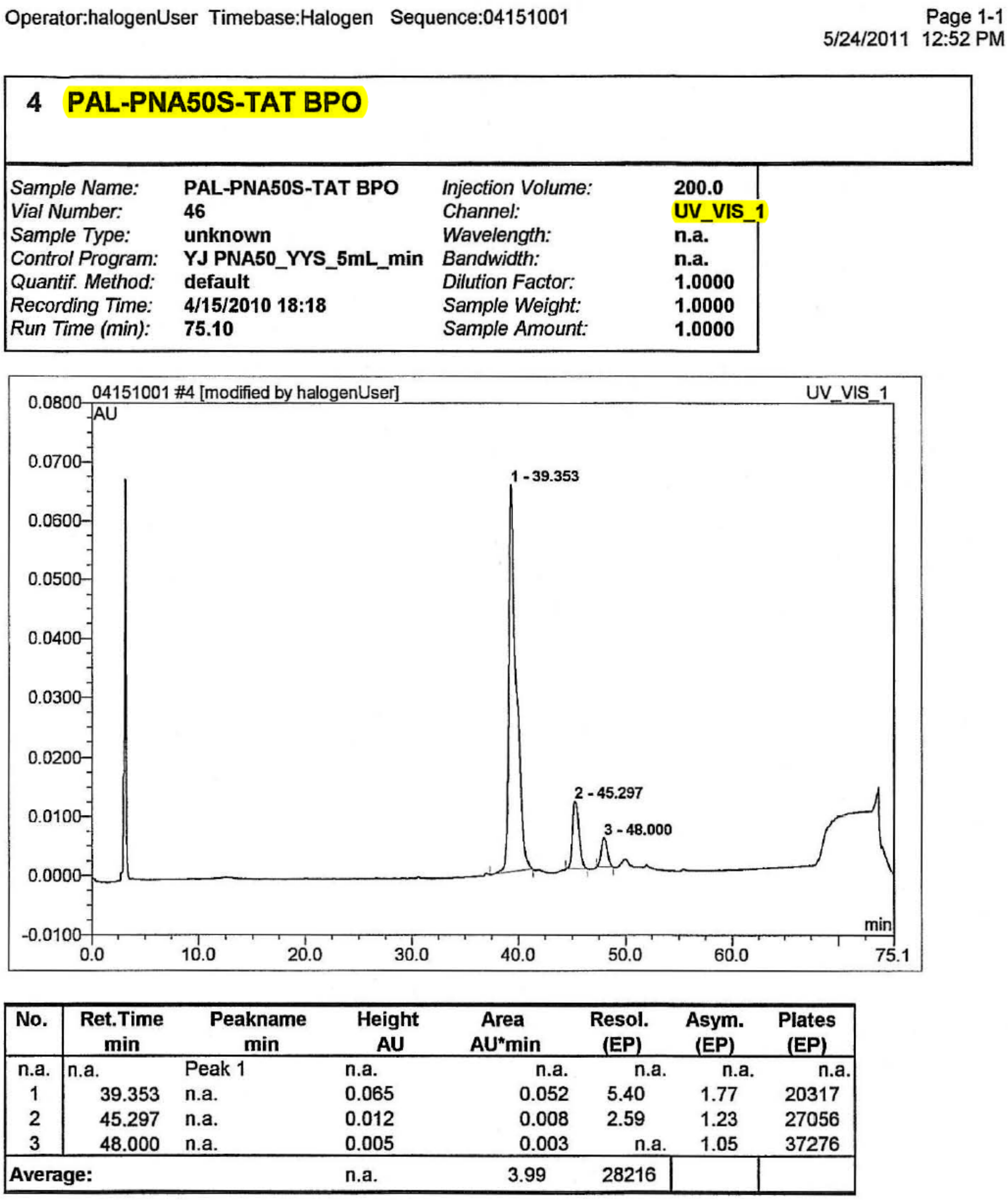

Operator:halogenUser Timebase:Halogen Sequence:04151001

Page 1-1
5/24/2011 12:52 PM

4 PAL-PNA50S-TAT BPO

Sample Name:	**PAL-PNA50S-TAT BPO**	*Injection Volume:*	**200.0**
Vial Number:	**46**	*Channel:*	**UV_VIS_1**
Sample Type:	**unknown**	*Wavelength:*	**n.a.**
Control Program:	**YJ PNA50_YYS_5mL_min**	*Bandwidth:*	**n.a.**
Quantif. Method:	**default**	*Dilution Factor:*	**1.0000**
Recording Time:	**4/15/2010 18:18**	*Sample Weight:*	**1.0000**
Run Time (min):	**75.10**	*Sample Amount:*	**1.0000**

No.	Ret.Time min	Peakname min	Height AU	Area AU*min	Resol. (EP)	Asym. (EP)	Plates (EP)
n.a.	n.a.	Peak 1	n.a.	n.a.	n.a.	n.a.	n.a.
1	39.353	n.a.	0.065	0.052	5.40	1.77	20317
2	45.297	n.a.	0.012	0.008	2.59	1.23	27056
3	48.000	n.a.	0.005	0.003	n.a.	1.05	37276
Average:			n.a.	3.99	28216		

Figure A3.81 HPLC of Br-76 Radiolabling of Pal-PNA50S-TAT conjugate, detected with UV-vis

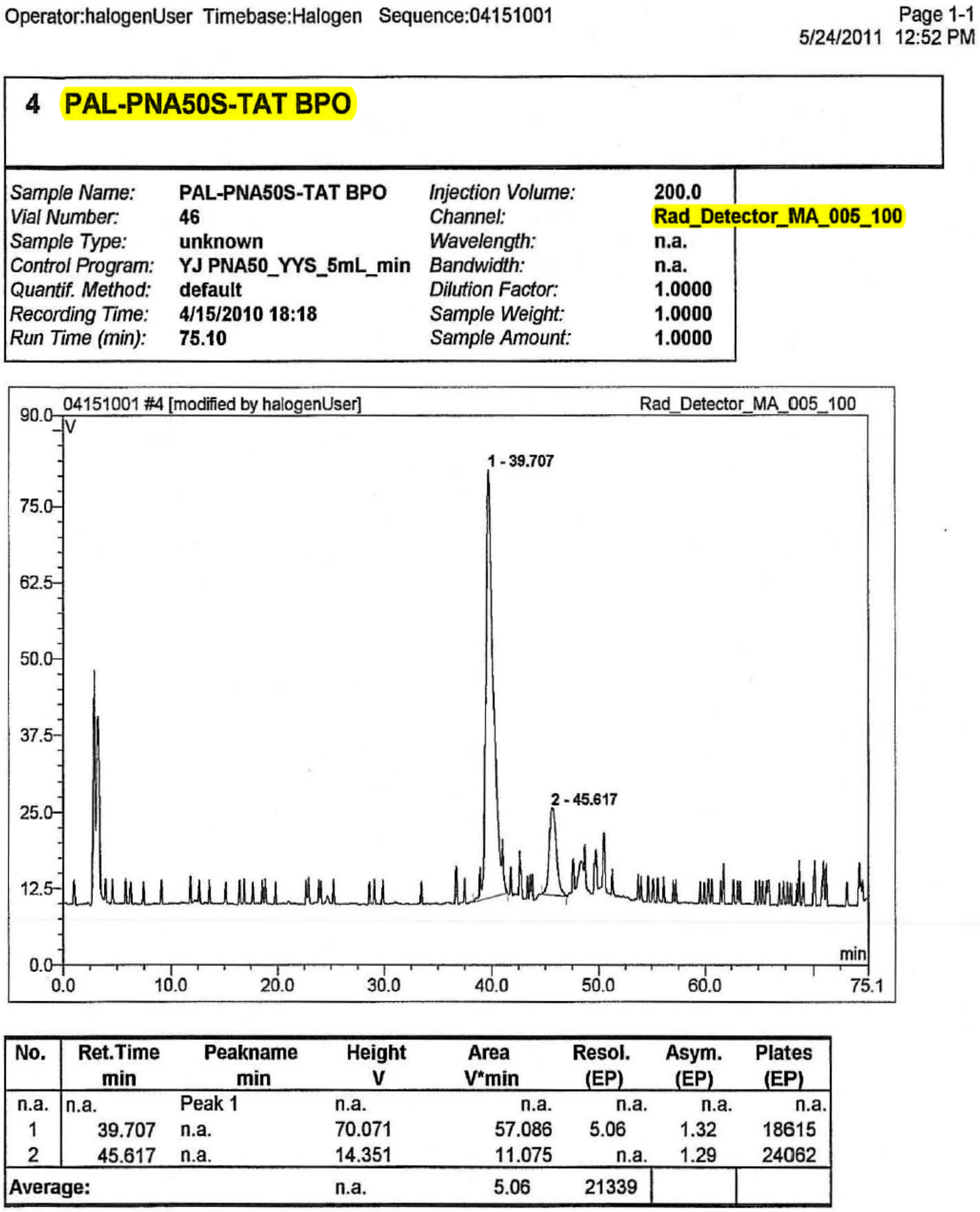

Operator:halogenUser Timebase:Halogen Sequence:04151001

Page 1-1
5/24/2011 12:52 PM

4 PAL-PNA50S-TAT BPO

Sample Name:	**PAL-PNA50S-TAT BPO**	*Injection Volume:*	**200.0**
Vial Number:	**46**	*Channel:*	**Rad_Detector_MA_005_100**
Sample Type:	**unknown**	*Wavelength:*	**n.a.**
Control Program:	**YJ PNA50_YYS_5mL_min**	*Bandwidth:*	**n.a.**
Quantif. Method:	**default**	*Dilution Factor:*	**1.0000**
Recording Time:	**4/15/2010 18:18**	*Sample Weight:*	**1.0000**
Run Time (min):	**75.10**	*Sample Amount:*	**1.0000**

No.	Ret.Time min	Peakname min	Height V	Area V*min	Resol. (EP)	Asym. (EP)	Plates (EP)
n.a.	n.a.	Peak 1	n.a.	n.a.	n.a.	n.a.	n.a.
1	39.707	n.a.	70.071	57.086	5.06	1.32	18615
2	45.617	n.a.	14.351	11.075	n.a.	1.29	24062
Average:			n.a.	5.06	21339		

Figure A3.82 HPLC of Br-76 Radiolabling of Pal-PNA50S-TAT conjugate, detected with Radioactivity

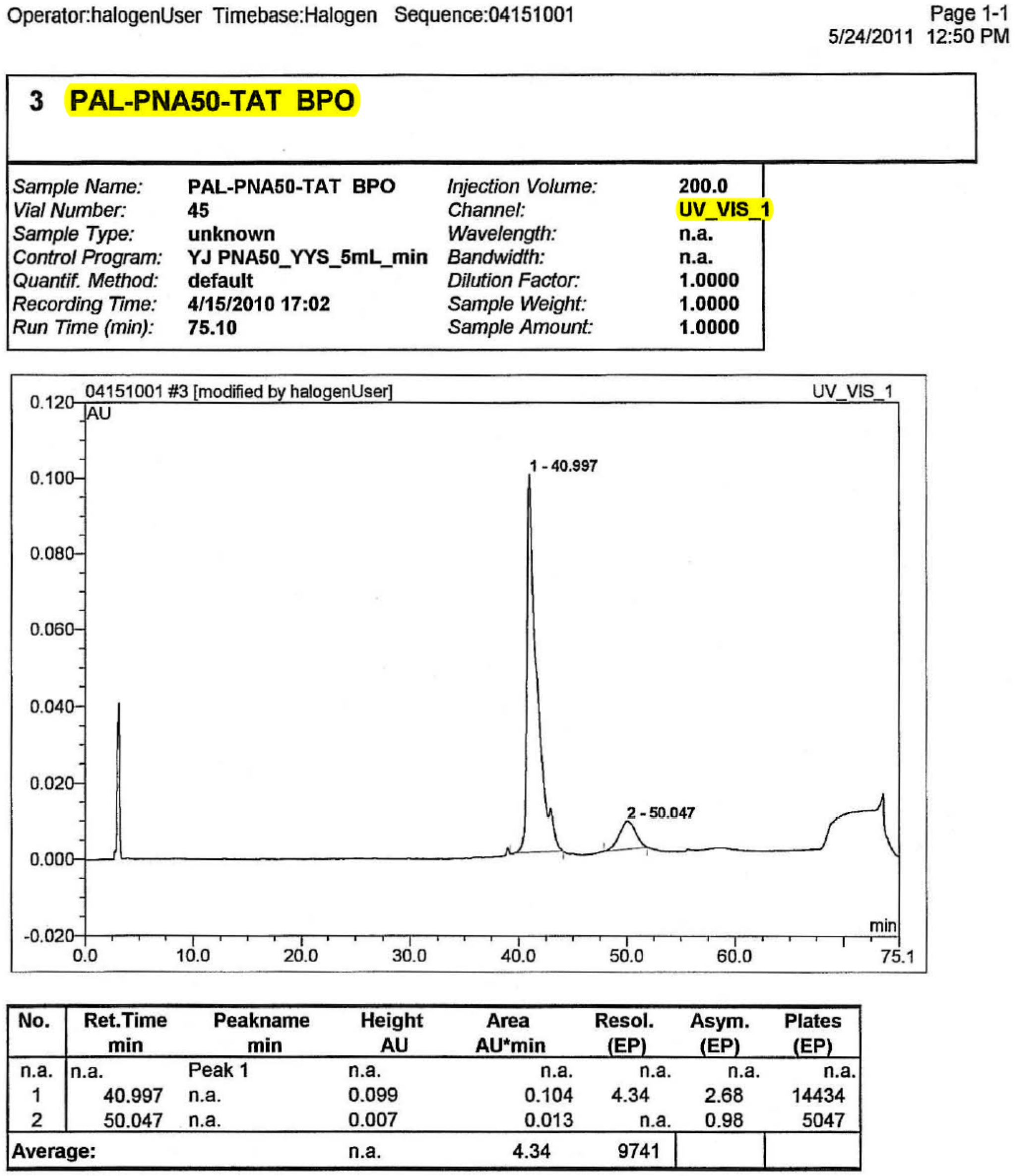

Operator:halogenUser Timebase:Halogen Sequence:04151001

Page 1-1
5/24/2011 12:50 PM

3 PAL-PNA50-TAT BPO

Sample Name:	**PAL-PNA50-TAT BPO**	*Injection Volume:*	**200.0**
Vial Number:	**45**	*Channel:*	**UV_VIS_1**
Sample Type:	**unknown**	*Wavelength:*	**n.a.**
Control Program:	**YJ PNA50_YYS_5mL_min**	*Bandwidth:*	**n.a.**
Quantif. Method:	**default**	*Dilution Factor:*	**1.0000**
Recording Time:	**4/15/2010 17:02**	*Sample Weight:*	**1.0000**
Run Time (min):	**75.10**	*Sample Amount:*	**1.0000**

No.	Ret.Time min	Peakname min	Height AU	Area AU*min	Resol. (EP)	Asym. (EP)	Plates (EP)
n.a.	n.a.	Peak 1	n.a.	n.a.	n.a.	n.a.	n.a.
1	40.997	n.a.	0.099	0.104	4.34	2.68	14434
2	50.047	n.a.	0.007	0.013	n.a.	0.98	5047
Average:			n.a.	4.34	9741		

Figure A3.83 HPLC of Br-76 Radiolabling of Pal-PNA50-TAT conjugate, detected with UV-vis

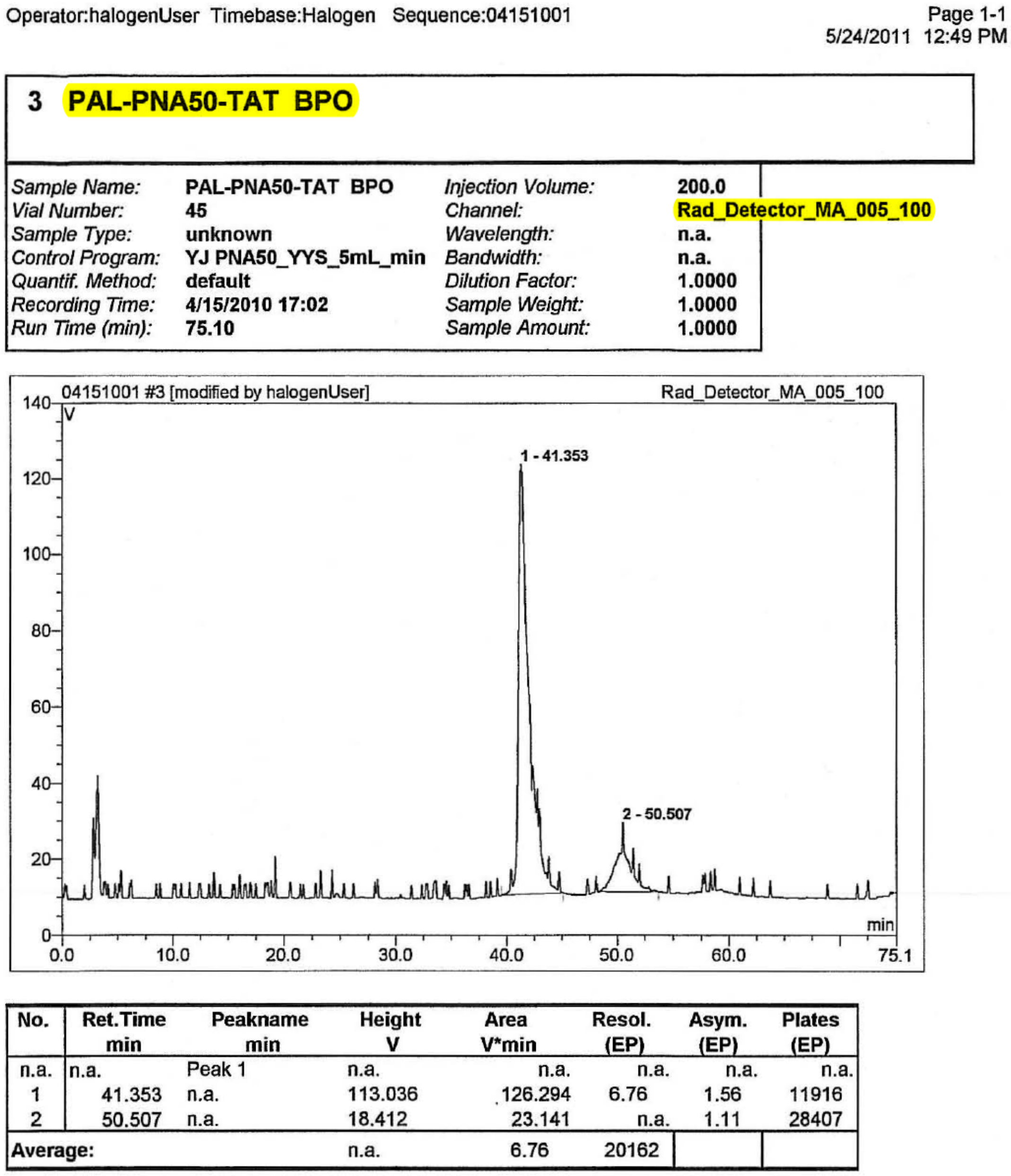

Operator:halogenUser Timebase:Halogen Sequence:04151001

Page 1-1
5/24/2011 12:49 PM

3 PAL-PNA50-TAT BPO

Sample Name:	**PAL-PNA50-TAT BPO**	*Injection Volume:*	**200.0**
Vial Number:	**45**	*Channel:*	**Rad_Detector_MA_005_100**
Sample Type:	**unknown**	*Wavelength:*	**n.a.**
Control Program:	**YJ PNA50_YYS_5mL_min**	*Bandwidth:*	**n.a.**
Quantif. Method:	**default**	*Dilution Factor:*	**1.0000**
Recording Time:	**4/15/2010 17:02**	*Sample Weight:*	**1.0000**
Run Time (min):	**75.10**	*Sample Amount:*	**1.0000**

No.	Ret.Time min	Peakname min	Height V	Area V*min	Resol. (EP)	Asym. (EP)	Plates (EP)
n.a.	n.a.	Peak 1	n.a.	n.a.	n.a.	n.a.	n.a.
1	41.353	n.a.	113.036	126.294	6.76	1.56	11916
2	50.507	n.a.	18.412	23.141	n.a.	1.11	28407
Average:			n.a.	6.76	20162		

Figure A3.84 HPLC of Br-76 Radiolabling of Pal-PNA50-TAT conjugate, detected with Radioactivity

Table3.85 Biodistribution of Pal-PNA50-TAT and Pal-PNA50S-TAT conjugates in %ID/organ

%ID/organ	1 h Pal-PNA50-TAT	1 h Pal-PNA50S-TAT	4 h Pal-PNA50-TAT
blood	3.5267+/-0.5914	2.4367+/-0.5013	3.9401+/-0.5872
lung	5.8026+/-0.7218	2.1946+/-0.2579	6.8217+/-1.5773
liver(all)	110.3009+/-14.4295	82.2869+/-1.8715	102.6267+/-15.5642
spleen	3.5004+/-0.6674	2.5148+/-1.3478	3.7839+/-0.9115
kidney	2.5938+/-0.5978	1.4569+/-0.0617	4.4577+/-0.5827
muscle	8.7607+/-1.9021	6.4658+/-0.9508	11.174+/-1.9442
heart	0.456+/-0.08	0.2922+/-0.0328	0.4349+/-0.024
brain	0.0598+/-0.0178	0.042+/-0.0116	0.1085+/-0.0171
tumor	0.7492+/-0.6395	0.2705+/-0.1295	0.5404+/-0.4389

%ID/organ	24 h Pal-PNA50-TAT	24 h Pal-PNA50S-TAT	4 h Pal-PNA50S-TAT
blood	2.1827+/-0.2305	3.8084+/-0.4801	3.3665+/-0.209
lung	3.0706+/-0.9454	1.8773+/-0.038	2.0778+/-0.7
liver(all)	85.0893+/-21.063	65.5309+/-8.4771	90.9395+/-4.2751
spleen	3.4026+/-1.4098	2.7523+/-1.5101	2.1899+/-0.4076
kidney	4.035+/-0.6656	1.7806+/-0.1255	1.5814+/-0.2333
muscle	7.7813+/-0.3184	9.4609+/-1.0251	6.4026+/-0.7722
heart	0.3509+/-0.0958	0.2853+/-0.0152	0.2406+/-0.044
brain	0.1086+/-0.0162	0.2056+/-0.009	0.075+/-0.0076

tumor	0.3431+/-0.0593	0.5391+/-0.425	0.3919+/-0.2019

Table3.86 Biodistribution Pal-PNA50-TAT and Pal-PNA50S-TAT conjugates in Sample weight (gram)

wt (gram)	1 h Pal-PNA50-TAT	1 h Pal-PNA50S-TAT	4 h Pal-PNA50-TAT
blood	0.2676+/-0.1318	0.3402+/-0.1999	0.4442+/-0.0687
lung	0.1645+/-0.022	0.1613+/-0.0288	0.1599+/-0.0149
liver(all)	1.1567+/-0.1603	1.2659+/-0.1598	1.1437+/-0.0771
spleen	0.2317+/-0.0774	0.2425+/-0.1292	0.2321+/-0.0537
kidney	0.2166+/-0.0525	0.2191+/-0.0306	0.2051+/-0.0283
muscle	0.1071+/-0.0093	0.1548+/-0.0322	0.1269+/-0.0688
heart	0.1268+/-0.0186	0.1368+/-0.0065	0.1154+/-0.0132
brain	0.3213+/-0.0214	0.358+/-0.0453	0.3807+/-0.0788
tumor	0.56+/-0.5337	0.2528+/-0.1334	0.2508+/-0.1686

wt (gram)	24 h Pal-PNA50-TAT	24 h Pal-PNA50S-TAT	4 h Pal-PNA50S-TAT
blood	0.5959+/-0.1165	0.6094+/-0.2643	0.3117+/-0.1327
lung	0.1888+/-0.0267	0.1832+/-0.022	0.2348+/-0.1029
liver(all)	1.5309+/-0.1258	1.4266+/-0.3498	1.0804+/-0.0108
spleen	0.3015+/-0.1314	0.3085+/-0.211	0.1665+/-0.0219
kidney	0.2504+/-0.0268	0.2259+/-0.0545	0.1893+/-0.0162
muscle	0.184+/-0.0321	0.1302+/-0.0459	0.1492+/-0.0525
heart	0.1489+/-0.0075	0.1382+/-0.0268	0.12+/-0.0089

brain	0.4008+/-0.0260	0.4062+/-0.0192	0.3748+/-0.0167
tumor	0.2025+/-0.0658	0.2674+/-0.1799	0.2693+/-0.1199

Table3.87 Biodistribution of Pal-PNA50-TAT and Pal-PNA50S-TAT conjugates in %ID/gram

%ID/gram	**1 h Pal-PNA50-TAT**	**1 h Pal-PNA50S-TAT**	**4 h Pal-PNA50-TAT**
blood	2.0077+/-0.3875	1.2354+/-0.2855	2.2076+/-0.2674
lung	35.9718+/-8.7477	13.7098+/-0.9727	43.068+/-11.9152
liver(all)	96.4465+/-16.3888	65.5584+/-6.6643	89.6468+/-11.7308
spleen	15.9572+/-4.1636	10.3434+/-0.5201	16.816+/-4.7261
kidney	12.0081+/-0.6155	6.7115+/-0.6675	22.1392+/-5.1684
muscle	0.8437+/-0.1324	0.5579+/-0.0843	1.0853+/-0.2669
heart	3.6537+/-0.9027	2.1463+/-0.3253	3.8065+/-0.5542
brain	0.1853+/-0.0498	0.1157+/-0.0190	0.2909+/-0.0556
tumor	1.3930+/-0.2775	1.1442+/-0.2775	2.0311+/-0.3291

%ID/gram	**24h Pal-PNA50-TAT**	**24h Pal-PNA50S-TAT**	**4 h Pal-PNA50S-TAT**
blood	1.1626+/-0.0297	2.2854+/-0.3606	1.9082+/-0.1367
lung	16.0818+/-2.9766	10.3461+/-1.2757	9.1070+/-1.3567
liver(all)	55.1865+/-10.764	48.87+/-18.0399	84.2028+/-4.7028
spleen	11.3394+/-1.901	9.5369+/-4.0526	13.0865+/-0.9366
kidney	16.0446+/-0.9774	8.3327+/-2.8174	8.3754+/-1.2118
muscle	0.7122+/-0.0707	0.9701+/-0.147	0.6185+/-0.0654
heart	2.3472+/-0.5908	2.1027+/-0.309	2.0043+/-0.3392
brain	0.2712+/-0.0389	0.5066+/-0.0282	0.2+/-0.0136

tumor	1.7763+/-0.4275	1.9314+/-0.2973	1.4332+/-0.1274

Appendix_Chapter 4

HPLC, UV, MALDI

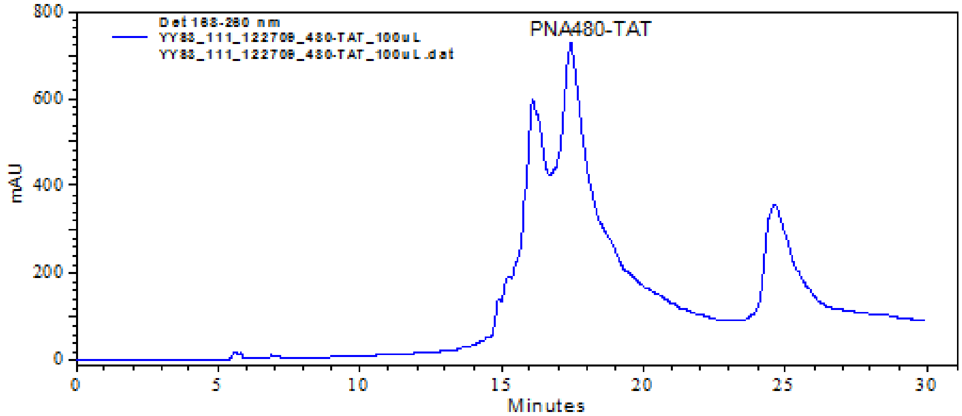

Figure A4.1 HPLC of Crude PNA480-TAT conjugate

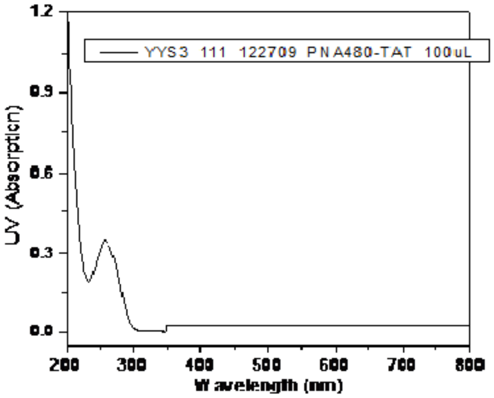

Figure A4.2 UV of PNA480-TAT conjugate

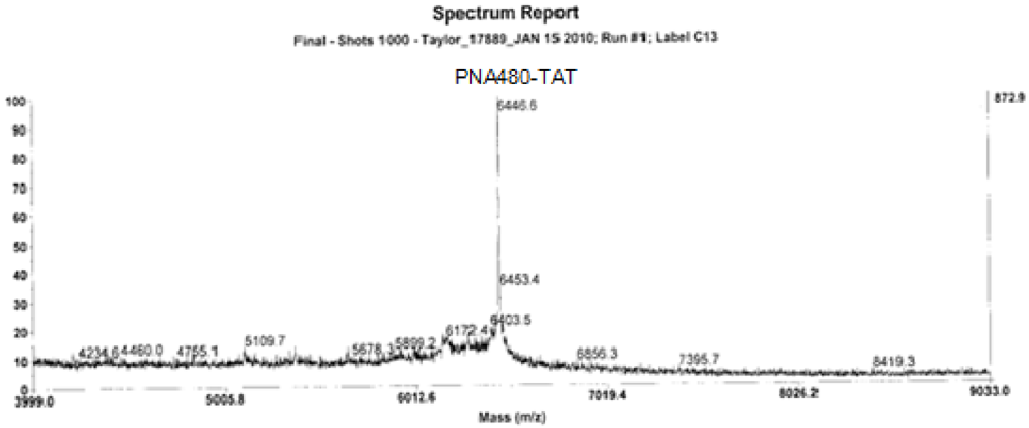

Figure A4.3 MALDI of PNA480-TAT conjugate

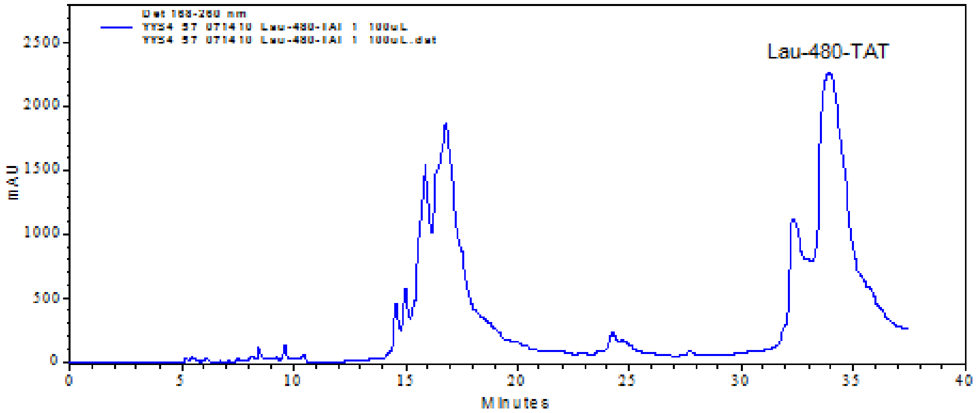

Figure A4.4 HPLC of Crude Lau-PNA480-TAT conjugate

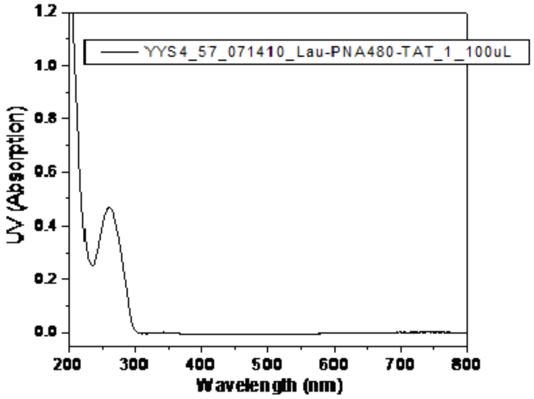

Figure A4.5 UV of Lau-PNA480-TAT conjugate

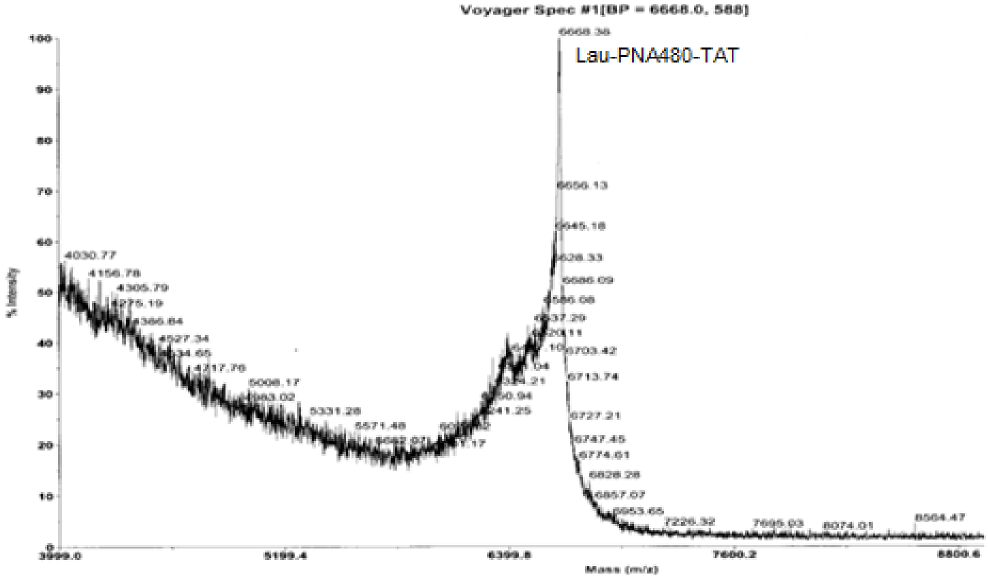

Figure A4.6 MALDI of Lau-PNA480-TAT conjugate

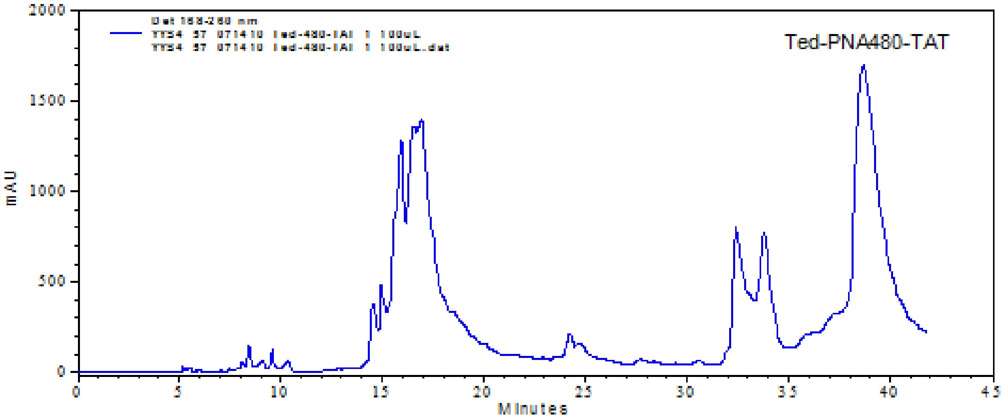

Figure A4.7 HPLC of Crude Ted-PNA480-TAT conjugate

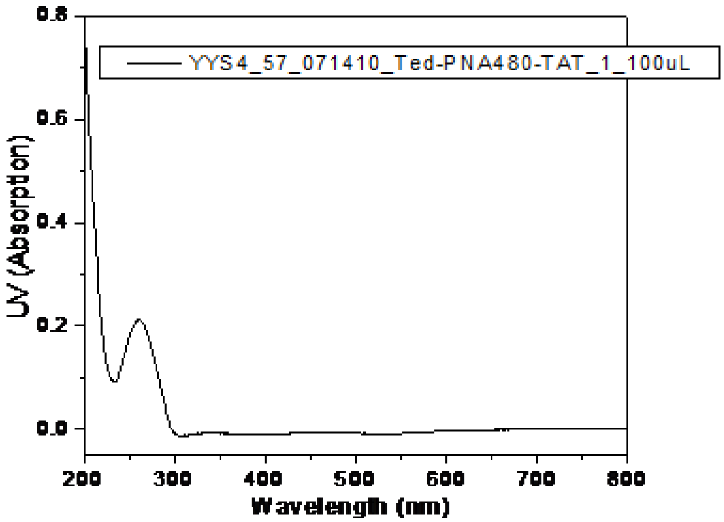

Figure A4.8 UV of Ted-PNA480-TAT conjugate

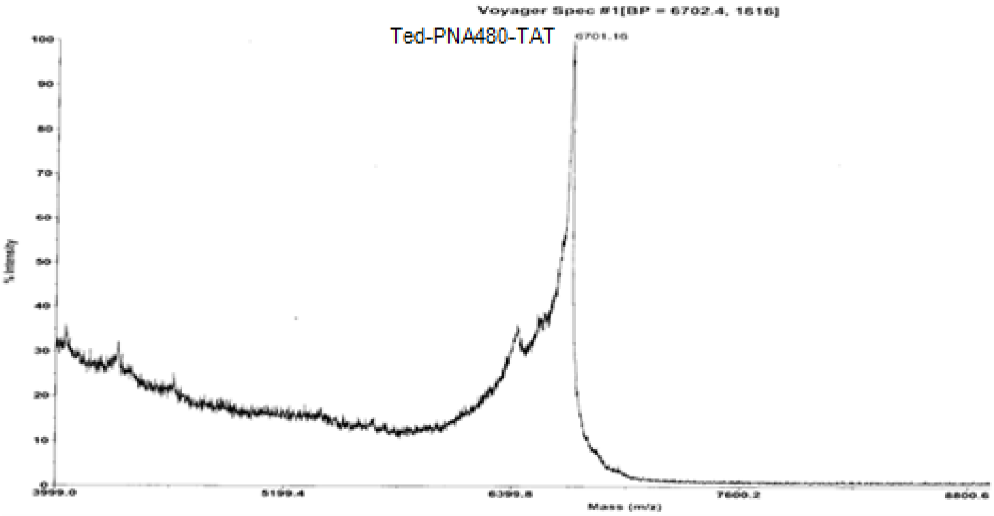

Figure A4.9 MALDI of Ted-PNA480-TAT conjugate

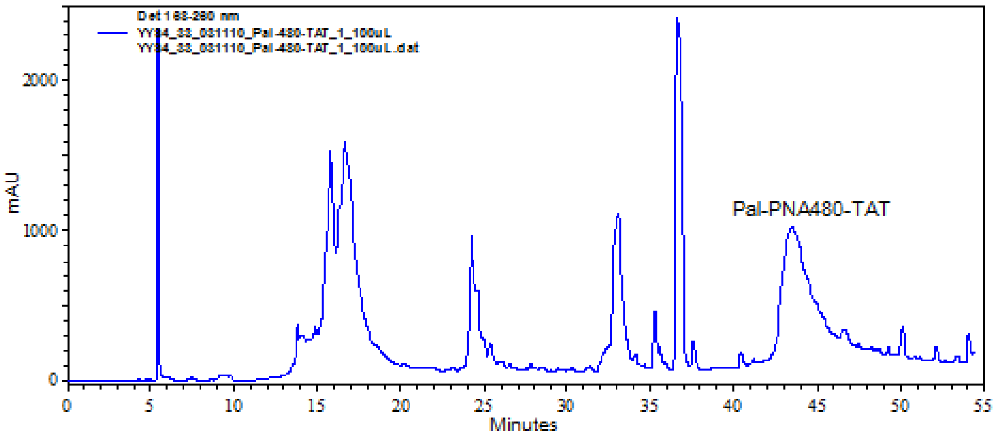

Figure A4.10 HPLC of Crude Pal-PNA480-TAT conjugate

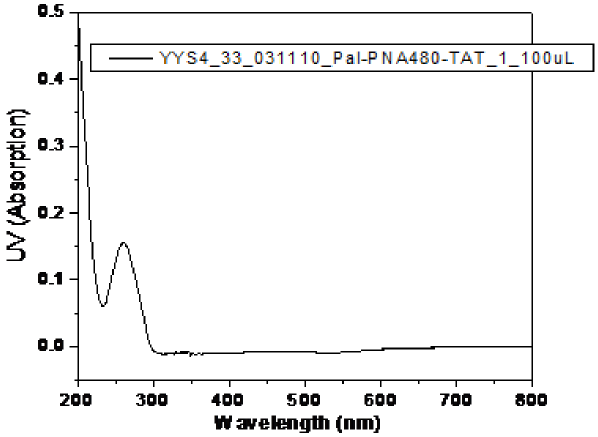

Figure A4.11 UV of Pal-PNA480-TAT conjugate

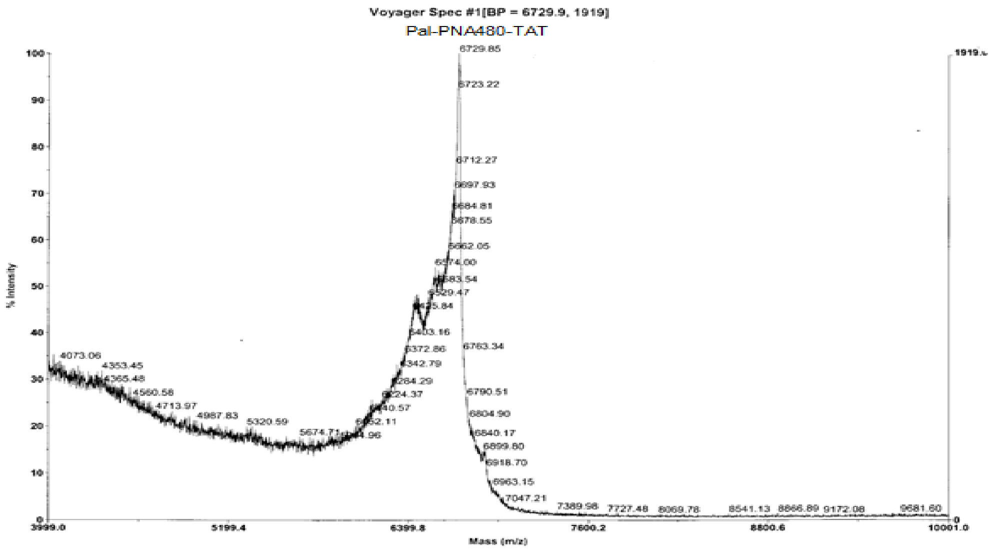

Figure A4.12 MALDI of Pal-PNA480-TAT conjugate

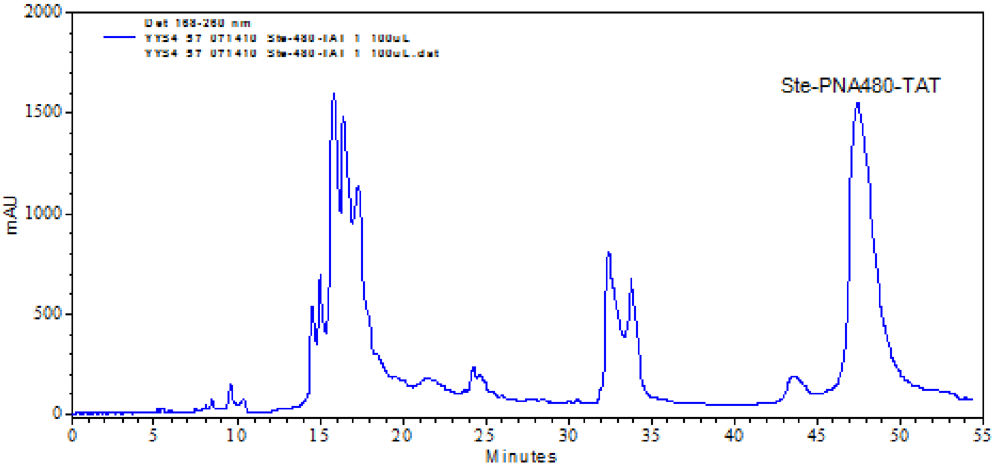

Figure A4.13 HPLC of Crude Ste-PNA480-TAT conjugate

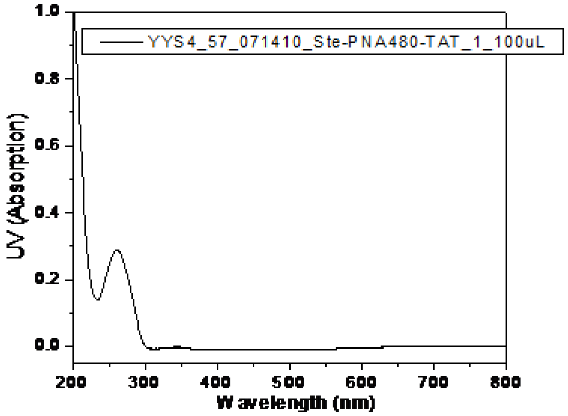

Figure A4.14 UV of Ste-PNA480-TAT conjugate

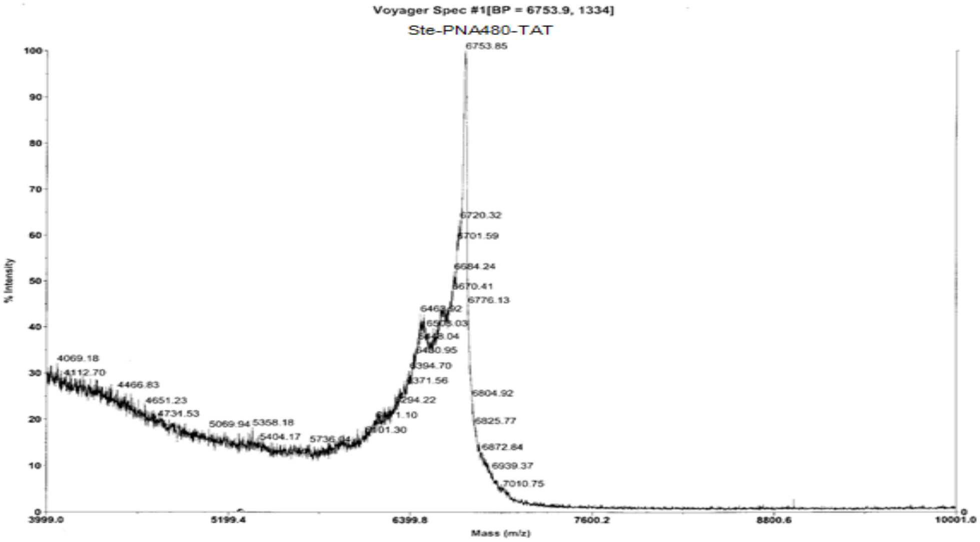

Figure A4.15 MALDI of Ste-PNA480-TAT conjugate

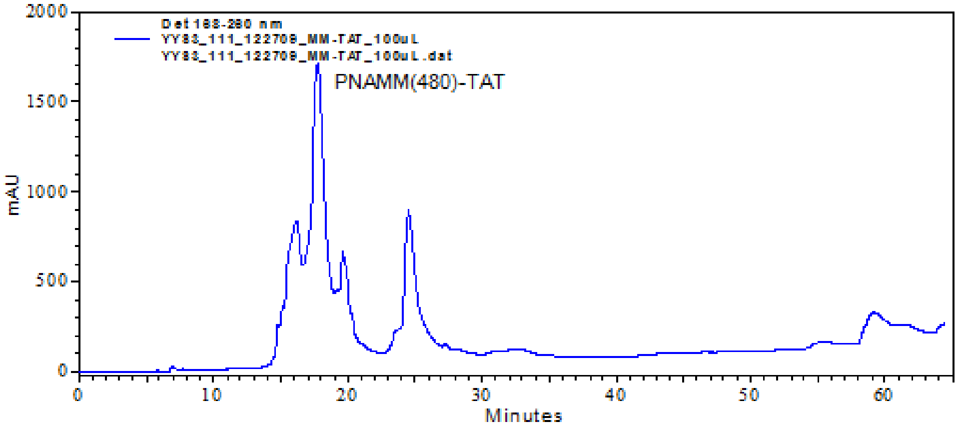

Figure A4.16 HPLC of Crude PNAMM(480)-TAT conjugate

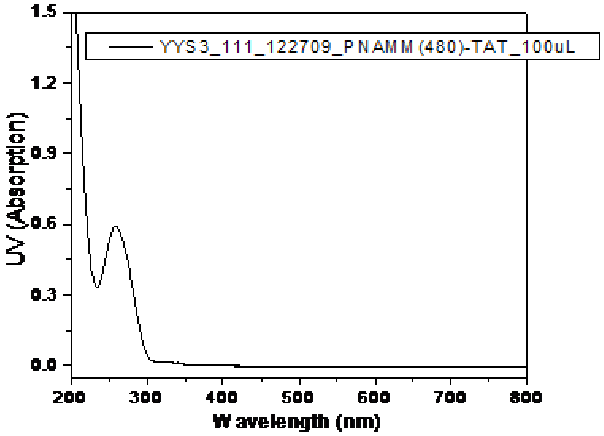

Figure A4.17 UV of PNAMM(480)-TAT conjugate

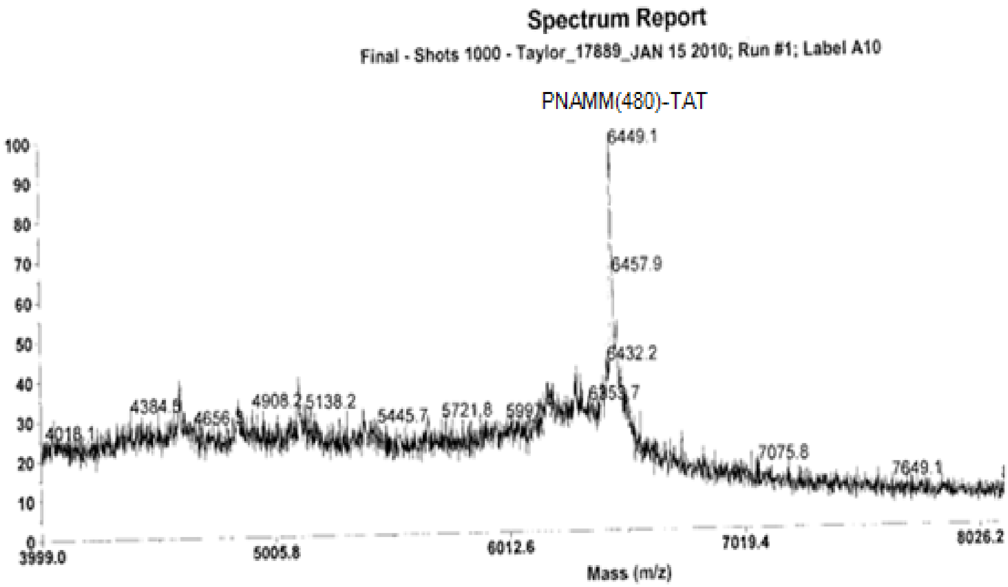

Figure A4.18 MALDI of PNAMM(480)-TAT conjugate

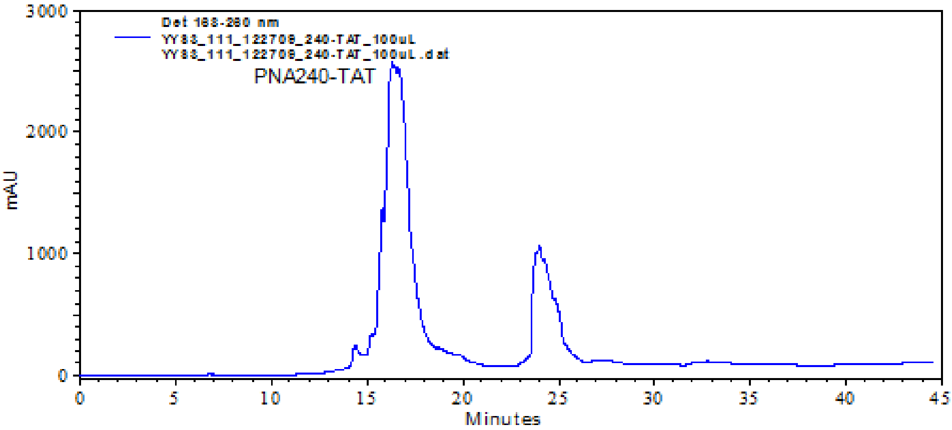

Figure A4.19 HPLC of Crude PNA240-TAT conjugate

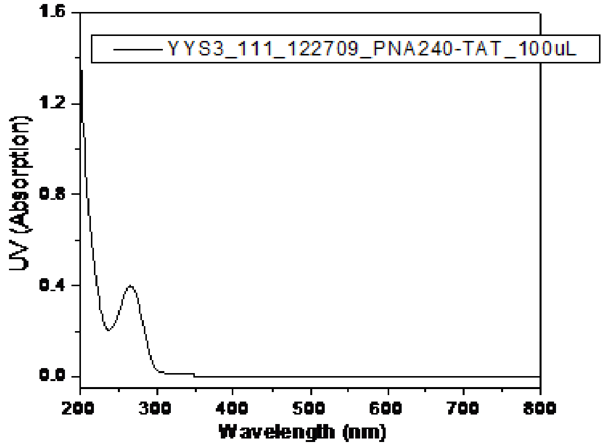

Figure A4.20 UV of PNA240-TAT conjugate

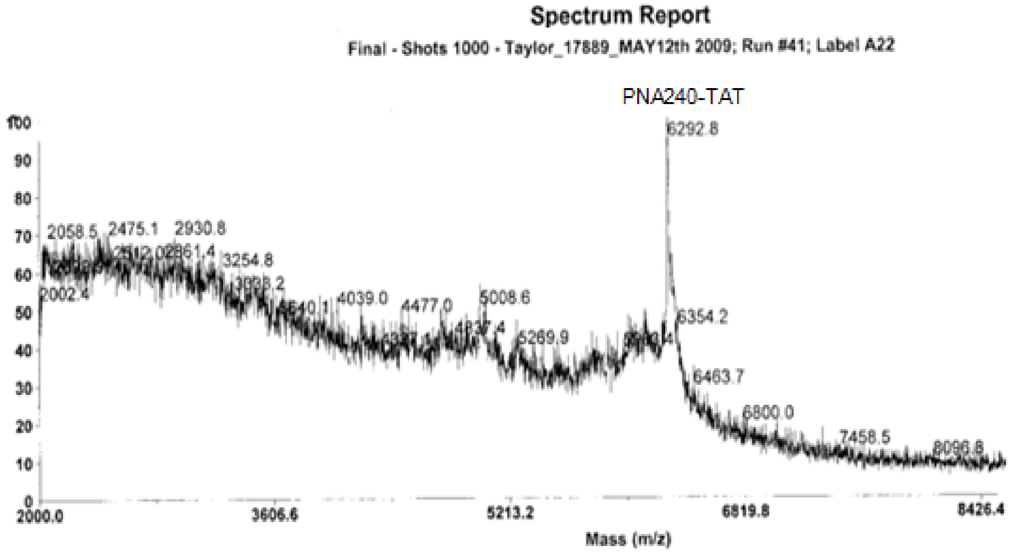

Figure A4.21 MALDI of PNA240-TAT conjugate

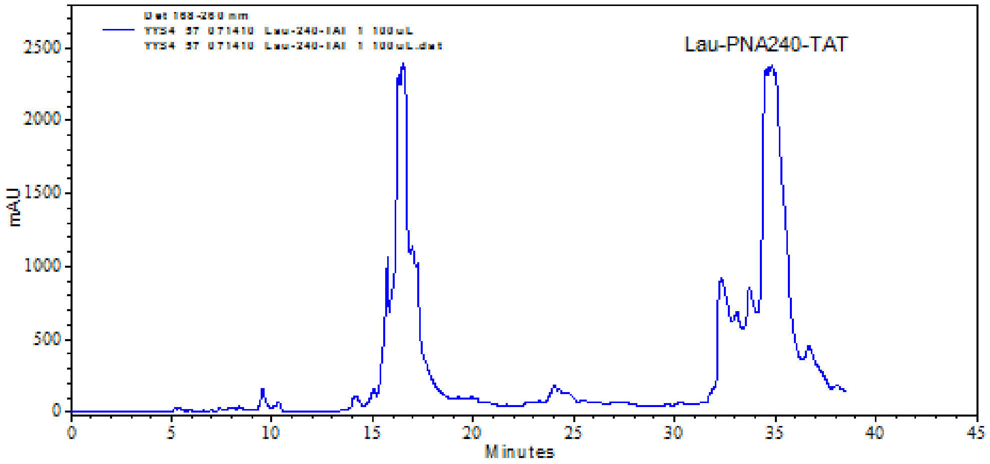

Figure A4.22 HPLC of Crude Lau-PNA240-TAT conjugate

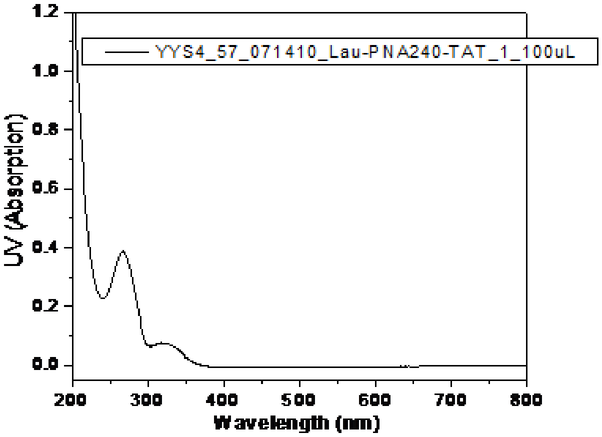

Figure A4.23 UV of Lau-PNA240-TAT conjugate

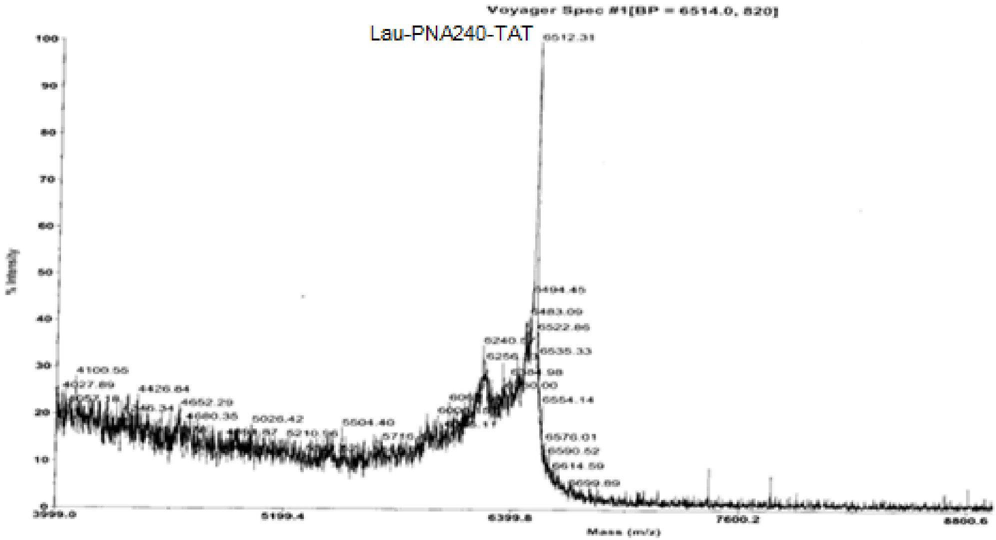

Figure A4.24 MALDI of Lau-PNA240-TAT conjugate

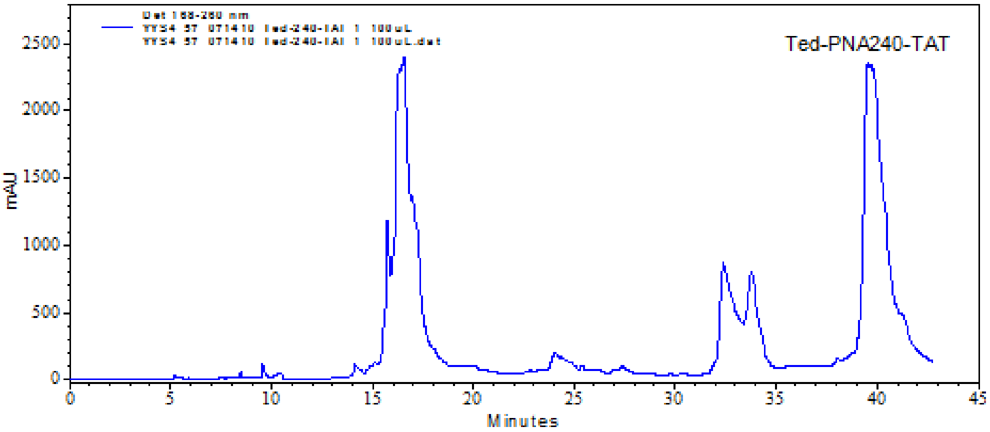

Figure A4.25 HPLC of Crude Ted-PNA240-TAT conjugate

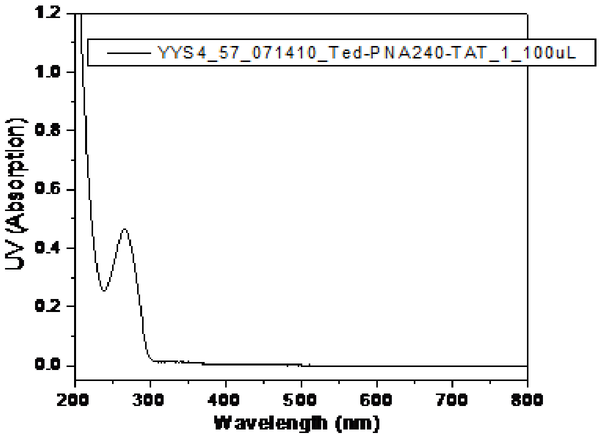

Figure A4.26 UV of Ted-PNA240-TAT conjugate

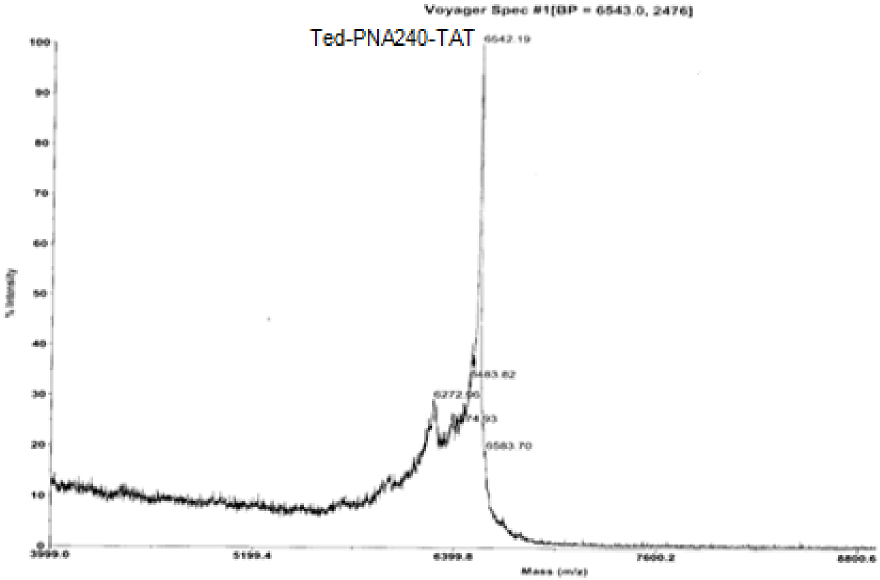

Figure A4.27 MALDI of Ted-PNA240-TAT conjugate

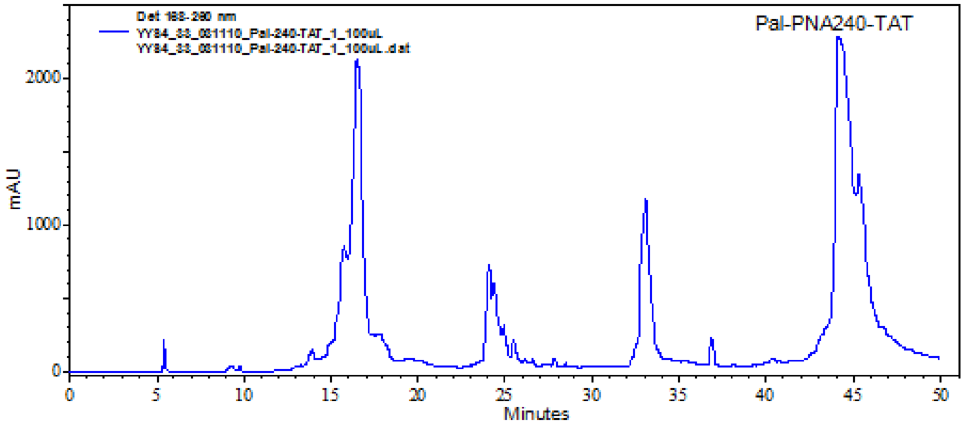

Figure A4.28 HPLC of Crude Pal-PNA240-TAT conjugate

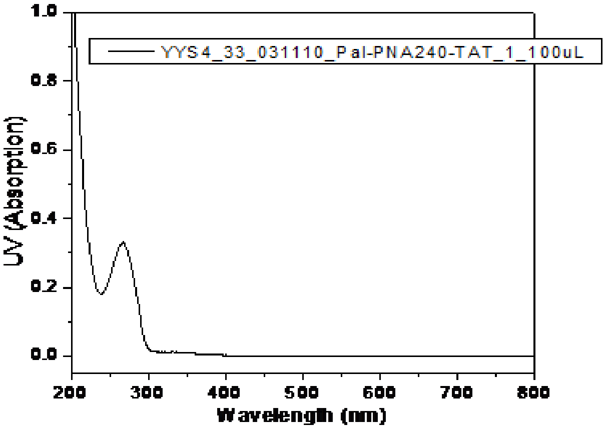

Figure A4.29 UV of Pal-PNA240-TAT conjugate

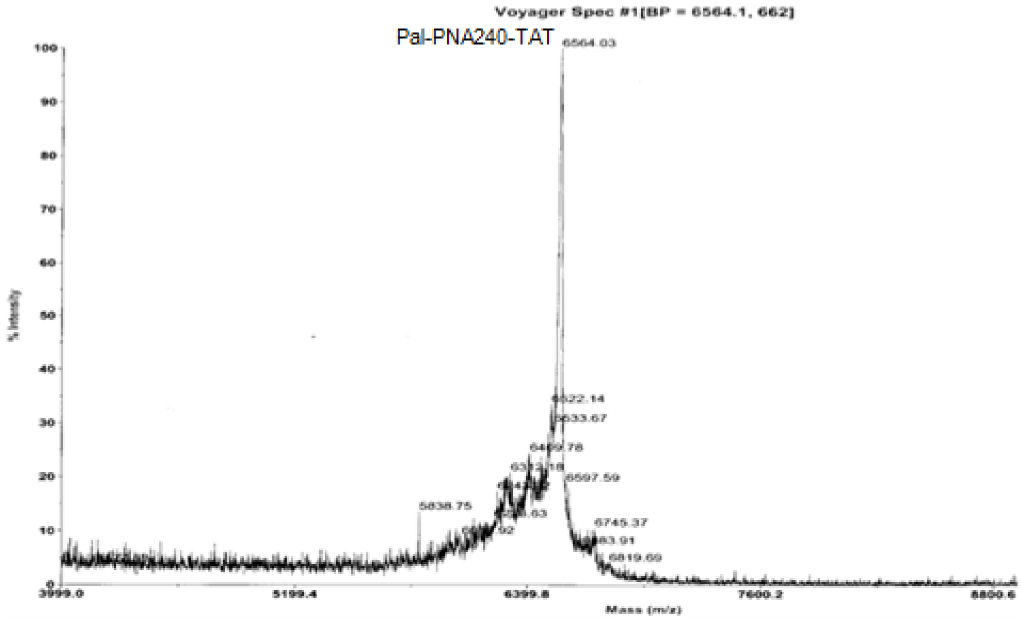

Figure A4.30 MALDI of Pal-PNA240-TAT conjugate

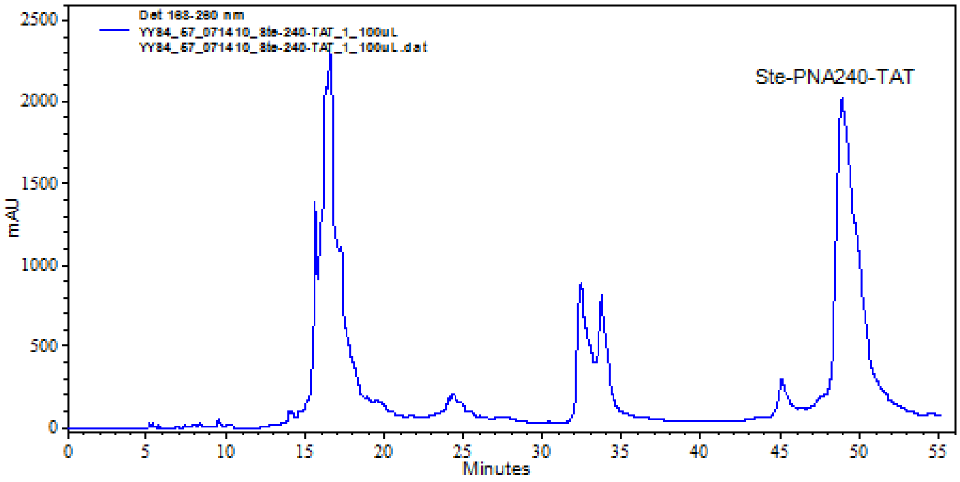

Figure A4.31 HPLC of Crude Ste-PNA240-TAT conjugate

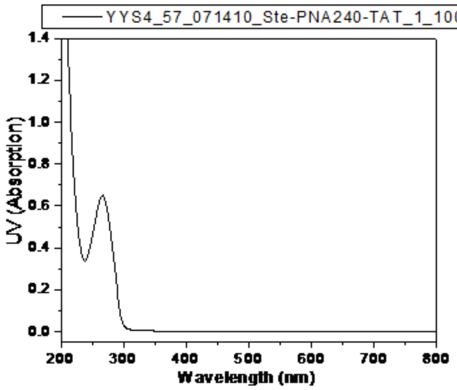

Figure A4.32 UV of Ste-PNA240-TAT conjugate

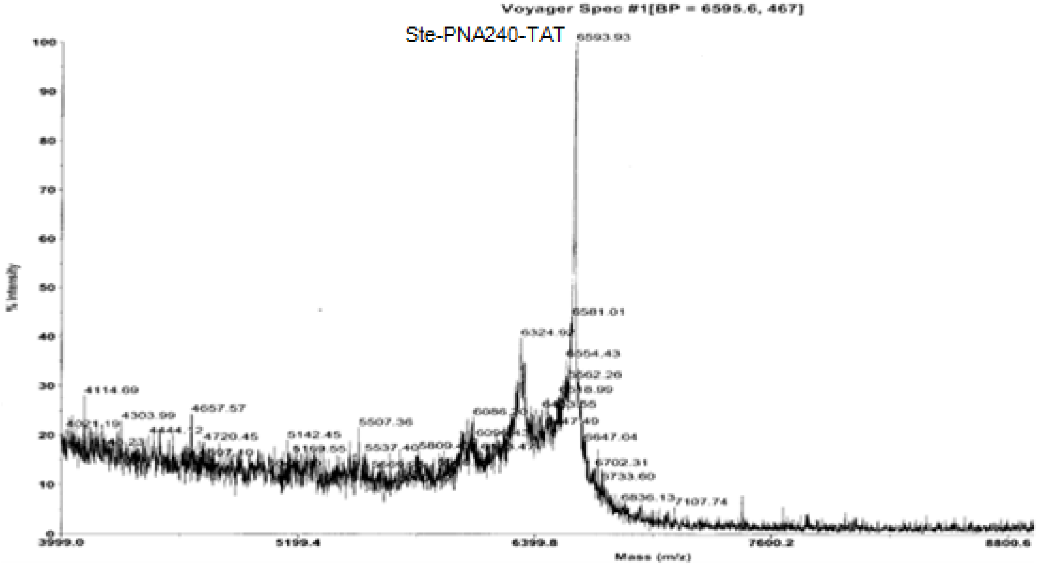

Figure A4.33 MALDI of Ste-PNA240-TAT conjugate

DLS, CMC

Conc (μM)	Z-Ave (d.nm)	PdI
961.2	211.4	0.706
451.764	201.2	0.729

225.882	219.7	0.483
112.941	222.2	0.514
56.4705	205.1	0.382
28.23525	233.4	0.413
14.117625	226.5	0.414
7.0588125	249.6	0.504
3.52940625	206.3	0.344
1.764703125	**232**	**0.3802**
0.882351563	242.2	0.333
0.441175781	252.7	0.422
0.220587891	284.8	0.435
0.110293945	390.6	0.415
0.055146973	482.5	0.467
0.027573486	454.6	0.411
0.013786743	496.8	0.585
0.006893372	618.5	0.512
0.003446686	543.8	0.584
0.001723343	601.8	0.576
0.000861671	639.5	0.547
0.000215418	611.2	0.518
0.000107709	725.4	0.523

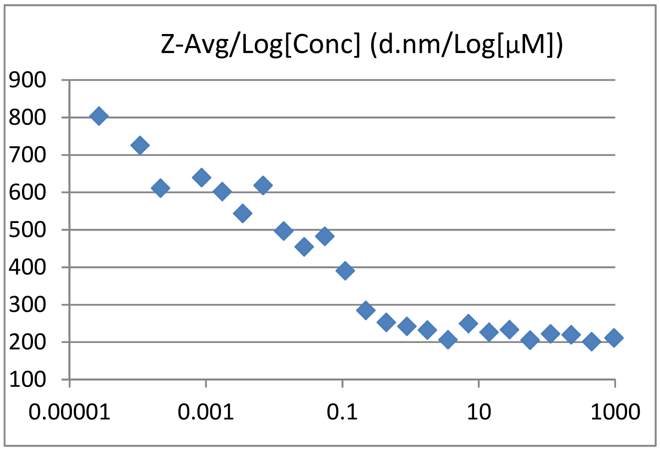

2.69272E-05	803.7	0.558

Figure A4.34 Lau-PNA480-TAT_DLS

Conc (μM)	Z-Ave (d.nm)	PdI
1037.07	218.7	0.722
259.2675	215.3	0.55
129.63375	224.8	0.692
64.816875	213.6	0.401
32.4084375	216	0.41
16.20421875	216.7	0.397
8.102109375	212.4	0.331
4.051054688	240.8	0.433
2.025527344	**234**	**0.355**
1.012763672	246.7	0.442
0.506381836	275.4	0.432
0.253190918	302.8	0.497
0.126595459	320.7	0.523
0.063297729	435.4	0.482
0.031648865	414	0.442
0.015824432	546.3	0.552
0.007912216	688.1	0.652
0.003956108	719	0.679
0.001978054	670.9	0.577
0.000989027	848.5	0.662

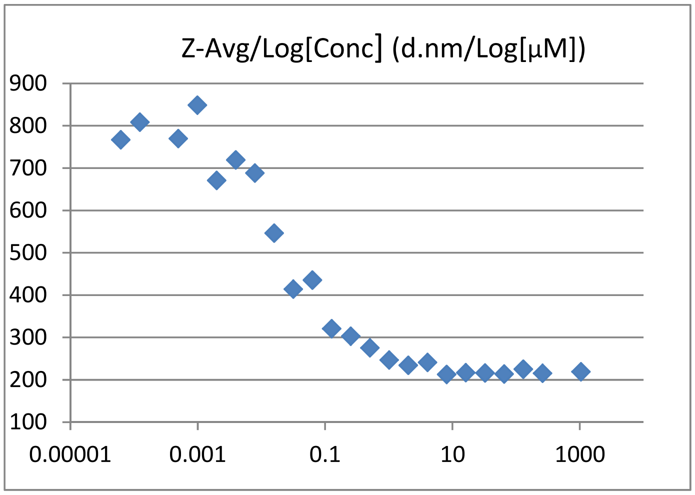

0.000494514	769.6	0.572
0.000123628	808.3	0.617
6.18142E-05	766.6	0.623

Figure A4.35 Ted-PNA480-TAT_DLS

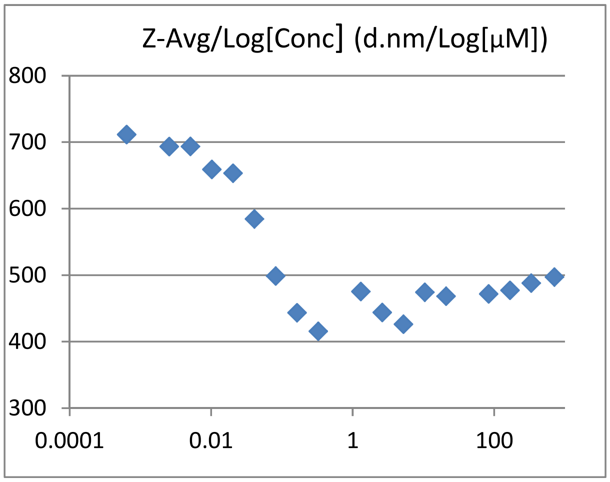

Figure A4.36 Pal–PNA480–TAT_DLS

Conc (µM)	Z-Ave (d.nm)	PdI
710.94	497.2	0.572
334.1418	488	0.476
167.0709	477.2	0.583
83.53545	471.7	0.625
20.883863	468.3	0.698
10.441931	474.3	0.637
5.2209656	426.3	0.584
2.6104828	443.8	0.692
1.3052414	475.3	0.547
0.3263104	**415.5**	**0.649**
0.1631552	443.5	0.52
0.0815776	498.7	0.462
0.0407888	584.6	0.611
0.0203944	653.4	0.696
0.0101972	658.9	0.678
0.0050986	693.6	0.531
0.0025493	693.5	0.626
0.0006373	711.5	0.536

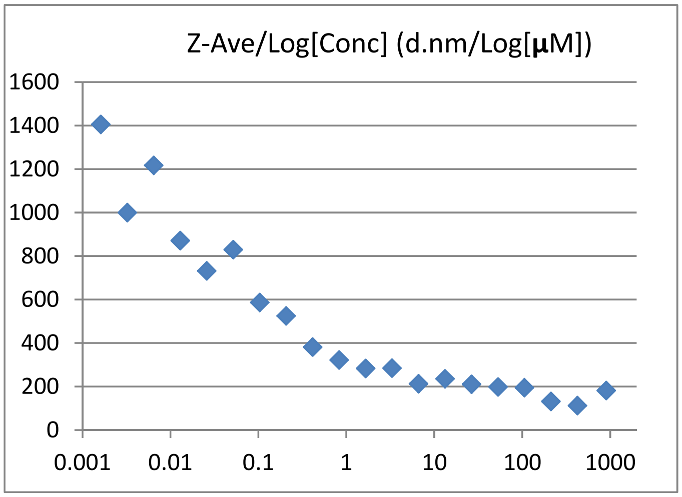

Figure A4.37 Ste-PNA480-TAT_DLS

Conc (μM)	Z-Ave (d.nm)	PdI
901.728	181.7	PdI
423.81216	112.7	0.797
211.90608	132.1	0.734
105.95304	195.1	0.481
52.97652	198.7	0.397
26.48826	210.9	0.35
13.24413	235.6	0.548
6.622065	212.7	0.453
3.3110325	284.6	0.348
1.65551625	**283.5**	**0.391**
0.827758125	322.5	0.508
0.413879063	381.6	0.391
0.206939531	525.2	0.49
0.103469766	586.9	0.582
0.051734883	829.7	0.632
0.025867441	732.3	0.585
0.012933721	871.4	0.662
0.00646686	1217	0.675
0.00323343	999.6	0.62
0.001616715	1405	0.697

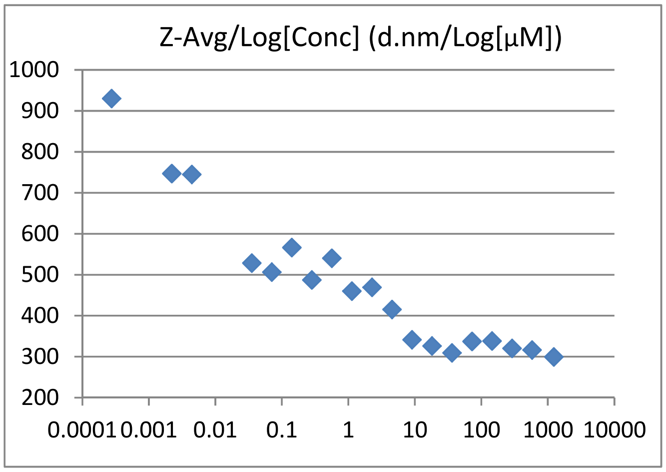

Figure A4.38 Lau-PNA240-TAT_DLS

Conc (µM)	Z-Ave (d.nm)	PdI
1233.255	299.2	0.559
579.62985	316.2	0.571
289.814925	320.2	0.493
144.9074625	338.1	0.546
72.45373125	337.1	0.447
36.22686563	309.1	0.597
18.11343281	326.2	0.461
9.056716406	**341.3**	**0.488**
4.528358203	415.2	0.647
2.264179102	469	0.655
1.132089551	460.1	0.473
0.566044775	540.2	0.624
0.283022388	487.2	0.494
0.141511194	566.2	0.564
0.070755597	506.4	0.581
0.035377798	528.5	0.501
0.004422225	744.5	0.559
0.002211112	746.9	0.59
0.000276389	929.9	0.723

Conc (μM)	Z-Ave (d.nm)	PdI
1162.332	212.3	0.489
546.29604	206.5	0.462
273.14802	203.6	0.404
136.57401	209.4	0.526
68.287005	220.5	0.422
34.1435025	232.3	0.529
17.07175125	**245.1**	0.374
8.535875625	274	0.45
4.267937813	297.2	0.412
2.133968906	326.3	0.467
1.066984453	312.2	0.506
0.533492227	353.1	0.492
0.266746113	368.6	0.517
0.133373057	433.7	0.538
0.066686528	436.8	0.554
0.033343264	660.7	0.489
0.016671632	522	0.573
0.008335816	658.8	0.594
0.004167908	684.7	0.649
0.001041977	961.1	0.486

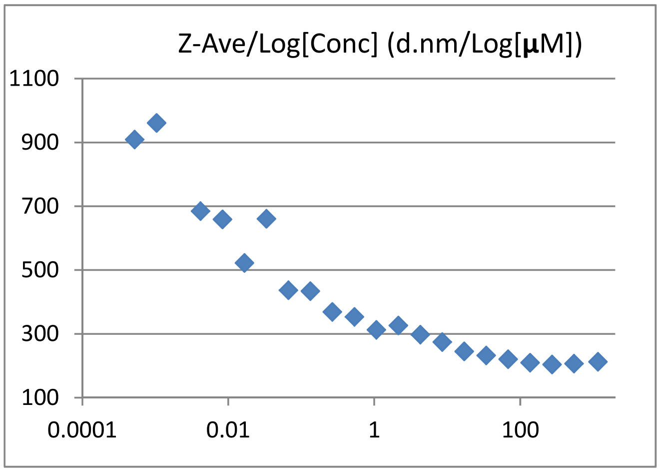

0.000520989	909	0.593

Figure A4.39 Ted−PNA240−TAT_DLS

Conc (μM)	Z-Ave (d.nm)	PdI
981	590.5	0.59
461.07	570.8	0.576
230.535	540.2	0.573
115.2675	522	0.531
57.63375	513	0.622
7.20421875	569	0.766
3.60210938	409.8	0.774
1.80105469	318.1	0.551
0.90052734	**320.3**	0.555
0.45026367	331.5	0.56
0.22513184	310.2	0.458
0.11256592	378	0.487
0.05628296	409.6	0.562
0.02814148	349.8	0.477
0.01407074	461.4	0.418
0.00703537	472.3	0.582
0.00351768	554	0.545
0.00175884	524.1	0.595
0.00087942	586.8	0.505

0.00043971	705.5	0.527

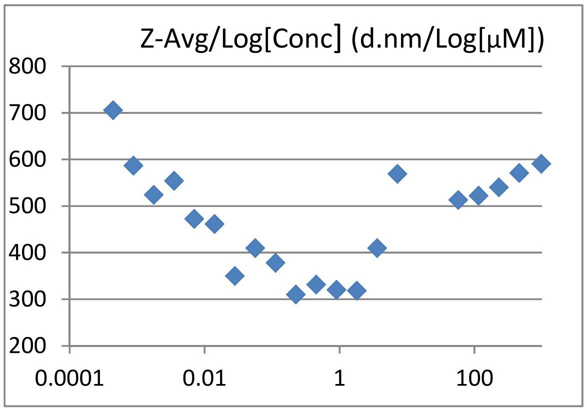

Figure A4.40 Pal–PNA240–TAT_DLS

Conc (µM)	Z-Ave (d.nm)	PdI
1160.36	202	0.602
545.3692	187.8	0.728
272.6846	188.9	0.538
136.3423	**213.4**	0.559
68.17115	254.4	0.667

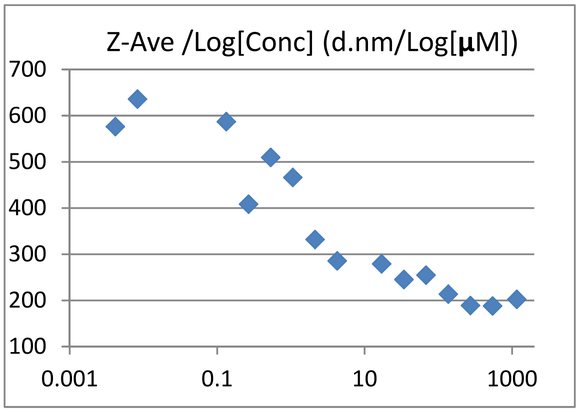

Figure A4.41 Ste-PNA240-TAT_DLS

34.085575	245.1	0.418
17.0427875	278.9	0.499
4.260696875	285.6	0.539
2.130348438	331.7	0.433
1.065174219	466.2	0.592
0.532587109	509.4	0.618
0.266293555	408.2	0.649
0.133146777	587	0.594
0.008321674	635.9	0.577
0.004160837	576.1	0.657
0.002080418	599.2	0.582

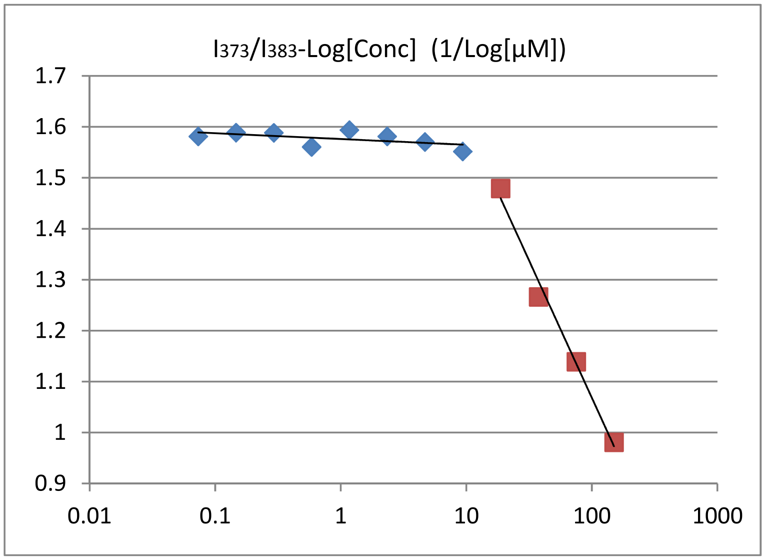

Figure A4.42 Lau-PNA480-TAT_CMC_without NaCl

Conc(µM)	I373/I383
0.073242	1.581367
0.146484	1.588811
0.292969	1.588511
0.585938	1.56073
1.171875	1.593696
2.34375	1.581242
4.6875	1.570455
9.375	1.551768
18.75	1.479367
37.5	1.266285
75	1.13928
150	0.980921

Conc(µM)	I373/I383
0.073242	1.556655
0.146484	1.574758
0.292969	1.562281
0.585938	1.570605
1.171875	1.576465
2.34375	1.534323
4.6875	1.528656
9.375	1.509151

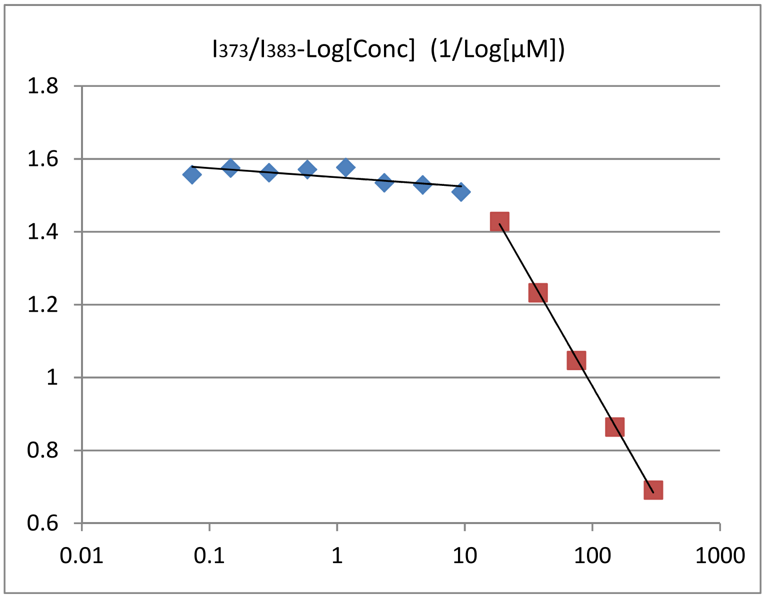

18.75	1.428272
37.5	1.232477
75	1.046993
150	0.863893
300	0.691212

Figure A4.43 Lau-PNA480-TAT_CMC_with NaCl

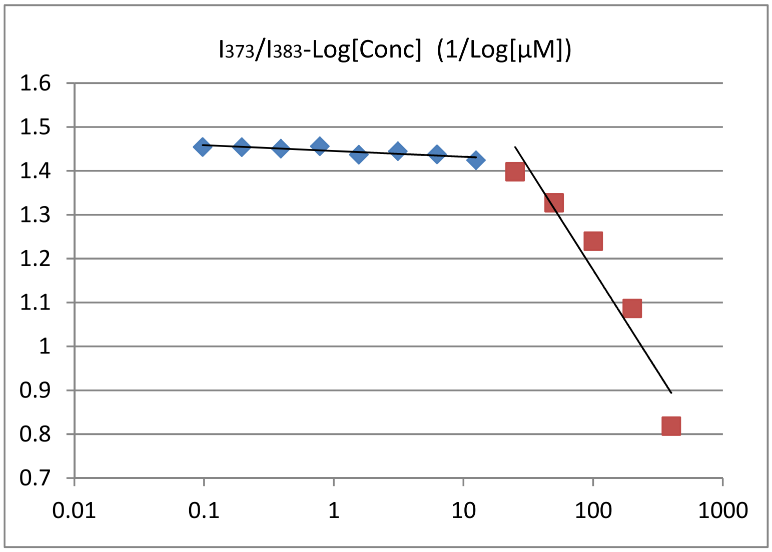

Conc(µM)	I373/I383
0.097656	1.454661
0.195313	1.454277
0.390625	1.450867
0.78125	1.456246
1.5625	1.436909
3.125	1.444806
6.25	1.437723
12.5	1.424193
25	1.39823
50	1.327589
100	1.240088
200	1.086773
400	0.818406

Figure A4.44 Ted-PNA480-TAT_CMC_without NaCl

Conc(µM)	I373/I383
0.036621	1.526893
0.073242	1.536426
0.146484	1.529303
0.292969	1.541453
0.585938	1.520196
1.171875	1.54228
2.34375	1.536197
4.6875	1.541397
9.375	1.4796

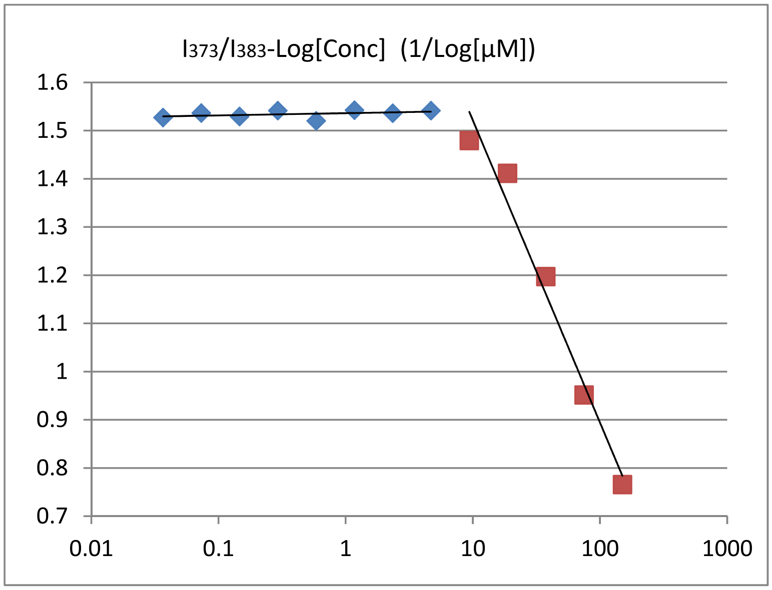

18.75	1.411491
37.5	1.197306
75	0.951847
150	0.765797

Figure A4.45 Ted-PNA480-TAT_CMC_with NaCl

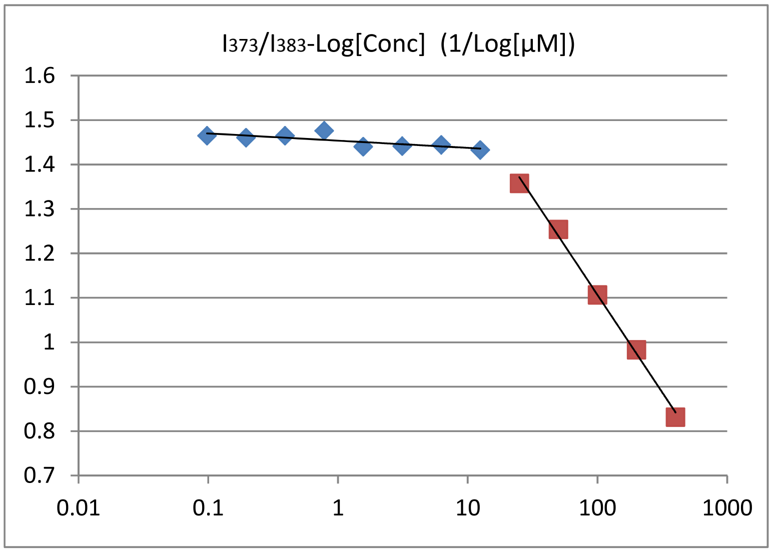

Figure A4.46 Pal-PNA480-TAT_CMC_without NaCl

Conc(µM)	I373/I383
0.097656	1.464744
0.195313	1.460314
0.390625	1.464765
0.78125	1.475964
1.5625	1.440084
3.125	1.441263
6.25	1.444291
12.5	1.432693
25	1.35777
50	1.254159
100	1.106794
200	0.983272
400	0.831756

Conc(µM)	I373/I383
0.097656	1.459827
0.195313	1.456325
0.390625	1.405575
0.78125	1.442397
1.5625	1.442334
3.125	1.432144
6.25	1.411607
12.5	1.386513
25	1.266136

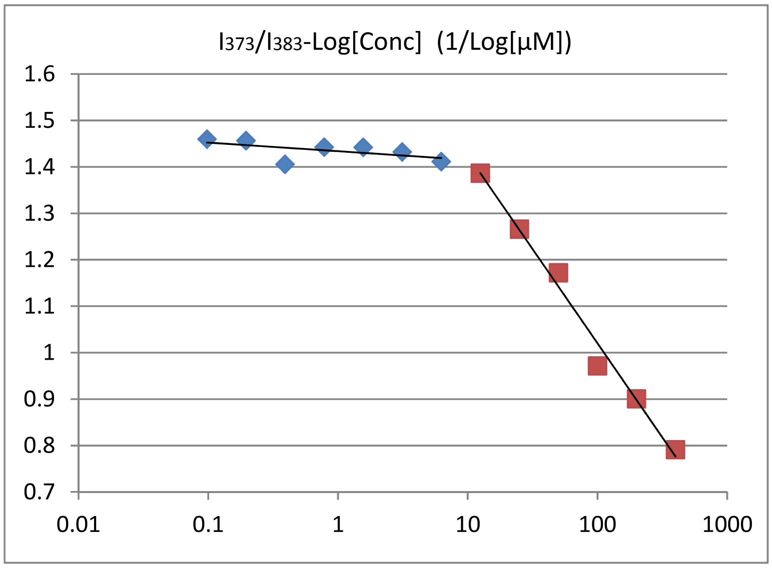

50	1.172032
100	0.971554
200	0.900779
400	0.791404

Figure A4.47 Pal-PNA480-TAT_CMC_with NaCl

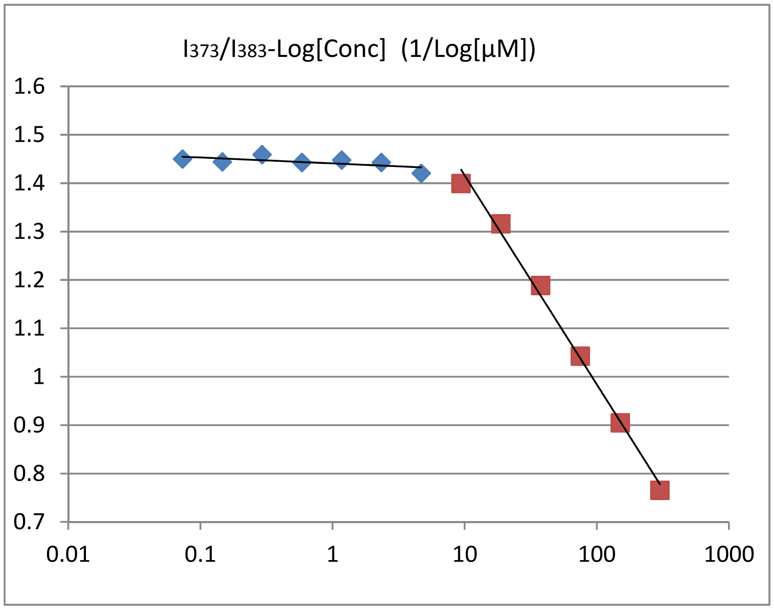

Figure A4.48 Ste-PNA480-TAT_CMC_without NaCl

Conc(µM)	I373/I383
0.073242	1.449829
0.146484	1.443933
0.292969	1.458856
0.585938	1.44262
1.171875	1.447509
2.34375	1.442779
4.6875	1.420226
9.375	1.399392
18.75	1.31609
37.5	1.188901
75	1.042792
150	0.905043
300	0.765537

Conc(µM)	I373/I383
0.073242	1.579493
0.146484	1.541111
0.292969	1.565289
0.585938	1.524181
1.171875	1.51309
3.34375	1.554108
4.6875	1.530509
9.375	1.494318

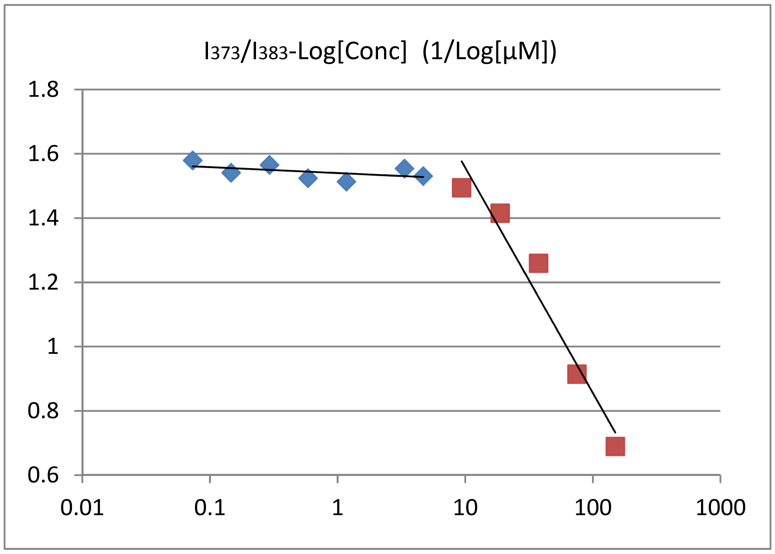

18.75	1.415011
37.5	1.259409
75	0.914326
150	0.68944

Figure A4.49 Ste-PNA480-TAT_CMC_with NaCl

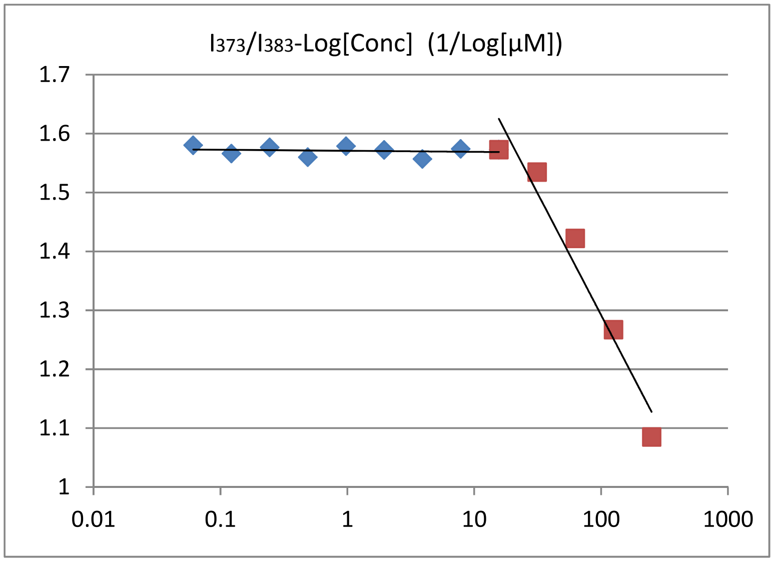

Figure A4.50 Lau-PNA240-TAT_CMC_without NaCl

Conc(µM)	I373/I383
0.061035	1.580097
0.12207	1.566195
0.244141	1.576519
0.488281	1.56004
0.976563	1.578724
1.953125	1.572363
3.90625	1.556951
7.8125	1.574057
15.625	1.572917
31.25	1.534576
62.5	1.422072
125	1.267044
250	1.084923

Conc(µM)	I373/I383
0.061035	1.510399
0.12207	1.507151
0.244141	1.482771
0.488281	1.491031
0.976563	1.490182
1.953125	1.465297
3.90625	1.436136
7.8125	1.452792

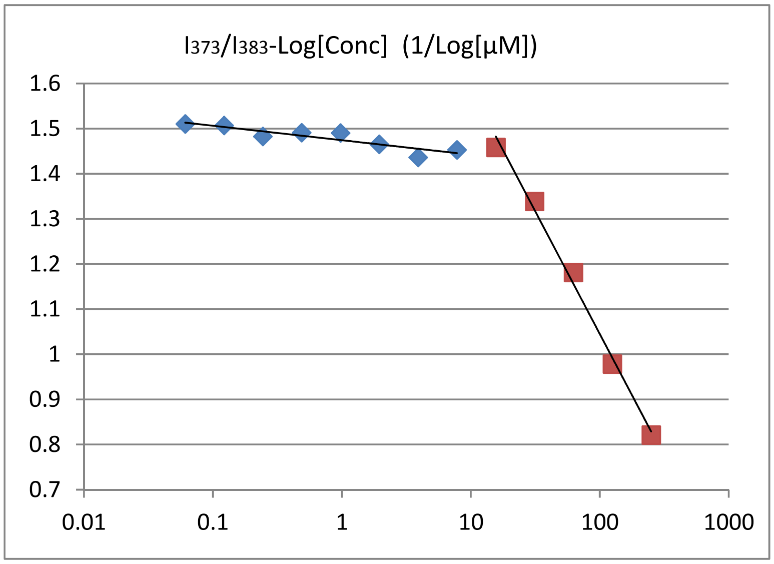

15.625	1.458524
31.25	1.338767
62.5	1.181405
125	0.978624
250	0.821311

Figure A4.51 Lau-PNA240-TAT_CMC_with NaCl

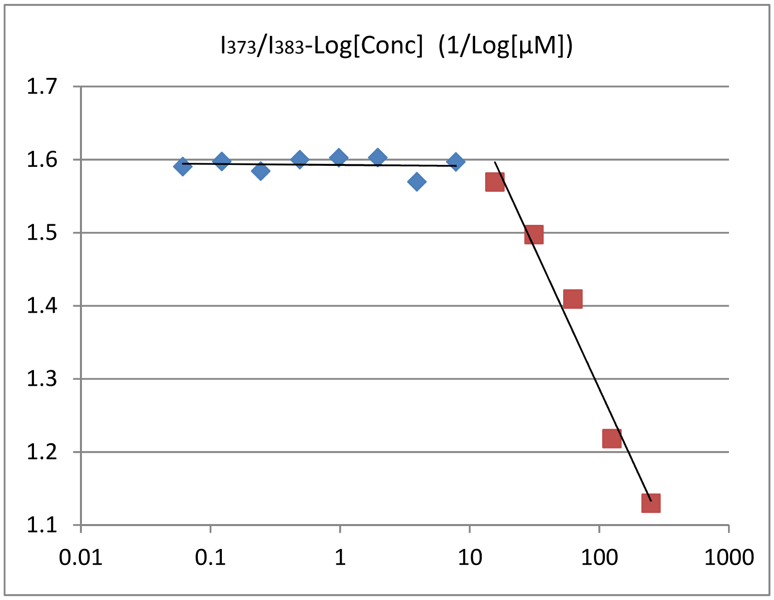

Figure A4.52 Ted-PNA240-TAT_CMC_without NaCl

Conc(μM)	I373/I383
0.061035	1.590531
0.12207	1.597446
0.244141	1.584178
0.488281	1.599921
0.976563	1.602548
1.953125	1.602843
3.90625	1.569634
7.8125	1.596793
15.625	1.569464
31.25	1.497474
62.5	1.409398
125	1.218324
250	1.129782

Conc(μM)	I373/I383
0.061035	1.532823
0.12207	1.53486
0.244141	1.535306
0.488281	1.545196
0.976563	1.521894
1.953125	1.519346
3.90625	1.503696
7.8125	1.483368

15.625	1.390903
31.25	1.341457
62.5	1.160732
125	0.987547
250	0.835676

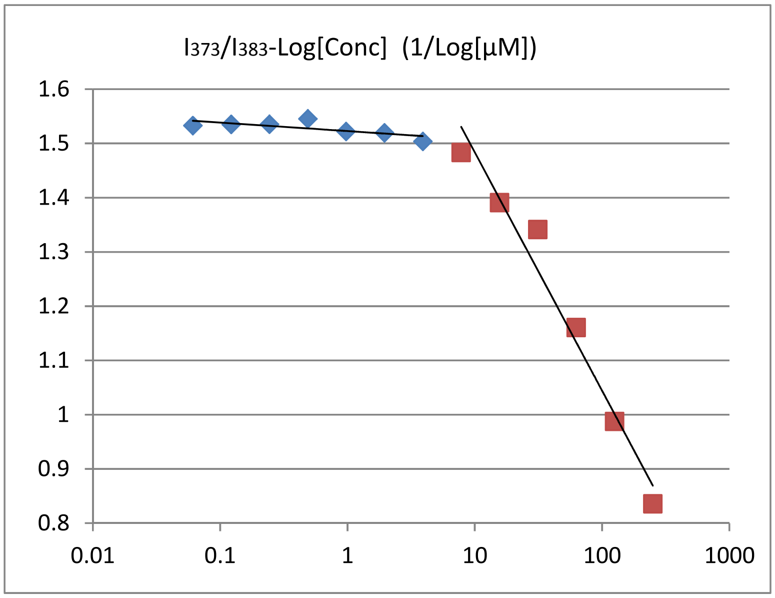

Figure A4.53 Ted-PNA240-TAT_CMC_with NaCl

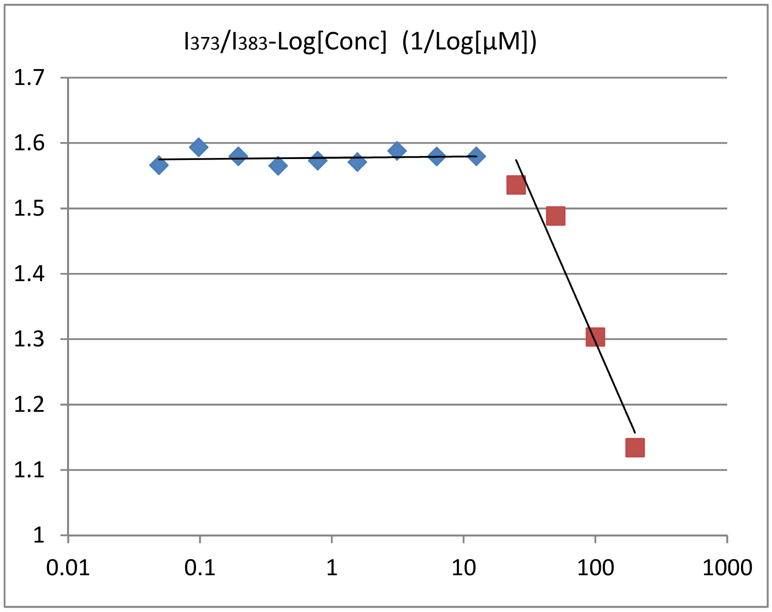

Figure A4.54 Pal-PNA240-TAT_CMC_without NaCl

Conc(µM)	I373/I383
0.048828	1.566147
0.097656	1.593499
0.195313	1.579615
0.390625	1.565286
0.78125	1.573115
1.5625	1.570933
3.125	1.587974
6.25	1.579529
12.5	1.579656
25	1.535961
50	1.488622
100	1.303337
200	1.134151

Conc(µM)	I373/I383
0.048828	1.545547
0.097656	1.560455
0.195313	1.556912
0.390625	1.562607
0.78125	1.570866
1.5625	1.552639
3.125	1.524215
6.25	1.517496

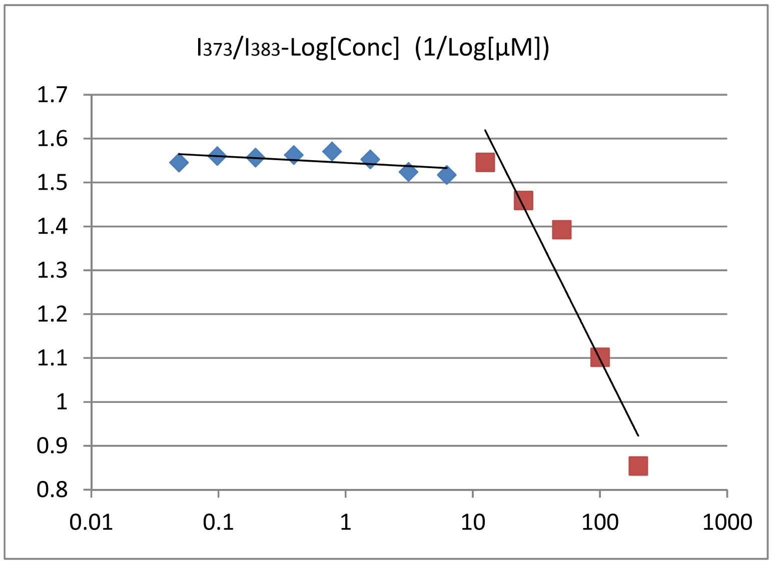

12.5	1.546312
25	1.459357
50	1.392954
100	1.102107
200	0.854315

Figure A4.55 Pal-PNA240-TAT_CMC_with NaCl

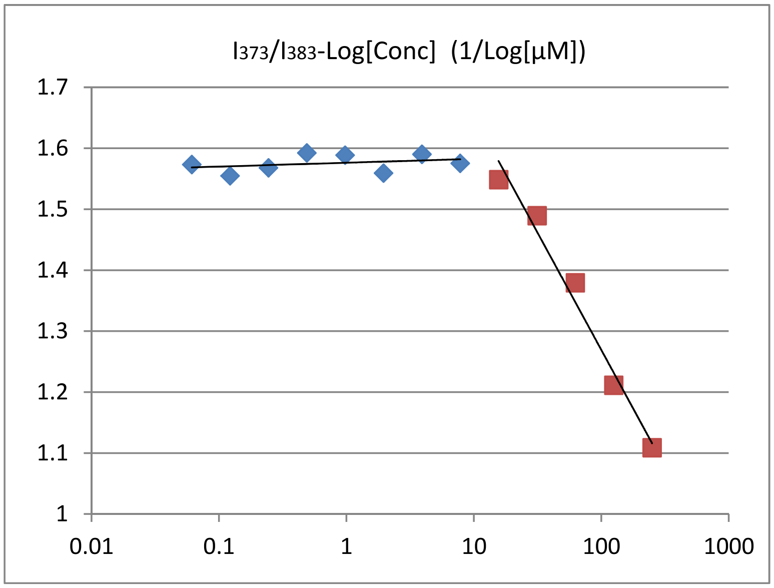

Figure A4.56 Ste-PNA240-TAT_CMC_without NaCl

Conc(µM)	I373/I383
0.061035	1.573348
0.12207	1.554733
0.244141	1.567925
0.488281	1.59228
0.976563	1.588709
1.953125	1.559211
3.90625	1.59015
7.8125	1.575167
15.625	1.548592
31.25	1.489413
62.5	1.379289
125	1.211344
250	1.10902

Conc(µM)	I373/I383
0.061035	1.550714
0.12207	1.515896
0.244141	1.525756
0.488281	1.557771
0.976563	1.548669
1.953125	1.54266
3.90625	1.519682
7.8125	1.509215

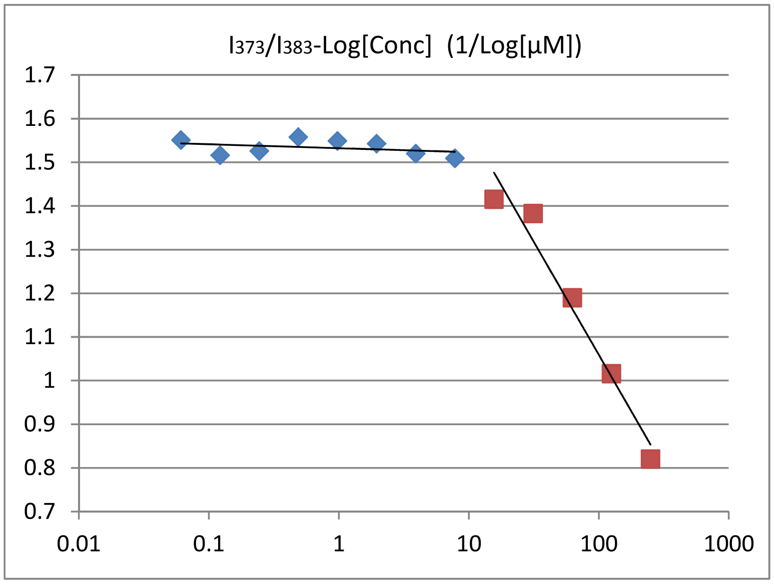

15.625	1.415584
31.25	1.382591
62.5	1.18969
125	1.01571
250	0.820413

Figure A4.57 Ste-PNA240-TAT_CMC_with NaCl

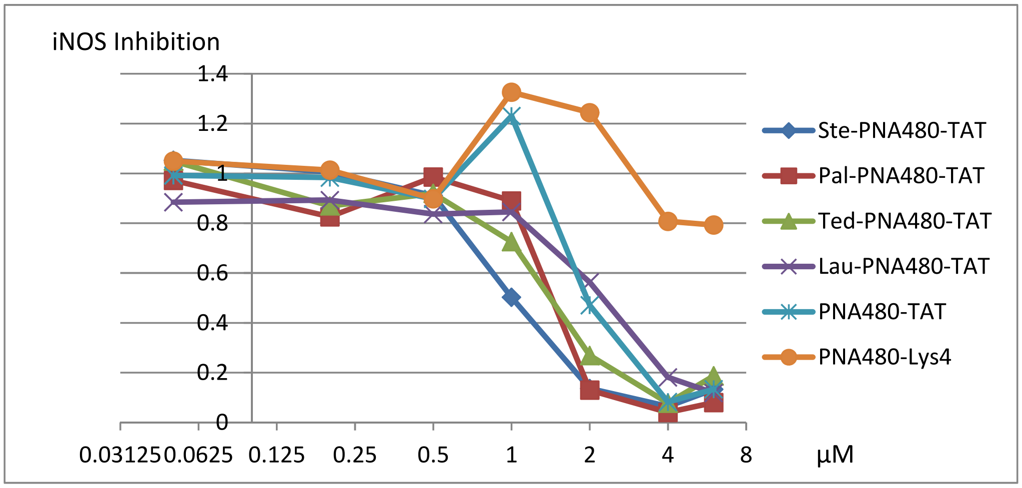

Figure A4.58 Griess Assay of iNOS Inhibition by Lipid-PNA480-TAT, PNA480-TAT and PNA480-Lys$_4$ conjugates

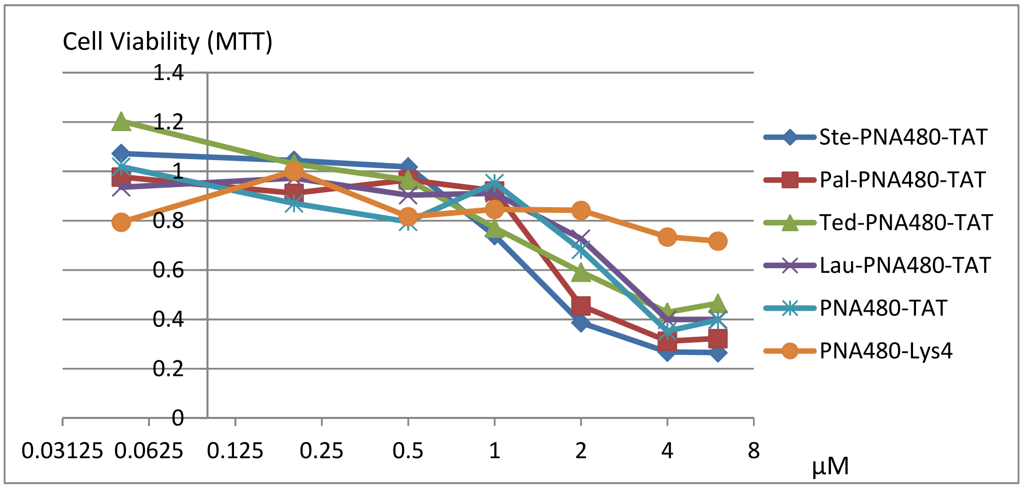

Figure A4.59 Cell Viability Assay of Lipid-PNA480-TAT, PNA480-TAT and PNA480-Lys4 conjugates

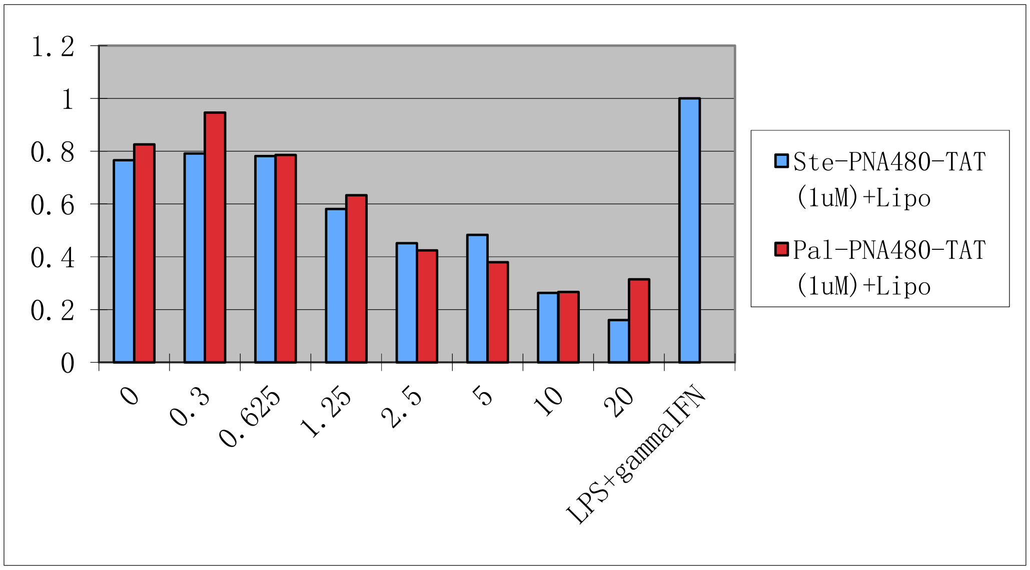

Figure A4.60 Griess Assay of iNOS Inhibition by Ste-PNA480-TAT and Pal-PNA480-TAT conjugates with different concentrations of Lipo

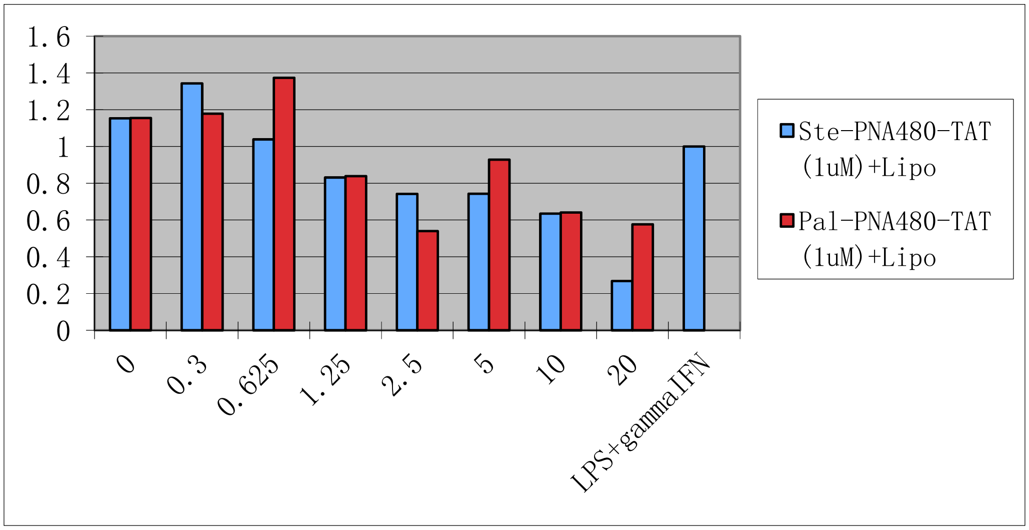

Figure A4.61 Cell Viability of Ste-PNA480-TAT and Pal-PNA480-TAT conjugates with different concentrations of Lipo